UNIONE EUROPEA
Fondo Sociale Europeo

Università degli Studi di Torino
Dipartimento di Fisica
Dottorato di Ricerca in Fisica

Solid-state detectors for beam monitoring in FLASH radiotherapy and for other harsh environment applications

Candidate: Elisabetta Medina

Cycle: 37th

Supervisor: Prof. Anna Vignati

Co-supervisor: Dr. Francesco Romano

PhD Program Coordinator: Dr. Paolo Olivero

Academic Years: 2021/22, 2022/23, 2023/24

Scientific-Disciplinary Sector: SSD PHYS-06/A

Project carried out with the financial support of:
Programma Operativo Nazionale Ricerca e Innovazione 2014-2020 (CCI2014IT16M2OP005), risorse FSE REACT-EU, Azione IV.4 "Dottorati e contratti di ricerca su tematiche dell'Innovazione".

UNIONE EUROPEA
Fondo Sociale Europeo

PON RICERCA E INNOVAZIONE

REACT EU

UNIVERSITÀ DI TORINO

Acknowledgements

I would like to express my deepest gratitude to those who have supported and guided me along the PhD:

- Dr. Anna Vignati, for her invaluable supervision throughout my doctoral years and for her support both scientifically and personally.
- Dr. Francesco Romano, for maintaining continuous communication and collaboration over these years, despite the distance.
- Dr. Massimo Camarda, for giving me the chance to explore diverse topics through SenSiC STLab and for the trust he has consistently placed in me.
- My colleagues in the Medical Physics group in Turin, for the shared dedication and valuable experiences we have had over these years.
- Dr. Arianna Morozzi and Dr. Faustino Gomez, the external reviewers of this thesis, for all your comments, suggestions, and for your time which helped to improve the manuscript.

I also gratefully acknowledge the support provided by:

- The National Operational Programme Research and Innovation 2014-2020 (CCI2014IT16M2OP005), funded by FSE REACT-EU, under Action IV.4 "PhDs and research contracts on innovation topics."
- The INFN CSN5 projects "FRIDA," "MIRO," and VIGA_S1921_EX-POST_21_01 (supported by Compagnia di San Paolo).
- The RADIATE project (European Union's Horizon 2020 research and innovation programme, grant agreement No 824096).

Your guidance, collaboration, and support have been instrumental in making this achievement possible.

Abstract

FLASH radiotherapy (RT) is an emerging technique characterized by single ultra-high dose-rate irradiation delivering therapeutic doses in less than 200 milliseconds. Preclinical studies have demonstrated that such irradiation profoundly alters the radiobiological response of tissues, achieving tumor control comparable to conventional RT while offering greater protection to healthy tissues.

In conventional RT, ionization chambers are the most commonly used beam monitoring devices. However, they are unsuitable for systematic radiobiological studies of FLASH irradiation due to the recombination effects at ultra-high dose-rates. This creates an urgent need to explore novel beam monitoring paradigms capable of supporting the unique demands of FLASH RT.

The INFN FRIDA project investigates several aspects posed by the FLASH effect and its revolutionary potential. Two of these aspects are the focus of this thesis: the exploration of innovative solutions based on solid-state technologies - specifically silicon, diamond, and silicon carbide (SiC) - for beam monitoring applications, and the modification of an ELEKTA LINAC SL18 linear accelerator at the Department of Physics, University of Turin (UNITO). This modification enables the LINAC to deliver electron beams at FLASH RT dose-rates, which were characterized in terms of beam output stability, pulse constancy, and beam flatness.

Various geometries of silicon sensors (strips, pads, and large segmented PIN sensors) coupled with multichannel front-end electronics readout systems were characterized under conventional and UHDR electron beams at the ELEKTA LINAC in Turin and the ElectronFLASH machine in Pisa, as well as under conventional proton beams at the CNAO National Hadrontherapy Center. Their response as a function of dose-per-pulse and bias voltage was evaluated.

Furthermore, a polycrystalline CVD diamond (pCVD) sample was studied and characterized under electron beams from the ELEKTA LINAC. Finally, SiC sensors, extensively tested on UHDR beams at Pisa, were also exposed to the electron beams from the LINAC to conduct comparative performance analyses of silicon and SiC detectors under identical experimental conditions.

The SiC sensors utilized in this work were manufactured by SenSiC STLab, a partner in this Ph.D. project. These sensors can be configured with a " freestanding membrane" by removing the substrate through selective electrochemical doping etching.

These devices were also studied beyond their FLASH RT applications, where SiC emerges as an ideal candidate for detection in harsh environments, requiring sensors to withstand high particle irradiation and/or elevated operating

temperatures.

For instance, this thesis includes a study on the radiation tolerance of SiC sensors to multiple damaging processes - both at room temperature and high temperatures - using the ion microprobe chamber installed at the Ruder Bošković Institute (Zagreb, Croatia), which allowed small areas within the same device to be exposed to different ion beams.

Additionally, I report on their potential use for X-ray beam position monitoring (XBPM), as an alternative to conventional beam intensity monitor (BIM) technologies which face numerous challenges, including diffraction effects, low signal strengths, non-uniform transparencies, and lack of position information. This study explores the potential of very thin SiC free-standing membranes as in-line, minimally-interfering beam position monitors with high lateral resolution for hard X-ray beamlines.

Contents

Nomenclature

ADR	Average Dose-Rate
ALLS	Absolute On-Line Dosimetry of Electron Beams in FLASH Regimen
AM	Advanced Markus
BIM	Beam Intensity Modulation
BPM	Beam Position Monitor
CCE	Charge Collection Efficiency
CCD	Charge Collection Distance
CMP	Comparator
CNAO	Centro Nazionale di Adroterapia Oncologica
CONV	Conventional
CPP	Charge Per Pulse
CPFR	Centro Pisano Flash Radiotherapy
DDS	Dose Delivery System
DPP	Dose-Per-Pulse
DR	Dose-Rate
EBRT	External Beam Radiation Therapy
EF	ElectronFlash
ESRF	European Synchrotron Radiation Facility
FBK	Fondazione Bruno Kessler
fD	FlashDiamond
FRIDA	FLASH Radiotherapy with hIgh Dose-rate particle beAms
FWHM	Full Width Half Maximum
HP	High Power
IAEA	International Atomic Energy Agency
IBIC	Beam Induced Charge Technique
IC	Ionization Chamber
IDR	Instantaneous Dose-Rate
INFN	National Institute of Nuclear Physics
IORT	Intraoperative Radiotherapy
LGAD	Low-Gain Avalanche Diodes
LINAC	Linear Accelerator
LP	Low Power
MBRT	Minibeam Radiotherapy
MLC	Multi-Leaf Collimators

MRT	Microbeam Radiotherapy
MU	Monitor Units
MV	Methyl Viologen
NTCP	Normal Tissue Complication Probability
OAR	Exposure to Organs at Risk
OSLDs	Optically Stimulated Luminescence Detectors
OTA	Operational Transconductance Amplifier
PCC	Pulse Counter
PDD	Percentage Depth Dose
PFN	Pulse-Forming Network
PG	Pulse Generator
PMMA	Polymethyl Methacrylate
PVD	Physical Vapor Deposition
PVDR	Peak-to-Valley Dose Ratio
QA	Quality Assurance
rXBPM	Resistive-XBPM
RBI	Ruder Bošković Institute
RCF	Radiochromic film
RF	Radiofrequency
ROI	Region of Interest
RT	Radiotherapy
SFRT	Spatially Fractionated Radiation Therapy
SiC	Silicon Carbide
SSD	Source-to-Skin Distance
STIM	Scanning Transmission Ion Microscopy
TCP	Tumor Control Probability
TCAD	Technology Computer-Aided Design
TLDs	Thermoluminescent Detectors
TLDs	Thermoluminescent Dosimeters
TPS	Treatment Planning System
UHDR	Ultra-High Dose-Rate
VHEE	Very High Energy Electron
WPlabels	Working Points Labels
XBPM	X-ray Beam Position Monitor
z_{ref}	Reference Depth
R_{50}	Depths Where the Absorbed Dose is 50% of the Maximum Dose
R_{80}	Depths Where the Absorbed Dose is 80% of the Maximum Dose
R_p	Practical Range

Chapter 1

Thesis outline

My activity is part of the INFN FRIDA project, which focuses the research on innovative techniques for the use of ionizing radiation for therapeutic purposes. Specifically, I have studied three solid-state technologies (silicon, diamond, and SiC) as potential solutions for monitoring ultra-high dose-rate (UHDR) beams, which find application in FLASH radiotherapy. Additionally, in collaboration with the industrial partner SenSiC STLab, I explored two aspects related to SiC detectors: the radiation hardness of these devices and their application as X-ray Beam Position Monitor (XBPM).

In Figure 1.0.1, I have graphically represented the topics covered in this thesis.

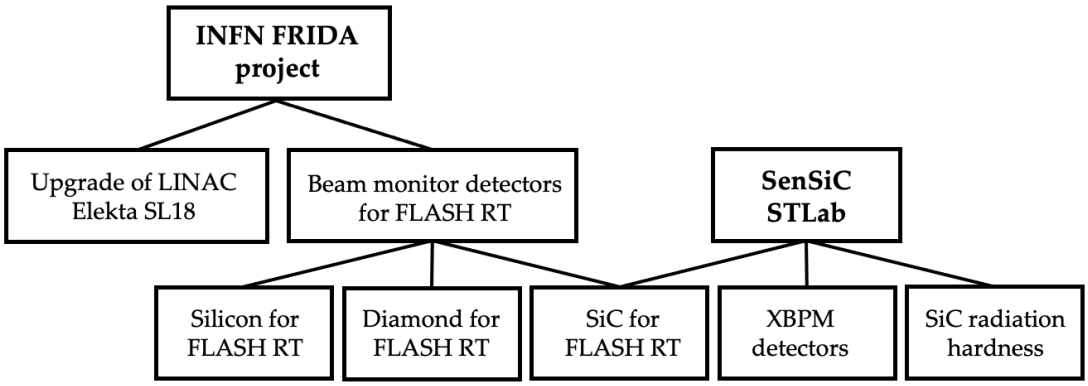

Figure 1.0.1: Schematization of the thesis content. Within the framework of the FRIDA project, the activities include the upgrade of the Elekta LINAC and the study of Si, diamond, and SiC as beam monitors for FLASH. In collaboration with SenSiC STLab, I also investigated SiC for X-ray beam monitoring applications and explored its radiation hardness.

A summary of the chapters included in this thesis, along with the publications in which the results of my work are presented. These include two journal articles and two conference proceedings as first author, as well as three co-authored journal articles.

Chapter 2 discusses the state-of-the-art of FLASH radiotherapy, the beam monitoring technologies currently used and proposed for this innovative form of radiotherapy, as well as a description of two FLASH beam facilities where I conducted measurement campaigns (Elekta LINAC in Turin and ElectronFLASH in Pisa). In preparation for the following chapters, in **Chapter 3**, I provide a

description of the functioning of semiconductor detectors, with a particular focus on the three technologies central to my PhD project (silicon, diamond, and SiC).

Before describing the results obtained with solid-state detectors, the modifications made to the ELEKTA LINAC at the Department of Physics in Turin, aimed at delivering UHDR beams, are presented in **Chapter** 4, and are also published in a co-authored paper (*Deut U. et al., "Characterization of a modified clinical linear accelerator for ultra-high dose-rate electron beam delivery"* [1]).

Afterwards, **Chapter 5** presents the results obtained from my work on silicon detectors. Here I focused on the characterization of silicon sensors and testing their performance under electron (both conventional and FLASH) and proton beams. The most significant results from these campaigns are reported in a paper (*Medina E. et al., "First experimental validation of silicon-based sensors for monitoring Ultra High dose-rate electron beams"* [2]) and a proceeding (*Medina E. et al., "Monitoring electron and proton beam profiles with segmented silicon sensors"* [3]).

Subsequently, in **Chapter 6**, I describe the work on a polycrystalline CVD diamond (pCVD) sample, in collaboration with a team of experts from the Department of Physics. I investigated the feasibility of using this technology for monitoring UHDR beams. The results of this study are detailed in a proceeding (*Medina E. et al., "Characterization of CVD diamond detector with FLASH electron beam from modified LINAC accelerator"* [4]).

Lastly, **Chapter 7** describes my research activities in the field of SiC detectors, in collaboration with SenSiC STLab (Catania), an industrial partner of my PhD. In particular, the study of SiC sensor as beam monitor for UHDR beams is reported in Section 7.1, where the content of two papers of which I am co-author is reported (*Romano F., et al., "First Characterization of Novel Silicon Carbide Detectors with Ultra-High dose-rate Electron Beams for FLASH Radiotherapy"* [5]; *Milluzzo G. et al., "Comprehensive dosimetric characterization of novel silicon carbide detectors with UHDR electron beams for FLASH radiotherapy"* [6]). To confront this technology with silicon, a comparative performance study of these two technologies under UHDR beams from the LINAC in Turin is described in Section 7.2.

Not strictly related to the topic of applications for FLASH radiotherapy, I also studied the radiation hardness of SiC sensors under proton beams at the Ruder Boskovic Institute (Zagreb, Croatia). The results are reported in Section 7.3, and a paper presents the findings from these measurements (*Medina E. et al., "Radiation Hardness Study of Silicon Carbide Sensors under High-Temperature Proton Beam Irradiations"* [7]).

While in Section 7.4, I explored the use of SiC devices also for X-ray beam position monitoring applications. In this regard, I am currently working on a paper to present these results (*Medina E. et al., "Ultra-thin Silicon Carbide free-standing membranes as beam intensity and position monitors for soft X-ray beamlines"*).

To summarize, in **Chapter 8** the discussions and the conclusions of all the research activity described in the thesis is presented.

Chapter 2

FLASH radiotherapy and beam monitor technologies

2.1 Charged Particle Radiotherapy

Radiotherapy (RT) plays a crucial role in cancer treatment, with approximately 50% of cancer patients receiving either curative or palliative RT, often in combination with surgery. It encompasses all methodologies that use radiation for therapeutic purposes, primarily focusing on cancer treatment. It can be divided into two main branches: External Beam Radiation Therapy (EBRT) and brachytherapy. Within EBRT, we find several techniques, including superficial X-ray therapy (also known as orthovoltage), megavoltage electron and photon beam therapy (using electron linear accelerators), gamma-ray therapy, hadrontherapy (protons and ions), and intraoperative RT.

When radiotherapy is used to treat tumors, there is a therapeutic window in which the dose delivered to the patient must be sufficient to achieve a high Tumor Control Probability (TCP ≥ 0.5) while maintaining a low Normal Tissue Complication Probability (NTCP ≤ 0.05). Advances in radiotherapy have consistently been tied to improvements in dose distribution, which is closely linked to the performance of accelerators, beam delivery methods, and treatment planning systems. Between the 1930s and 1950s, progress was made by increasing photon energy, improving the depth of maximum dose penetration, and reaching the megavoltage range, which significantly enhanced patient survival rates. However, despite the ongoing advancements in photon-based RT, the physical limitations of photon beams prevent avoiding high doses in the tissue regions both before and beyond the tumor, as illustrated in Figure 2.1.1. Particle therapy exploits the Bragg peak phenomenon to concentrate the maximum dose within the tumor while minimizing exposure to surrounding healthy tissues. As a result, particle therapy delivers targeted radiation to tumors and nearby areas, reducing the overall radiation dose to healthy tissues and theoretically minimizing collateral damage.

As of the end of 2021, approximately 325000 patients worldwide had been treated with particle therapy, primarily using protons (280000) and carbon ions (42000) [9]. Although the number of centers offering treatment with light ions (mainly protons) has increased over the past decade, its growth remains limited compared

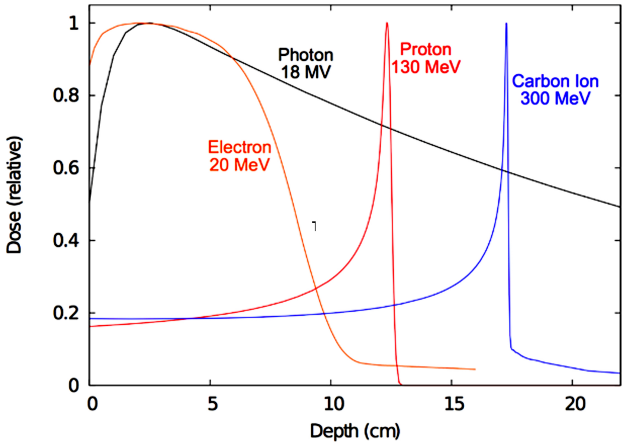

Figure 2.1.1: Depth dose curves for radiotherapy. Dose distributions as a function of depth in water shown for various clinical radiation beams. [8]

to conventional RT, mainly due to the high costs involved. For instance, the construction of a proton therapy center can range from 20 million for a single-room setup to over 225 million for multi-room facilities, making them some of the most expensive medical devices ever built. In comparison, facilities for conventional RT, like IMRT, are far less expensive to establish.

2.2 FLASH Radiotherapy

Technological advancements in imaging technology and RT delivery methods have significantly increased patient survival rates and improved the precision in delivering doses to tumor targets with minimal exposure to organs at risk (OAR) and the reduction of side effects. Some hypofractionated treatments (e.g., stereotactic RT) have demonstrated that very high doses in a single treatment or in a few fractions greatly increase the overall survival probability. However, patients may still experience severe toxicity from RT treatment.

An aspect of radiotherapy currently under extensive study is the radiobiological response occurring at ultra-high dose-rates (UHDR). Studies related to the reduction of cell death at extremely high doses began around 1960-1980 [10, 11], when it was observed, for example, that there was a sparing of intestinal cell death in mice, when exposed to such levels of radiation. Since 2014, thanks to the work of Favaudon [12], interest in this area has resurfaced, and research activity in the field has surged.

Unlike conventional clinical dose-rates (CONV), which range from 0.01 to 0.40 Gy/s, UHDR RT was initially implemented through microsecond pulses of electrons (at 5 MeV energy) with intra-pulse dose-rates between 10^6 and 10^7 Gy/s, an average dose-rate over time exceeding 40 Gy/s, and a duty time of less than 500 ms [13]. Table 2.1 compares the beam temporal characteristics of UHDR and conventional radiation therapy using electrons, while Figure 2.2.1 (a) illustrates different interpretations of dose-rate, defined over the course of an entire treatment, one fraction, or within a single pulse.

Beam Characteristics	CONV	UHDR
Dose-per-pulse (D_p)	$\sim$ 0.4 mGy	$\sim$ 1 Gy
Dose-rate: Single Pulse ($\dot{D}_p$)	$\sim$ 100 Gy/s	$\sim 10^5$ Gy/s
Mean dose-rate: Single Fraction ($\dot{D}_m$)	$\sim$ 0.1 Gy/s	$\sim$ 100 Gy/s
Total Treatment Time (T)	$\sim$ days/minutes	$<$ 500 ms

Table 2.1: Typical temporal beam characteristics for conventional (CONV) and UHDR using electrons.

The use of this type of treatment has shown a significant reduction in normal tissue toxicity in various organs while maintaining at least equivalent levels of tumor control. This phenomenon is recognized in the literature as the "FLASH effect". This effect theoretically allows for a drastic mitigation of adverse reactions to aggressive RT treatments even with limited geometric conformity, and/or the extension of the prescribed dose to unprecedented levels of tumor control.

Figure 2.2.1 (b) shows the trends of TCP, normal tissue complications (NTC), and tumor control without normal tissue complications (TC without NTC) for both conventional and FLASH therapies. The therapeutic window, which is the dose range optimized to ensure an effective and safe treatment, is located at the peak of the TC without NTC curve. This window expands in the case of FLASH treatment.

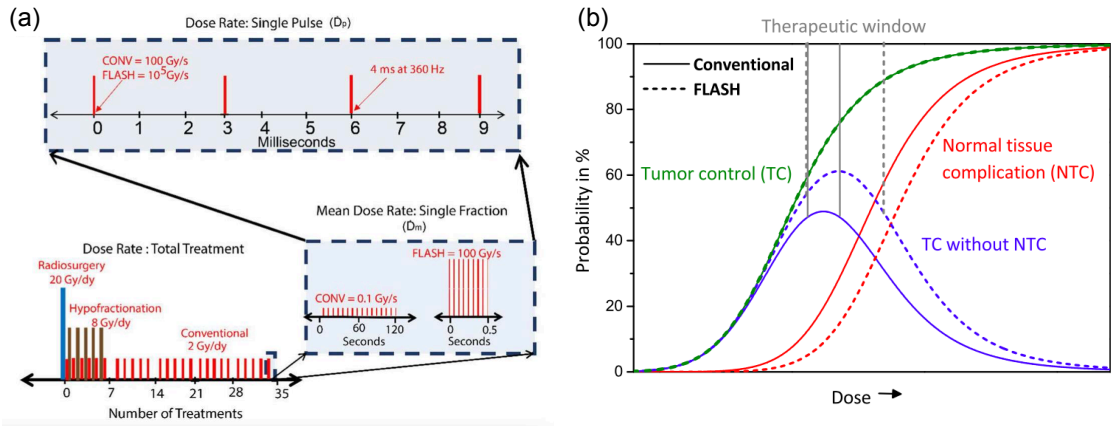

Figure 2.2.1: (a) Dose-rate schemes in radiation therapy indicating different interpretation of dose-rates [13]. (b) Illustration of the dependence of tumor control probability (TCP, green) and normal tissue complication probability (NTCP, red) on dose for conventional (solid lines) and FLASH (dashed lines) radiotherapy. The maximum of the TCP without NTCP curve (blue) defines the therapeutic window [14].

Recent research into FLASH-RT has highlighted its association with biological effects linked to oxygen, although the brief exposure duration complicates direct evidence gathering [15]. Consequently, the exact biological mechanisms behind FLASH-RT remain incompletely understood and sometimes contradictory. These mechanisms encompass physical-chemical hypothesis (i.e. oxygen depletion, the Fenton effect, free radical recombination) and biological mechanism (i.e. stem cell response, immune modulation, and vascular effects). The oxygen depletion

hypothesis, for example, is explained as follows: tissues rich in oxygen exhibit greater radiosensitivity compared to hypoxic tissues under the same irradiation conditions. Considering the extremely brief duration of a FLASH beam (on the order of microseconds), tissue oxygen is depleted and not replenished in time by surrounding blood. This temporary lack of oxygen may be one reason for the protection of healthy tissues compared to conventional therapy. Indeed, hypoxia is believed to lead to radiation resistance when exposed to very high dose-rates [16]. However, increasing evidence suggests that the oxygen depletion hypothesis alone cannot fully explain the protective effect of FLASH-RT on normal tissues.

Current studies have not fully elucidated these mechanisms, necessitating further investigation to clarify the true mechanisms of FLASH-RT and determine their respective contributions.

It is not yet known whether the FLASH effect depends on the type of radiation that activates it [17]. It has been observed with photons and protons, but most preclinical studies showing this effect have used **electron** beams generated by dedicated or modified LINACs, with energies not exceeding 20 MeV, energy levels suitable only for the treatment of superficial tumors. Numerous in vivo radiobiological experiments with ultra-high dose-rate electron beams have been conducted on various species including small rodents, developing organisms, and large mammals on clinical endpoints [18, 19, 20]. The expected sparing effect has been observed on normal cells at ultra-high dose-rates, as well as an effect on tumor tissues comparable to conventional RT.

Studies have also been conducted with **proton** beams at ultra-high doses. In this case, research has been performed employing pulses from an RF accelerator and also with laser-accelerated protons. Recent technological developments have been investigated by several groups aiming to harness the potential modern clinical proton therapy facilities in the context of FLASH RT. Current pencil beam scanning systems are already capable of delivering high doses, reaching up to thousands of Gy/s, presenting a promising environment for future research and potential rapid clinical translation. Advancements in diagnostic capabilities and beam dosimetry will be crucial for moving forward.

The potential use of very high-energy electron (**VHEE**) beams for radiotherapy was first proposed in 2000 [21]. Studies conducted so far have demonstrated several advantages: VHEE beams can penetrate up to 40 cm into tissues, making them ideal for treating deep-seated tumors, even in the FLASH RT regime. Additionally, they offer precise penumbra and are less sensitive to tissue inhomogeneities compared to X-rays and protons, allowing for more controlled delivery of conformal doses to lesions near tissues of varying densities. Clinical prototypes for VHEE RT machines are still under development [22, 23].

2.3 Beam monitor technologies

To achieve global consensus on the FLASH method, *in vivo* biological validations are required. However, the reliability and precision of current experimental studies are limited by the lack of traceable active detectors.

In **conventional therapy**, the beam monitor consists of a set of transmission ionization chambers that cover the entire beam cross-section. These chambers are designed to monitor the delivered dose, dose-rate, and other operational parameters such as beam homogeneity and symmetry. The collected charge is monitored during irradiation and quantified in terms of "Monitor Units" (MU), where one MU corresponds to 1 cGy under standard reference conditions. Once the predefined number of MUs is reached in the primary chamber, irradiation is interrupted. A secondary chamber is used for redundancy and safety during treatment.

Ionization chambers are also employed for LINAC commissioning in radiotherapy and for quality assurance (QA). Due to their simplicity and robustness, they offer several advantages, including ease of use and resistance to aging, even after years of irradiation. Figure 2.3.1 shows a picture of an ionisation chamber used in Varian TrueBeam.

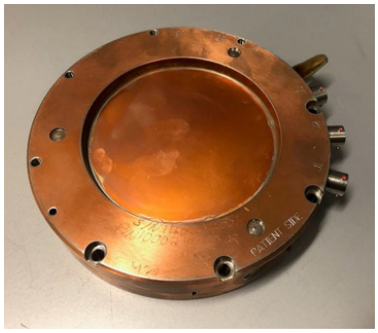

Figure 2.3.1: Kapton monitor chamber (P/N100029495-02) used in Varian TrueBeam [24].

Historically, several efforts have been made in the field of ionization chambers by the medical physics group in Turin. For instance, Figure 2.3.2 illustrates the MATRIX3 segmented ionization chamber, developed by the TERA Foundation (INFN of Turin), which enables the acquisition of a two-dimensional map of a clinical beam. Additionally, the ionization chambers developed by the Turin group in collaboration with the Fondazione CNAO (the Centro Nazionale di Adroterapia Oncologica) are currently used in the dose delivery system (DDS) to monitor and guide ion beams accelerated by a dedicated synchrotron and to distribute the dose with a full 3D scanning technique [25, 26].

However, FLASH irradiations lead to radical changes in beam characteristics, delivery time structure, and, most importantly, in both the average and instantaneous dose-rates. This highlights the limitations of ionization chambers. These chambers cannot be used for ultra-high dose-rates because of the high recombination rate, which depends on the amount of charge created per unit volume and time, i.e., the dose-rate to be measured. Furthermore, ionization chambers require tens of microseconds to collect the charges (30–300 μs for air gaps between 0.5 to 5 mm), making them too slow to monitor a pulsed FLASH beam, which delivers tens of Gy in a few microseconds. This situation underscores the need for new monitoring devices, which are crucial for conducting preclinical studies on the biological mechanisms supporting the effectiveness of FLASH therapy.

Currently, in **FLASH radiotherapy** (FLASH-RT), passive detectors such as

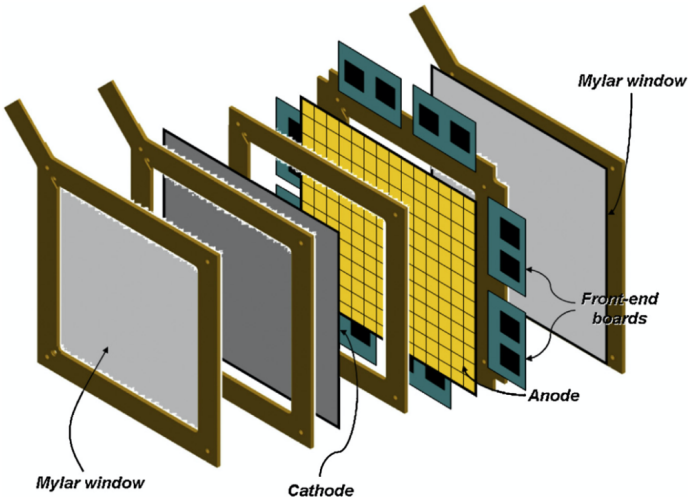

Figure 2.3.2: Schematic view of the MATRIX pixel ionization chamber [27, 28].

alanine, radiochromic films, thermoluminescent dosimeters (TLDs), and methyl viologen (MV) are employed. These detectors are characterized by dose-rate linearity (dose-rate independence) and have been successfully used for dosimetry in small fields (TLD, film, and alanine). However, the evaluation procedure for passive detectors is complex, time-consuming (requiring post-irradiation processing and calibration for each batch), and labor-intensive. Moreover, the associated uncertainties can be significant if the evaluation process is not well-defined (for the alanines an accuracy of 2%-7% for doses larger than 10 Gy is reported in [29]).

Some studies have focused on reducing the reading time to optimize alanine measurements, aiming for rapid and accurate dosimetry in FLASH RT [30]. Nevertheless, despite the robustness and reliability of these devices, the lack of real-time information limits their use as beam monitors in the context of future clinical translation.

Among the active detectors that can meet this need are: adapted ionization chambers (ICs), silicon, diamond, and silicon carbide (SiC) detectors.

With regard to **ionization chambers**, corrections are necessary when implemented under ultra-high dose-rate beams due to ion recombination, a phenomenon that has been extensively studied [31]. Several methods exist to calculate the ion recombination factor k_s - and thus chamber collection efficiencies $1/k_s$ - for ICs [32]. First of all, analytical recombination models developed by *Boag et al* [33] have been studied, which take into account the fraction of charge measured by the chamber as result of the collection of free electrons before they attached to neutral oxygen molecules. However, for high dose-per-pulse IORT beams, this standard recombination correction technique could overestimate the recombination factor by 20%. As such, *Di Martino et al* [34] developed a high dose-per-pulse specific analytical recombination models for Intraoperative Radiotherapy (IORT) applications. Additionally, a logistic model for the recombination in high dose-per-pulse beams, used by *Petersson et al* [35], has also been proposed, investigating the dose-per-pulse from 7 mGy to 15 Gy, determined through relative methods.

As an alternative to using correction factors, it is possible to modify the geometry of ionization chambers. One possible instrumental solution, for example, is the use of small-gap chambers, which enhance the free-electron component (with higher mobility than the ions produced in air) and reduce the carrier densities in the gap, thus mitigating the recombination effect [14]. Among these studies, [36] simulations have shown that the ion recombination factor (k_s) for plane-parallel ionization chambers at 300 V for 5 Gy/pulse is nearly 1 when the electrode spacing is less than 0.30 mm. Consequently, the authors developed a prototype ionization chamber with a 0.27 mm gap between electrodes. The prototype was tested in a real beam, where the charge measured per pulse (in nC) exhibited an excellent linear response as a function of dose-per-pulse, and the results were in agreement with the simulation predictions (Figure 2.3.3).

Another possible solution to address the challenges faced by ionization chambers

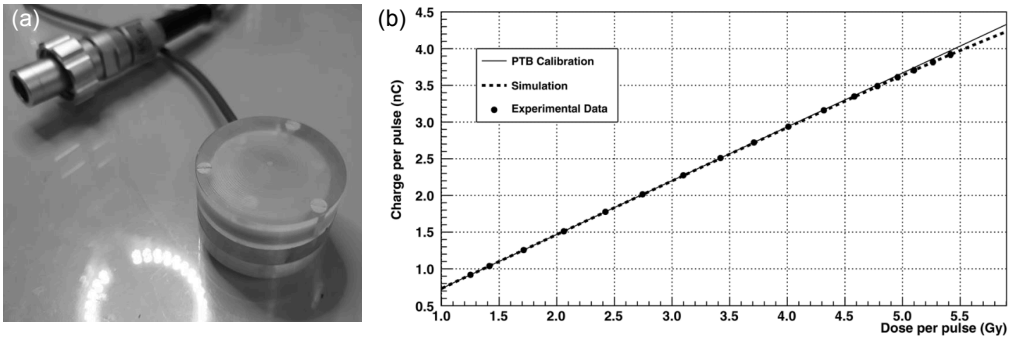

Figure 2.3.3: (a) UTIC1 prototype with electrode spacing. (b) Results obtained at PTB in the water tank for the UTIC1 prototype at a bias voltage of +250 V. The experimental charge obtained as a function of dose-per-pulse is depicted. The dashed line corresponds to the expected results from the simulation. [36]

in FLASH conditions, such as the electric field distortion throughout the sensitive volume, is to modify the gas inside the chamber. The ALLS (Absolute On-Line Dosimetry of Electron Beams in FLASH Regimen) chamber [37] was designed using noble gases and by adjusting the pressure, ensuring accurate dosimetry with an error margin of less than 1% for dose-per-pulse values up to 40 Gy. The use of a noble gas eliminates recombination issues and ensures that only direct recombination between positive ions and electrons occurs. This setup allows for an analytical description of the electric field during the charge collection process. Unfortunately, these strategies for using ionization chambers in FLASH regimes are more effective for dosimetry applications rather than as beam-monitor detectors. Distinct challenge for transmission detectors lies in their need for a fast-feedback signal, which can be problematic due to the timing structure of UHDR beams.

Some prototypes of **2D transmission ICs** have been developed specifically for FLASH proton beams accelerated by cyclotrons, where the dose-per-pulse allows their use [38]. However, this becomes problematic for pulsed beams such as those generated by LINACs for radiotherapy, where the higher doses per pulse required to achieve comparable average dose rates increase the risk of ion recombination effects.

Beam current transformers hold promise for monitoring FLASH electron beams [31]. However, although commonly used in high-energy physics, these systems have not yet been applied in clinical environments. This is likely due to their fixed placement along the beamline, which may not fulfill the ideal requirement of being positioned beyond the last element that disturbs the beam, their inability to resolve the beam spatially, and challenges related to their limited dynamic range for current measurements.

The physical properties of luminescent detectors make them particularly valuable for FLASH applications. These technologies include thermoluminescent detectors (TLDs), optically stimulated luminescence detectors (OSLDs), organic and inorganic scintillators, and Cherenkov radiation detectors. **TLDs and OSLDs**, despite lacking real-time readout capabilities, are highly relevant for high dose-rate dosimetry due to their remarkable independence from dose rate [39]. Additionally, TLDs can be fabricated in small or powdered forms, which is advantageous for small-field dosimetry where high spatial resolution is required. However, their primary limitation lies in being restricted to point-based measurements. **Scintillators** also hold great promise in the context of FLASH. Their rapid rise and decay times, radiation hardness, and high detection efficiency make inorganic scintillators particularly suitable for applications requiring precise time resolution. The immediate emission of light, when combined with the high frame-rate imaging capabilities of modern sensors, enables scintillators to perform online monitoring of machine output and dose delivery during FLASH irradiation [40, 41]. **Cherenkov radiation detectors** have also been investigated for their potential in FLASH online dose monitoring, notably by Favaudon et al. [42]. Their study showed that Cherenkov emission scales proportionally with beam energy, pulse duration, and dose, while avoiding saturation effects. These findings highlight Cherenkov radiation as a promising candidate for real-time dose monitoring in both high and low dose-rate scenarios.

My research work has focused on the use of solid-state technology as a potentially useful solution for monitoring ultra-high dose-rate (UHDR) beams.

Among solid-state technologies, **diamond** has already been extensively studied, as evidenced by the literature. Diamond detectors offer advantageous properties such as radiation hardness, high intrinsic resistivity, and high saturated carrier velocity, making them especially suitable for the high charge density environment in FLASH RT. They also maintain a high water equivalence in the sensitive volume in terms of effective atomic number. Additionally, their response remains stable with respect to the accumulated dose. Nevertheless, challenges remain in achieving dose-rate linearity in high-intensity electron beams and the capacity to cover areas of several cm^2.

A commercially available synthetic single crystal diamond detector, the microDiamond from PTW-Dosimetry, has been recently studied under UHDR conditions [43]. The authors investigated the dose-per-pulse in the microDiamond relative to the reference dose for different sensitive areas and series resistance introduced directly at the output of the detector. It was observed that saturation occurs in the commercial microDiamond detector at various dose-per-pulse levels. The linear range can be extended into the ultra-high dose region by reducing the

sensitivity and series resistance. Furthermore it has been demonstrated that the flashDiamond (fD) prototype, proposed by [44], exhibits a linear response across the entire studied dose-per-pulse range (ranging from 1.2 to 11.9 Gy, by varying the beam applicator or pulse duration from 1 to 4 μs) as shown in Figure 2.3.4 [45].

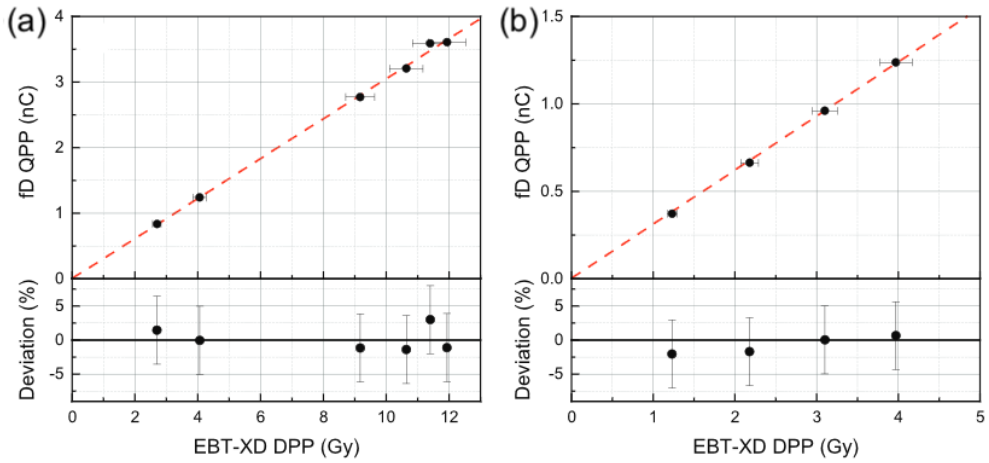

Figure 2.3.4: Charge per pulse of the flashDiamond (fD) as a function of the dose-per-pulse measured by EBT-XD films. The DPP was varied by changing the PMMA applicator (a) and the pulse duration (b) with 9 MeV electrons [45].

Two alternative solid-state technologies that could be used for this purpose are silicon and silicon carbide.

Silicon-based devices were initially proposed for dosimetry and beam monitoring due to their advanced manufacturing processes, exceptionally high sensitivity (tens of thousands of times greater than ionization chambers with the same active volume), and rapid response times. Today, silicon detectors devices are widely used in advanced RT techniques [46] for relative and in vivo dosimetry and quality assurance (QA) procedures. However, standard silicon, when exposed to ultra-high dose-rates, generate sufficient charge to potentially saturate both the sensor and the readout system. Efforts to address this challenge have emerged in the dosimetry of synchrotron microbeam RT, employing thin sensors to enhance stability and response linearity [47, 48]. Exploiting the performance of ultra-thin ($\sim$ 10 μm thick), segmented, and highly polarized silicon sensors makes them promising candidates for addressing the challenges of monitoring FLASH beams. Their high sensitivity, exceptional spatial resolution, and the advantages of well-established manufacturing technology contribute to their suitability for this application [49]. However, several unknowns remain regarding the use of silicon sensors for ultra-high dose-rate monitoring, including dose-rate linearity, recombination effects, and radiation resistance, necessitating parallel exploration of various alternatives.

Silicon Carbide (SiC) could be considered the ideal compromise between the industrial maturity of silicon and the robustness of diamond, with particularly high electrical stiffness, high speed of electrical charges, high melting temperature, high thermal diffusivity and a high industrial maturity. At the start of this project, preliminary simulations have shown a dose-rate linearity up to 10^{11} Gy/s on

X-ray beams for SiC membrane (2 μm thickness).

This thesis explores innovative silicon, diamond, and SiC detectors to identify necessary improvements for optimizing spatial resolution, dose-rate linearity, response speed, and radiation hardness in the field of FLASH RT.

2.4 FRIDA project

The FRIDA INFN project addresses several challenges posed by the FLASH effect and its potential revolution. The aim of the FRIDA project is to contribute to finding answers to many unresolved questions and to contribute to a definitive assessment of the feasibility of clinical routine FLASH irradiation for oncology patients. Among the objectives of FRIDA are contributing to the scientific community's understanding of the mechanism, mastering beam delivery technologies, and implementing beam monitoring and dosimetry detectors supported by reliable treatment planning software. Very high energy electrons (VHEE) will also play a central role, providing an additional tool for treating deep-seated tumors that are challenging to address with traditional electrons radiotherapy.

The Medical Physics group of the University of Turin is primarily involved in the FRIDA project on two fronts:

- **Work Package "WP2 - FLASH beam delivery":**
  Turin unit is tasked with the modification of a conventional clinical ELEKTA LINAC (4-18 MeV) of Turin Physics Department (UNITO) and INFN, fully dedicated to research. The modifications allow delivering electron beams achieving FLASH RT rates, controlling electron pulses, beam output stability, pulse constancy and beam flatness. The upgraded LINAC will be used to test beam monitors/dosimeters.

- **Work Package "WP3 - FLASH beam monitoring & dosimetry":**
  The group is involved in the development and characterization of detector systems based on solid-state technologies for Beam Monitoring and Dosimetry. In particular the performances of thin silicon and diamond detectors, and "Free-standing membranes" Silicon Carbide (SiC) detectors, developed by SenSiC STLab, are studied and compared.

2.5 UHDR beams facilities

Preclinical studies on FLASH have primarily utilized prototype linear accelerators (linacs) with fixed horizontal electron beams capable of achieving ultra-high dose rates [12, 50, 51, 19, 52]. Additionally, synchrotron radiation at ultra-high dose rates has been shown to induce the FLASH effect at the European Synchrotron Radiation Facility (ESRF) in Grenoble, France [53]. However, these highly specialized and expensive research tools are not easily accessible to many researchers in the field. Researchers at the Stanford University School of Medicine (Stanford, California, USA) have demonstrated that ultra-high dose rates can be achieved using a conventional clinical linac for radiotherapy, with technical assistance

from the linac manufacturer (Varian Medical Systems, Palo Alto, California, USA) [54]. This procedure was repeated in several conventional LINACs in different facilities [55, 56, 57, 58, 59]. Similarly, researchers from the Institut Curie (Orsay, France) have presented a setup enabling FLASH irradiation with protons using their clinical proton therapy system with pencil beam scanning [60]. However, proton therapy machines are complex and costly, and to expand the scientific foundation and explore the benefits of FLASH-RT, simplified research platforms are necessary.

Table 2.2 provides an overview of various FLASH radiation sources, including their type, energy, and mean and instantaneous dose rates [61].

During my doctoral research, I conducted experiments with FLASH electron beams at two facilities: the Elekta LINAC at the Department of Physics in Turin and the ElectronFlash accelerator in Pisa. Below, I provide further details about these setups.

Table 2.2: Various FLASH radiation sources with their type, energy, and mean and instantaneous dose rates.

Source	Radiation Type	Energy (MeV)	Mean DR (Gy/s)	Instantaneous DR (Gy/s)
Kinetron [42]	Electrons	4.5	1000	2×10^7
Varian 21 EX [59]	Electrons	9	900	1.7×10^6
NLCTA [62]	VHEEs	120	90	9×10^{12}
ESRF [63]	X-rays	0.102	37	1.8×10^4
HyperScan [64]	Protons	230	200	1.3×10^4

2.5.1 Elekta SL18 LINAC

The LINAC Elekta SL 18 MV was installed in 2016 at the Physics Department of the University of Turin (UNITO) and is entirely dedicated to research. This machine can generate both X-rays (up to 18 MV) and electrons (4 - 18 MeV), delivering the beam in 2 μs pulses at a Pulse Repetition Frequency (PRF) between 6 and 400 Hz. The accelerator head is equipped with multi-leaf collimators (MLC) and diaphragms that precisely shape the beam, allowing radiation fields from 3×3 cm^2 to 40×40 cm^2 at the isocenter position. The latter corresponds to a distance of 100 cm from the source, and therefore to a source-to-skin distance (SSD) of 100 cm. It also contains a monitoring system consisting of two independent ionization chambers (ICs), one acting as the primary reference and the second as a backup. Chapter 4 of this thesis is entirely dedicated to the description of this machine and the modifications made to enable the delivery of high dose-rate beams.

2.5.2 ElectronFlash LINAC

Some of the experiments described in this thesis have been performed at the LINAC ElectronFlash of the CPFR in Pisa, funded by Fondazione Pisa and

manufactured by the Italian company SIT-Sordina [65]. Below is a brief history of this machine.

In 2020, a work has been published [66] about the successfull convertion of an intraoperative radiation therapy (IORT) accelerator into a FLASH research machine, drawing inspiration from the work of other groups, such as [55]. The accelerator, the IORT NOVAC7, operates with four nominal electron energies (3, 5, 7, and 9 MeV) and can achieve a maximum dose-per-pulse of up to 13 cGy/pulse with a pulse duration of approximately 2.5 μs. The transformation involved a series of modifications to the collimation system of the clinical accelerator. Passive applicators of varying lengths were mounted on the accelerator head to modify the source-to-skin distance (SSD), thereby achieving different doses per pulse. These applicators are cylindrical PMMA tubes with 5 mm thick walls and internal diameters up to 10 cm. Utilizing a 7 MeV electron beam (the most commonly used in clinical practice), four different SSD configurations (100 cm, 50 cm, 7 cm, and 1.6 cm) were tested. Two of these configurations exhibited dose-rates exceeding 40 Gy/s, with the maximum dose-per-pulse measured being 0.03, 0.3, 3.9, and 18.2 Gy, respectively.

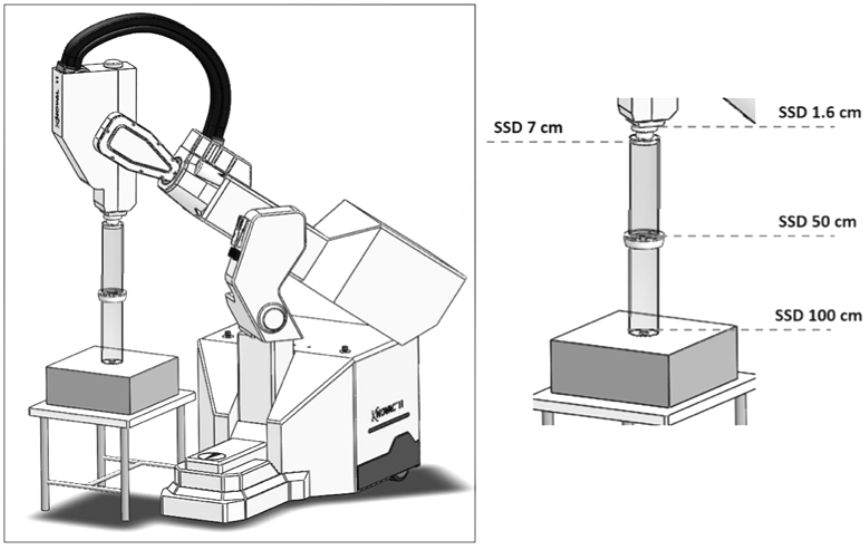

Figure 2.5.1: Four collimation configurations obtained acting on Novac7 collimation system architecture [66].

Following this successful adaptation, Sordina IORT Technologies S.p.A (S.I.T) developed and constructed the ElectronFlash accelerators, initially without a gun triode. The ElectronFlash accelerator is compact (1.315 m $\times$ 2.131 m), allowing for installation in a standard RT bunker. Three versions were designed, each offering two different electron energies: 5 and 7 MeV, 7 and 9 MeV, and 10 and 12 MeV. The first version employs the same collimation system as mounted on the NOVAC7 accelerator head and can achieve maximum average dose-rates of 1500 Gy/s for a 10 cm field and up to 10^4 Gy/s for small fields (with doses per pulse up to 40 Gy/pulse). The pulse duration can be adjusted between 0.5 μs and 4 μs in 0.5 μs increments. The beam monitoring system consists of a non-invasive fluence measurement using toroidal inductors near the exit window and energy measurement using a pick-up inside the resonant cavity. However, this version

has two notable drawbacks: the interdependence of key parameters (dose-rate, dose-per-pulse, and pulse duration), and the slight difference in the electron spectrum between non-FLASH and FLASH modes.

The updated version of this accelerator was built with a gun triode, as the one installed at the Centro Pisano Flash Radiotherapy (CPFR) for 7 and 9 MeV [67] used for the test described below. This improved version can irradiate under various conditions, such as conventional and FLASH, without altering the energy spectrum and experimental setup. The electron beam at the exit window has

Figure 2.5.2: SIT ElectronFlash (EF) accelerator of the Centro Pisano Multidisciplinare sulla Ricerca e Implementazione Clinica della Flash Radiotherapy (CPFR) in Pisa, Italy.

a gaussian shape of around 1 cm FWHM. The uniformity of the dose profile at the surface of a patient or water phantom is obtained by means of the PMMA plastic applicators of different lengths and diameters. For a fixed beam current, the size of the applicator (from 1 to 12 cm diameter) changes the dose-per-pulse values at the irradiation point. Maintaining the energy spectrum unchanged (i.e., keeping the same experimental setup), it is possible to choose among twelve values of beam current (in the range 1-100 mA at the exit window), and change the pulse duration (in the range 0.5 - 4 μs) and the pulse frequency (in the range 1-249 Hz). This allows varying each beam parameter of interest for the FLASH effect investigation, such as dose-per-pulse, pulse duration, average-dose-rate, instantaneous dose-per-pulse in a wide range, one independently from the others, minimizing the setup uncertainties.

During the experiments reported in this thesis, the electron beam energy of 9 MeV and the applicator of 30 mm diameter and 15 cm length were used. The pulse duration was set at 4 μs, and 10 pulses were delivered in each shot of the accelerator at a frequency of 1 Hz. A trigger signal, provided by the accelerator control, was used to synchronize the data acquisition with the beam pulse delivery.

Chapter 3

Charged particles detection

3.1 Semiconductor physics

In this section, the functioning of semiconductors is described, with the aim of understanding how detectors work [68, 69].

Solid materials can be classified based on their electrical conductivity and resistivity into three main categories: metals, semiconductors, and insulators. Metals are characterized by high electrical conductivity due to the presence of a large number of free electrons, allowing efficient current flow. Semiconductors have intermediate conductivity, which can vary significantly depending on factors like temperature, impurities, and external conditions; their conductivity can be enhanced through processes such as doping. Insulators, on the other hand, exhibit low conductivity and high resistivity, as they lack free charge carriers, making it difficult for electrical current to flow through them.

Semiconductors can be of two types: elemental semiconductors (such as Si and Ge) or compounds (inorganic such as CdS, GaAs, CdSe, InP, etc; organic such as anthracene, dopedpthalocyanines,etc; organic polymers such as polypyrrole, polyaniline, polythiophene, etc). Most semiconductor-based devices are composed of elemental semiconductor Si or Ge and compound inorganic semiconductors.

This chapter focuses on inorganic semiconductors (especially Si and Ge).

While at low temperatures all electrons remain in their lattice site, at higher temperatures, thermal energy can provide enough energy to overcome the potential barriers in solid materials, potentially allowing covalent bonds to break. This can result in the release of valence electrons and the creation of holes, which are vacancies left by electrons. In semiconductors, both free electrons and holes contribute to electrical conduction. The energy levels as a function of lattice spacing has been evaluated using quantum mechanics. Considering n the number of atoms, for $N \rightarrow \infty$ it is possible to describe the system in terms of energy bands: E_V in the valence band edge and E_C in the conduction band edge. The bandgap energy E_g (E_C - E_V) is the so-called forbidden energy band. At low temperatures, the valence band is full while the conduction band is empty. As the temperature increases, electrons in the valence band may have enough thermal energy to create weak conductivity.

In the case of insulating materials, the band gap is much wider (the probability

of occupying states in the conduction band is zero), while in conducting materials the two bands may even overlap. In case of semiconductors the bandgap is large enough to excite thermally a not negligible fraction of electrons into the conduction band.

In the case of intrinsic semiconductors, in which the impurities present are negligible compared to the thermally generated carriers, it is possible to estimate the density of free electrons n (or holes h) in the equilibrium state. This is obtained by integrating the carrier concentrations, given by the product of the density of the N states and the probability of their occupancy in the conduction (or valence) band. The probability of occupying an electronic state is given by the Fermi-Dirac function:

$$F(E) = \frac{1}{1 + e^{\frac{E-E_F}{k \cdot T}}} \tag{3.1}$$

where E_F is the Fermi energy, k is the Boltzmann constant and T is the absolute temperature. If E_F is located in the band gap at a distance from both edges of at least $3kT$ (as is the case of intrinsic semiconductors where it is close to the middle of the gap), then the formula 3.1 can be expressed for electrons and holes as follows:

$$F_n(E) \simeq e^{-\frac{E-E_F}{k \cdot T}} \tag{3.2}$$

$$F_p(E) = 1 - F(E) \simeq e^{-\frac{E-E_F}{k \cdot T}} \tag{3.3}$$

Whereas the density of N states is obtained by considering standing waves in a unit volume of physical space. Considering the two spin directions, the number of $N(E_{kin})$ states per unit volume in an interval of kinetic energy dE_{kin} around E_{kin} is expressed as follows:

$$N\left(E_{\text{kin}}\right) \mathrm{d}E_{\text{kin}} = 4\pi \cdot \left(\frac{2m}{h^2}\right)^{\frac{3}{2}} E_{\text{kin}}^{\frac{1}{2}} \ \mathrm{d}E_{\text{kin}} \tag{3.4}$$

where m the effective mass of electrons m_n or holes m_p respectively, h is Planck's constant, and E_{kin} is kinetic energy.

Considering formula 3.2,3.3 and 3.4 , the density of free electrons n and holes p are equal to:

$$n = 2\left(\frac{2\pi m_n kT}{h^2}\right)^{\frac{3}{2}} \mathrm{e}^{-\frac{E_{\mathrm{C}}-E_{\mathrm{F}}}{kT}} = N_{\mathrm{C}} \mathrm{e}^{-\frac{E_{\mathrm{C}}-E_{\mathrm{F}}}{kT}} \tag{3.5}$$

$$p = 2\left(\frac{2\pi m_p kT}{h^2}\right)^{\frac{3}{2}} \mathrm{e}^{-\frac{E_{\mathrm{F}}-E_{\mathrm{V}}}{kT}} = N_{\mathrm{V}} \mathrm{e}^{-\frac{E_{\mathrm{F}}-E_{\mathrm{V}}}{kT}} \tag{3.6}$$

where N_C and N_V rapresent the effective density of state in conduction and valence bands.

The product n and p depends on the energy gap and it is not dependent on the Fermi energy. To define the Fermi level in the case of intrinsic semiconductors, it suffices to consider the number of electrons and holes to be identical (n =p= ni). Re-elaborating the previous formulas, we obtain:

$$E_{\mathrm{i}} = \frac{E_{\mathrm{C}} + E_{\mathrm{V}}}{2} + \frac{3kT}{4} \ln\left(\frac{m_p}{m_n}\right) \tag{3.7}$$

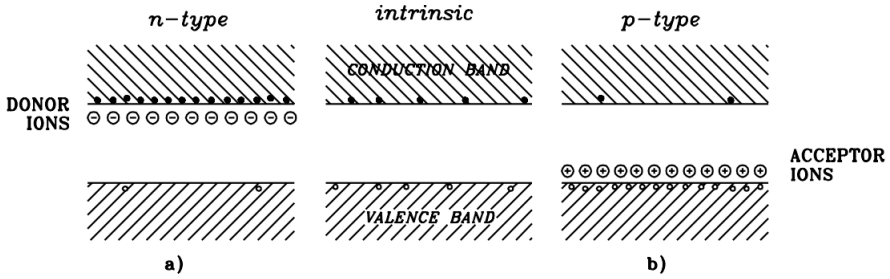

Figure 3.1.1: Energy band representation for intrinsic (center) extrinsic n-type (a) and p-type (b) semiconductors

and introducing in formula 3.5 and 3.6 the intrinsic carrier density n_i they become:

$$n = n_{\mathrm{i}} \mathrm{e}^{\frac{E_{\mathrm{F}} - E_{\mathrm{i}}}{kT}} \quad p = n_{\mathrm{i}} \mathrm{e}^{\frac{E_{\mathrm{i}} - E_{\mathrm{F}}}{kT}} \tag{3.8}$$

In reality, it is extremely difficult to have a material with so few impurities that it can be defined as intrinsic. In most cases, the material is *doped*: specific impurities are artificially injected into the material. *N-type* semiconductors are doped with an excess of electrons in the conduction band, while *p-type* semiconductors with an excess of holes in the valence band. Looking at this with the band model, the replacement of a lattice atom leads to the creation of new energy levels in the forbidden energy band. In the case of donor-type energy levels (E_D), the level is close to the conduction band, as is the case for phosphorous ($E_C - E_D = 0.045$ eV) or arsenic in silicon. At room temperature these states are completely ionised. Similarly, acceptor-type states (e.g. boron in silicon $E_A - E_V = 0.045$ eV) are close to the valence band and are immediately filled, creating holes in the valence band. In the case of extrinsic semiconductors, the addition of dopant levels leads to a shift of the Fermi level compared to intrinsic semiconductors (E_i). From formulas 3.5 and 3.6, setting the electron concentration n in the valence band equal to the concentration of the N_D donors, and p equal to N_A, we obtain:

$$E_{\mathrm{C}} - E_{\mathrm{F}} = kT \ln \frac{N_{\mathrm{C}}}{N_{\mathrm{D}}} \quad E_{\mathrm{F}} - E_{\mathrm{V}} = kT \ln \frac{N_{\mathrm{V}}}{N_{\mathrm{A}}} \tag{3.9}$$

It is therefore possible to express the electron concentration n and the hole concentration p in an extrinsic semiconductor (n,p) as a function of the concentrations in the intrinsic case (n_i,p_i) as follows:

$$n = n_{\mathrm{i}} \mathrm{e}^{\frac{E_{\mathrm{F}} - E_{\mathrm{i}}}{kT}} \quad p = n_{\mathrm{i}} \mathrm{e}^{\frac{E_{\mathrm{i}} - E_{\mathrm{F}}}{kT}} \tag{3.10}$$

From this follows the mass-action law:

$$n \cdot p = {n_i}^2 \tag{3.11}$$

So far, only the case of a semiconductor in equilibrium has been considered. In the case of an externally applied electric field or an inhomogeneous distribution of charge carriers, the so-called *drift current* and *diffusion current* are created. We consider the mobile charge carriers as free particles with an average kinetic

energy of $\frac{3}{2}kT$ and, in the case of electrons, an average velocity at room temperature of 10^7 cm/s, a mean free path of 10^{-5} cm, and an average lifetime τ_c of approximately 10^{-12} s.

If an external electric field is present, the charge carriers are accelerated, and the average velocities of the electrons and holes are:

$$\boldsymbol{v}_n = -\frac{q \cdot \tau_c}{m_n}\mathcal{E} = -\mu_n \mathcal{E} \quad \boldsymbol{v}_p = \frac{q \cdot \tau_c}{m_p}\mathcal{E} = \mu_p \mathcal{E} \tag{3.12}$$

where the mobilities μ_n and μ_p depend on temperature and doping. If the electric field is sufficiently high (such that the energy of the electrons and holes is greater than their thermal energy), then the two velocities become independent of the electric field and reach saturation values $v_{n,s}$ and $v_{p,s}$.

On the other hand, ignoring effects related to the presence of an electric field, an inhomogeneous distribution of free charge carriers (electrically neutral) can be considered. Choosing a boundary between the two sides where the carriers are concentrated, the probability that a carrier crosses the boundary from the region of higher concentration exists and is lower than in the opposite direction. This movement generates the *diffusion* current, described by the following equations:

$$\boldsymbol{F}_n = -D_n \nabla n \quad \boldsymbol{F}_p = -D_p \nabla p \tag{3.13}$$

where $\boldsymbol{F}_n$ and $\boldsymbol{F}_p$ are the fluxes of electrons and holes, D_n and D_p the diffusion constants and ∇n and ∇p the carrier concentration gradient.

Combining the effects of the two currents just described, the total current density for electrons and holes can be obtained:

$$\boldsymbol{J}_n = q\mu_n n\mathcal{E} + qD_n \nabla n \quad \boldsymbol{J}_p = q\mu_p p\mathcal{E} + qD_p \nabla p \tag{3.14}$$

Various mechanisms exist for generating free electrons and holes.

One of these is the thermal generation of charge carriers, which is significant for radiation detector semiconductors because it constitutes an important source of noise. In some direct semiconductors, the band gap is small enough so that electrons may be excited directly from the valence band to the conduction band, thus requiring operation at low temperatures. In others, the probability of direct excitation is extremely low. For indirect semiconductors, in particular, the energy required for band-to-band transition is greater than the band gap energy alone because the maximum of the valence band and the minimum of the conduction band are located at different momenta.

A second mechanism for charge generation is via electromagnetic radiation, which is the basis for the operation of photodetectors and solar cells. In this case, the energy of a photon E_γ causes an electron to transit from the valence band to the conduction band. If $E_\gamma > E_G$, the electron will occupy an empty state in the conduction band, leaving behind a hole in the valence band. The electron and hole thus generated subsequently move to the band edges, emitting energy in the form of phonons (lattice vibrations) or photons of lower energy. Absorption of a photon with $E_\gamma < E_G$ is also possible if local states exist within the band gap due to lattice imperfections.

This first two mechanisms are represented in Figure 3.1.2. The third cause of free carrier generation in a semiconductor is via charged particles.

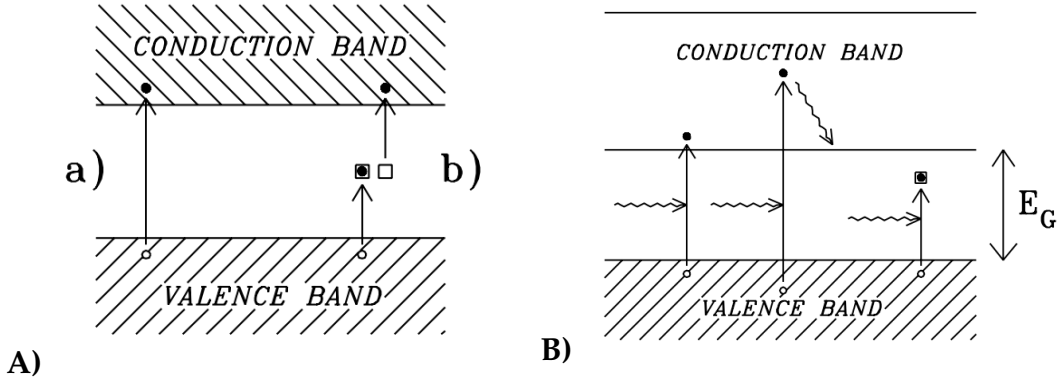

Figure 3.1.2: A) Direct (a) and indirect (b) excitation of electrons **B)** Generation of electrons and holes by absorption of photons of energies $E = E_G$, $E > E_G$ and $E < E_G$

3.1.1 Charged particle interaction

When charged particles traverse a material, they experience two primary effects: energy loss and deflection from their initial trajectory. These effects arise due to various underlying processes, such as inelastic collisions with the material's electrons, elastic scattering of nuclei, Cherenkov radiation, and bremsstrahlung, the latter being particularly significant for lighter particles like electrons and positrons. For heavy particles, where $M \gg m_e$, energy loss is primarily due to inelastic collisions with atomic electrons in the target material, leading to the ionization process. The average energy loss due to ionization is described by the Bethe-Bloch formula [70, 71], which characterizes the rate of ionization energy loss for charged particles passing through matter. This formula also includes corrections for density and shell effects.

$$\frac{dE}{dx} = 2\pi N_0 r_e^2 m_e c^2 \rho \frac{Z}{A} \frac{z^2}{\beta^2} \left[\ln \left(\frac{2m_e \gamma^2 v^2 W_{\max}}{I^2} \right) - 2\beta^2 - \delta - 2C \right], \tag{3.15}$$

where:

$2\pi N_0 r_e^2 m_e c^2 = 0.1535\,\mathrm{MeV\,c^2/g}$,
x is the path length in $\mathrm{g/cm^2}$,
$r_e = \dfrac{e^2}{4\pi m_e c^2} = 2.817 \times 10^{-13}\,\mathrm{cm}$ (classical electron radius),
m_e is the electron mass,
$N_0 = 6.022 \times 10^{23}\,\mathrm{mol^{-1}}$ (Avogadro's number),
I is the effective ionization potential averaged over all electrons,
Z is the atomic number of the medium,
A is the atomic weight of the medium,
ρ is the density of the medium,
z is the charge of the traversing particle,
$\beta = \dfrac{v}{c}$, the velocity of the traversing particle in units of the speed of light,
$\gamma = \dfrac{1}{\sqrt{1-\beta^2}}$ (Lorentz factor),
δ is a density correction,
C is a shell correction,
W_{max} is the maximum energy transfer in a single collision.

The equation reveals several important characteristics of ionization energy loss. It depends on the charge and velocity of the incident particle, but not on its mass. This implies that for a beam of particles with a given charge, the energy loss per unit distance (dE/dx) is solely a function of the particle's velocity. The dependence on the traversed material, however, appears in the terms A, Z, and I, as well as in the correction term δ.

The energy loss rate as a function of particle energy is shown in Figure 3.1.3 [72]. For values of $\beta\gamma < 0.007$, the Bethe-Bloch formula is no longer valid, as the projectile's velocity becomes comparable to that of atomic electrons. For higher velocities ($0.08 < \beta\gamma < 1$), the energy loss per unit distance (dE/dx) decreases according to the $1/\beta^2$ dependence, reaching a region of minimum ionization for $\beta\gamma \sim 3-4$. Particles with energies corresponding to this range are commonly referred to as minimum ionizing particles (MIPs). As β increases, dE/dx begins to rise due to the presence of the logarithmic factor. At even higher kinetic energies ($\beta\gamma \sim 100$), an additional phenomenon mitigates energy loss: in high-density materials, the outer atomic electrons partially shield the inner electrons, reducing the energy loss from distant collisions of the incident particle. Finally, for $\beta\gamma \geq 200$, the energy loss reaches an approximately constant value known as the Fermi plateau.

Charged particles lose energy not only through ionization, but also through radiation (*bremsstrahlung*). This process is particularly significant for electrons due to their relatively small mass: when interacting with atomic nuclei, they undergo rapid deceleration, emitting electromagnetic radiation. The radiated power is

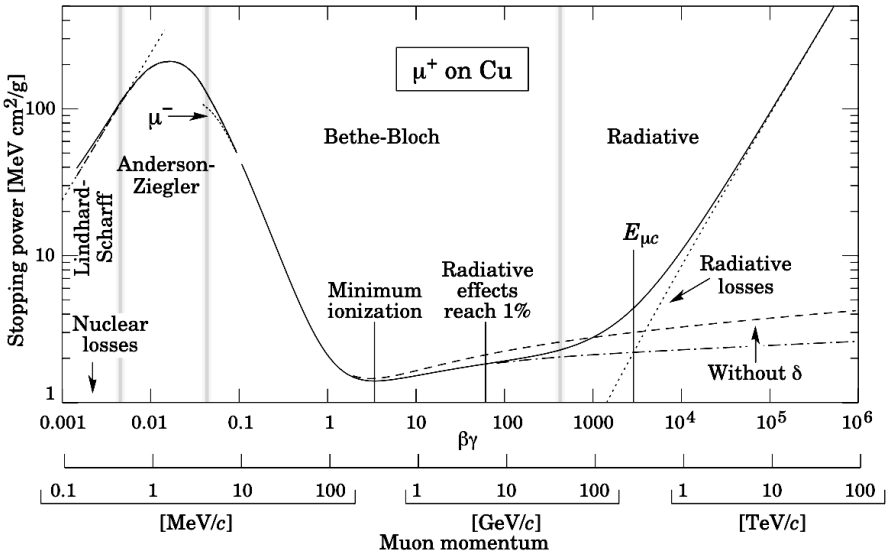

Figure 3.1.3: Stopping power for positive muons in copper as a function of $\beta\gamma = p/Mc$ (or momentum p). The solid curve indicates the total stopping power.

proportional to the inverse square of the particle's mass. The contribution of bremsstrahlung to the energy loss for light charged particles must be considered when calculating the total energy loss:

$$\left\langle \frac{dE}{dx} \right\rangle = \left(\frac{dE}{dx} \right)_{\text{ion}} + \left(\frac{dE}{dx} \right)_{\text{brem}} . \tag{3.16}$$

The contribution of energy loss due to bremsstrahlung can be written as:

$$-\frac{1}{\rho} \left(\frac{dE}{dx} \right)_{\text{brem}} = \frac{E}{X_0}, \tag{3.17}$$

where X_0 is the radiation length, defined as the average distance over which an electron reduces its energy by a factor of e. The expression for X_0 is given by:

$$\frac{1}{X_0} = \frac{4Z(Z+1)N_A}{137A} r_e^2 \ln\left(\frac{183}{Z^{\frac{1}{3}}} \right) \tag{3.18}$$

where Z is the atomic number, A is the atomic mass, N_A is Avogadro's number, and r_e is the classical electron radius.

3.1.2 The p-n diode junctions

One of the most common semiconductor-based structures is the p-n junction diode [73], formed by joining two extrinsically doped semiconductors with opposite doping. This structure allows current to predominantly flow in one direction.

The homogeneously doped n and p regions are first considered separately, electrically neutral, and in thermal equilibrium, i.e., without any applied external bias. When the two regions come into contact (Figure 3.1.4), electrons diffuse into the p-region (resulting in an excess of negative charge in the p-region), while holes

diffuse into the n-region (resulting in an excess of positive charge in the n-region). This diffusion process generates an electric field that opposes further diffusion of charges and sweeps away mobile charge carriers in the area near the contact, thus forming the space-charge region. This process can also be represented using the band model, where the Fermi levels, in equilibrium, must align, resulting in the creation of the built-in voltage V_{bi}. Using the abrupt junction approximation, the extent of the space-charge region in the n and p regions can be derived, knowing that the electric field at the boundaries of the space-charge region is zero and the potential difference across it is V_{bi}. This leads to the following expression for the total depletion width:

$$d = d_n + d_p = \sqrt{\frac{2\epsilon\epsilon_0(N_A + N_D)}{qN_AN_D}V_{bi}} \tag{3.19}$$

The carrier concentration at an arbitrary position within the junction is given by:

$$n = n_{\mathrm{i}}\,\mathrm{e}^{\frac{E_{\mathrm{F}}-E_{\mathrm{i}}}{kT}} \quad n_n = n_{\mathrm{i}}\,\mathrm{e}^{\frac{E_{\mathrm{F}}-E_{\mathrm{i}}^n}{kT}} \tag{3.20}$$

$$\frac{n}{n_n} = \mathrm{e}^{-\frac{E_{\mathrm{i}}-E_{\mathrm{i}}^n}{kT}} \quad \frac{p}{p_p} = \mathrm{e}^{-\frac{E_{\mathrm{i}}^p-E_{\mathrm{i}}}{kT}} \tag{3.21}$$

where n_n, E_i^n, p_p, and E_i^p are the electron and hole concentrations, and the intrinsic energy levels in the neutral n and p regions, respectively.

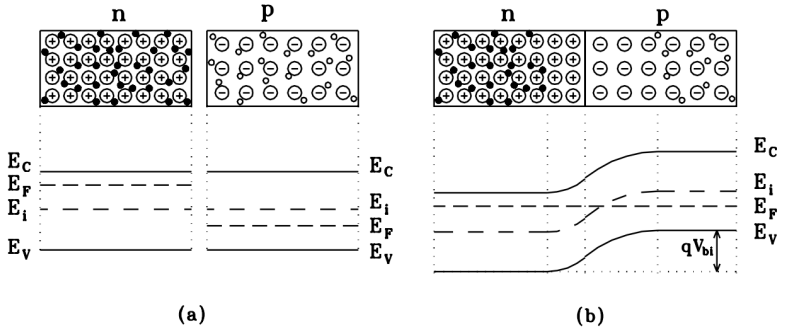

Figure 3.1.4: A p–n diode junction in thermal equilibrium, with its parts separated (a) and brought together (b)

With the application of an external electric field, the system moves out of equilibrium. In the case of forward bias, the potential difference across the junction decreases from the equilibrium value V_{bi} by an amount equal to the applied external field, resulting in $V_{bi} - V$ (with $V > 0$). The depletion width is then given by:

$$d = \sqrt{\frac{2\epsilon\epsilon_0(N_A + N_D)}{qN_AN_D}(V_{bi} - V)} \tag{3.22}$$

The minority charge carrier concentrations at the edges of space-charge regions become:

$$n_p = n_n\,\mathrm{e}^{-q\frac{V_{bi}-V}{kT}} = n_{p0}\mathrm{e}^{q\frac{V}{kT}} \qquad p_n = p_{n0}\mathrm{e}^{q\frac{V}{kT}} \tag{3.23}$$

Here, n_{p0} represents the electron density at the boundary of the neutral p-region under thermal equilibrium, which is equal to the electron density in the non-equilibrium case within the neutral p-region, far from the boundary. Since the minority carrier diffusion currents are proportional to the deviation of minority carrier concentrations from their equilibrium values, an exponential dependence of electron and hole densities, as well as the total diode current, is expected. This can be expressed as:

$$J = (J_{sn} + J_{sp}) \left(e^{\frac{V}{kT}} - 1 \right) = J_s \left(e^{\frac{V}{kT}} - 1 \right) \tag{3.24}$$

The saturation current density, J_s, can be calculated by solving the steady-state continuity equation for minority carriers. Considering the boundary condition of zero minority carrier concentration at the edge of the space-charge region, we obtain:

$$J_s = q \left(\frac{n_{p0} D_n}{\sqrt{D_n \tau_{r_n}}} + \frac{p_{n0} D_p}{\sqrt{D_p \tau_{r_p}}} \right) \tag{3.25}$$

where τ_{r_n} and τ_{r_p} represent the recombination lifetimes for electrons and holes, respectively. Therefore, the total diode current can be expressed using the "Diode Law":

$$J = q \left(\frac{n_{p0} D_n}{\sqrt{D_n \tau_{r_n}}} + \frac{p_{n0} D_p}{\sqrt{D_p \tau_{r_p}}} \right) \left(e^{\frac{V}{kT}} - 1 \right) \tag{3.26}$$

From this equation, it can be inferred that the diode current is inversely proportional to the doping concentration and the square root of the carrier lifetime. This law is derived under the assumption that no charge is generated in the space-charge region, which, in the case of reverse-biased diodes made from detector-grade material, is an oversimplification.

For forward bias, the exponential term dominates, and the current increases rapidly with the applied voltage. However, when the values of V become negative (reverse bias), the exponential term approaches zero. Once it becomes negligible ($e^{\frac{V}{kT}} \ll 1$), the reverse-biased current density becomes independent of the applied reverse voltage, and the value of J reaches $-J_s$, which represents the reverse saturation current density. The current density, J, can be multiplied by the device area (A) to obtain the current (I) instead of its density:

$$I = I_s \left(e^{\frac{V}{kT}} - 1 \right) \tag{3.27}$$

At very high reverse bias voltages, however, the behavior of the device deviates from the Diode Law and enters the multiplication region. In this condition, the electric field becomes so strong that a carrier entering the depletion region can gain sufficient energy to generate additional charge pairs, primarily through impact ionization. This phenomenon is known as junction breakdown and is characterized by a super-exponential increase in the device current.

For radiation detectors, as is the case in this thesis, the device is operated exclusively under reverse bias. Since the depletion region is a volume depleted of mobile carriers, it acts as a capacitor. The non-depleted p and n regions serve as the electrodes, while the depletion region functions as the dielectric. The electric field in the depletion region directs the mobile carriers toward the electrodes, inducing a signal, as explained in the next section.

3.1.3 Reverse-Biased Detectors

As previously mentioned, the interaction of radiation with semiconductors leads to the creation of electron-hole pairs that can be detected as electrical signals [74]. If the particles are charged, ionization can occur along the flight path through numerous low-recoil collisions with electrons. Photons, on the other hand, must first interact with a target electron or the semiconductor nucleus. In both cases, a fraction of the absorbed energy in the semiconductor is converted into pair creation (the rest is dissipated into phonons, i.e., lattice vibrations), and this fraction is a property of the detector material.

When a diode is reverse-biased, the width of the depletion layer increases, and consequently, the sensitive volume of the detector increases, leading to a decrease in the detector's capacitance. The operation principle of reverse-biased detectors can be illustrated with the example of a p-n junction detector (Figure 3.1.5). The diode consists of a highly doped and shallow p^+ region on a very lightly doped n^- substrate, with a highly doped n^+ layer at the back (which provides a good ohmic contact between the aluminum and the substrate, while also allowing the device to operate in overdepleted mode).

The electron-hole pairs generated within the space-charge region are separated by the electric field, with the holes moving toward the p^+ junction and the electrons toward the n^+ electrode. The signals in the detector appear already during the separation process, and the holes and electrons will induce different charges on the electrodes due to their varying distances, as simplistically represented in Figure 3.1.6.

The induced signal can be calculated using the Ramo-Shockley theorem [75], which states that the current induced by charge carriers is proportional to their charge q, drift velocity $\vec{v}$, and the weighting field $\vec{E}_w$, representing the capacitive coupling of a charge q to the read-out electrode. The current induced on the k-th electrode by a charge q is given by the Shockley-Ramo's equation:

$$i_k(t) = -q\vec{v} \cdot \vec{E}_w. \tag{3.28}$$

The weighting field $\vec{E}_w$ describes the coupling between the charge q and the k-th electrode. Numerically, the weighting field corresponds to an electric field calculated by setting the read-out electrode at 1 V and all other electrodes at 0 V. Consequently, $\vec{E}_w$ has the same geometric dependence as an electric field: it decreases with distance d as $1/d^2$ for point electrodes, as $1/d$ for line electrodes, and remains constant between two large electrodes.

To illustrate this, consider a single electron-hole (e-h) pair created within the bulk of a sensor. The drift of the electron moving toward the cathode and the

hole drifting away from it induces two currents on the electrode with the same sign. The integral of these two currents is equal to the total charge q:

$$\int (i_e(t) + i_h(t))dt = q. \tag{3.29}$$

Although this integral is always equal to q, the relative contributions of $i_e(t)$ and $i_h(t)$ to the total signal depend on the geometry of the electrodes and the applied electric field. In a simple configuration where the sensor has the geometry of a parallel plate capacitor, with the anode and cathode representing the two plates, the weighting field is constant and is $\vec{E}_w = 1/d$. With a constant weighing field, a charge's induced signal depends uniquely upon its velocity and not upon its position.

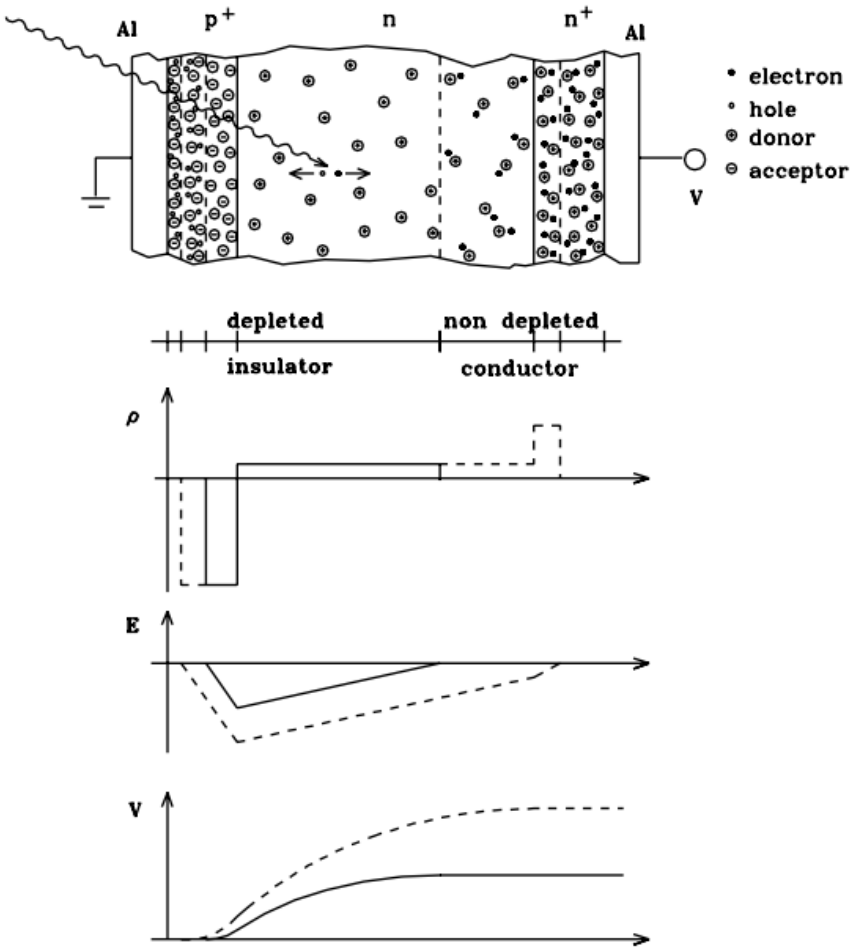

Figure 3.1.5: A p–n diode junction detector: charge density, electric field and potential for partial (continuous line) and full (dashed line) depletion

3.2 Silicon detector

Silicon is the most well-known semiconductor, widely used in advanced technologies. Its atomic structure includes four valence electrons: two in the p orbital and

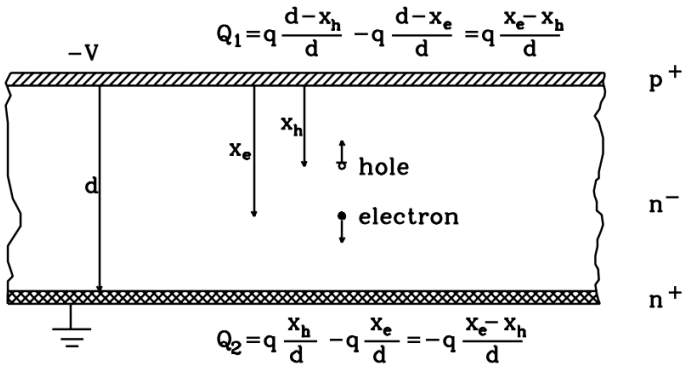

Figure 3.1.6: Signal formation by the separation of electron–hole pairs due to the electric field in the space-charge region of the detector

two in the *s* orbital. When two silicon atoms bond, their eight valence electrons form two energy levels corresponding to these subshells. The higher-energy level is the conduction band, while the lower-energy level is the valence band, with an energy gap of 1.12 eV between them.

Table 3.1 presents the key electrical properties of silicon, compared with those of the other two primary materials discussed in this thesis, diamond and SiC.

Properties	Si	Diamond	4H-SiC
Bandgap (eV)	1.12	5.47	3.26
W e-h pair energy (eV)	3.62	13	7.78
Density (g/cm^3)	2.33	3.52	3.21
Atomic Number	14	6	10
Electron mobility (cm^2/Vs) (300 K)	1400-1500	1800-2200	800-1000
Hole mobility (cm^2/Vs) (300 K)	450-600	1200-1600	100-115
Saturated electron drift velocity (10^7 cm/s)	1.0	2.2	2
Dielectric constant	11.9	5.7	9.7
Thermal conductivity (W/cmK)	1.48	25	4.9
Displacement energy (eV)	13 - 20	37 - 47	30 - 40
Breakdown field (10^5 V/cm)	3	100	30
Hardness (kg/mm^2)	1000	10000	4000
Young's modulus (GPa)	1000	1200	380-700
Debye temperature (K)	645	1860	1200

Table 3.1: Basic properties of Si, Diamond, and SiC.

Silicon is widely used in electronic devices because it offers several advantages over many other materials. First and foremost, it has an excellent intrinsic energy resolution: for every 3.6 eV released by a particle passing through the material, an electron-hole pair is generated. This is a crucial factor since silicon detectors can be considered as solid-state ionization chambers. While in ionization chambers ionization occurs in gases, in silicon detectors it occurs within a semiconductor. Given that approximately 30 eV are required to ionize a gas molecule in an ionization chamber, silicon, for the same energy, yields about ten times the number of charge carriers.

Other significant advantages include its abundance —SiO_2 is the most abundant compound in the Earth's crust — its low bandgap energy, and the ability to modify its electronic properties by adding dopant atoms.

As previously introduced, by adding trivalent or pentavalent atoms, one can produce p-type and n-type silicon, which can be combined to form a p-n junction.

The two types of silicon sensors employed by our group are PIN sensors and LGADs. The PIN sensors consist of a structure made up of a sequence of p-doped/intrinsic/n-doped silicon layers, although the bulk is not truly intrinsic but rather lightly doped, as shown in Figure 3.2.1. A modification of this standard technology, which is of particular interest for the development of timing and radiation-resistant detectors, is the LGAD (Low Gain Avalanche Diode) sensor. In LGAD detectors, a highly doped p^+ layer is introduced, as illustrated in Figure 3.2.1. Charge multiplication by impact ionization occurs primarily for electrons when charge carriers drift through the region where the electric field can exceed 300 kV/cm.

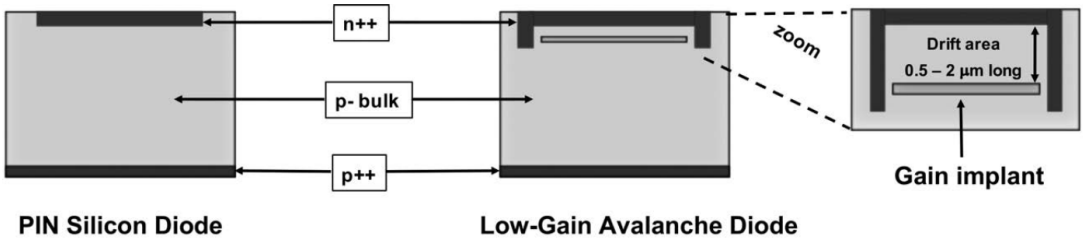

Figure 3.2.1: Schematic view of: (left) an n-in-p PIN diode; (right) a Low-Gain Avalanche Diode. The LGAD design is characterized by an additional p^+ implant under-neath the pn junction. [76]

3.3 Diamond detector

Diamond is made up of carbon atoms with an atomic number of Z = 6 and an atomic weight of 12.011 u. Diamonds can be found in nature or produced artificially in laboratories and industries. Among the stable isotopes of carbon, diamond and graphite are the most common.

The carbon atoms in diamond are arranged in a face-centered cubic (*fcc*) crystal structure, with bonding achieved through tetrahedral sp^3 hybridization. Each unit cell of the diamond lattice contains 8 atoms and has an atomic density of 1.76×10^{23} atoms/cm^3, the highest known. Like other group IV elements (e.g., silicon, germanium), diamond exhibits strong covalent bonding, with cohesive energies of 3.62 eV/bond and 7.24 eV for the total cohesive energy.

Diamond is the hardest natural material, with a Mohs hardness of 10. It is also isotropic, and optically it can range from transparent to translucent. The displacement energy of carbon atoms in the diamond lattice is 43 eV, much higher than that of silicon (13 - 20 eV), due to the stronger covalent bonds in diamond.

In terms of electrical properties, diamond is classified as a wide bandgap semiconductor with a bandgap of 5.47 eV, significantly larger than silicon (E_{gap} = 1.12 eV) and germanium (E_{gap} = 0.76 eV). Although diamond has near-zero

intrinsic conductivity at room temperature, many of its electrical behaviors are governed by semiconductor physics. Like silicon and germanium, diamond has an indirect bandgap, requiring a phonon to excite an electron into the conduction band. Diamond also possesses a direct bandgap of $E_{gap,direct}$ = 7.3 eV.

The mobility of electrons and holes in diamond is higher than in silicon. However, the energy needed to create an electron-hole pair is 13 eV, which is considerably greater than the 3.62 eV required in silicon. As a result, the ionization signal produced by an ionizing particle in diamond is smaller (36 e/μm versus 89 e/μm in silicon for reasonably thick sensors[77]).

Both natural and synthetic diamonds always possess characteristic defects that arise from the circumstances of their crystalline growth. Additionally, defects can form due to irradiation with particles. These defects can be categorized as point, linear, planar, and volumetric defects [78]. If the microscopic regions of these defects grow, the properties of the diamond can change significantly. For instance, volumetric defects that extend throughout the thickness can drastically reduce the breakdown field, rendering the diamond unsuitable for detectors.

Synthetic diamonds are primarily produced using two methods: through a high-pressure, high-temperature (HPHT) crystallization process and by chemical vapor deposition (CVD) [79, 80].

- The **HPHT process** aims to replicate the conditions that occur deep within the Earth's crust to form synthetic diamonds from graphite. The temperatures required range from 1500°C to 2000°C, while the pressure must exceed 5 GPa. These diamonds typically exhibit high levels of nitrogen impurities and numerous crystalline defects, rendering them unsuitable for detector applications.

- In the **CVD process**, diamonds grow from a gaseous mixture of hydrocarbons. Its advantages include the ability to grow large diamonds and improved control over impurities within the diamond, thereby enhancing the quality of the synthetic diamond. The growth of CVD diamonds occurs at relatively low pressures (1 kPa - 27 kPa). In this method, a chemical reaction takes place in the gas phase above a solid surface, known as the substrate, which results in the deposition of material on that surface. This gas is typically a mixture of hydrogen and methane [81].

For electronic-grade diamonds, the *homoepitaxial* growth technique is usually employed, which utilizes a substrate with a crystal structure similar to that of diamond. There are two types of diamonds grown homoepitaxially: single-crystal CVD diamonds (scCVD) and polycrystalline CVD diamonds (pCVD). Most scCVD diamonds are grown on surface-treated HPHT diamonds, while pCVD diamonds utilize diamond powder as the substrate, resulting in a typical grain structure, more evident for thicker pCVD diamond (Figure 3.3.1).

Diamond can function as a simple solid-state ionization chamber due to its high charge carrier mobility by applying a bias voltage V_B across the diamond.

The high breakdown field allows the detector to operate with electric fields greater than 2 V/μm or more. This results in bias voltages of V_B = 1000 V for a

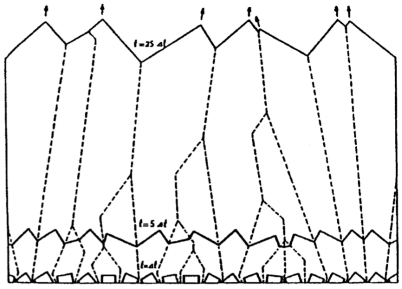

Figure 3.3.1: A schematic illustration of pCVD diamond film growth, starting from individual, randomly oriented crystals. Dashed lines represent grain boundaries, while solid lines indicate the film surface at various time intervals. As the film thickens, the grain size progressively increases.

diamond with a thickness of t = 500 μm (a typical thickness for diamond sensor material).

Atoms at lattice sites in the crystal are ionized by the passage of a charged particle, promoting electrons into the conduction band and leaving holes in the valence band. The average energy required to generate an electron-hole pair in diamond is 13 eV. Using the Bethe-Bloch formula, described in Section 3, the average number of electrons and holes produced by a Minimum Ionizing Particle (MIP) in 1 μm of diamond material is $q_0 = 36$ e$/\mu m$. The movement of the carriers within the electric field across the diamond induces the signal.

The Charge Collection Distance (CCD) is typically used to quantify the signal response in a CVD diamond detector. A particle traversing the detector produces a charge amount $Q_0 = d \cdot q_0$ of ionizations within the material, where d rapresents the sensor thickness. However, the measured charge Q_m is reduced compared to the generated charge Q_0, due to trapping during the movement through the detector. The CCD corresponds to the average drift distance of an electron or hole under the influence of the electric field and is related to the ratio of these two charges, describing the quality of the CVD diamond:

$$CCD = \frac{Q_m}{q_0} = \left(\frac{Q_m}{Q_0}\right) \cdot d \tag{3.30}$$

This corresponds to the average drift distance of an electron or hole under the influence of the electric field. The CCD, together with the sample thickness t, describes the quality of a CVD diamond.

While scCVD diamond detectors can have a CCD equal to their thickness, pCVD diamond detectors have lower CCDs primarily due to charge traps within the material induced by grain boundaries. A state-of-the-art pCVD diamond detector typically has CCDs exceeding 300 μm. One method to improve charge collection efficiency and hence increase the CCD is by raising the electric field, which increases the charge carrier drift velocity and reduces the drift time. At high fields, the drift velocity saturates, and consequently, so does the CCD.

Non-irradiated scCVD diamonds, which are grown nearly defect-free, have a CCD similar or equal to their thickness, called "complete charge collection", even under low electric field conditions. The CCD of a pCVD diamond, however, continues to increase with increasing bias voltage, as shown in Figure 3.3.2.

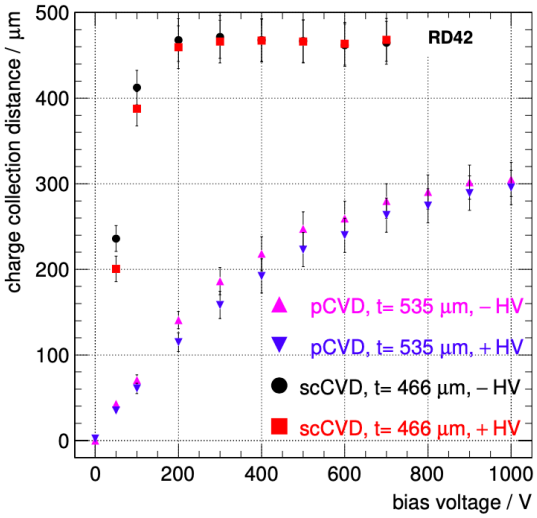

Figure 3.3.2: Charge collection distance as a function of bias voltage for a pCVD diamond with a thickness d = 535 μm and a scCVD diamond with a thickness d = 466 μm [81].

It has been observed that one method to improve the signal response of detectors is to irradiate them with a small amount of radiation. This effect is called "pumping" [82], and it has been shown to lead to increases in the CCD of more than 40%. The pumping process is likely related to the filling of deep traps within the material: primary free charge carriers become trapped and neutralize these deep traps, resulting in an increase in the free charge carrier lifetime and, consequently, an improvement in the signal response.

3.4 SiC detectors

Silicon carbide (SiC) is a compound semiconductor consisting of 50% silicon and 50% carbon. Both Si and C atoms are tetravalent and are bonded tetrahedrally through covalent bonds, sharing electron pairs in sp^3 orbitals to form the SiC crystal. SiC is the most well-known example of polytypism: the material can exhibit different crystal structures without a change in chemical composition. The most common polytypes are 3C-SiC, 4H-SiC, and 6H-SiC (Figure 3.4.1). The stability of the polytype strongly depends on temperature, making 4H-SiC and 6H-SiC more widely used and studied. By observing the values reported in Table 3.1, it can be noted that some characteristics make SiC a highly interesting material when compared with silicon and diamond in their application as radiation detector materials [83, 84].

Its high thermal conductivity allows 4H-SiC to efficiently dissipate heat buildup, which can degrade performance. This is particularly useful for SiC-based detectors such as X-ray beam position monitors (XBPM) in synchrotron facilities. Although the thermal conductivity of SiC is much lower than that of diamond, SiC has demonstrated comparable performance to diamond in XBPM detector applications. Thermal conductivity also makes SiC highly radiation-hard, as solid-state detectors benefit from cooling of the device.

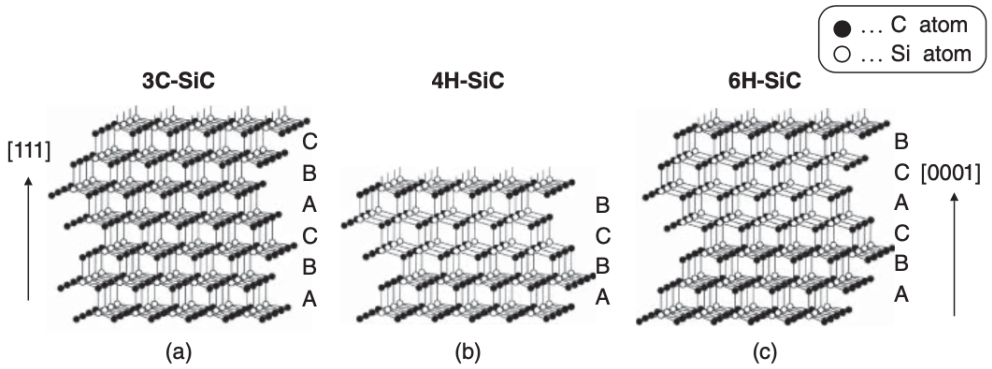

Figure 3.4.1: Structures of (a) 3C-SiC, (b) 4H-SiC, and (c) 6H-SiC in a ball-stick model [85]

The large bandgap (2.36 eV for 3C-SiC, 3.02 for 6H-SiC, and 3.26 eV for 4H-SiC) of SiC makes it an optimal material for radiation detection because it leads to a low leakage current (and consequently low noise) even at high reverse bias voltages. Furthermore, the wide bandgap results in a low intrinsic carrier density, allowing the use of SiC at high temperatures with minimal leakage current, and in insensibility to light, an advantage in various applications such UV radiation detection.

Since SiC is an indirect bandgap semiconductor, the absorption coefficient of photons in a SiC detector increases with the energy of the incident photon, while the penetration decreases with the reduction in wavelength. The minimum energy required for a photon to induce a transition from the conduction band to the valence band defines the *absorption edge* of SiC. Interestingly, SiC exhibits an absorption that is ten times greater than that of diamond for X-rays at 8 keV (650 μm versus 70 μm of attenuation length). However, the transparency of SiC is sufficiently high to enable its application in XBPM detectors.

Among the other noteworthy characteristics, it is important to mention the high saturation velocity of charge carriers (200 μm/ns compared to 100 μm/ns for Si), which results in a faster signal and consequently a more effective charge collection when defects are present in the lattice. Additionally, the breakdown electric field strength of SiC (about eight times higher than Si at a given doping density) makes SiC highly attractive for power device applications and enables operation under high reverse bias voltage conditions.

The hardness and mechanical properties of SiC are also unique: it is one of the hardest known materials, with a Young's modulus (380-700 GPa) significantly higher than those of silicon, and retaining its high hardness and elasticity even at very elevated temperatures.

A typical SiC detector is illustrated in Figure 3.4.2. It consists of an epitaxial layer, with thicknesses ranging from a few μm up to 250 μm, doped with nitrogen (with typical concentrations around 10^{15} cm^{-3}), and a conducting SiC substrate with a thickness of about 300–350 μm, which has a much higher dopant concentration, on the order of 10^{18} cm^{-3}. A metallic ohmic contact (made from materials such as gold, titanium, or nickel) is applied to the back of the detector. The front contact can be a Schottky contact using a suitable metal, such as nickel

(Figure 3.4.2 (a)), or a Ohmic contact consisting of a metal applied to the p^+ layer in p–n junctions (Figure 3.4.2 (b)), formed by diffusing or implanting materials (i.e. aluminum, phosphorus, or boron) but generally more difficult to fabricate. For this reason, most SiC radiation detectors are based on Schottky contacts. By

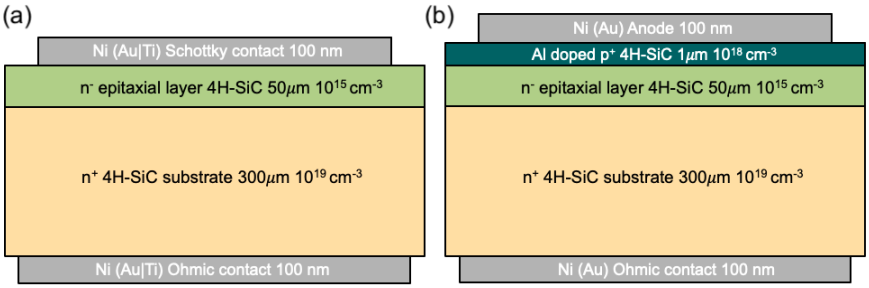

Figure 3.4.2: Schematic layout of two SiC detectors. (a) Scheme of a SiC Schottky diode. (b) Scheme of a standard n-type 4H-SiC p-n diode where an heavily doped p^+ layer forms the junction with the n^- epitaxial layer [84].

applying a reverse bias between the Schottky contact (or *p* contact) and the ohmic contact, a depletion region is created in the epitaxial layer, which constitutes the active region of the detector. To increase the thickness of this depletion region, it is possible either to increase the bias voltage (up to the maximum limit to protect the electronics, bonding, etc.) or decrease the doping levels. The minimum doping level achieved in a SiC detector is on the order of 10^{13} Nitrogen/cm^3.

SiC detectors have been implemented for the detection of electrons, protons, alpha and heavy ions and photons (both as UV photodiodes and as X-ray detectors).

Chapter 4

Modification of a LINAC Elekta SL18 for UHDR beam delivery

The LINAC I will discuss in this thesis is an Elekta SL18 with Precise software. It was decommissioned from a hospital, carefully dismantled, and reinstalled at the Department of Physics, University of Turin, for research purposes. It has been placed in a bunker at the Department, where a 100 MeV electron synchrotron was operational in the 1960s [86]. Over the years, the LINAC has been involved in various research projects, including neutron physics projects that achieved an intense thermal neutron source by converting X-ray beams into neutrons using a lead photoconverter structure [87].

In section 4.1, the accelerator machine and the various steps of the acceleration process to produce high-energy electron or X-ray beams will be described. Instead, in section 4.2 the process of modification of the machine to enable the delivery of UHDR beams is described. This work is reported in the published article [1]:

Deut, Umberto, et al. "Characterization of a Modified Clinical Linear Accelerator for Ultra-High Dose Rate Beam Delivery." ***Applied Sciences 14.17*** **(2024): 7582.**

4.1 LINAC Elekta SL18 description

The Elekta LINAC at the Physics Department of Turin can produce and accelerate high-energy electron and X-ray beams.

The first phase of the acceleration process involves the generation of electrons. The electron source consists of a diode electron gun located at the entrance of the waveguide. Electrons are generated by thermionic emission through the heating of a tungsten filament inside the cathode. Once extracted from the filament, they are focused into a fine beam by the electrostatic action of the gun's focusing electrode and then injected into the accelerating waveguide through a hole. Here, the power and frequency of the RF waves (pulsed into the waveguide by a magnetron) determine the energy of the X-rays or electron beam. To synchronize the RF with electron injection, the same high-voltage pulse is supplied to both the magnetron cathode and the electron gun cathode. For generating an X-ray beam,

electrons hit a tungsten target, producing X-rays through bremsstrahlung effect. When operating in electron mode, a nickel exit window replaces the target.

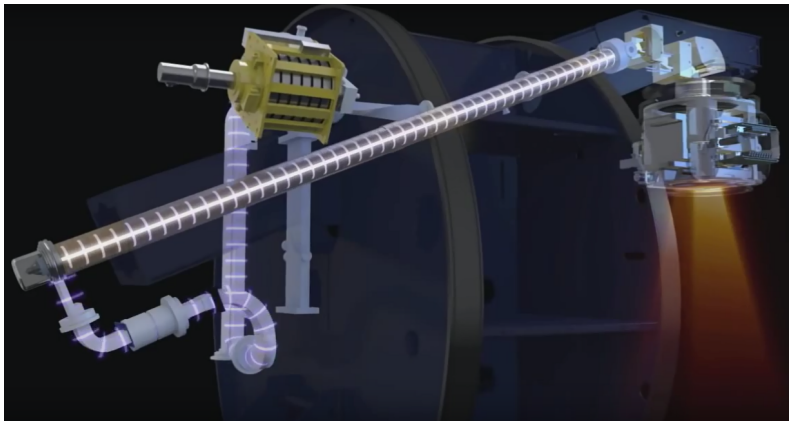

Figure 4.1.1: Schematic representation of the radiofrequency (RF) system of the Elekta LINAC, showing the magnetron, RF waveguide, and acceleration waveguide.

The waveguide contains a series of copper cells that facilitate the travel of electrons along the waveguide and assist in focusing the beam. A vacuum (10^{-6} mbar) is created to ensure that electrons are not impeded by other particles in the air. A water cooling system maintains an adequate temperature throughout the entire system. A static axial magnetic field, provided by focusing coils surrounding the waveguide, influences and focuses the beam, ensuring its centrality within the waveguide.

At the culmination of the tube, the electrons enter the flight tube, where the beam is bent by 112° and redirected towards the target. The electrons travel along a slalom path within the flight tube. A system of three pairs of magnets ensures that the electron beam bends through the slalom curves and focuses it on the target with a diameter of 1 mm. To ensure precise control of the delivered radiation, two independent ionization chambers are implemented. A third chamber is used to monitor the beam's centrality along the axis. The feedback from these chambers is used to automatically adjust the current of the electromagnets and the entire beam delivery system.

Beam shaping occurs differently for photon and electron beams in the LINAC head. For X-rays modality, a primary collimator made of tungsten and lead allows only the photons traveling forward after emission from the target to pass through, creating a cone-shaped beam with an opening angle of 28°. The collimator also includes a beam-hardening filter to absorb the low-energy component of the bremsstrahlung photon spectrum. In electron mode, the electron beam exiting the window is directed forward and is scattered widely by primary scatter foils located before the primary collimator. The secondary filters, inserted in a rotating filter carrier (picture A in Figure 4.1.2) just before the ionization chamber, consist of flattening filters for X-rays (picture B in Figure 4.1.2) and secondary scatter foils for electrons (picture C in Figure 4.1.2). Both types of filters help achieve a uniform dose on the treatment surface. The appropriate filter position is selected in console according to the radiation type and energy requirements. Additional beam shaping can be achieved using a multi-leaf collimator composed of 80 pairs

of fine tungsten leaves. These leaves can be adjusted to create a wide range of complex beam shapes.

Figure 4.1.2: (a) Rotating filter carrier with secondary filters housings. (b) Flattening filter for high energy X-rays. (c) Secondary scatter foils for electron beams.

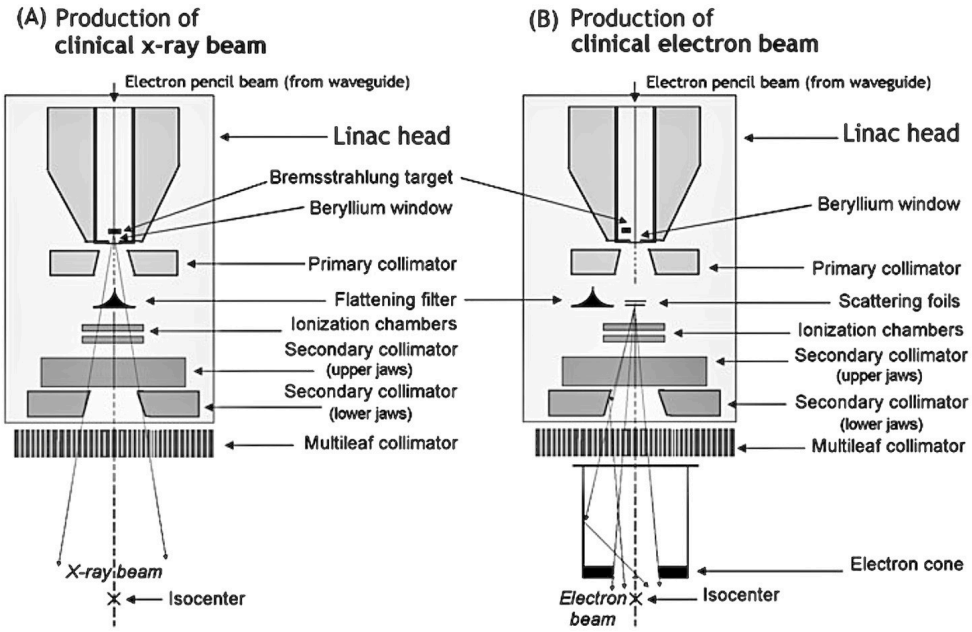

Figure 4.1.3: Schematic representation of a typical medical linac head with (A) depicting the important components for production of clinical x-ray beams and (B) depicting the important components for production of clinical electron beams [88].

4.2 Upgrade description

Machines capable of delivering UHDR beams are crucial both for radiobiology experiments [51, 19, 89, 31, 29, 90] and for the development of dedicated Treatment Planning Systems (TPS) [91, 92]. Recently, there has been increasing interest in modifying clinical LINACs for this purpose [55, 56, 57, 58, 59]. In this section, I will describe the modification performed on the accelerator in our department (LINAC Elekta SL 18 MV), to enable the delivery of UHDR electron

beams at 10 MeV of energy in a reversible way, so that the linac could switch from conventional to UHDR mode according to the experiments to be carried out.

The 10 MeV electron beam in conventional mode refers to the clinical configuration of the LINAC and served as a baseline for comparison with the beam after the modifications.

The dosimetric characterization was carried out using GafChromic EBT XD film in various configurations, represented in Figure 4.2.1 and here described:

- At the isocenter position (SSD = 100 cm);
- At the isocenter position with a cylindrical PMMA applicator with an internal diameter of 5 cm;
- At the cross-hair foil (SSD = 52.9 cm), just outside the LINAC head;
- At the wedge (SSD = 18.6 cm), inside the LINAC head.

A field size of 10×10 cm^2 was set at the isocenter, with the field size decreasing as the distance to the source decreases.

The results were compared with measurements taken in conventional mode using both film and an Advanced Markus ionization chamber (AM). By using thin silicon sensors, it was possible to monitor the output beam pulses, evaluate their temporal consistency, and assess their stability.

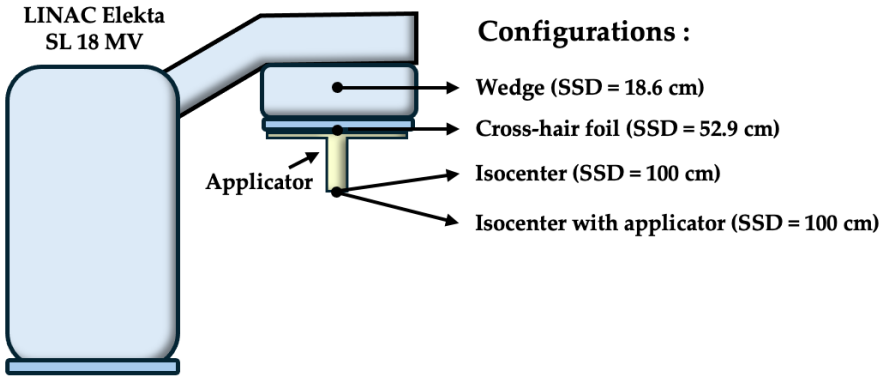

Figure 4.2.1: Schematization of the LINAC Elekta SL 18 MV and the configurations used for the beam characterization: isocenter, isocenter with 5 cm PMMA applicator, cross-hair foil, and wedge.

4.2.1 Hardware and software modification

The modifications to the machine, both hardware and software, were carried out in collaboration with Elekta technicians. The main changes are described below:

- The control console parameters for the 10 MV photon mode were adjusted to deliver an electron beam: the X-ray target was moved out of the beam path, and all filters (including the wedge and the shutter foil) were removed.
- The filament current of the electron gun was increased from 5.6 A to 7.3 A.

- The bending magnet intensity was adjusted to optimize beam transport and maximize the accelerated beam current under the new conditions.
- The power absorbed by the magnetron was increased to approximately 6 kW.

Following several trials, a standard procedure was established to ensure the proper functioning of the machine under these new conditions. First, a warm-up of the machine is necessary when turning on the LINAC (approximately 1000 MU of a 15 MV X-ray beam and approximately 1000 MU of the clinical 10 MeV electron beam) to reach optimal working conditions. Subsequently, some parameters, such as the electron gun current, gun aim, gun standby, and tuner control, are manually set to values identified as optimal. The water temperature is maintained between 26 °C and 28 °C during LINAC operation, an interval within which the performance is optimal.

Since the LINAC operates under clinical conditions, certain safety mechanisms are in place. To operate in FLASH conditions, a method to bypass the machine's interlocks was necessary [55, 56, 58]. An attenuator circuit (provided by Elekta) was inserted to avoid the interlock of the internal ionization chambers (IC). This way, the current signal from the IC is attenuated, preventing the interlock activation, but making the IC reading unreliable. This is the reason why an alternative dose monitoring system was developed by our group to read the number of delivered pulses and interrupt irradiation after the desired number of pulses. The pulse counter (PCC) converts the current signal generated in an unbiased silicon diode sensor into voltage signals using a transimpedance amplifier, as shown in Figure 4.2.2. The voltage signals are then filtered through a Sallen-Key filter and amplified to produce an acceptable input signal for a Schmitt Trigger. The resulting 5 V square pulses are counted using an Arduino NANO board. The PCC is connected to the LINAC to allow the trigger signal to reach the thyratron until the desired number of beam pulses is delivered, after which it blocks it.

It is possible to operate in two modes related to the RF injection cycle of the magnetron: the High Power (HP) mode, where two charging cycles occur before the thyratron is triggered by the Pulse-Forming Network (PFN), resulting in the highest dose-rates, and the Low Power (LP) mode, which yields dose-rates intermediate between conventional and FLASH modes.

Therefore, the LINAC can operate in three modes (conventional, UHDR LP, and UHDR HP), which can be utilized to achieve different dose ranges while maintaining the same experimental setup.

4.2.2 Silicon Sensors for Beam Monitoring

The sensor employed for these measurements is a silicon pad from the ExFlu FBK production line, as detailed in Section 5.1. This sensor comprises an epitaxial substrate grown on a low-resistivity silicon layer. The device is a square with sides measuring 4.5 mm, featuring an active thickness of 45 μm and a support layer of 570 μm. The selected pad has an active area of 2 mm^2 and was reverse-biased at 200 V.

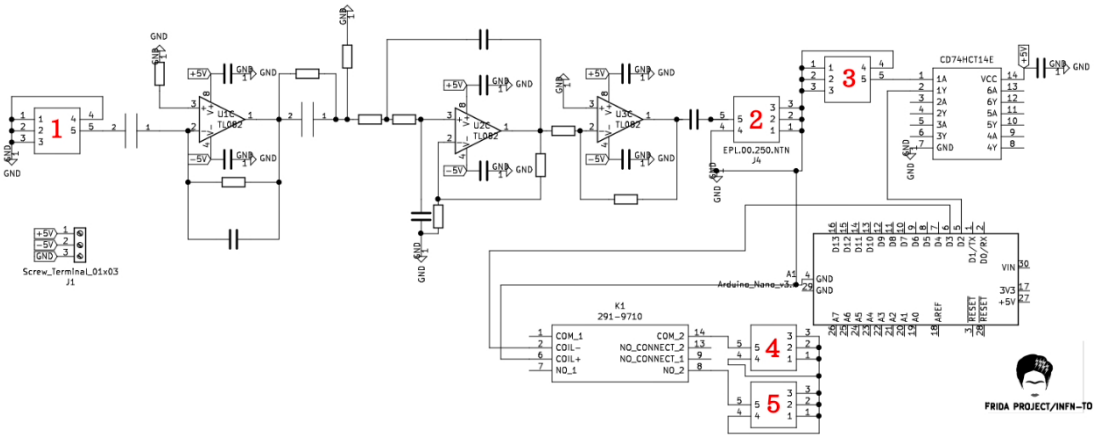

Figure 4.2.2: Schematic representation of the Pulse counter. The circuit has three stages of amplification (from the label 1 to 3 in red) using in each one an operational amplifier "TL082CP". This circuit produced an square pulses of approximately 5 V, used as input signals to the Arduino NANO board. In the Arduino NANO board, the pulses are counted (concurrently with his separations). The interface with the LINAC occurs between the connector 4 and 5 and a relay. When a certain amount of pulses is reached (decided by the user) the relay changes its mode to open, preventing any additional trigger pulse reach the Linac's thyratron.

For the described measurements, a 10×10 cm^2 field at the isocenter was chosen, and the sensor was positioned at the cross-hair foil with an uncertainty of approximately 5 mm in the transverse plane. The output channel was connected via a coaxial cable to a Keysight Infiniium Series S oscilloscope (2.5 GHz, 20 GSa/s, model: DSOS254A), as represented in Figure 4.2.3 (a). The charge deposited per pulse was determined by dividing the signal area by the oscilloscope's input impedance (50 Ω). The stability and reproducibility of the delivered pulses were assessed through repeated measurements of the charge per pulse generated in consecutive pulses and across different days.

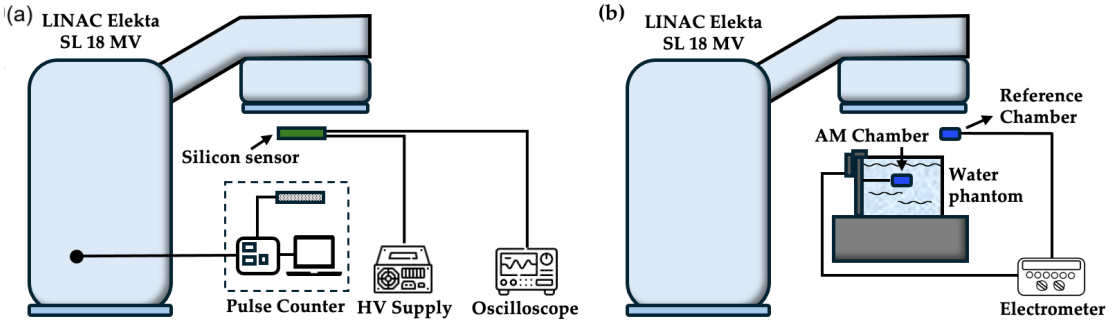

Figure 4.2.3: Experimental setup used for: (a) the stability and reproducibility study of the beam; (b) the PDD measurement in conventional mode.

4.2.3 Dosimetric Measurements

Following the machine modifications, the beam energy was verified by measuring the percentage depth dose (PDD) curves.

In conventional mode, these measurements were carried out using the Advanced Markus (AM) ionization chamber (Type 34045, PTW, Freiburg, Germany) and a 1D water tank scanner (Sun Nuclear Corporation, Melbourne, USA), shown in Figure 4.2.3 (b), following the TRS-398 guidelines of the International Atomic Energy Agency (IAEA) [93].

For UHDR irradiations, PDD curves were acquired using GafChromic EBT XD films (Ashland, Bridgewater, USA) placed between PMMA slabs to avoid recombination issues in ionization chambers [94, 95]. PDD curves were measured

Figure 4.2.4: (a) One-dimensional water phantom positioned at the isocenter; (b) Setup wit applicator and the PMMA phantom.

in two configurations: at the isocenter position and at the same position with the applicator in place. A holder secured the applicator at the crosshair foil position, with its exit side aligned with the surface of the water tank or the PMMA (Right plot of Figure 4.2.4). The detector was always positioned transversely at the beam center. From these measurements, the practical range (Rp) and the depths where the absorbed dose was 50% (R_{50}) and 80% (R_{80}) of the maximum dose were calculated, as these are essential dosimetric quantities. Based on R_{50}, the reference depth (z_{ref}) was calculated, which is the position at which the absorbed dose evaluation should be performed:

$$z_{\text{ref}} = 0.6R_{50} - 0.1 \tag{4.1}$$

From the measurements with GafChromic EBT XD films, it was possible to quantify the dose-per-pulse (DPP), the instantaneous dose-rate within the pulse, and the average dose-rate of the beam. The instantaneous dose-rate was obtained by dividing the mean DPP by the pulse duration τ (2 μs), while the average dose-rate (ADR) was calculated from the number of pulses delivered (N) at a fixed PRF of 100 Hz [58]:

$$\mathrm{ADR} = \frac{\text{total dose}}{\left(\frac{N-1}{\mathrm{PRF}} + \tau\right)} \tag{4.2}$$

In this case, the EBT XD films were placed inside the PMMA phantom under a buildup layer of 18 mm, thickness selected based on the z_{ref} values determined from the PDD analysis, and taking into account the correction factors for the transition between water and PMMA. In the wedge tray position, due to space constraints, the films were irradiated without buildup.

From the GafChromic film measurements, it was also possible to evaluate the spatial profiles of the beam. When using films, the total number of pulses N was adjusted depending on the setup to avoid saturation issues.

The procedure for evaluating the absolute dose from the irradiated films is as follows. The films were scanned using a flatbed color scanner (Model: Epson Expression 12000XL) in transmission mode, acquiring 48-bit RGB images at a resolution of 100 dpi. Scanning was always performed twice: once before irradiation to acquire the background image, and again 24 hours after irradiation to measure the delivered dose. The net Optical Density (OD) was calculated as the pixel-by-pixel difference between the OD of the irradiated images and the background images, over a Region of Interest (ROI) with a size similar to the active area of the AM chamber (0.20 cm^2) [96, 97].

Two different calibration curves were used to convert the net OD: the first was based on the conventional electron beam from the Elekta LINAC at 10 MeV in the range of 0.5 – 10 Gy, and the second was based on the UHDR electron beam at 9 MeV from CPFR (Pisa, Italy) for the range of 0.5 – 40 Gy. Below the 10 Gy threshold, the difference observed between the calibration curves was less than 5%, which corresponds to the standard uncertainty associated with the dose obtained using GafChromic films [98]. For doses above 10 Gy, only the calibration based on CPFR irradiations was used. For additional reliability, a calibration curve was also determined by scanning the films one week after irradiation. The difference between the curves from 24 hours and one week was 2.5% (Figure 4.2.5). All calibration curves were fitted using the following rational function:

$$\mathrm{netOD} = a + \frac{b}{\mathrm{Dose} - c} \tag{4.3}$$

where a, b, and c are free parameters.

Finally, an Output Factor (OF) study was conducted in both irradiation modes at the isocenter position, varying the beam field size from 3 × 3 cm^2 to 30 × 30 cm^2.

4.3 Results

4.3.1 Beam pulse characterization

The study of charge deposited in silicon per pulse was conducted under various measurement conditions, as illustrated in Figure 4.2.1. Figure 4.3.1 displays the superimposed waveforms acquired from the same sensor under different

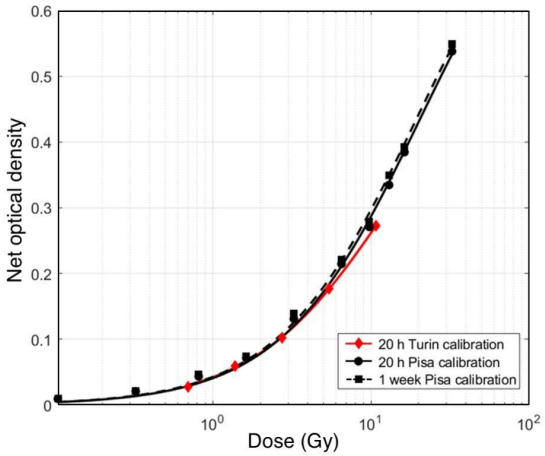

Figure 4.2.5: Different EBT XD calibrations with best fit curves.

measurement conditions. A significant increase in charge is immediately apparent at the wedge position. Additionally, it is observed that the pulse duration is maintained at 2 μs, as set from the accelerator.

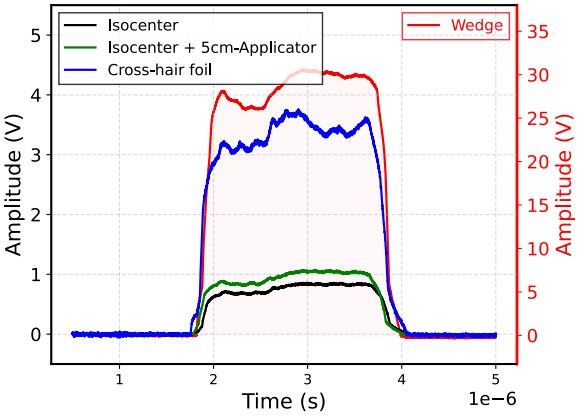

Figure 4.3.1: Output voltage pulse generated by the 10 MeV UDHR electron beam from silicon sensor (60 μm thickness) recorded by the oscilloscope with the different irradiation settings. The input impedance of the oscilloscope was 50 Ω. The wedge signal amplitude is shown in right vertical axis for ease of comparison.

To provide a more detailed description of the accelerator's performance, Figure 4.3.2 shows the analysis of the charge collected per pulse in UHDR mode at the crosshair foil. The median value, along with the 25th and 75th percentiles, is presented to give an indication of the measurement variability. In the first plot (a), the charge collected per pulse at the crosshair foil position (irradiating 20 consecutive pulses) is shown as a function of PRF. The median charge value between the lowest and highest PRF differs by approximately 7%, while for a constant PRF, the deviation per pulse from the median value does not exceed 5%. In the second plot (b), the charge per pulse is compared for two different delivery modes: 10 single pulses versus a sequence of 30 consecutive pulses, for both RF injection cycle modes (LP and HP). The maximum observed difference is 3.7%,

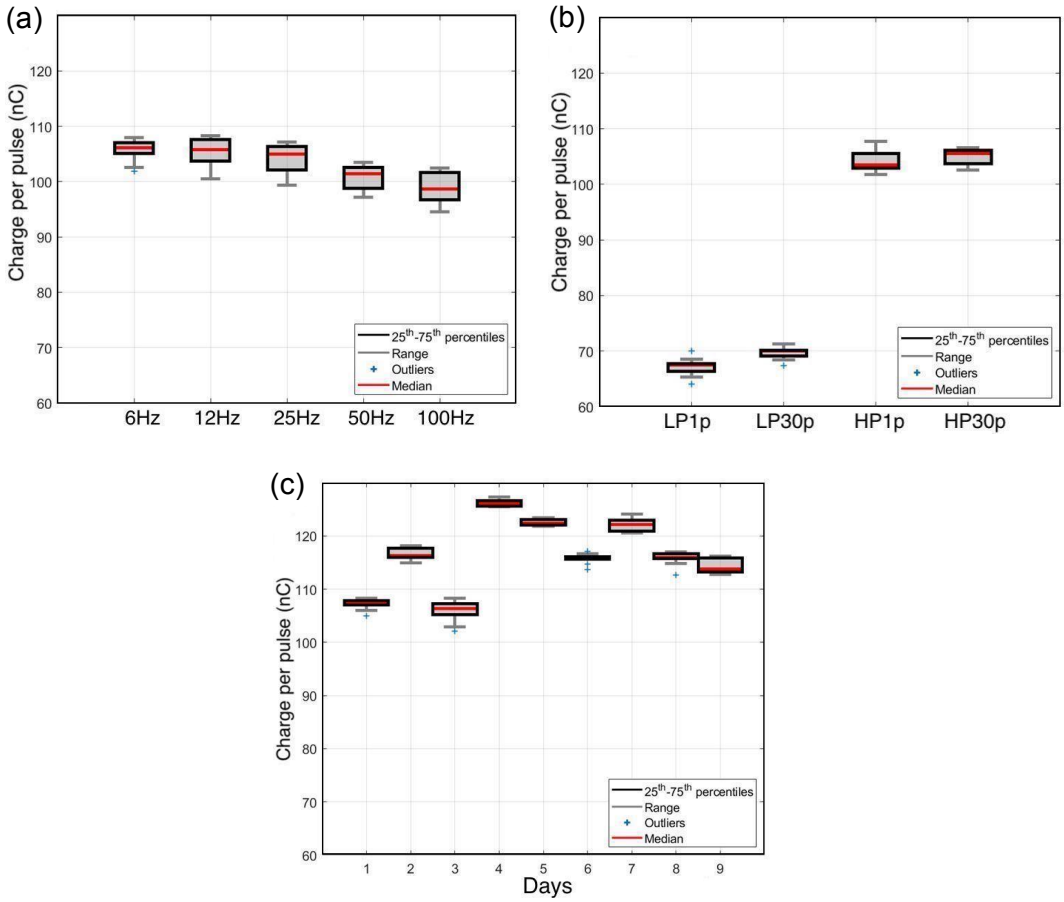

Figure 4.3.2: (a) Collected charge per pulse at the crosshair foil position for different PRFs. Each boxplot represents a total of 20 pulses delivered in HP mode. (b) Comparison of the charge per pulse at the crosshair foil position in LP and HP modes considering single pulse irradiations repeated 10 times (LP1p and HP1p) and 30 consecutive pulses (LP30p and HP30p. (c) Repeatability of the charge per pulse at the crosshair foil position acquired on different days in HP mode.

with the LP mode showing better pulse-to-pulse stability at the cost of a lower charge per pulse, which is 35% lower than in HP mode. Consecutive pulses in LP mode exhibit a 2% variation in charge, while in HP mode, this variation increases to 3.8%.
The third plot (c) illustrates the reproducibility of pulses in HP mode, where the charge per pulse was measured at the crosshair foil during identical irradiations of 30 pulses with a PRF of 100 Hz. This measurement was repeated over nine different days across a three-month period. The deviation from the median value was less than 8% for 90% of the measurements.

4.3.2 Dosimetry

From the PDD results obtained in UHDR mode using GafChromic films, a good agreement was achieved with the PDD curves (obtained from both the AM chamber and the films) for the conventional electron beam at 10 MeV (Figure 4.3.3). The maximum difference between the R_{50} values is 3.6%. Near the surface

(the initial points of the curve), there is an observed underdose, which could be attributed to potential air gaps between the PMMA plates or the proximity to the film edge [99]. The dosimetric parameters calculated are presented in Table 4.1. Different detectors yield comparable parameter values and confirm that the modification of the LINAC did not affect the beam's energy distribution. The uncertainties for the R_{80} and R_{50} values are at most 3%, while the R_p values exhibit larger uncertainties of 5%, as they are calculated from the intersection of two interpolation lines. The R_{50} values reported in Table 4.1 are 7% lower than the expected value for 10 MeV electrons [100], indicating that the most probable energy of the beam is slightly below 10 MeV.

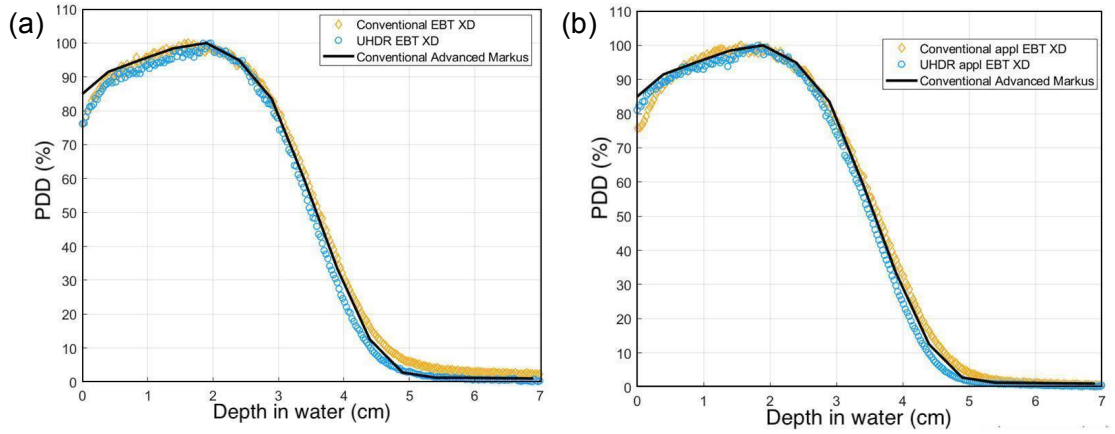

Figure 4.3.3: Comparison between PDD curves measured with the Advanced Markus and GafChromic films EBT XD in conventional and UHDR regimes (a) without the applicator and (b) with the applicator

Mode	Setup	R_{80} (cm)	R_{50} (cm)	R_p (cm)	z_{ref} (cm)
Conv	Advanced Markus	2.95 ± 0.10	3.61 ± 0.11	4.75 ± 0.18	2.07 ± 0.07
	EBT XD	2.94 ± 0.07	3.65 ± 0.05	4.69 ± 0.26	2.09 ± 0.03
	EBT XD with the applicator	2.97 ± 0.05	3.67 ± 0.02	4.72 ± 0.24	2.10 ± 0.01
UHDR	EBT XD	2.88 ± 0.10	3.54 ± 0.10	4.55 ± 0.28	2.03 ± 0.06
	EBT XD with the applicator	2.89 ± 0.04	3.54 ± 0.02	4.55 ± 0.19	2.03 ± 0.01

Table 4.1: Comparison of range parameters in water in conventional and UHDR modes.

Table 4.2 and Table 4.3 presents the values of charge per pulse (CPP) measured by the silicon sensor, the dose-per-pulse (DPP), the average dose-rate (ADR), and the instantaneous dose-rate (IDR) per pulse , evaluated from the absorbed dose at the reference depth Z_{ref} across the four configurations, in conventional (CONV) and UHDR mode respectively. The charge per pulse as a function of the dose under UHDR conditions is shown in Figure 4.3.4. In this case, the measurement at the wedge was not considered, as only a single pulse was acquired. Significantly more statistical data would be required for the measurement to be deemed reliable. The calibration factor was determined from the slope of the linear fit of the charge as a function of the dose. For this calculation, having acquired the dose using the buildup layer and the charge with silicon in air, the latter was

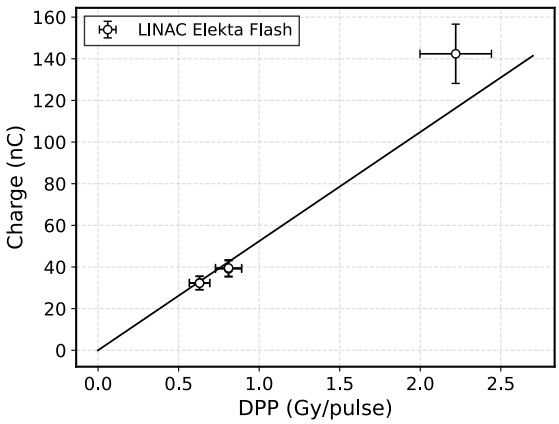

Figure 4.3.4: Charge per pulse as a function of the dose under UHDR conditions at the isocenter, at the exit of the applicator and at the cross-hair foil.

corrected by a factor of 7%, calculated from previous measurements with silicon with and without the buildup layer. The calibration factor is equal to:

$$\text{CalibrationFactor} = (19.08 \pm 0.99)\ \text{Gy}/\mu C \tag{4.4}$$

An important increase in dose of at least three orders of magnitude can be observed when transitioning from conventional to UHDR mode for all irradiation settings. At the wedge tray position in UHDR mode, only a single pulse was delivered to avoid exceeding the dose range of the EBT XD films (40 Gy), and therefore, it was not possible to calculate the average dose intensity for multiple pulses. The use of the PMMA applicator results in a 57% increase in DPP at the isocenter in conventional mode and a 28% increase in UHDR mode.

CONV				
	CPP (pC)	**DPP (Gy)**	**ADR (Gy/s)**	**IDR (Gy/s)**
Isoc	7.14	$(1.60 \pm 0.08) \cdot 10^{-4}$	$(1.60 \pm 0.08) \cdot 10^{-2}$	$(7.99 \pm 0.04) \cdot 10^{1}$
Appl	11.76	$(2.52 \pm 0.13) \cdot 10^{-4}$	$(2.52 \pm 0.13) \cdot 10^{-2}$	$(1.26 \pm 0.06) \cdot 10^{2}$
Cross	33.7	$(6.76 \pm 0.34) \cdot 10^{-4}$	$(6.76 \pm 0.34) \cdot 10^{-2}$	$(3.38 \pm 0.17) \cdot 10^{2}$
Wedge*	362.24	$(0.92 \pm 0.05) \cdot 10^{-2}$	$(92.3 \pm 4.6) \cdot 10^{-2}$	$(4.61 \pm 0.23) \cdot 10^{3}$

* Dose in air without build up.

Table 4.2: Dosimetry results for CONV mode

UHDR				
	CPP (nC)	**DPP (Gy)**	**ADR (Gy/s)**	**IDR (Gy/s)**
Isoc	29.85	0.63 ± 0.04	83.6 ± 4.2	$(3.6 \pm 0.18) \cdot 10^{5}$
Appl	36.59	0.81 ± 0.04	89.5 ± 4.5	$(4.03 \pm 0.20) \cdot 10^{5}$
Cross	131.84	2.22 ± 0.11	309 ± 16	$(12.3 \pm 0.6) \cdot 10^{5}$
Wedge*	1103.59	27.2 ± 1.4	n.d.**	$(136 \pm 7) \cdot 10^{5}$

* Dose in air without build up. ** n.d.: not determined.

Table 4.3: Dosimetry results for UHDR mode

The beam profiles obtained from the scanned images are shown in Figure 4.3.5. In conventional mode, the profile at the wedge exhibits some irregularities, likely

attributed to the geometry of the primary filters and the secondary scattering foils, which feature two inclined sections corresponding to specific scattering angles [55].

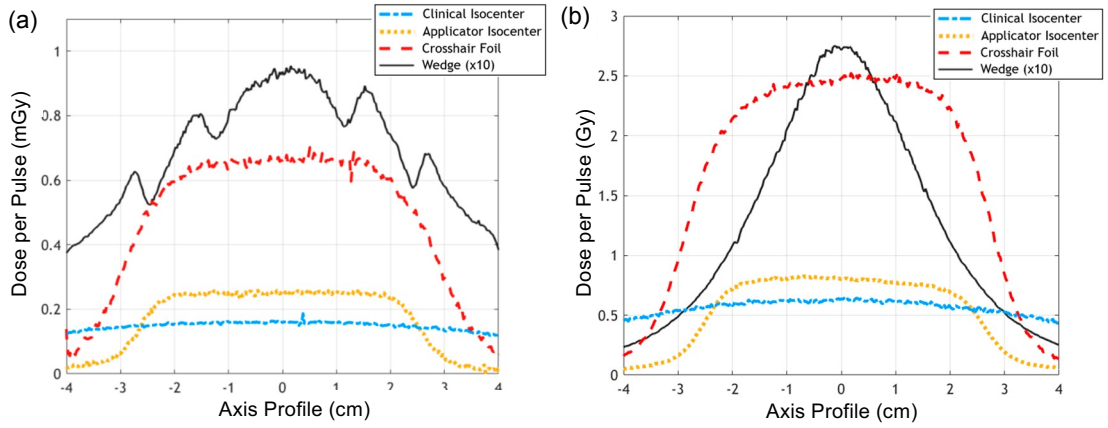

Figure 4.3.5: Dose profiles obtained from GafChromic films for the conventional (a) and UHDR modes (b). In both figures, the dose profiles at the wedge tray were divided by a factor of 10 for ease of comparison.

Figure 4.3.6 shows that, in conventional mode, there is good agreement between the output factor measured by the AM chamber and the GafChromic films. The analysis of the UHDR mode data reveals a similar trend to that of the conventional mode data. For field sizes larger than 10×10 cm^2, the UHDR values are systematically lower, as also reported by [57], although all differences remain within the error bars.

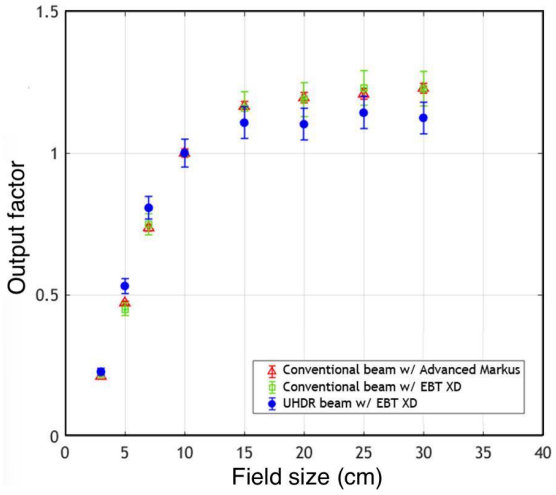

Figure 4.3.6: Output factor measured with the Advanced Markus and GafChromic films EBT XD in conventional and UHDR modes for different square field sizes.

4.4 Discussion and conclusion

An Elekta SL 18 MV LINAC was upgraded to deliver a 10 MeV electron beam under ultra-high dose-rate (UHDR) conditions, and its performance was characterized. Key modifications involved removing the primary and secondary scattering sheets, increasing gun current and magnetron power, and adjusting certain beam transport parameters. Additionally, a custom pulse control circuit (PCC) was developed to count the LINAC's pulses and stop irradiation after the required number, since the ionization chamber's reliability was affected by the use of an attenuator.

A silicon diode sensor was used to verify pulse stability during single deliveries and across multiple deliveries over different days. A 3.7% variation in charge per pulse was observed between individual and consecutive beam deliveries. Irradiations performed on the same day showed good reproducibility, with a maximum charge deviation of 2% for the low-power (LP) mode and 4% for the high-power (HP) mode. Notably, pulse stability in UHDR mode included the first pulse, which was up to 4% smaller than the stable pulses. This slightly increased the percentage variation compared to the findings by Konradsson et al. [101], who excluded the first pulse from their analysis and reported deviations below 3%. Since standby periods are known to affect LINAC performance, reproducibility was assessed over three months, with the silicon diode showing pulse charge deviations within 8% of the median value, which is acceptable for in vitro radiobiology studies.

The energy distribution of the beam remained unchanged despite the LINAC modifications, as confirmed by the PDD curves and associated parameters. The DPP and dose-rates achieved in this study are comparable to those obtained from other modified LINACs, delivering a minimum of 0.6 Gy/pulse ($3.6 \cdot 10^5$ Gy/s instantaneous dose-rate) at the isocenter and up to 27 Gy/pulse ($136 \cdot 10^5$ Gy/s instantaneous dose-rate) at the wedge tray position. Average dose-rates above 300 Gy/s were reached at the crosshair foil position with a pulse repetition frequency (PRF) of 100 Hz. These dose-rates allow for planning both radiobiological experiments and instrumentation tests to compare conventional and UHDR regimes, though careful attention must be paid to the limited space in the wedge irradiation setup when designing experimental configurations.

Further performance improvements will be explored in the coming months. The results reported here reflect a PRF of 100 Hz and hardware and software modifications that draw up to 6 kW from the magnetron. Given that the maximum PRF achievable with this LINAC is 400 Hz and the magnetron power can be increased to 7 kW, additional optimizations will be investigated to achieve higher DPPs and dose-rates. Additionally, a correlation study between the signal from silicon sensors and the delivered dose in a PMMA (or solid water) phantom, measured with the AM chamber or GafChromic films, is planned. This may lead to a dose-based beam monitoring approach, for instance, by placing silicon sensors at the beam field edges and integrating dose control based on pulse counting by the PCC.

The beam characterization reported in this study is a preliminary step toward its use in spatial fractionation studies. Like UHDR irradiations, Spatially Fraction-

ated Radiation Therapy (SFRT) has shown potential to spare healthy tissue while maintaining tumor control efficacy. Several research groups are studying the effects of FLASH and mini-beams, both separately and in combination, to assess possible synergies. The PMMA applicator used in this study, which increased dose at the isocenter, could be used to hold perforated models along the beam path to study the dosimetric properties of different configurations (e.g., number, geometry, and spacing of the holes). Parameters such as peak width at half maximum and peak-to-valley dose ratio could be characterized for various available energies (6 to 18 MeV) and dose-rates for the 10 MeV electron beam. This would provide insights into differentiating tissue-sparing effects from UHDR beams and spatial fractionation. Preliminary tests in this context are described in Section 5.4.

The possibility of delivering 18 MeV electron beams will also be explored to investigate UHDR at higher energies [102].

To conclude, the Elekta SL 18 MV LINAC has been successfully modified to deliver UHDR electron beams at 10 MeV. These modifications are fully reversible, and switching between conventional and UHDR modes takes only a few minutes. The LINAC now reaches a maximum of 2.2 Gy/pulse and an instantaneous dose-rate exceeding 10^5 Gy/s at the crosshair foil position, with a pulse duration of 2 μs. A silicon sensor device monitors the stability and reproducibility of pulses across different beam deliveries and days.

In the future, this LINAC could serve as a platform for testing beam monitoring and dosimetry devices, as well as for conducting radiobiological experiments to further investigate the FLASH effect. The use of applicators with various geometries and perforated models may facilitate studies on the combined effects of SFRT and UHDR irradiation.

Chapter 5

Silicon: Characterization of silicon sensors on FLASH electron (and proton) beams

Silicon devices are strong candidates for monitoring FLASH radiotherapy (RT) beams due to their highly developed manufacturing technology and significantly fast response times. The use of silicon sensors with a small sensitive thickness further reduces the generation of charge carriers in the active volume and decreases charge collection time, thus limiting recombination and saturation effects. This chapter presents the work performed in the field of thin silicon detectors for monitoring UHDR beams. Specifically:

- Section 5.1 provides an overview of the silicon sensors employed in this study, covering both strip and pad geometries from various FBK productions, alongside the front-end electronics (TERA08 and TERA09).
- Characterization of these sensors using conventional electron beams, delivered by the Elekta SL18 LINAC at the Physics Department in Turin, is detailed in Section 5.2.
- Preliminary results from experiments on FLASH electron beams, conducted at the ElectronFLASH facility, are presented in Section 5.3.
- Finally, Section 5.4 explores the use of a large segmented sensor with 146 strips for single-shot study of the beam shape and its possible applications in spatially fractionated radiotherapy (SFRT).

5.1 Sensors and readout electronics description

PIN sensors of various geometries (described in Section 3), all manufactured by FBK [103] within different productions were used during my PhD research. The strip sensors (11 and 146 strips) were selected from the *MoVe-IT 2020* production [104, 105], while the pad sensors from the *eXFlu* production.
The readout electronics consist of TERA chips (TERA08 and TERA09), featuring 64 identical channels, each implemented as a current-to-frequency converter.

5.1.1 Strip segmented silicon sensors from MoVe-IT production

The MoVe-IT production includes 14 wafers, subdivided into three groups based on wafer substrate and gain implant dose [105]. Most sensors from this production are LGAD sensors and thus feature a gain layer: a p^+ gain layer was added to each strip by implanting boron below the n^{++} electrode, with a doping concentration of approximately $10^{16}/cm^3$ and a thickness of approximately 1 μm. This allows for creation of a very high local electric field, sufficient to activate charge multiplication [106]. Two different silicon substrates were used in the production, exploiting a low-resistivity silicon back handling support: an epitaxially grown silicon layer (Epi) with a resistivity greater than 200 Ωcm and an active thickness of 45 μm, and a high-resistivity ($>$ 3000 Ωcm) glued silicon layer (Si-Si) with an active thickness of 60 μm. As said, only PIN sensors from this production were used for FLASH applications.

The initial sensor chosen for testing the experimental setup under conventional beams is illustrated in Figure 5.1.1 (a). It is without the implanted gain layer in any of its strips (T1, T8, and T10 sensors) [107]. This geometry was designed for timing applications [104, 108]. Specifically, the W1-T1 variant, previously characterized in the laboratory with an active thickness of 45 μm, was chosen. The sensor is segmented in 11 strips, all demonstrating breakdown voltages exceeding 300 V under reverse bias, indicating excellent performance. The strip dimensions are 0.55 mm width, 4 mm length (sensitive area of 2.2 mm^2), with a pitch of 0.591 mm.

The sensor was mounted to a passive PCB board for biasing and signal extraction, utilizing three output channels for potentially reading out three separate strips via wire bonding. Strips not connected to the output channels were bonded to ground to optimize charge collection. The signal generated on a strip was analysed by two methods: through the TERA08 chip for integrated charge measurements, splitting the signal into the 64 TERA08 channels as will be explained in Section 5.1.3, and through an oscilloscope, where individual voltage signals can be converted to charge, taking into account the input impedance of the oscilloscope. The sensor segmentation is not fully expoited, as only up to three strips are measured, corresponding to the three readout channels on the mounted board. However, as demonstrated in the following sections, the implementation of these sensors confirmed the feasibility of using them to provide spatial information.

The larger sensor we have tested has a sensitive area of 2.6 $\times$ 2.6 cm^2 and it is shown in Figure 5.1.1 (b). It was designed to cover the entire clinical proton beam spot at the isocenter (i.e. in the treatment rooms at CNAO, the proton beam FWHM ranges between 0.7 and 2.2 cm in the clinical energy range). It is segmented into 146 strips with a pitch of 180 μm, an inter-strip spacing of 66 μm, and each strip has an active area of 180 $\times$ 26214 μm^2. [109]. Each wafer from the production batch included eight large-area sensors of this type, in which the gain layer was not implanted (designated as A3 in MoVe-IT production). The TERA09 chip, described in the following section, was used for reading signals from individual strips. The central 128 strips of the 146 strips were connected to

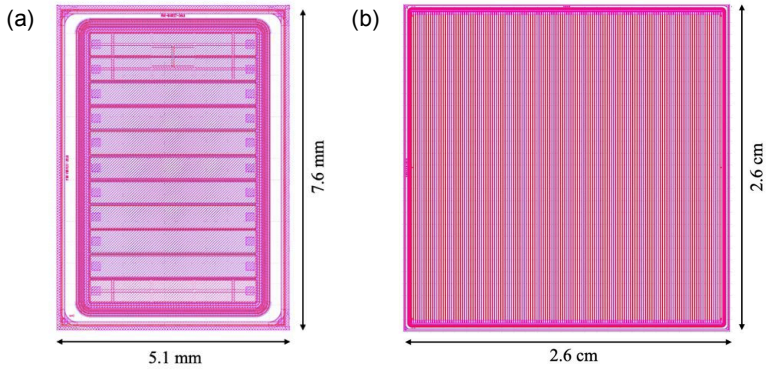

Figure 5.1.1: Silicon sensor summarized layout: (a) Segmented into 11 strips selected from MoVe-IT production. Each strip is characterized by a sensitive area of 2.2 mm^2 (4 mm $\times$ 0.55 mm), an interstrip pitch of 0.591 mm, and a interstrip distance of 51 μm. (b) Large segmented sensor from MoVe-IT production. The 146 strips are visible, each one with a pitch of 180 μm, an inter-strip spacing of 66 μm, and an active area of 180 $\times$ 26214 μm^2.

the readout, fully exploiting the 64 channels of two TERA09 chips. This setup was employed with conventional electron and proton beams to verify the ability to study beam shape.

5.1.2 Pad sensors from exFlu production

The eXFlu production batch [110, 111] was developed for a new design of silicon sensors with internal gain. The new design consists implanting the gain layer by overlapping a p^+ and an n^+ implants. This technology is expected to be more resilient to radiation and will empower the 4D tracking ability typical of the LGAD sensors well above fluences of $10^{16}/cm^2$ [112]. The production includes several thin wafers of varying thicknesses (between 15 μm and 45 μm), with a dedicated area for samples specifically designed for the FRIDA project. These samples consist of sensors with different geometries (strip/pad, varying active areas) to facilitate the study of how sensor performance depends on geometry under FLASH beam conditions.

The samples selected for the first validation on FLASH beams are PIN silicon sensors without the gain layer. The design of these sensors allowed us to compare signal collection across different geometries. Indeed, each silicon square device (4.7 mm side length) contains six pad sensors (2 mm^2, 1 mm^2, 0.56 mm^2, 0.25 mm^2, 0.06 mm^2, 0.03 mm^2), one pixel sensor (with 8 pads), and one strip sensor (with 4 strips of varying widths). Three of them were selected, as shown in Figure 5.1.2 on two wafer featuring different active thickness (30 μm and 45 μm) and a total thickness of 655 and 570 μm, respectively.

The active thickness is epitaxially grown (Epi) over a thick low-resistivity handling wafer. The sensors were preliminary characterized in our department lab to verify their electrical properties. Through the analysis of the I-V curves, it was verified that they fully deplete at 10 V and the breakdown voltage occurs over 300 V of reverse bias. The sensors were mounted with conductive glue

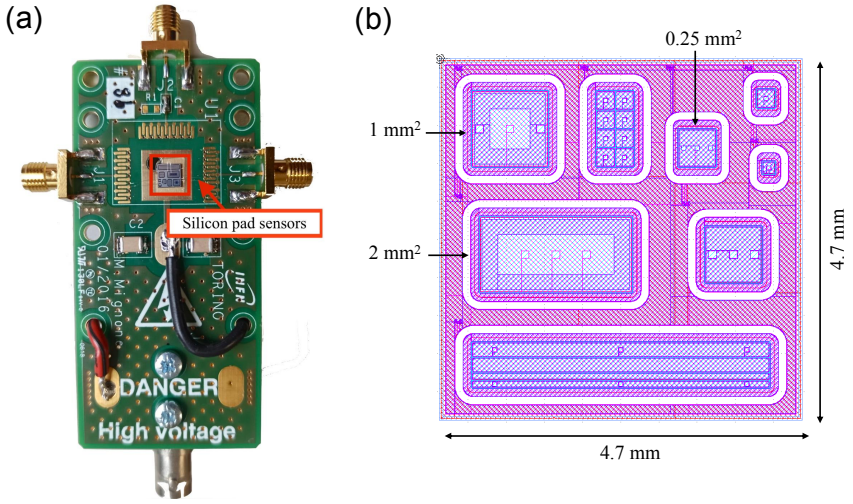

Figure 5.1.2: (a) The sensor mounted on the HV distribution board is represented. (b) Technical drawing of the sensors used in the experiment. Among the different implanted pads, the arrows point out the ones tested (0.25 mm^2, 1 mm^2, 2 mm^2).

on the high-voltage distribution boards cited above, shown in Figure 5.1.2 (a), allowing simultaneous reading of the three chosen pads connected to the output channels through wire-bonding. The guard ring of each pad was grounded. The measurements performed with these pads allowed us to evaluate the performance dependence on geometry, with detection on electron beams. Again, signal measurements were conducted with both the TERA08 chip and the oscilloscope.

5.1.3 Front-end electronic readout

TERA08 The TERA08 chip was used for charge measurements. This readout system was designed for medical applications by the INFN group of Turin and it is currently in use at the Italian National Center for Oncological Hadrontherapy (CNAO) as a front-end electronic readout for gas monitor chamber for the real-time monitoring and control of the dose delivered during treatment [25].

This chip features 64 identical channels and is designed using CMOS AMS 0.35 μm technology. In each channel, TERA08 performs a conversion from the instantaneous current to a digital pulse frequency, where each digital pulse corresponds to a fixed input charge quantum [113]. Each converter is followed by a 32 bit counter. The conversion occurs at a maximum frequency of 20 MHz, meaning that even when selecting the largest possible charge quantum (1.115 pC), the maximum current each channel can convert is 20 μA. The chip is sensitive to both negative and positive charges, as the converter is designed to accept inputs of both polarities. The operating principle of the counter, based on the recycling integrator principle, is illustrated in Figure 5.1.3.

From the schematic, it can be seen that the input current I_{in} is integrated on a 600 fF capacitor C_{int} via an operational transconductance amplifier (OTA). The output voltage from the OTA is compared to two thresholds (one positive and one negative) by two synchronous comparators (CMP1 and CMP2). If the voltage

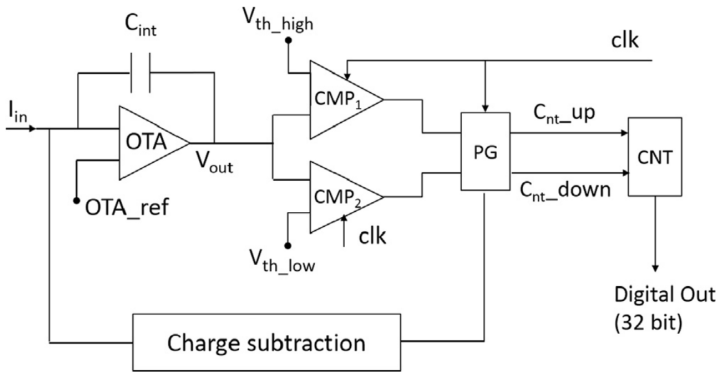

Figure 5.1.3: Schematic of a channel of TERA08 based on recycling integrator principle.

exceeds one of the thresholds, the counter (CNT) is incremented or decremented by a pulse sent from the pulse generator (PG). At the same time, the PG sends a pulse to the charge subtraction circuit, which subtracts a positive or negative charge quantum from the capacitor C_{int}.

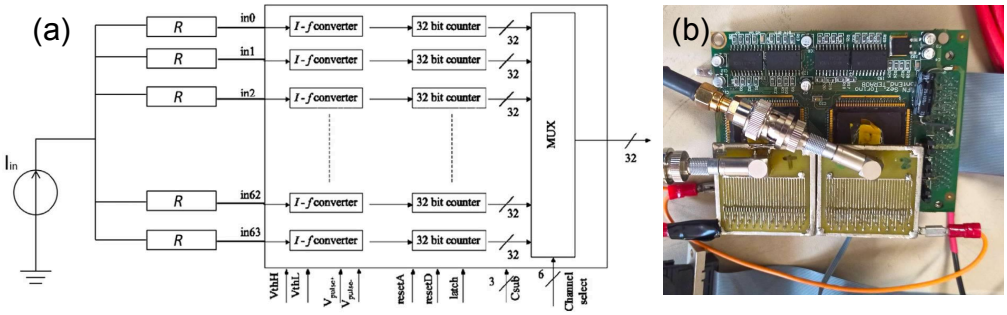

Figure 5.1.4: (a) Schematic of the setup used for measurements. I_{in} represents the input current and for each channel the own resistor is represented. (b) Picture of the board with two TERA08 chips mounted on.

For all measurements presented in this work, the value of the charge quantum was measured to be (211 $\pm$ 1) fC, in accordance with the chosen nominal setting of 200 fC, setting used for clinical applications and demonstrated to perform fairly uniform gain across the channels [114]. In this configuration the maximum current that a channel can convert without saturation is about 4 μA.

The TERA08 chip was employed by injecting an input current (from one single strip) split into the 64 channels, at the end of which the total counts are summed and converted into charge using the set quantum of charge. This approach was conceived within the FRIDA project to avoid the risk of channel saturation due to the very high charge release while still providing a reliable measurement of the input current.

In this setup, to avoid the direct connection of two or more operational amplifier inputs an upper-board adapter was used. Here high-value resistors (10 MΩ) are connected between the channel inputs and the common input node, as long as the input current is significantly larger than the offset currents needed to keep each OTA input at the correct voltage.

Figure 5.1.4 (a) shows the schematic of the board and Figure 5.1.4 (b) a picture of two TERA08 chips mounted on the same board on the right, for a total of 128 channels. An NI FlexRIO FPGA DAQ module was used for reading the individual channels, and LabView software was used for data acquisition and storage.

TERA09 A new 64-channel current-to-frequency converter ASIC has been designed to handle high-flux pulsed beams [115, 116]. The previous version of the chip, TERA08, can convert up to 4 μA of current without saturation using a charge quantum of 200 fC, making it suitable for monitoring currents in current particle therapy facilities (hundreds of nA). However, the pulsed beam structure provided by the next generation of accelerators, which implement new acceleration technologies, leads to a significant increase in beam flux per pulse [117, 118]. In the TERA09 chip version, the charge-to-frequency converter has been redesigned to increase the maximum conversion frequency. Additionally, automatic readout of the partial and total sums of the counter values has been implemented, which are directly accessible in dedicated registers. This technology achieves an increase of about two orders of magnitude in the dynamic range compared to the TERA08, while maintaining sensitivity and linearity.

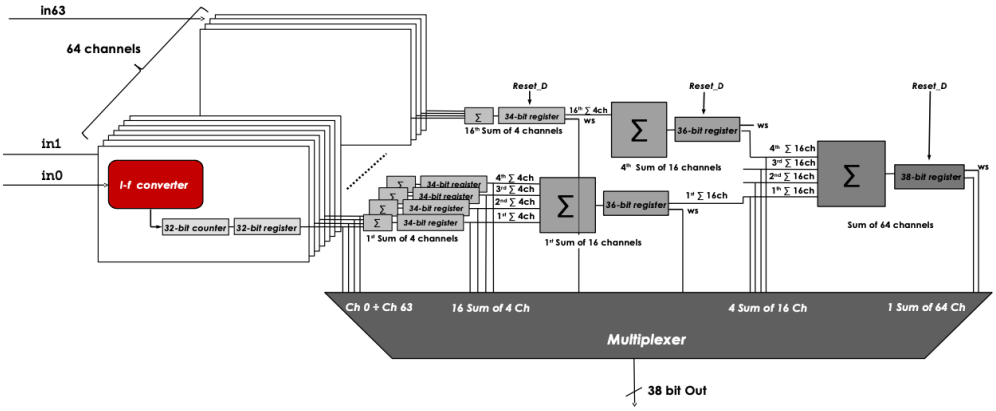

Figure 5.1.5: The overall schematic of the TERA09 chip.

Measurements performed with a charge quantum set to 200 fC (the value used for TERA application at cnao) and a clock frequency of 250 MHz have shown a maximum counter increment frequency of 62.5 MHz. It has been demonstrated that the counter frequency as a function of the input current for a single channel exhibits linearity up to $\pm$ 12 μA, which is the new saturation current, three times higher than the one obtained with TERA08 in the same conditions.

Figure 5.1.6 shows the setup used for the measurements with TERA09 reported in this thesis. A motherboard houses four TERA09 chips (two on the front side and two on the back side), allowing the reading of a total of 64 x 4 channels. The analog signals are sent to the individual channels via an analog adapter with 64 $\times$ 4 pins. The digital output signals are read individually through two VHDCI cables from a NI FlexRIO FPGA DAQ module (as done for TERA08) coupled with suitable LabView software for data acquisition.

A custom-designed PCB accommodates a 146-strip segmented sensor from the MoVe-IT 2020 production series, as previously detailed. Out of the 146 strips, only the central 128 are connected for reading 64 strips are routed to one chip and another 64 to a second TERA chip. The board is designed to enable the reading of signals from individual strips as well as from groups of strips, providing flexibility in data acquisition.

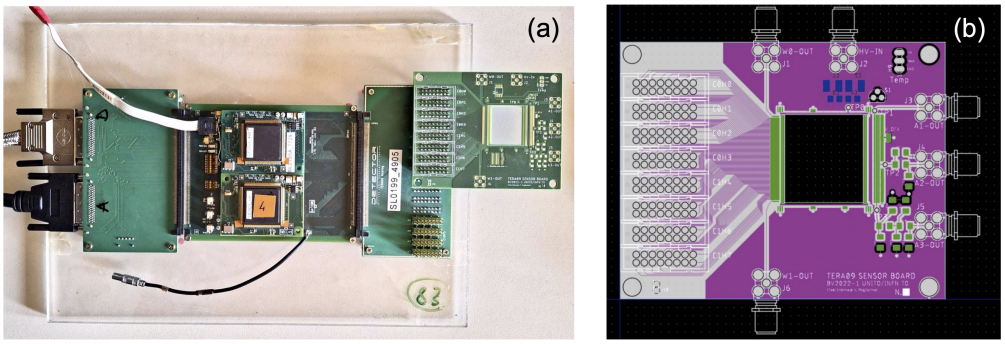

Figure 5.1.6: (a) Experimental setup used for measurements with the TERA09 chip. On the right side of the photo, the board for the 146-strip sensor from the MoVe-IT production is visible. (b) Design of the board intended to host the 146-strip sensor. On the left side of the board, the output channels for the 128 strips are present. The remaining three sides feature alternative signal readout options (individual strips, groups of strips, with the possibility of soldering resistors/capacitors for modified output signals).

5.2 First characterization on conventional electron beams from LINAC Elekta

To verify the effective functioning of the setup, preliminary tests were conducted with conventional electron beams on the Elekta LINAC machine at the Department of Physics, University of Turin.

One T-type sensor from the MoVe-IT 2020 production, without implanted gain layer in any strips, was used in this test. As mentioned in Section 5.1, these 11-strip sensors have a breakdown voltage greater than 300 V. Each strip has an active area of 2.2 mm^2 and an active thickness of 45 μm. Only one strip was connected to the readout electronics, while the remaining 10 strips were grounded.

The sensor was reverse biased at 50 V and the output of one strips was read out by a TERA08 chip. To avoid reaching the saturation current per channel (4 μA), an upper-board adapter was used, which allowed the splitting of the detector's input current into 64 readout channels, and then summing the counts of these channels to reconstruct the input current.

The sensor was tested on LINAC electron beam, positioned at the isocenter (SSD = 100 cm). The experimental setup is illustrated in Figure 5.2.1. Measurements were acquired at different energies (4 MeV, 6 MeV, and 10 MeV) by varying the dose-rate (100 MU/min, 200 MU/min, and 400 MU/min) while keeping the

total dose constant (100 MU). Measurements were also taken on different days to verify the reproducibility of the data.

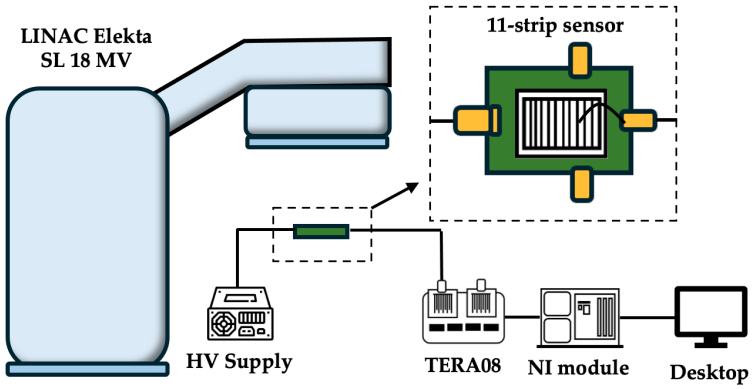

Figure 5.2.1: The experimental setup used for the initial measurements with an 11-strip silicon sensor on conventional electron beams. The sensor is biased using a high voltage module, and the sensor output is split into 64 channels of a TERA08 chip

In Figure 5.2.2, the steps of the raw data analysis acquired with TERA08 are shown. From the integral counts of the 64 channels, it is possible to evaluate the differential counts, clearly showing the start and end of the irradiation. Subsequently, the signals from the 64 channels are summed, and the pedestal is subtracted. To obtain charge values, the counts are multiplied by the charge quantum ($q_c = 200$ fC). To obtain the total charge, it is sufficient to sum the total measured counts, while to evaluate the average current, the total charge is divided by the total irradiation time:

$$I = \frac{q_c \left(\sum_t \mathrm{CNT}_t\right)}{t_{end} - t_{start}} = \frac{\left(\sum_t Q_t\right)}{t_{end} - t_{start}} \tag{5.1}$$

where q_c is the charge quantum, CNT_t are the counts measured over a time interval, and t_{start} and t_{end} represent the start and end of the irradiation, respectively.

In Figure 5.2.3, the measurements acquired with TERA08 for the three different energies and the three different dose-rates are represented (Total Dose : 100 MU). For the same total dose, changing the dose rate means changing the duration of irradiation, as shown in Figure 5.2.3.

In Figure 5.2.4 the trend of the average current during irradiation as a function of dose-rate for the three different energies is shown. For all three cases, a linear trend of the data was observed, with a coefficient of determination (R^2) greater than 0.99 and minimal deviations from the linear model. This result suggests the potential to calibrate the charge measured by TERA08 in terms of dose within the conventional range studied.

The data were acquired on two different days to verify the reproducibility of the data, as can be seen in Figure 5.2.5, were the charge measured in different dose-rate conditions in two different days is shown for three energies. The boxplot in 5.2.5 (b) shows that the deviation of the data from the median value does not exceed 2.5%.

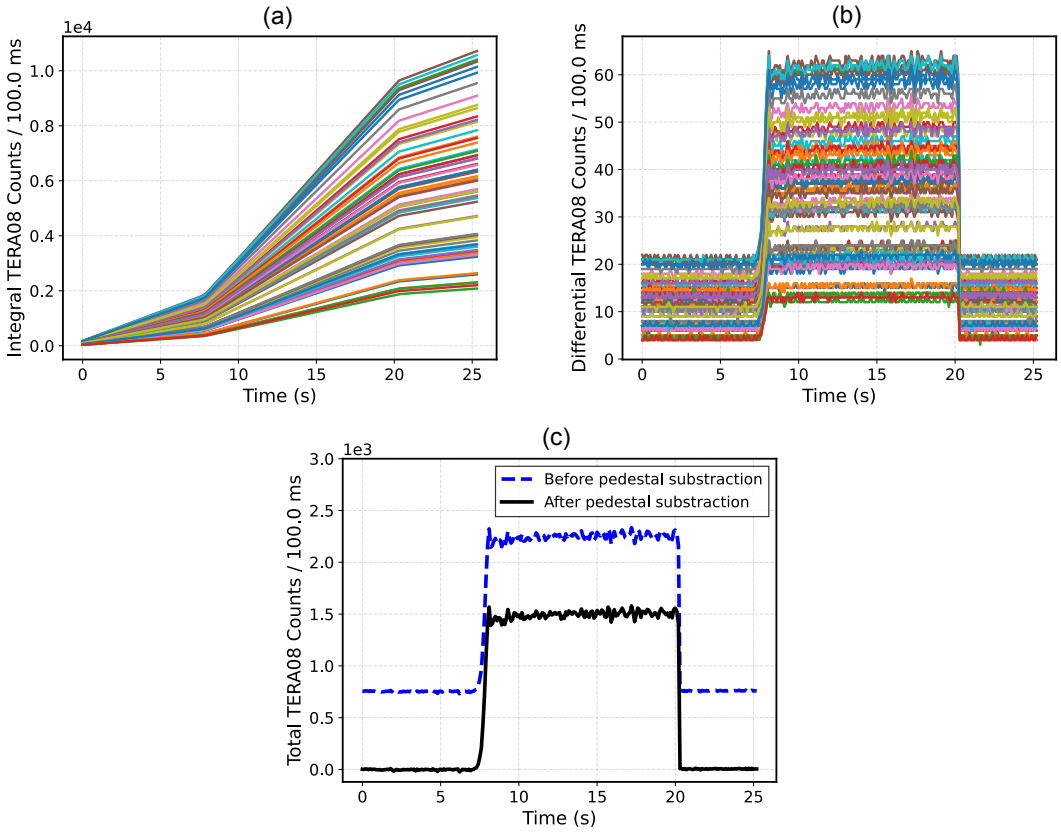

Figure 5.2.2: The initial steps of analysis performed on the raw data acquired with TERA08: (a) integral counts measured by each of the 64 channels in different colors, for each acquisition interval (set at 100 ms); (b) differential counts; (c) the sum of signals from the 64 channels is depicted in blue (corresponding to the total signal), and in black after pedestal subtraction.

The final aspect we aimed to investigate through these preliminary tests on conventional beams is the feasibility of studying the beam's shape. Although we are using individual sensors and thus performing point measurements, we sought to verify the dependence of these measurements on the position within the beam. This has been done by adopting two approaches:

- The first method involved moving the sensor in discrete steps along the beam field of view, and acquiring a complete irradiation at each step.
- The second method involved continuous acquisition during a single irradiation while the sensor scanned transversely to the beam.

In both cases, an automated motor system capable of moving in two dimensions was used. The distance between steps and the time the sensor remained stationary at each position were adjustable. For this test, two strips were connected via wire bonding to two output channels of the HV board, and the two signals were sent separately to two TERA08 chips.

In the first case, a 6 MeV electron beam with a frequency of 200 MU/min and a total dose of 50 MU was used, with a field size of 10×10 cm^2 at the isocenter. Measurements were taken on the XZ plane, where Z represents the beam direction and X is one of the two orthogonal directions to the beam direction.

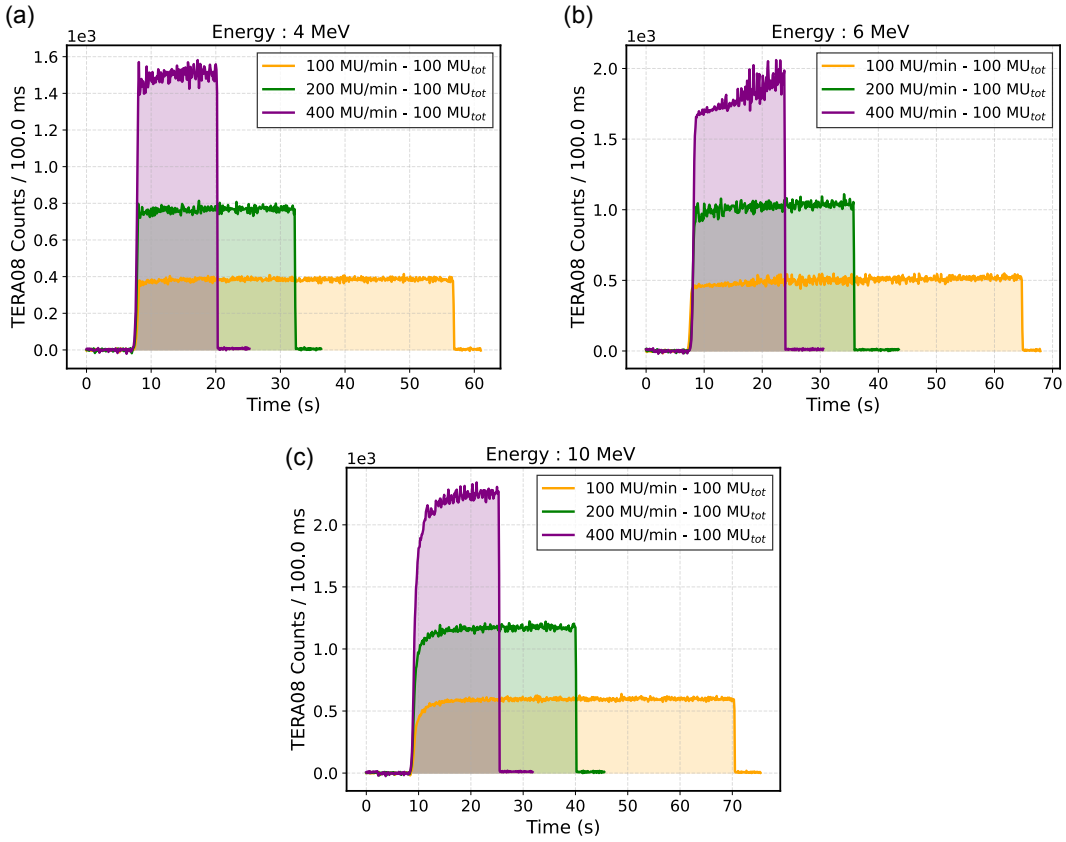

Figure 5.2.3: Counts measured for 3 electron energies (a) 4 MeV, (b) 6 MeV, (c) 10 MeV, under three different dose-rate conditions (100 MU/min, 200 MU/min, 400 MU/min), while maintaining a total dose of 100 MU are represented.

Five positions were tested along the Z axis, starting from the isocenter (Z = 100 cm) and moving away in 25 mm steps. Along the X axis, up to 20 positions were measured (in 10 mm steps) from one edge to the other of the field. The results are shown in Figure 5.2.6, which clearly indicates that the measured charge at the beam center decreases as the distance from the source increases and the beam width increases. In particular, when analyzing the measurements acquired at the isocenter (Figure 5.2.7), a FWHM of 100.2 mm was evaluated, which is consistent with the nominal beam size under these conditions (10×10 cm^2). The offset between the two curves in the plot is due to the fact that the two strips connected to TERA08 are separated by a certain distance, causing the beam center to cross the strips at different times. The transverse profile of the beam, and thus its dependence on Z, was verified at the center of the beam (fixed X) not only for 6 MeV and 200 MU/min, but also for two additional dose-rate values (100 and 400 MU/min) and for 10 MeV. The results are shown in Figure 5.2.8, where the event rate is plotted as a function of the distance from the source. In all cases, the event rate as a function of the distance was fitted using the following three-parameter inverse square law, that provides a good fit for the data at both energies and across all tested dose-rates:

$$\text{Rate(Z)} = a + \frac{b}{Z^2} \tag{5.2}$$

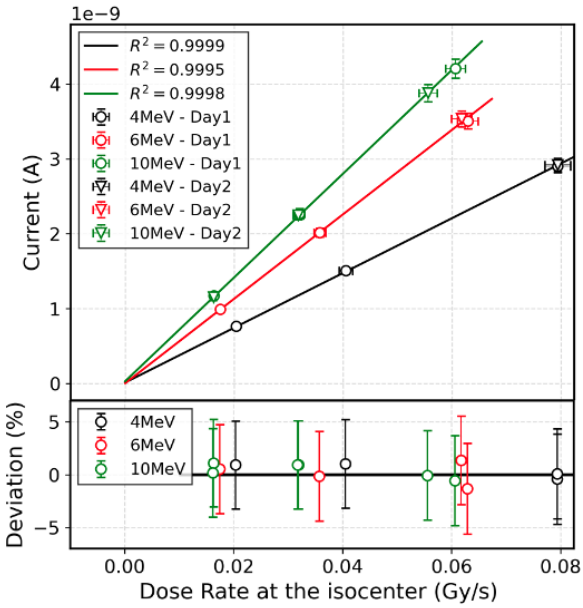

Figure 5.2.4: The instantaneous current measured with TERA08 in three different dose-rate conditions (100 MU/min, 200 MU/min, 400 MU/min) on two separate days and for three different energies (4 MeV, 6 MeV, 10 MeV). The coefficient of determination was found to be $R^2 > 0.99$. Deviations from linearity plots are also reported.

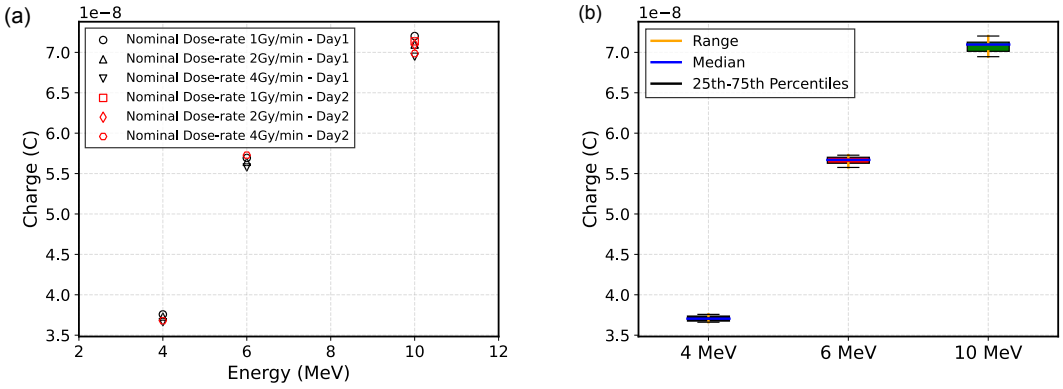

Figure 5.2.5: (a) Charge measured with TERA08 in three different dose-rate conditions (100 MU/min, 200 MU/min, 400 MU/min) on two separate days and for three different energies (4 MeV, 6 MeV, 10 MeV). (b) The boxplot shows the median value, along with the 25th and 75th percentiles to give an indication of the measurement variability.

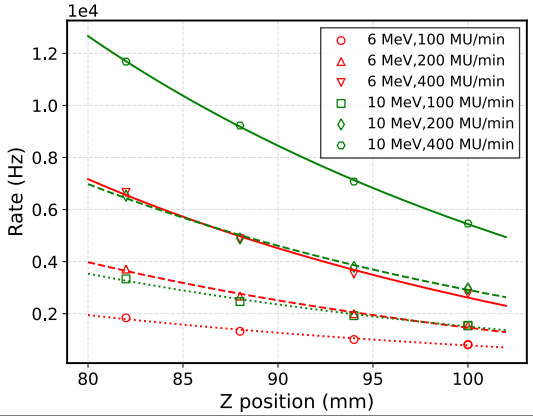

Figure 5.2.8: TERA08 count rates as a function of the position Z. The TERA08 counts follow an inverse square law ($I(r) = I_0/r^2$) with respect to distance, as expected from theory.

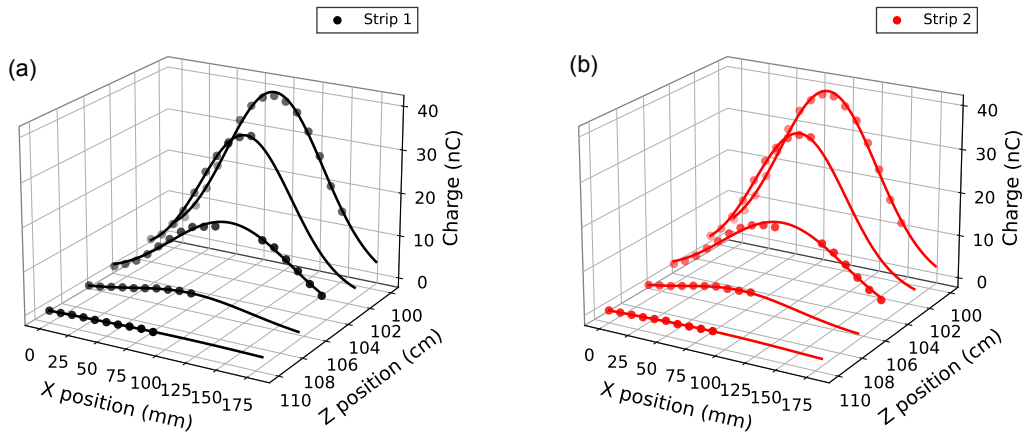

Figure 5.2.6: The charge measured by TERA08 at different positions along the X and Z axes. The position Z = 100 cm corresponds to the isocenter, and a decrease in Z corresponds to a further distance from the LINAC head. At each point, a complete irradiation was acquired. The data measured on the strip 1 are shown in black, while those measured on the strip 2 are shown in red.

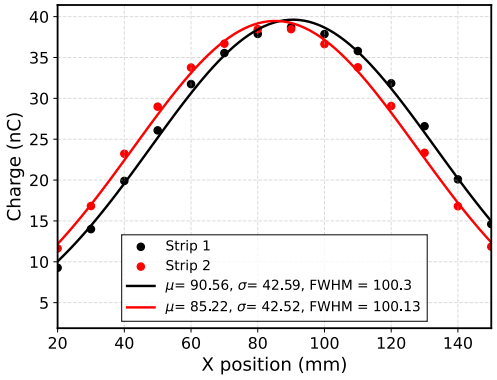

Figure 5.2.7: The charge measured by TERA08 at the isocenter (Z = 100 cm). (a) The data measured on the Strip 1 are shown in black; (b) The data measured on on the Strip 2 are shown in red.

Subsequently the beam shape was studied by continuously scanning the sensor along the X direction (fixed at the isocenter) during a single irradiation. Irradiations of 400 MU at 200 MU/min with 6 MeV energy were performed in this case. In Figure 5.2.9 (a) the obtained beam shape is due to light from the LINAC head and the presence of a centering cross on the crosshair foil. The sensor is sensitive to light, causing the TERA08 counts to decrease when the sensor passes through the shadow of the cross and when it exits the illuminated area. By acquiring data at the same positions with the beam both on and off (beam ON/OFF), it was possible to reconstruct the signal generated by the electron beam by subtracting the light background (the pink line).

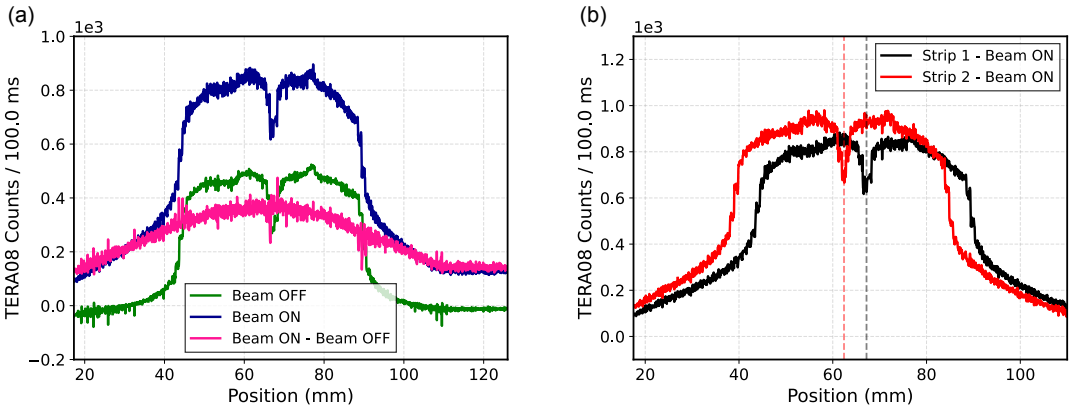

Figure 5.2.9: TERA counts acquired during a single irradiation while moving the sensor from one edge to the other of the beam, at the isocenter. The noise caused by the light and shadows from the LINAC centering system is clearly identifiable. (a) The beam OFF data are rapresented in green, the beam ON data in blue and the actual signal generated by the beam (subtracting the measurement acquired with the beam OFF from that with the beam ON) is shown in pink. (b) The data acquired by strip 1 and strip 2 are rapresented in red and black. The actual distance between the strips (4.7 mm) can be determined from the horizontal offset of the curves acquired from the two strips.

By connecting two strips to the readout, it was also possible to reconstruct the distance between the two strips. Observing the right graph of Figure 5.2.9, the position corresponding to the cross's shadow on the strips was identified, and a distance of 4.8 mm was evaluated (the actual distance between the two strips is 4.7 mm). To avoid the influence of light noise in the data, it is sufficient to place a black cardboard over the crosshair foil.

5.3 First experimental validation of silicon-based sensors for monitoring UHDR electron beams

The preliminary tests on conventional electron beams from the Elekta SL 18 LINAC at the Physics Department of Turin were described in Section 5.2. The tests confirmed a linear trend of the charge measured on silicon strips with dose-rate, good reproducibility of the data, and the ability to reconstruct the beam shape both transversely and longitudinally. The tests were conducted using a silicon sensor segmented into 11 strips with an active thickness of 45 μm and an active area of 2.2 mm^2, and using TERA08 as the readout electronics, splitting the signal from one strip into the 64 channels of TERA08.
This section describes the initial characterization of the setup on ultra-high dose-rate (UHDR) electron beams. The results of the tests of thin silicon pad sensors on UHDR electron beams delivered by the SIT ElectronFLASH (EF) machine at the "Centro Pisano Multidisciplinare sulla Ricerca e Implementazione Clinica della Flash Radiotherapy" (CPFR) in Pisa (Italy) are presented.

Most of the results presented in this section have been reported in the following publication [7]:

Medina, Elisabetta, et al. "First experimental validation of silicon-based sensors for monitoring ultra-high dose-rate electron beams." *Frontiers in Physics 12* (2024): 1258832.

5.3.1 Experimental setup

The samples chosen for the experiment are PIN silicon sensors, manufactured within the FBK EXFLU1 production batch, described in detail in 5.1. Two silicon square devices (4.5 mm side length) were selected from two wafers featuring different active thickness (30 μm and 45 μm) and a total thickness of 655 and 570 μm, respectively. Areas of 2 mm^2, 1 mm^2, and 0.25 mm^2 were chosen for the measurements. Through preliminary I-V characterization, it was verified that they fully deplete at 10 V and the breakdown voltage occurs over 300 V of reverse bias. The sensors were mounted with conductive glue on high-voltage distribution boards, allowing simultaneous reading of the three chosen pads connected to the output channels through wire-bonding. The guard ring of each pad was grounded.

The silicon device was aligned along the beamline, at the exit of the EF applicator, at the center of the beam spot and it was mounted on a fixed motor system positioned on a table in the EF room (Figure 5.3.1). Measurements performed with the FlashDiamond (FD) [44] set in the same position of the silicon sensors were considered as reference. The configuration allowed moving the silicon sensors and the FD, used to provide the reference dose measurements, in and out of the beam in the same experimental conditions, as shown in Figure 5.3.1 (b). All the measurements were performed at the maximum of the depth-dose distribution in water for the 9 MeV electron beam, obtained by placing a 12 mm thick solid water slab sandwiched between the applicator and the detector holder. Both silicon sensors and FD were enclosed in 3D-printed PLA boxes with an opening window

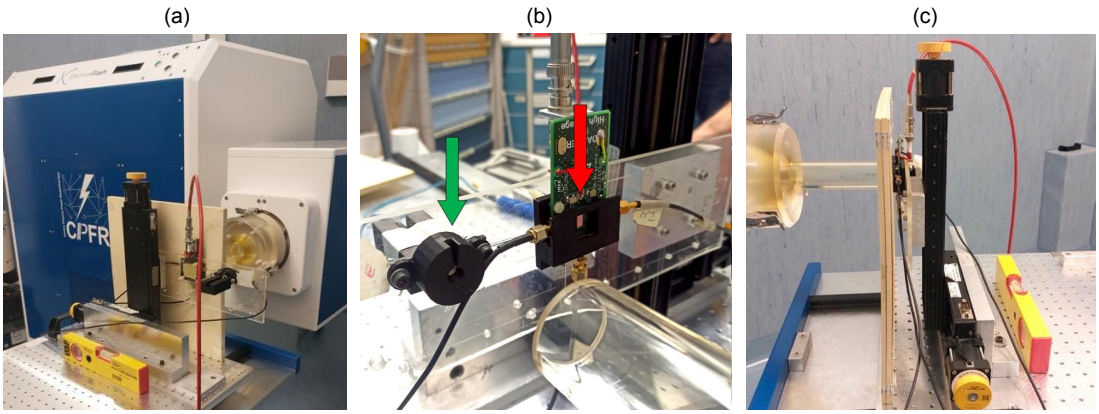

Figure 5.3.1: (a) The experimental setup positioned on the table is shown. (b) The silicon sensor (right arrow) and the FlashDiamond (left arrow) mounted on the same supporting structure. The two 3D printed boxes (in black) in which the sensors are positioned are visible. (c) The EF applicator, in contact with the solid water slab, adjacent to the sensor support box is shown.

in front of the active sensor surface to ensure the same air-gap distance (7 mm) between the sensors and the 12 mm thick solid water slab. For twelve values of the beam current at the exit window in the available range (1-100 mA), several EF parameters, such as magnetron power and bias of the cathode, have been optimized in order to have a constant energy spectrum. These twelve "working points" have been named according to the dose values measured in water at the build-up depth, using the 10 cm diameter applicator during the commissioning procedure. The "working points" labels (WPlabels) need to be converted into the actual dose related to the specific irradiation point and applicator considered. Table 5.1 reports the correspondence between the nine (out of the twelve possible) WPlabels considered in the test and the corresponding values measured by the FD for the 30 mm diameter applicator, also illustrated in the Figure 5.3.2.

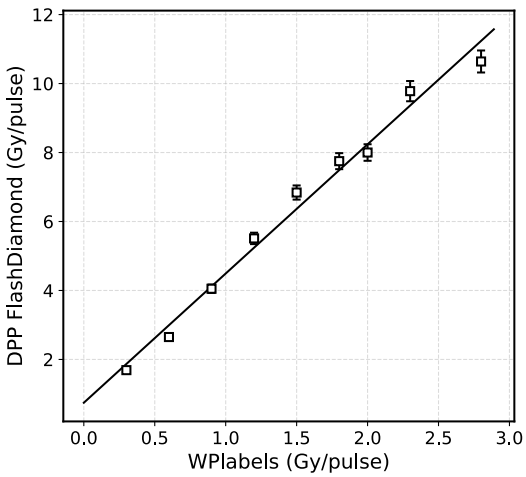

Figure 5.3.2: Reference dose-per-pulse (DPP) values measured by the FlashDiamond at nine increasing beam current values, identified by the corresponding nine "working points" labels (WPlables) on x axis.

Reference dose-per-pulse values

WPlabels (Gy/pulse)	0.3	0.6	0.9	1.2	1.5	1.8	2.0	2.3	2.8
DPP_{ref} (Gy/pulse) ±ERR%	1.62 ±0.05	2.55 ±0.08	3.9 ±0.1	5.3 ±0.2	6.6 ±0.2	7.4 ±0.2	7.7 ±0.2	9.4 ±0.3	10.2 ±0.3

Table 5.1: Reference dose-per-pulse (DPP) values measured by the FlashDiamond at nine increasing beam current values, identified by the corresponding nine "working points" labels (WPlables), for the irradiation point and the EF applicator considered in the test experimental setup. One measurement was performed for each WPlabel. The values measured with the FlashDiamond are reported with the corresponding error (±3%).

The reference setup for measurements with the FD relies in positioning it in a cylindrical PMMA phantom of 120 mm diameter (*ref setup*), while in the experimental setup considered in this test the FD was positioned in the already described 3D-printed PLA box (*test setup*). Therefore, in order to obtain the values of effective dose-in-water, the discrepancy in the response of the FD in the ref or test setup was studied by means of Geant4 Monte Carlo simulations. More specifically, the Monte Carlo simulations included the support structure of the sensor, the 3D-printed PLA box and the 12 mm thick build-up slab for the test setup, the PMMA cylindrical water equivalent holder and the build-up slab for the ref setup. All the components were positioned at the applicator exit. In both cases, simulations were based on the "eFLASH radiotherapy" example code, available in Geant4 11.0, which includes the EF accelerator and different applicator geometries. The energy spectrum of the primary electrons was measured, showing a slight decrease in the beam's mean energy due to the low-energy tail presence. The lateral scattering contribution due to the presence of the FD holder was quantified. The Geant4 simulations were run with "G4EmStandardPhysics-option4", "G4RadioactiveDecayPhysics" and "G4DecayPhysics" physics list, while cut-offs for all particle productions were set to 0.01 mm. The electron dose was scored along a $1.9 \times 1.9 \times 10$ cm^3 water volume in a grid with $1.9 \times 1.9 \times 1$ mm^3 resolution, with and without a $10 \times 10 \times 10$ cm^3 water phantom all around to simulate the contribution of the cylindrical PMMA phantom. The simulations were performed with 10^8 particles. In these conditions, a 3.9 % increase in the deposited dose was found when considering the cylindrical PMMA phantom. The values reported in the following table were corrected for this effect. A maximum dose-per-pulse of (10.2 ± 0.3) Gy was reached.

For part of the test, a sensor pad of 2 mm^2 active area from the device of 45 μm thickness was connected to the TERA08 chip. Since the latter can read a maximum current of 4 μA per channel before saturation, the sensor signal was split into 64 channels. As reported in a previous publication [113], such an arrangement allows to extend the current range up of 256 μA preserving a linearity better than 1% in the whole range. A specific upper-board adapter was used to allow the splitting of the input into the TERA08 channels. Moreover, in order to cope with the large instantaneous input current during each pulse, an RC circuit was added between the sensor output and the TERA08 input such that the charge produced by each pulse is stored in the capacitor, which discharges into the TERA08 input with a time constant much larger than the pulse duration. A series resistance value of 156 kΩ and a capacitance value of 470 nF, connected

to the reference voltage of the TERA08 input, were used. On left panel of Figure 5.3.3 shows a typical signal consisting of 10 pulses at a frequency of 5 Hz after software acquisition. On right panel of Figure 5.3.3, the value of the time constant τ, determined by fitting an exponential curve to a single-pulse discharge data, is reported and is found to be in good agreement with the product RC. The experimental setup is schematically represented in the Figure 5.3.4.

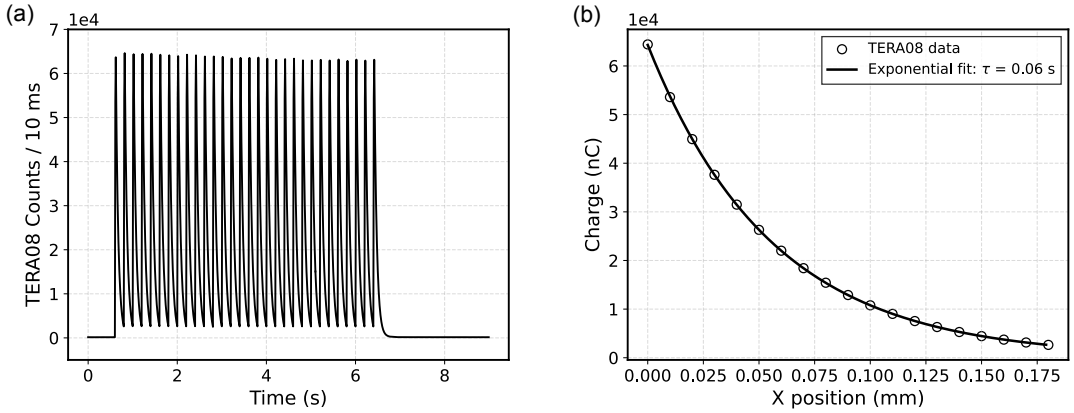

Figure 5.3.3: Example of acquisition with the TERA08 chip. (a) TERA08 counts as a function of acquisition time for an entire run, where 10 pulses with a frequency of 5 Hz are clearly distinguishable. (b) Zoom on a single signal of the discharge of the capacitor. The exponential fit results for the τ value is reported in the figure legend.

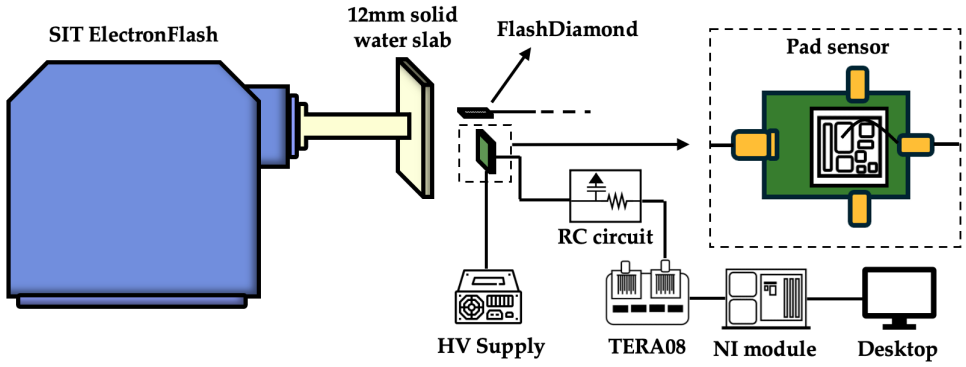

Figure 5.3.4: Schematic of the experimental setup used for first measurements. A 12 mm solid water slab is placed at the exit of the applicator. The silicon sensor was positioned under the same measurement conditions as the FlashDiamond. One pad of the sensor (2 mm^2 of area and 45 μm of active thickness) was bonded to the output channel, and the signal first passed through an RC circuit before being split into the 64 channels of TERA08.

A second part of the beam time was dedicated to the test of three sensor pads of active areas 2 mm^2, 1 mm^2 and 0.25 mm^2 from the 45 μm active thickness wafer connected directly to three input channels of an oscilloscope (Keysight Infiniium S-series DSOS254, 20 GS/s sampling rate), with input impedance of 50 Ω. Through the oscilloscope, it was possible to visualize and store the voltage signal generated from the pulses delivered by the EF and its temporal structure.

An example of an acquisition with the oscilloscope of one single pulse of 4 μs duration is shown in Figure 5.3.6, where three waveforms corresponding to each output channel are represented with three different colors. The shapes of the signals, characterized by an initial spike followed by an increase up to a broad maximum at the center of the pulse, were found to be perfectly compatible with those recorded by the machine's internal BCTs. The total charge of each pulse was obtained by dividing the integral of the acquired waveforms by the input impedance of the oscilloscope. The experimental setup for these measurements is schematically represented in the Figure 5.3.5.

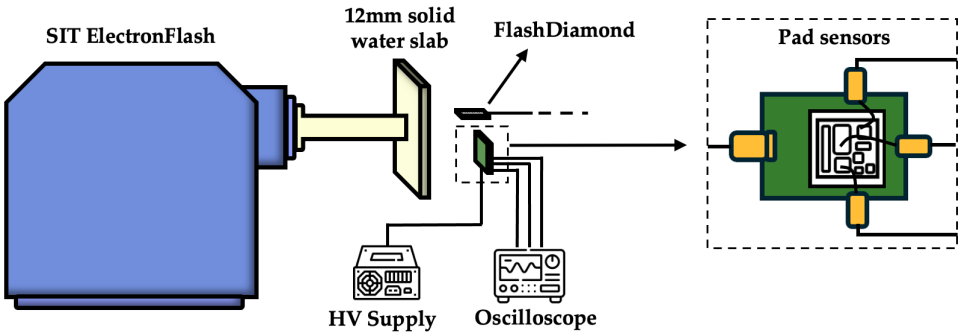

Figure 5.3.5: Schematic of the experimental setup used for the comparison of different areas. Three pads (0.25 mm^2, 1 mm^2 and 2 mm^2 of areas) of both sensors (30 μm e 45 μm of active thickness) were bonded to the readout, and then sent to three channels of the oscilloscope.

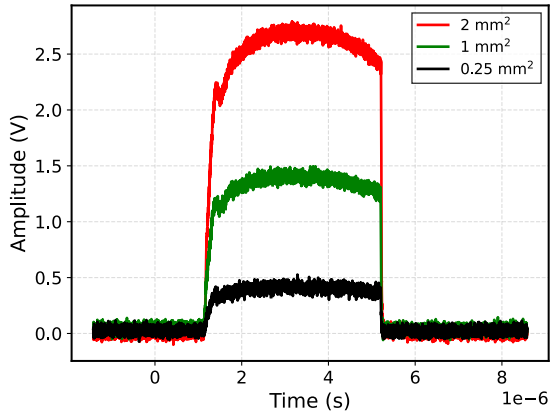

Figure 5.3.6: Waveforms acquired by the oscilloscope for a 4 μs pulse delivered by the EF at 3.89 Gy/pulse dose-per-pulse. The input impedance was 50 Ω. Three sensors of different active areas (2, 1, 0.25 mm^2) were connected to 3 channels of the oscilloscope. The data correspond to the 45 μm thick sensor.

5.3.2 Results

The charge per pulse measurements acquired with a silicon pad of 2 mm^2 area and 45 μm active thickness, using both TERA08 and the oscilloscope, are shown in Figure 5.3.7 as a function of the dose-per-pulse up to $\sim$ 10 Gy/pulse. The

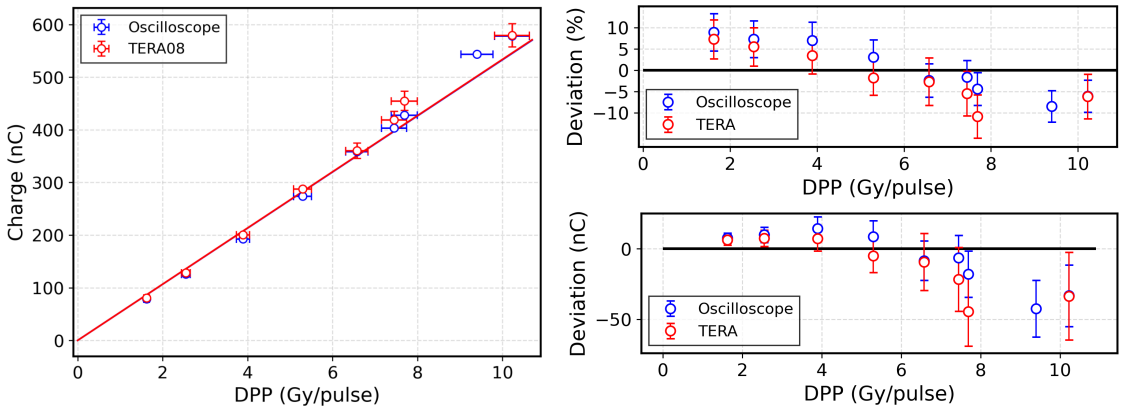

Figure 5.3.7: The charge produced in one pulse of 4 μs duration as a function of the dose-per-pulse is represented for both TERA08 and oscilloscope data. A coefficient of determination $R^2 > 0.98$ was obtained in both cases. Relative and absolute deviations from linearity plot are also reported. The data correspond to the pad of 2 mm^2 area and 45 μm active thickness, inversely polarized at 200 V.

sensor was reverse-biased at 200 V, well above his depletion voltage, to ensure operating the sensor under saturated drift velocity of charge carriers. Each point represents the average charge of the ten pulses used for the measurement. The charges measured with TERA08 and using the oscilloscope are found to be compatible within the uncertainties. Both data sets show a linear trend, resulting in a coefficient of determination of a linear fit $R^2 > 0.98$. The slope parameters of the two linear fits were compared using the statistical *test z*, resulting in compatibility at the 95% confidence level and demonstrating a strong correlation between the two readout systems.

Figure 5.3.8 shows the charge collected in the six different pads considered (2 mm^2, 1 mm^2 and 0.25 mm^2 active areas for both 45 and 30 μm thicknesses), where the bias voltage in the case of the thinner device was set to 133.34 V to achieve the same internal electric field (~ 4.44 V/μm) and thus saturation of the charge carriers drift velocity. For all the pads, the collected charge showed a very linear behavior as a function of the dose-per-pulse. At the same dose-per-pulse, the collected charge varies proportionally to the pad area and to the sensor thickness. Table 5.2 lists the calibration factors from charge to dose (in Gy/μC) for the six tested pads. Notably, the calibration factor for the 45 μm, 2 mm^2 sensor is consistent with the value obtained for the same sensor on the Elekta LINAC at the Department of Physics in Torino, as discussed in Chapter 4.2 in formula 4.4. The fit-derived value for the Torino accelerator is:

$$\text{CalibrationFactor}_{\text{Elekta}} = (19.08 \pm 0.99)\ \text{Gy}/\mu C \tag{5.3}$$

which aligns well with the value determined at the ElectronFLASH:

$$\text{CalibrationFactor}_{\text{ElectronFLASH}} = (18.76 \pm 0.40)\ \text{Gy}/\mu C \tag{5.4}$$

The two calibration factors, were compared using the statistical *test z*, indicating that the two values are fully compatible within a 95% confidence level ($z = 0.3$).

However, observing Figure 5.3.9, an effect related to the active volume of the different pads studied can be seen. The charge collected per unit volume, which

Table 5.2: Calibration Factors (Gy/μC) for all tested pad geometries

Thickness (μm)	Area (mm^2)	Calibration factor (Gy/μC)
45	2	18.76 ± 0.40
	1	37.48 ± 0.81
	0.25	130.68 ± 2.78
30	2	29.11 ± 0.35
	1	58.34 ± 0.69
	0.25	202.20 ± 2.64

theoretically should be identical as it depends only on the material characteristics, is greater for the smaller area studied (0.25 mm^2) compared to the other two areas (1 mm^2 and 2 mm^2). To gain further insights into this effect, the ratio of

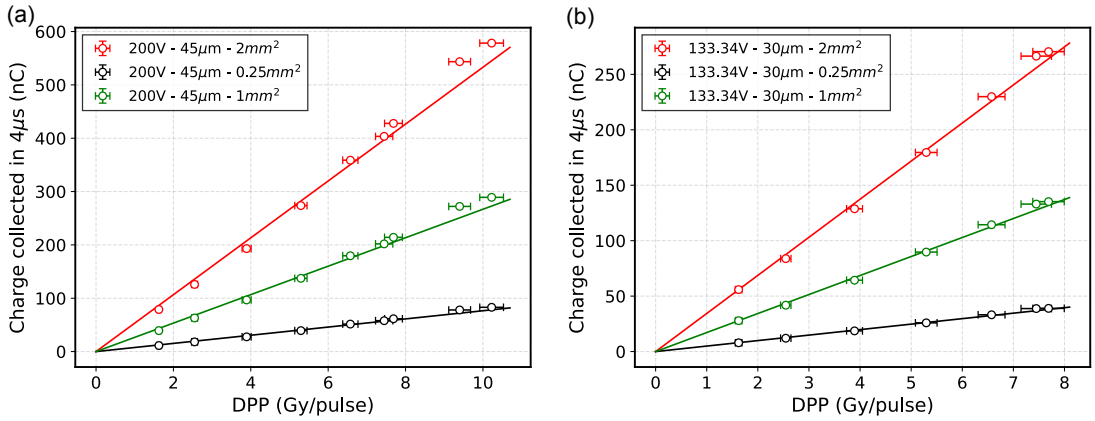

Figure 5.3.8: The results of the charge collected in each pulse with the TERA08 chip for the 3 sensor pads for the two thickness. (a) The 45 μm thick sensor was inversely polarized at 200 V. (b) The 30 μm was inversely polarized at 133.34 V, in order to have the same electric field condition within the active thickness.

the charge measured in different areas under identical dose-per-pulse conditions was studied. Figure 5.3.10 shows that the ratio of the charges measured in area A_1 and a second area A_2 (Q_{A1}/Q_{A2}) is constant under different dose-per-pulse conditions, but it differs from the ratio of the two areas (A_1/A_2), as represented by the dashed lines in the figure. To address this issue, it was hypothesized that the charge deposited in a pad depends not only on its active area but also on its perimeter:

$$Q = k \cdot A + g \cdot P \tag{5.5}$$

where Q is the charge deposited in a pad, A and P are the active area and perimeter of the pad, respectively. Using this model to describe the actual data, two values for the parameters k and g were identified, one for each tested thickness. Specifically, the following values were obtained:

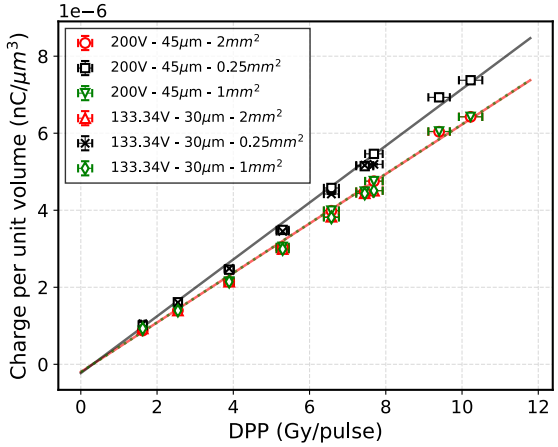

Figure 5.3.9: Charges per pulse per unit volume collected with TERA08 chip for the 3 sensor pads and the two available thicknesses (45 μm and 30 μm) are shown. For the smallest area (0.25 mm^2) the charge per unit volume results different (higher) than those acquired from the 2 mm^2 and 1 mm^2 pads.

$$30\ \mu\text{m}: \quad k_{30} = (8.01 \pm 4.69) \times 10^{-5}\ \text{Cm}^{-2}, \quad g_{30} = (0.28 \pm 1.39) \times 10^{-2}\ \text{Cm}^{-1} \tag{5.6}$$

$$45\ \mu\text{m}: \quad k_{45} = (15.29 \pm 8.48) \times 10^{-5}\ \text{Cm}^{-2}, \quad g_{45} = (0.53 \pm 2.51) \times 10^{-2}\ \text{Cm}^{-1} \tag{5.7}$$

Using these parameters, it was found that the values of the ratios

$$\frac{Q_{A1}}{Q_{A2}} = \frac{k \cdot A_1 + g \cdot P_1}{k \cdot A_2 + g \cdot P_2} \tag{5.8}$$

perfectly coincide with the ratio of the charges measured in the respective pads. This suggests that there is an effect related to the sensor's perimeter, where the electric field might not be well-defined, leading to an effective collection volume different from the geometrical collection volume.

The energy deposited in the active layer of silicon sensors of different geometries and the corresponding total charge produced was simulated with Allpix Squared framework (v 2.4.0) [119]. The electron source was defined with a radius of 2 mm and the energy spectrum was set as the one obtained at the applicator exit from the "eFLASH radiotherapy" Geant4 example. The deposited charges have been assumed to be equal to the propagated charges at the readout electronics. For both sensor thicknesses 10^7 events have been simulated. Assuming a linear increase of the charge with the number of initial particles, the collection of charge can be estimated for a larger number of initial particles. In the case of 30 μm thick sensors, the simulation results are compatible with all those obtained experimentally within 2.0 % for the 2 mm^2 area, 6.2 % for the 1 mm^2 one, and 4.1 % for the 0.25 mm^2 one. In the case of 45 μm thick sensors, the simulation results are compatible with the experimental ones within 8.1 % for the 2 mm^2 area, 13.5 % for the 1 mm^2 area, and 17.6 % for the 0.25 mm^2 area. Although the

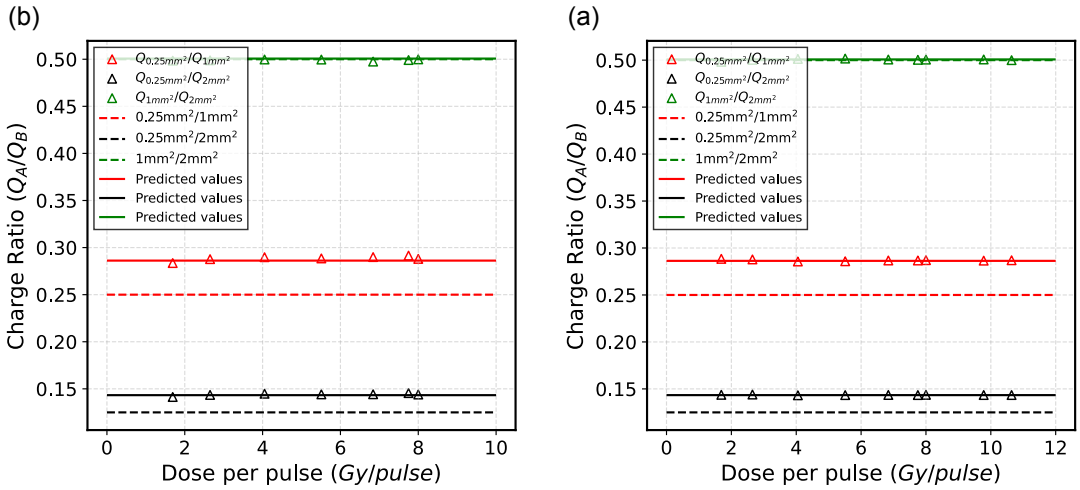

Figure 5.3.10: The ratios of the areas 0.25 mm^2 / 1 mm^2, 2 mm^2 / 0.25 mm^2, and 1 mm^2 / 2 mm^2 are studied for (a) the 45 μm thick sensor and (b) the 30 μm thick sensor. The markers represent the ratio of the measured charges per pulse, the dashed line represents the ratio of the areas, and the solid line represents the predicted charge ratios assuming a dependence on both area and perimeter.

grounded guard ring, a slight broadening of the depletion region into the silicon could explain the higher value of the charge collected in respect to the simulated one, and this has a larger impact in the 45 μm case. Further studies are ongoing to investigate and verify this effect.

As previously reported, data acquired at 200 V bias voltage show perfect linearity for the whole range of dose-per-pulse values investigated. However, by decreasing the bias voltage, a saturation effect of the charge collected was observed. This effect is illustrated in Figures 5.3.11 which show the charge collected in a 4 μs pulse in the 45 μm thickness sensor and 30 μm thickness sensor in panels (a, c, e) and (b, d, f) respectively, for all the three studied areas, as a function of the dose-per-pulse for different polarization voltages.

To further investigate the effect, Figure 5.3.12 (a) shows the waveforms of a pulse as a function of the dose-per-pulse for 200 V polarization, acquired with the oscilloscope. As expected, the signal amplitude increases as the dose-per-pulse increases, while keeping the pulse duration constant (4 μs). A peak is present at the beginning of the pulse, which is more evident at higher dose-per-pulse, and was also present in the BCT signal, thus not relying on the internal effects of the sensor. On the other hand, the waveforms for the measurements taken at 50 V are represented in Figure 5.3.12 (b). They show a distortion of the signal shape for dose-per-pulse values $>$ 3.89 Gy/pulse. The signal duration is shorter than 4 μs, and the integrated value reaches a constant value. The detector continues to be irradiated but the e/h pairs created are no longer collected.

To verify for this hypothesis, simulations were performed using Sentaurus TCAD from Synopsys [120, 121]. Sentaurus TCAD, developed by Synopsys, is a powerful software platform used for simulating and analyzing semiconductor devices and fabrication processes. It allows the modeling of the physical behavior of semiconductor materials, such as transistors and diodes, during both their

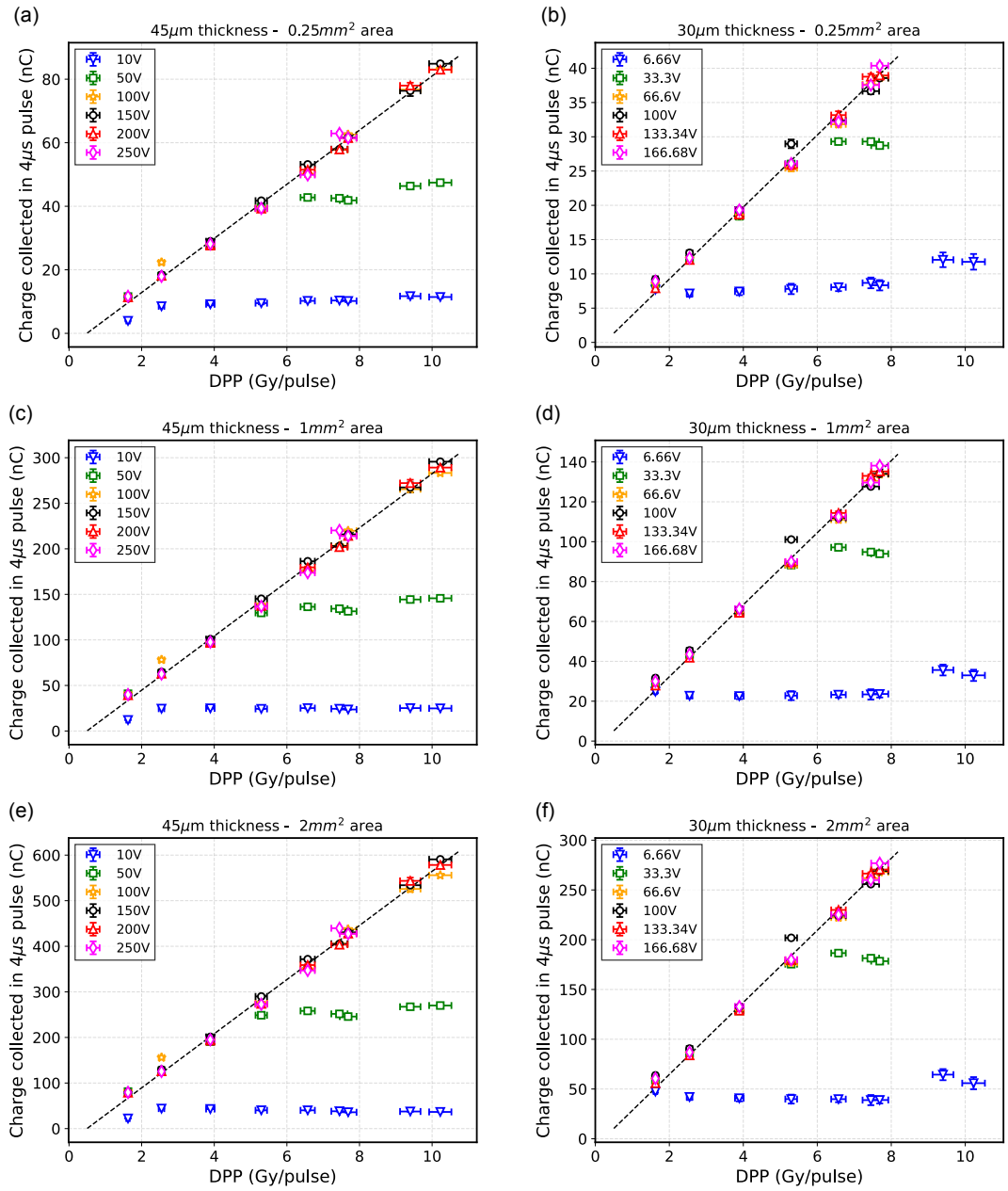

Figure 5.3.11: Charge produced in 4 μs pulses as a function of the dose in each pulse in the 0.25, 1 and 2 mm^2 area for the 45 μm active thickness pad and (a, c, e) and for the 45 μm active thickness pad (b, d, f) . The sensors were inversely polarized at 10, 50, 100, 150, 200 and 250 V. The data were acquired with the oscilloscope.

manufacturing and operational stages. The platform is primarily based on solving the Poisson equation along with the continuity equations for electrons and holes, typically using the drift-diffusion current model. Sentaurus TCAD also supports mixed-mode simulations, where external circuits can be incorporated via the integrated SPICE package to predict device behavior in real-world applications. This simulation approach provides valuable insights into both macroscopic and microscopic quantities, which are often difficult to obtain experimentally, making it an essential tool for optimizing device performance and understanding complex phenomena in semiconductor technology.

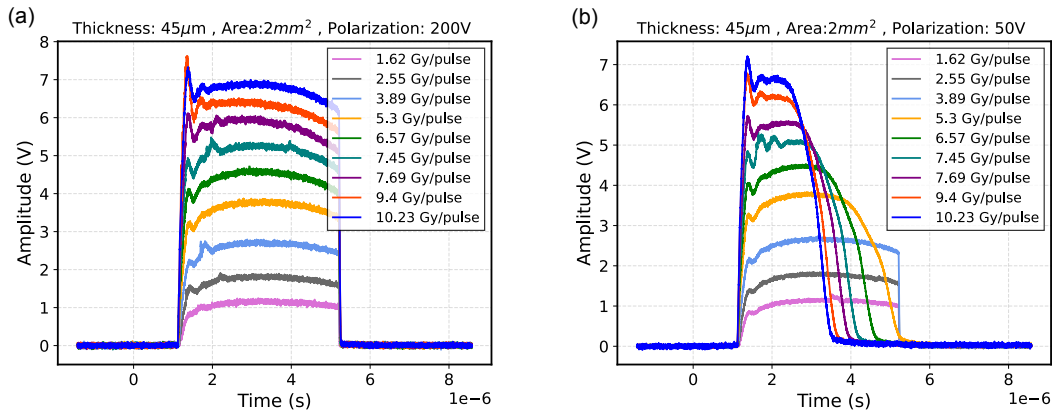

Figure 5.3.12: Signal waveforms acquired with the oscilloscope for pulses at nine different dose-per-pulse conditions. The input impedance was 50 Ω. The data correspond to the pad with 2 mm^2 area and 45 μm active thickness, inversely polarized at 200 V (a) and 50 V (b).

A 2D simplified geometry of the device was implemented in the software, as shown in Figure 5.3.13. The simulated active thickness is equal to that of the real device (X = 45 μm), while the active area (reduced to a length) is reduced to Y = 25 μm. A p^+ layer with a thickness of 0.3 μm doped with boron concentration of 10^{19}

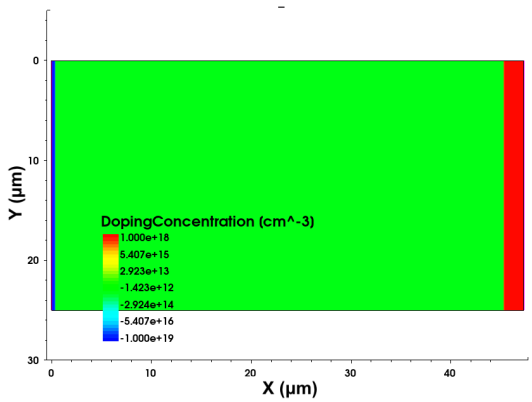

Figure 5.3.13: Schematization of the silicon sensor in TCAD software simulations. The p^+ layer has a thickness of 0.3 μm and doping concentration of 10^{19} cm^{-3}, the active region p^- is 45 μm thick and 25 μm large with a concentration of 10^{13} cm^{-3}, and the n^+ substrate layer is 2 μm thickn doped with a concentration of 10^{18} cm^{-3}

cm^{-3} was defined, along with an p^- layer of thickness 45 μm and doped with a boron concentration of 10^{13} cm^{-3}, and an n^+ substrate layer with a thickness of only 2 μm (to reduce simulation computational time), doped with a phosphorus concentration of 10^{18} cm^{-3}. Both the anode and cathode were defined as ohmic contacts.The charge release within the device was simulated using the *Radiation* carrier generation model, defined in TCAD as electric field–dependent process as follows [122]:

$$G_r = g_0 D \cdot Y(F) \tag{5.9}$$

where D is the dose-rate, g_0 is the generation rate of electron–hole pairs (default value: $7.6 \cdot 10^{12}$ $rad^{-1}cm^{-3}$) , and Y(F) is the electric field-dependent term. The model allows for the definition of the parameters DoseRate (in rad / s), that

represents D in 5.9, the optional DoseTime (in s) which allows you to specify the time period during which exposure occurs, and DoseTSigma (in s) that specify the standard deviation of a Gaussian rise and fall of the radiation exposure. Ideally, these parameters require calibration on real experimental data; however, an initial study was conducted to observe the variation of the electric field as the injected dose increased, maintaining a constant irradiation time. The simulation was carried out under different reverse bias conditions, including values of 200 V and 50 V. In this case, the irradiation time was set to 4 μs as for the experimental data, with a very short rise/fall time (10^{-13} s) and the dose-rate parameter was varied in a wide range of values between 10^{10} rad/s and $3 \cdot 10^{11}$ rad/s, identified as the critical range in which the electric field begins to show important distortions. The electric field within the device is shown as a function of the device thickness for 200 V of bias in Figure 5.3.14 (a) and for 50 V in Figure 5.3.14 (b). Each curve represents a different dose-rate released during the simulation. Observing the two plots reveals that, while maintaining the device characteristics and the same charge injection, the electric field varies differently for the two bias conditions. At 200 V, significant distortion of the electric field is observed only in the case of the maximum simulated dose, which reaches levels close to zero in certain micrometers of the active thickness. In the case of the sensor biased at 50 V, distortion is evident even at the lower simulated dose values. This confirms our hypothesis and requires further investigation through additional simulations.

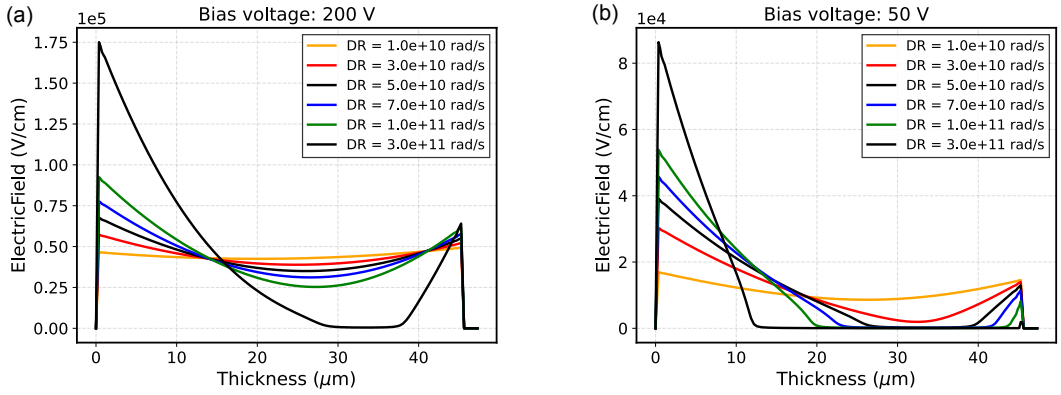

Figure 5.3.14: Electric field across the thickness of the simulated sensor, at half of the width (12.5 μm) at a time instant chosen during the irradiation. The simulations with a bias voltage of 200 V (a) and 50 V (b) are shown. The different colors correspond to different charges released simulated.

5.3.3 Conclusions

Silicon pads of 30/655 μm or 45/570 μm active/total thickness and areas 2 mm^2, 1 mm^2, 0.25 mm^2 were investigated as potential solutions for monitoring UHDR beams. Future tests will be performed with thinner active thicknesses (10 and 20 μm, also available within the same batch) and with thinned down sensors (100 or 120 μm total thickness) to verify beam transparency. The charge collected

by the sensors during irradiation was measured with an oscilloscope and the TERA08 chip. Several measurements were conducted at extremely high dose rates, reaching up to 2.5×10^6 Gy/s, corresponding to approximately 10 Gy delivered in pulses lasting 4 μs. The data exhibit a satisfactory linear trend, with a coefficient of determination $R^2 > 0.98$ for both readout systems. This work aimed at studying the response linearity of silicon sensors as a first step towards their possible application in UHDR electron beams. However, it also allowed verifying that no sign of signal degradation, e.g. depletion voltage or leakage current increase [123], appeared after a total cumulative dose of more than 9 kGy. The cumulative dose a beam monitor needs to withstand to comply with the UHDR requirements is still difficult to be estimated, but the radiation hardness is obviously a critical characteristic for solid-state sensors in this realm. Although the larger bandgap and e-h pair production energy of SiC and diamond compared to silicon make them more suitable for applications in UHDR beams [7, 5], it is interesting to evaluate the limits in terms of radiation hardness of silicon sensors, which could benefit of a greater technological maturity in respect to SiC and diamonds. Simulation tools (Geant4 Monte Carlo and Allpix Squared) were implemented, and the simulation results were in good agreement with the experimental data, opening the possibility to simulate the performance of different silicon geometries and experimental setups configurations. Preliminary simulations using the Sentaurus TCAD software were performed to investigate the signal distortion observed at lower bias voltages. The results indicate a significant distortion of the electric field at high doses when the sensor is operated under low bias conditions. Further studies and simulations are ongoing.

The results obtained by splitting the sensor output in all 64 chip channels of the TERA08 chip open the way to the chip adaptation towards the readout of multiple silicon pads/strips, aiming at enlarging the sensitive area of the beam monitoring device. Taking into account the maximum current that a single channel of the TERA08 can sustain (4 μA), the total number of chip channels (64), and the charge measured by the chip under high dose-rate conditions (about 600 nC at the maximum 10.2 Gy/pulse dose-rate value), more than one chip can be considered to measure the charge collected in an hypothetical multiple strip/pad silicon sensor. Keeping constant the signal readout circuit ($R \simeq 156$ kΩ and $C \simeq 470$ nF) and the silicon pad characteristics (2 mm^2, 45 μm thickness) used in the described test and by computing the maximum of the function describing the number of counts read by TERA08 chip ($N(t) \cong Ntot\ (1 - \exp(t/\tau))$), splitting the sensor output in only 3 TERA08 channels (instead of the all 64 channels, as done in the test) would be sufficient to avoid reaching electronic saturation. This would then allow to simultaneously readout ~ 20 sensors with the same chip. These estimations would improve with the use of sensors thinner than those presented in this work and with the use of an upgraded version of TERA08 with a higher current range (TERA09, 12 μA of maximum instantaneous current per channel using a charge quantum of 200 fC). In conclusion, this preliminary work demonstrates the response linearity of thin silicon sensors' prototypes in UHDR electron beam irradiation.

5.4 Segmented silicon sensor on electron and proton beams

Through the results described in the previous section, the FRIDA INFN project characterized thin silicon sensors for monitoring electron FLASH beams, showing a response linearity up to $\sim$ 10 Gy/pulse on 9 MeV electrons. The use of segmented silicon configurations, introduced to overcome the drawbacks of point-like dose measurements in FLASH irradiations, provide the spatial resolution useful for applications in Spatially Fractionated Radiotherapy (SFRT). Within the FRIDA and MIRO INFN project, a strip sensor integrated with a multichannel readout chip is being developed and tested for monitoring FLASH and SFRT electron and proton beams. The 128 strips of the large strip sensor from MoVe-IT FBK production are independently read by two front-end TERA chips (as described in Section 5.1). Preliminary tests were performed on 6 - 10 MeV electron beams at the LINAC at Physics Department of the University of Turin and on 62 - 226 MeV proton beams at CNAO (Pavia). The capability to spatially resolve electron and proton beams at conventional dose-rates has been proved.

Part of the results presented in this section have been reported in the following proceeding [3]:

Medina, Elisabetta, et al. "Monitoring electron and proton beam profiles with segmented silicon sensors" ***Nuclear Instruments and Methods in Physics Research Section A: Accelerators, Spectrometers, Detectors and Associated Equipment*** **(2024): 169897.**

5.4.1 Spatially Fractionated Radiotherapy

In 1909, Dr. Alban Köhler discovered that introducing an X-ray shielding grid system (the only radiation source available at the time) could enhance the treatment of skin tumors by significantly reducing damage to healthy tissues. This discovery marked the beginning of spatially fractionated radiotherapy (SFRT) development [124]. Initially, SFRT was considered suitable only for treating certain superficial tumors. However, since the 1990s, several research groups have explored the potential of spatial fractionation in radiotherapy, supported by radiobiological studies involving X-rays [125, 126, 127, 128] and proton beams [125, 126, 129, 130]. With advancements in radiotherapy accelerators, SFRT shows promising clinical prospects.

Currently, most SFRT techniques protect normal tissue using conventional dose-rates [131, 132], although some experiments have combined ultra-high dose-rates (UHDR) with SFRT via microbeam radiotherapy (MRT) and minibeam radiotherapy (MBRT) [133, 134]. However, further investigation is needed into the potential additive or synergistic effects of these combined techniques. SFRT employs a spatially periodic beam structure, generating a recurring pattern of "peaks and valleys" [126], but the optimal peak-to-valley dose ratio (PVDR) and the ideal spatial configuration of the individual beams are still under study.

SFRT can be implemented in two main modes: a spatially uniform beam divided into sub-beams by a periodic grid with alternating slits and solid sections,

known as the GRID technique [135, 136, 137, 138]; or through the use of multiple "pencil beams" to create a desired dose distribution pattern (the latter method requires charged particles). Proton accelerators have proven particularly suitable for implementing this approach, although most radiobiological studies rely on passive collimation [139, 140, 141, 142, 143, 144]. Despite the substantial potential of GRID therapy, SFRT has not yet seen widespread adoption, due to both the technological limitations of available devices and the high heterogeneity in tumor coverage. Additionally, as discussed in [125], the optimal application of SFRT with low-energy electron beams is most effective in a FLASH delivery context, and investigating the combined effects of FLASH and mini-beam techniques remains a key area of research. A dedicated beam system is thus essential to advance radiobiological research and facilitate precise dosimetric studies.

The Pisa group conducted a study through simulations and experimental tests using the ElectronFLASH machine at the CPFR center [145]. They designed tungsten collimators with a 5 mm diameter, chosen based on the 9 MeV electron practical range. Tungsten, a high-Z material, was essential to prevent electron bleed-through across the septa and to ensure a high peak-to-valley dose ratio. Various hole structures (grid or planar slits) and center-to-center distances were tested to assess the effects of these parameters. The same template used in the Pisa was tested in Turin on the electron beam of the Elekta LINAC, with the future aim of establishing a facility in Turin capable of delivering conventional mode, FLASH mode (4.2), conventional mini-beam mode, and FLASH mini-beam mode. Our initial measurements in Turin, using silicon sensors, were conducted in conventional mini-beam mode. This approach was necessary because the segmented 146-strip sensor requires an upgrade to the readout electronics for proper data acquisition in FLASH modality.

5.4.2 Characterization of conventional electron and proton beams

The selected sensor features an active thickness of 60 μm and a 2.6 $\times$ 2.6 cm^2 sensitive area, as described in Section 5.1. It is segmented into 146 strips with a pitch of 180 μm and an inter-strip spacing of 66 μm. Each strip has an active area of 180 $\times$ 26214 μm^2. The TERA09 chip, was used for the charge integration measurements [115]. A custom-designed PCB was developed to enable the reading of signals from 128 individual inputs and accommodate the segmented sensor. Out of the 146 strips, 128 are connected to two TERA chips, allowing coverage of a reduced area compared to the full sensor size (2.6 $\times$ 2.3 cm^2). Throughout all measurements, the sensor was reverse-biased at 100 V, well above its depletion voltage. Data acquisition from the individual channels was performed using an NI FlexRIO FPGA DAQ module, with a LabView software for data acquisition and storage. The schematization of the setup is illustrated in Figure 5.4.1.

Conventional electron beams at the Turin Elekta LINAC

An initial verification of the experimental setup was conducted on electron

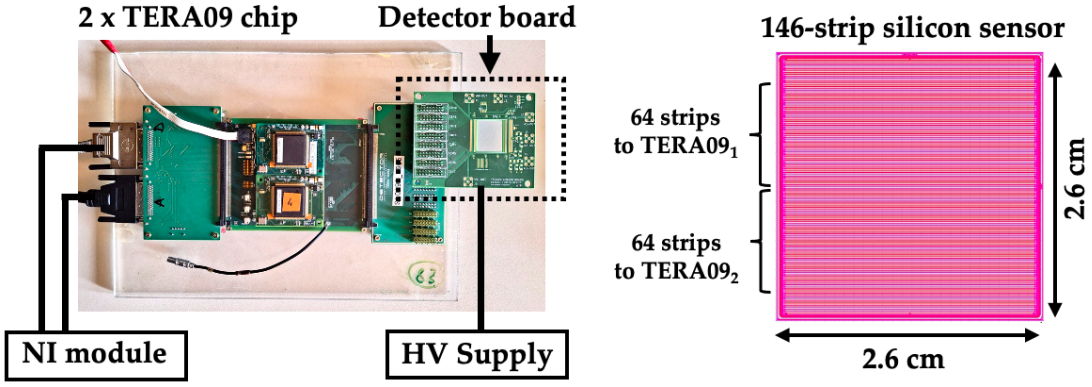

Figure 5.4.1: Schematic of the experimental setup used for measurements of 146-strip segmented sensor with TERA09 chip.

beams in conventional regimes at the Turin Elekta LINAC, using a standard mode (without any spatial fractionation of the beam) to study the beam shape as detected by the silicon sensor. In this case, a beam with dimensions of 3×3 cm^2 and energy of 6 MeV was used. The test confirmed the feasibility of studying the beam profile delivered in a single shot using a sensor with an area comparable to the size of the beam. An example of this result is represented in Figure 5.4.5. The sensor was positioned at 70 cm source-to-surface distance (SSD), and a 6 MeV electron beam (conventional regime) was chosen at a dose-rate of 200 MU/min. Measurements were taken with the sensor centered, as well as with the sensor displaced to capture the edges of the beam, and these two acquisitions were subsequently overlaid appropriately. The position values rapresented on the x-axis is obtained by multiplying the strip number by the sensor pitch (180 μm).

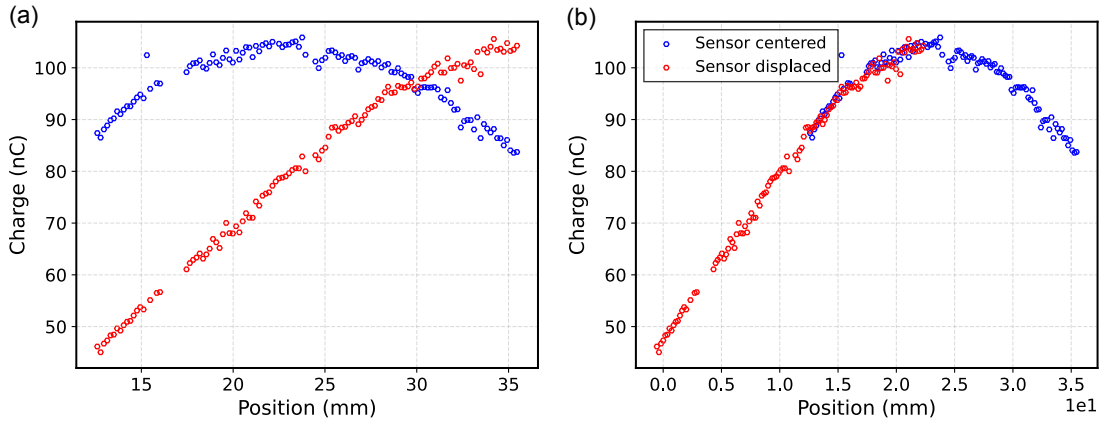

Figure 5.4.2: Charge measured on 128 strips of the segmented sensor as a function of the position (x-axis). (a) In blue are represented the measurements acquired by manually centring the sensor on the beam, in red the measurements after displacing the sensor. (b) The curves have been shifted to reconstruct the shape of the beam by combining the two measurements. (dose-rate: 200 MU/min; Position: 70 cm SSD).

A comparative study was conducted between dose measurements obtained using GafChromic EBT XD films placed in the crosshair foil position of the LINAC

and charge measurements acquired by 128-strip (out of the 146 available) of the segmented sensor under identical conditions. These measurements were performed at the isocenter. A strong agreement was observed between the beam profile derived from the normalized dose of the GafChromic EBT XD films and the counts acquired by the TERA09, as illustrated in Figure 5.4.3.

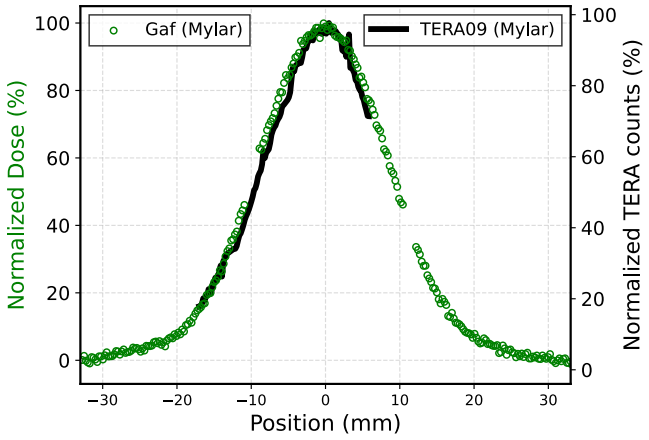

Figure 5.4.3: Normalized dose acquired with GafChromic films (left y-axis) compared with the charge measured on 128 strips of the segmented sensor (right y-axis) with 6MeV Flattering Filter Free electron beam, SSD = 52.9 cm. The position values (x-axis) is obtained by multiplying the strip number by the sensor pitch (180 μm).

Conventional proton beams at the CNAO

The same experimental setup was also tested at CNAO, the National Centre for Hadrontherapy in Pavia. The CNAO synchrotron has a 25m-diameter ring, in which the ion sources, injection lines and the linear accelerator are located. The extracted beam are sent to three treatment rooms through four extraction lines (each about 50 m long). The protons are accelerated through a radiofrequency cavity until they reach a set of predefined energies in the range of 60-250 MeV, corresponding to a water depth of 3 to 32 g cm^{-2}. During the beam-on time, the ions are bunched and extracted in periodic time intervals, the so-called spills, that last between a tenth of a millisecond and a few seconds, depending on the energy and number of particles required, which for protons can vary between 10^{10} protons per spill up to about 10% of this value [26]. The maximum field size is 20 $\times$ 20 cm^2 and the beam shape corresponds approximately to a Gaussian shape, whose Full Width Half Maximum (FWHM) for the proton beam in air varies between 0.7 and 2 cm, from the highest to the lowest energy, in the isocenter position [109]. Our measurements were performed with proton beam energies ranging from 62.28 to 226.91 MeV and a flux of 5 $\times$ 10^8 protons per spill. A picture of the treatment room is shown in Figure 5.4.4.

Charge measurements performed per spill at the CNAO center are reported in Figure 5.4.5 (a), where 7 different proton beam energies in the range 62.28-226.91 MeV are shown. Figure 5.4.6 represents an example of TERA09 acquisition

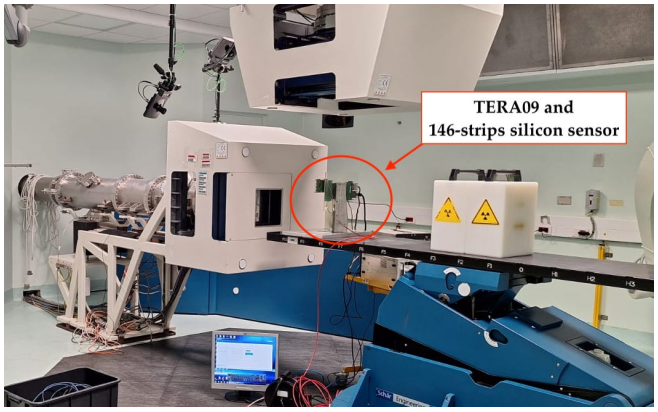

Figure 5.4.4: Picture of the experimental setup in CNAO's treatment room. The structure on which TERA09 is mounted and the board with the 146-strip sensor is circled in red. The sensor was positioned at the isocentre.

during 20 spill of irradiation of 110.96 MeV proton beam. The 20 spill delivered are clearly visible on the data, each of about 1 s duration. The results clearly demonstrate the energy dependence of the beam profile. Table 5.3 presents the parameters of the Gaussian fits for each curve at different energies. The FWHM values are consistent with those reported in the literature for the CNAO beam spots at the respective energies. Furthermore, when plotting the Total Collected Charge, measured as the integral of the Gaussian fit across the entire beam width as shown in Figure 5.4.5 (b), an inverse relationship with energy (1/E) is observed. The data were fitted with the function: $y = a + \frac{b}{x+c}$ and the free parameters were found equal to: $a = (-52 \pm 55)$ nC ; $b = (7.2 \times 10^4 \pm 2.5 \times 10^4)$ nC $\cdot$ MeV; $c = (100 \pm 39)$ MeV.

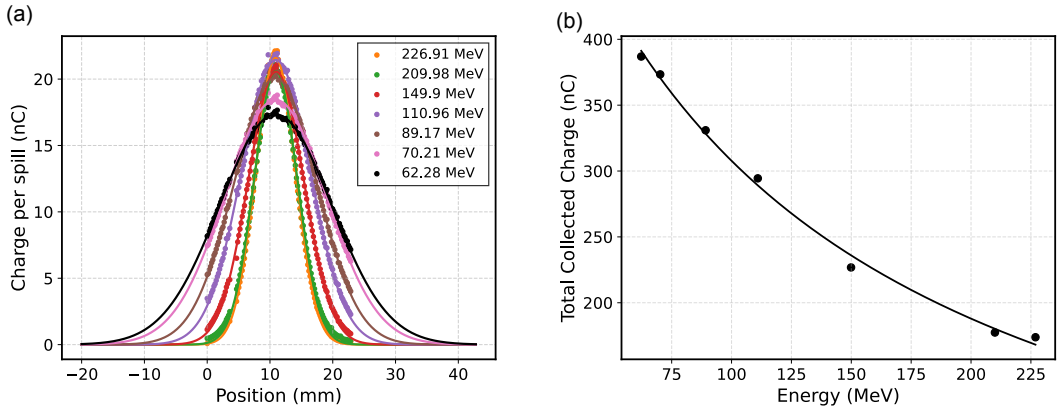

Figure 5.4.5: (a) Measured charge on each strip of the segmented sensor with proton beams in the energy range from 62.28 MeV to 226.91 MeV. The dots represent the measurements with the TERA chip while the continuous line represents the Gaussian fit. (b) Total Collected Charge across the entire beam width as a function of the beam energy. An inverse relationship with energy is observed (Flux: 5×10^8 protons/spill, Position: isocenter).

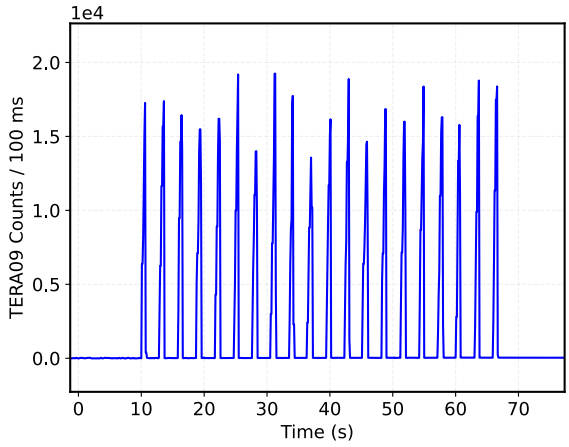

Figure 5.4.6: TERA09 counts acquired each 100 ms during irradiation of 110.96 MeV proton beam. The value of one central strip is considered in this case. The 20 spill delivered are clearly visible, each of about 1 s pulse spill duration.

Energy (MeV)	μ (mm)	σ (mm)	FWHM (mm)	Total Collected Charge (nC)
226.91	10.89 ± 0.01	3.21 ± 0.01	7.56 ± 0.02	173.82 ± 0.74
209.98	10.91 ± 0.01	3.44 ± 0.01	8.09 ± 0.03	177.39 ± 0.80
149.90	10.96 ± 0.01	4.40 ± 0.01	10.36 ± 0.03	226.80 ± 0.75
110.96	10.93 ± 0.01	5.48 ± 0.01	12.90 ± 0.03	294.45 ± 0.78
89.17	10.86 ± 0.01	6.57 ± 0.01	15.48 ± 0.03	330.94 ± 0.69
70.21	10.88 ± 0.01	8.08 ± 0.01	19.03 ± 0.03	373.38 ± 0.84
62.28	10.90 ± 0.01	8.90 ± 0.02	20.96 ± 0.04	386.92 ± 0.97

Table 5.3: For each proton beam energy, the parameters of the Gaussian fit, μ and σ, are reported along with the FWHM and the Total Collected Charge obtained as the integral of the Gaussian fit over the entire width of the beam spot.

Conventional spatial fractionated electron beam

The spatial fractionation of the beam was studied again at the Turin LINAC Elekta at the isocenter in air, using the PMMA applicator equipped with a tungsten grid of 7×7 holes spaced 3 mm apart (center-to-center), each hole covering an area of 1 mm^2, as shown in Figure 5.4.7.

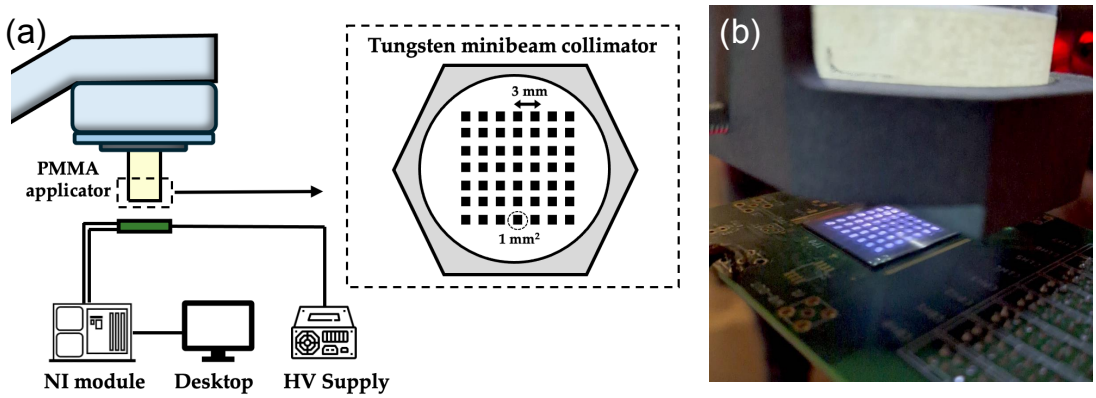

Figure 5.4.7: (a) Schematic diagram of the experimental setup used for segmented sensor measurements on minibeams. The tungsten collimator is mounted at the exit of the PMMA applicator. (b) Photo representing the segmented sensor centred on minibeams.

For this study a 10 MeV conventional electron beam was used with a field size of 10×10 cm^2 at the isocenter, for about 3 minutes of irradiation. Figure 5.4.8 shows seven charge peaks (summed over the total irradiation time) corresponding to the seven rows of holes in the collimator. The parameters of the Gaussian fit are reported in Table 5.4. The center-to-center distance was determined to be (3.02 ± 0.02) mm, while the full width at half maximum (FWHM) of the peaks was measured at (1.17 ± 0.06) mm. Both values are consistent with the actual specifications of the tungsten grid. However, from these measurements it is not useful to consider the peak-to-valley ratios because were taken with a segmented strip sensor, meaning the results represent the projection of the beam along one of the two transverse directions and include all seven mini-beams aligned along that strip.

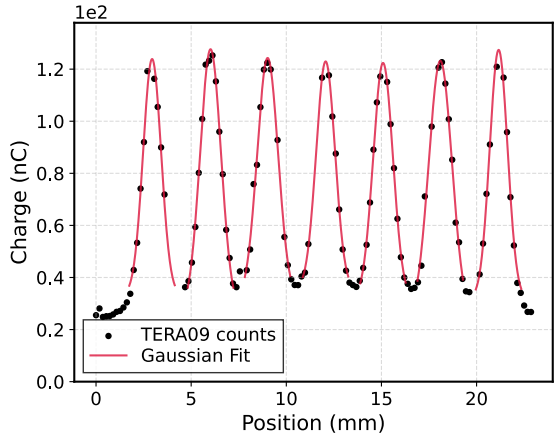

Figure 5.4.8: Measured charge on each strip of the segmented sensor with 10 MeV electron beam and field size 10×10 cm^2 at the isocenter. The peaks correspond to the minibeams generated through the Tungsten collimator mounted on the PMMA applicator at the isocenter.

Beam (MB)	μ (mm)	σ (mm)	FWHM (mm)
MB1	3.01	0.46	1.09
MB2	6.02	0.53	1.26
MB3	9.05	0.51	1.21
MB4	12.08	0.49	1.15
MB5	15.09	0.51	1.19
MB6	18.12	0.47	1.12
MB7	21.10	0.49	1.16

Table 5.4: Parameters of the Gaussian fit of peaks data corresponding to the minibeams signals on the strip sensor. Parameters μ, σ and FWHM are reported.

5.4.3 TERA charge measurements in FLASH conditions

A primary future goal for our research group is to enable monitoring with the 146-strips segmented sensor not only of electron and proton beams in conventional regimes but also, and especially, in FLASH regimes. During tests conducted with the ElectronFLASH machine at the CPFR center, we observed that the TERA08 readout electronics saturates at very high dose-rates (up to approximately 10 Gy/pulse) and an RC circuit was used to extend the output signal duration from a single silicon pad and consequently reduce the peak instantaneous current, allowing accurate measurements with the TERA08 (where the signal was split across its 64 channels), as explained in Chapter 5.3.

To use TERA09 in FLASH conditions, coupling each of the 128 strips of the segmented sensor with a single TERA09 channel, it will be necessary to redesign the chip structure, potentially integrating a current divider for each channel. This will be the focus of future work by our group.

For preliminary tests, measurements were performed using a single silicon pad with a 2 mm^2 area and 45 μm thickness, connected to the TERA08, under UHDR beam conditions of the Elekta LINAC. The setup was arranged such that the electronics would not saturate. Specifically, the sensor was positioned at a source-to-sensor distance (SSD) ensuring safe conditions for chip operation without using an RC filter. This SSD was determined by positioning two identical silicon pads (each with a 2 mm^2 area and 45 μm thickness), one located at the cross-hair foil and connected to an oscilloscope, and the other placed immediately beneath it (approximately 1.5 cm lower) and connected to one channel of the TERA08. Measurements were repeated six times while progressively increasing the SSD from the cross-hair foil under FLASH conditions (10 MeV, 6 Hz pulse repetition frequency). The results showed that for the tested SSDs (ranging from 8.8 cm to 44.5 cm from the cross-hair foil), both the charge recorded by the oscilloscope and the counts measured by the TERA08 increased as the SSD decreased, without reaching saturation.
Subsequently, the TERA08 was used for the first time to measure the FLASH beam profile from the LINAC. The sensor was positioned at an SSD within the previously tested range, ensuring that the electronics operated far from saturation levels.

Automated motor system, also used in Section 5.2, allowed a sensor to cross the beam transversely at a distance of 15.5 cm from the cross-hair foil, where we expected a charge of approximately 50 nC. Figure 5.4.9 shows the beam shape

measured with TERA08 in two different ways: in the first approach (a), the sensor was moved in 0.5 cm increments, with six pulses delivered at each step, and the average charge across these pulses was calculated; in the second approach (b) the sensor was moved in 1 mm steps during a single pulse delivery of 263 total pulses, subsequently converting the TERA08 acquisition time into sensor position. Both methods show a uniform charge value of approximately 47 nC at the center of the beam.

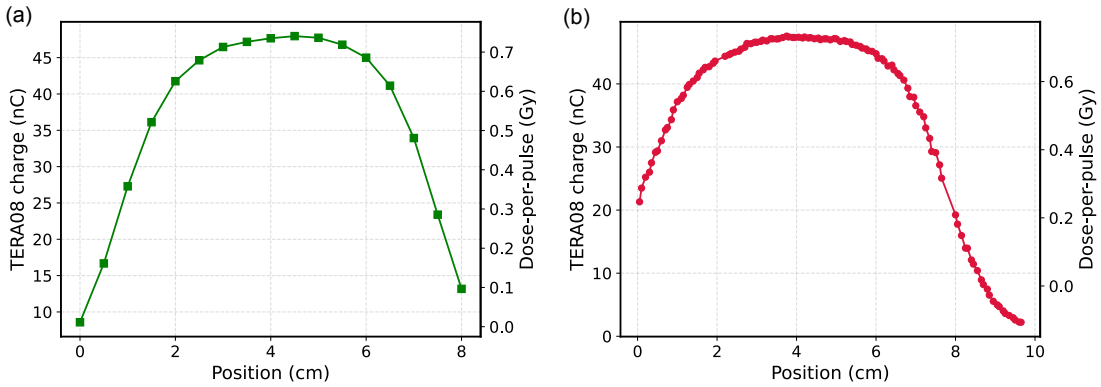

Figure 5.4.9: Charge and corresponding dose-per-pulse in the right y-axis measured by TERA08 as a function of the position of the silicon pad sensor across the beam. The measurement was performed in two ways: (a) by recording 6 LINAC pulsus in each position step; (b) by moving the sensor during a single irradiation of 653 pulses.

5.4.4 Summary

A strip silicon sensor with an active thickness of 60 μm, covering an area of 2.6×2.3 cm^2 with 128 strips was coupled with a 64-channels readout electronics system. Beam shape studies were conducted using 6-10 MeV electrons from an Elekta LINAC, with a conventional and a fractionated beam obtained with a Tungsten collimator mounted on a PMMA applicator, and with proton beams at the CNAO center in Pavia, with energies from 62.28 MeV to 226.91 MeV. The measurements demonstrated good compatibility with data acquired using GafChromic EBT XD films and proved the ability to spatially resolve electron and proton beams at conventional dose-rates. This makes the technology promising for beam monitoring applications in SFRT.

Future activities will focus on modifying the readout chip to ensure compatibility with FLASH operation modes. As part of this preparation, tests have been conducted using a silicon pad sensor (with an active area of 2 mm^2 and thickness of 45 μm) to study the beam profile in FLASH conditions with the TERA08 system, specifically in a non-saturated electronics regime. The signal from the pad was directed into a single TERA08 channel. Preliminary tests are also underway with a current divider, which channels only a portion of the incoming current into a single TERA chip channel. This approach anticipates the eventual integration of a current divider for each channel in a redesigned chip. A secondary key objective is to enable a 2D reconstruction of the beam spot, rather

than limiting measurements to projections along two axes. To achieve this, a system with rotating motors is currently under design to facilitate comprehensive shape reconstruction of the beam spot.

Chapter 6

Diamond: Characterization of CVD diamond detectors with FLASH electron beams

Diamond could be a viable alternative for monitoring FLASH beams. Its atomic number (Z = 6, close to the human tissue one, i.e. Z = 7.5) and its strong binding energy makes it an ideal dosimeter, chemically inert and radiation hard material. Due to the typical average energy for the generation of an electron-hole pair (3.62 eV for silicon and 13 eV for diamond), for equivalent geometries, diamond is expected to be less sensitive than silicon, which represents an advantage in ultrahigh dose-rate applications and reduces the total charge produced in the sensor channel. The first tests were carried out in Turin, and the sensor response was studied in terms of polarization voltage, integrated charge, charge collection efficiency and sensitivity. Most of the results presented in this section have been reported in the following proceeding [4]:

Medina, Elisabetta, et al. "*Characterization of CVD diamond detector with FLASH electron beam from modified LINAC accelerator.*" Nuclear Instruments and Methods in Physics Research Section A: Accelerators, Spectrometers, Detectors and Associated Equipment 1063 (2024): 169308.

6.1 Materials and methods

In collaboration with the diamond detector expert group of the INFN and Physics Department of the University of Turin [146], we have identified CVD polycrystalline diamond samples of various geometries suitable for initial tests related to our applications of interest.
Two methods are possible for creating contacts on the samples: via graphitization or metallic contacts. The first method involves ion implantation, which, depending on the ion species and beam energy, transforms the diamond into graphite at specific depths. However, this process requires high beam fluences and very long irradiation times.
The second method is relatively simpler. Surface metallization can be achieved through Physical Vapor Deposition (PVD), a process that involves depositing a

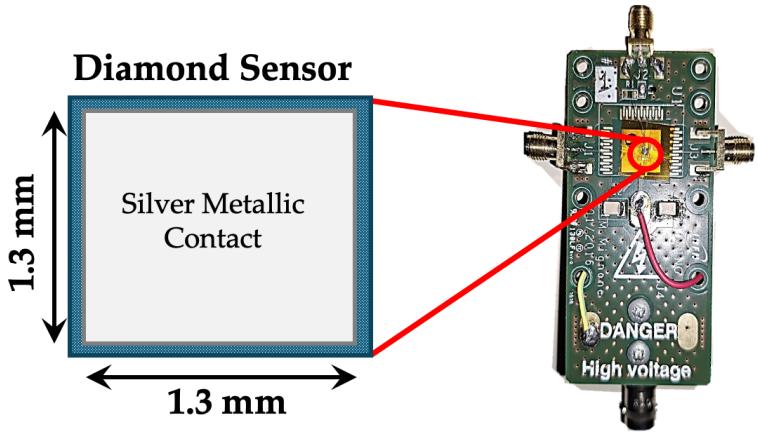

Figure 6.1.1: Schematic diagram of the polycrystalline CVD diamond used (active area of 1.3 x 1.3 mm^2, thickness of 100 μm) B) and picture of the diamond detector positioned on the high voltage (HV) distribution board.

thin film of material onto a surface by evaporating the material in a vacuum (@ 10^{-6} mbar, 300 - 400°C) and protecting the unexposed surface with an aluminum mask. The first detector we tested features contacts produced using this method in the Physics Department laboratories of the University of Turin. The detector is a CVD polycrystalline diamond, characterized by an active area of 1.3 $\times$ 1.3 mm^2 and a thickness of 100 μm for a total active volume of 0.17 mm^3. Dual side contacts were made on the top and bottom faces of the diamond sample by evaporating 125 nm thick silver layer. Subsequently, the detector was glued onto a high-voltage distribution board and connected by wire bonding to the readout channels (Figure 6.1.1). Radiation (in this case electrons), passing through the diamond thickness, interacts with the atoms in the lattice and pairs of electrons and holes are generated, which, due to the internal electric field, move towards the electrodes and generate a measurable current.

To measure this current a fast oscilloscope (Keysight Infiniium S-series DSOS254, 20 GS/s sampling rate) with input impedance of 50 Ω is used. Through the oscilloscope, it was possible to visualize and store the voltage signal generated inside the sensor. The linear accelerator (LINAC Elekta SL 25 MV) of the Physics Department of the University of Turin was used to test the diamond sensor. The LINAC was modified to deliver 10 MeV electron beams at high dose-rates, as described in Chapter 4. The diamond detector was placed adjacent to the mylar film (Figure 6.1.2) and an electron beam of energy 10 MeV and size 10 $\times$ 10 cm^2 was chosen in FLASH mode. The pulses have a duration of 2 μs and a frequency of 6 Hz. A study of the signal was made as a function of the electric field inside the sensor, which varied between 50 and 600 kV/cm.

6.2 Results

Figure 6.2.1 shows the signal generated in the diamond by an electron beam pulse at different polarization voltages and shows the charge per pulse as a function of bias voltage, obtained by dividing the integral of the acquired waveforms

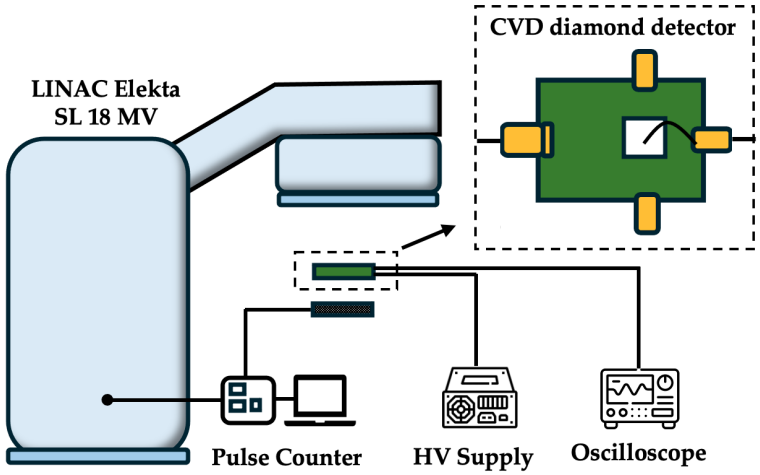

Figure 6.1.2: Experimental setup used for electron beam measurements. A high voltage (HV) module was used to polarize the sensor, a home-built circuit was used as a pulse counter and an oscilloscope was implemented to record the signals generated inside the diamond.

by the input impedance of the oscilloscope (50 Ω). Charge per pulse values increase linearly with the polarization voltage, up to 18 nC for 600 V, because of the material defects that trap the charge carriers. From the measured charge values, the charge collection efficiency (CCE) was determined, which is a quantity strongly correlated with the quality of the crystal:

$$CCE = \frac{Q_{collected}}{Q_{produced}} = \frac{Q_{collected}}{(DPP\rho Ade)/w} \tag{6.1}$$

where $Q_{collected}$ is the charge collected, $Q_{produced}$ is the charge produced by ionization, DPP (1.25 Gy/pulse) is the dose-per-pulse in water (that is assumed to be the same absorbed by the detector sensitive volume), ρ is the density of the diamond (3.53 g/cm^3), A is the active surface of the detector (1.3 $\times$ 1.3 mm^2), d is the crystal thickness (100 μm), w is the energy required to produce an electron-hole pair in the material (13 eV). For the range of bias voltages explored, it was obtained that only 35% of the total charge produced in the detector is actually collected and measured at 600V. For polycrystalline diamonds, CCE values generally range from 10% to 60%, according to literature [147]. The Charge Collection Distance (CCD) of the charge carriers can be derived from the Charge Collection Efficiency (CCE). It is defined as the CCE multiplied by the device thickness d:

$$\text{CCD} = CCE \cdot d$$

This represents the average distance that a pair of charge carriers can travel within the material before being recombined or trapped by crystalline defects or impurities. Our measurements indicate that at the maximum electric field (60 kV cm^{-1}), the charges travel 35 μm in the device, which corresponds to 35% of its total thickness.

The specific sensitivity was assessed as the charge per pulse per unit dose and volume. A sensitivity between 10 and 90 nC mm^{-3}Gy^{-1} was found, which is within the values (2.4–100 nC mm^{-3}Gy^{-1}) reported in the literature for other

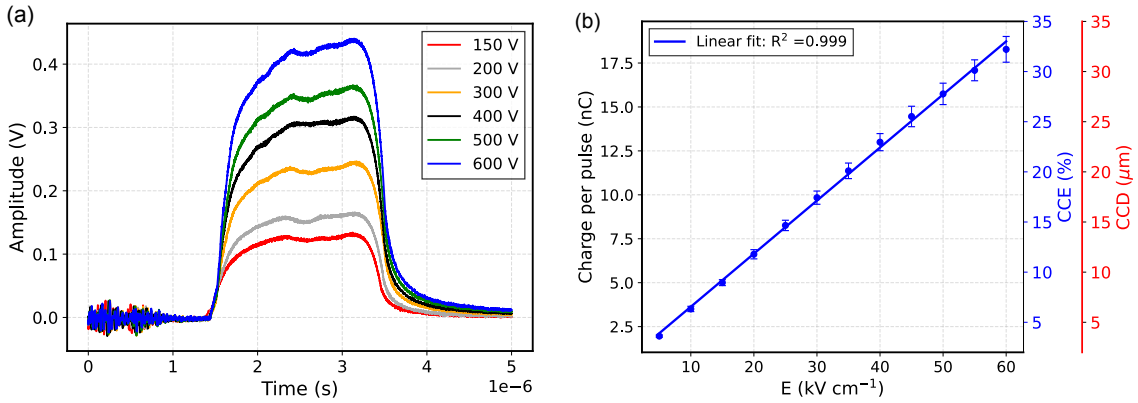

Figure 6.2.1: (a) Signals in the diamond acquired with the oscilloscope for single pulses under different polarization conditions. (b) Charge per pulse as a function of the electric field and corresponding charge collection efficiency.

sensors based on polycrystalline diamonds, taking into account the voltage range used in this study [5, 90]. However, compared to silicon sensors, the specific sensitivity of diamonds can be up to 10 times lower [55].
The comparative test performed in our laboratory maintaining the same beam conditions and the same electric field intensity (44.4 kV/cm) inside the diamond and silicon sensors showed specific sensitivity values of 71 and 507 nC $mm^{-3}Gy^{-1}$, respectively. This difference may be mainly related to the fact that the energy required to form an e-h pair in a diamond is almost four times greater than in silicon and that the trapping effect in diamond is not negligible [79]. The diamond integrated charge increases as the delivery progresses, and this effect is particularly noticeable when considering the first 50 pulses out of the 150 pulses delivered (Figure 6.2.3). The comparison with a silicon sensor (2 mm^2 area and 30 μm thickness), shown in Figure 6.2.2, demonstrates that this effect does not rely on the beam delivery and it might be related to the defects of the polycrystalline diamond, causing the trapping of the charge carries during the first pulses. When the traps have been filled, the charge effectively collected in each pulse reaches a fairly constant value. It is reported in literature that a pre-irradiation of a few tens of Gy, which was not performed during our initial sensor evaluation tests, can overcome this problem by stabilizing the dark current at a constant value after a growth phase [148]. It is commonly known as the "pumping" process, and can be performed with different penetrating radiation, such as β and X ray sources. [149]. The characteristic slow fall time of the diamond response with respect to silicon, probably caused by carrier trapping-detrapping mechanisms in the material, is evident when looking at the figures. Curves with such trends, which show clear memory effects of polycrystalline diamond detectors, are reported in the literature. In Table 6.1, the quantities evaluated through this measurement for both silicon and diamond are summarized, allowing a direct comparison between the two. The rise time and fall time were calculated as the time intervals between 10% and 90% of the signal amplitude on the rising and falling edges, respectively.

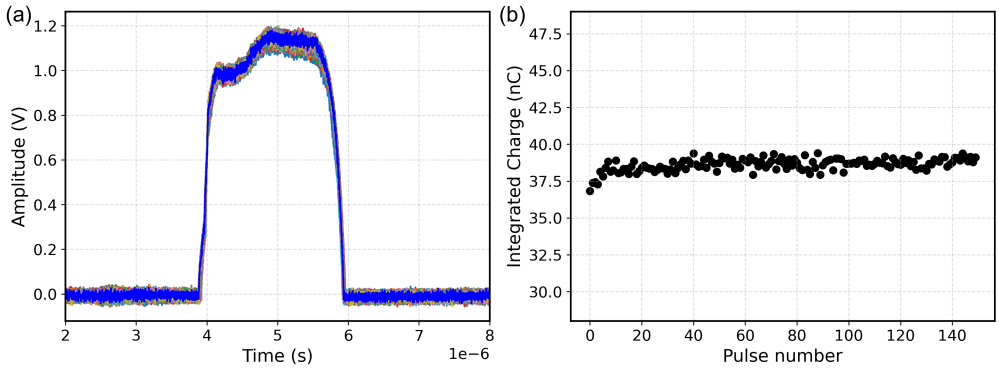

Figure 6.2.2: (a) Signals of 150 consecutive pulses recorded by the oscilloscope for silicon. (b) Charge per pulse as a function of the number of pulses for silicon is shown in right plots.

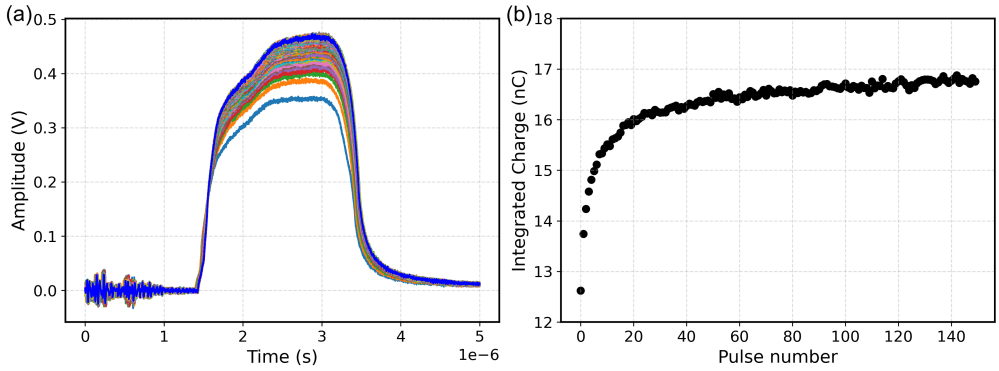

Figure 6.2.3: (a) Signals of 150 consecutive pulses recorded by the oscilloscope for diamond. (b) Charge per pulse as a function of the number of pulses for diamond is shown in right plots.

Parameter	Silicon	Diamond
Active volume (mm^3)	0.99	0.17
Bias Voltage (V)	200	444
Electric Field ($kVcm^{-1}$)	44.4	44.4
Signal amplitude (V)	1.54 ± 0.09	0.44 ± 0.02
Signal duration (μs)	2.018 ± 0.003	2.275 ± 0.006
Rise time (μs)	0.26 ± 0.01	0.72 ± 0.01
Fall time (μs)	0.41 ± 0.09	0.49 ± 0.09
Charge (nC)	57 ± 1	15 ± 1
CCE (%)	79	26
Specific sensibility (nC Gy mm^{-3})	507	71

Table 6.1: Summary of quantities evaluated for silicon and diamond detector under the same beam conditions and electric field strength (44.4 kV/cm).

6.3 Summary

A polycrystalline CVD diamond (pCVD) sensor with an active area of 1.3×1.3 mm^2 and a thickness of 100 μm was tested on electron beams of a high dose-rate enable LINAC Elekta. The charge collection efficiency (CCE) and sensitivity

found are within the literature ranges for pCVDs. In comparison with the silicon detector, a lower charge per pulse is obtained (as expected from the physics of the material), but the pulse characteristics are compatible. These results make the use of a polycrystalline CVD diamond detector as a beam monitor plausible. More in-depth studies of the sensor's response at higher dose-rates, as well as pre-irradiation measurements are necessary to confirm its usability for real-time beam monitoring in ultra-high dose-rate conditions. Two pCVD diamond samples, each with an active area of 5×5 mm^2, have undergone graphitization. The first sample was processed at the Ion Implantation facility in Legnaro, where a He^+ ion beam with an energy of 2 MeV (corresponding to a 3.5 μm range in diamond) was applied to an area of 1.3×1.3 mm^2. The second sample was implanted with a 35 keV fluorine ion beam (50 nm range in diamond) in the Ion Implantation facility at the Physics Department of the University of Turin, also in an area of 1.3×1.3 mm^2. Testing on this two samples is scheduled to be performed shortly.

Chapter 7

SiC: from FLASH radiotherapy to other harsh environments applications

In collaboration with SenSiC STLab s.r.l., a company active in the microelectronics field with whom I am collaborating as part of my doctoral research, I have undertaken several projects involving SiC sensors for diverse applications. These activities will be outlined in this chapter.

- In Section 7.1, I will briefly describe the testing and characterization of these sensors under high-dose-rate electron beams at the ElectronFLASH facility in Pisa. These tests were conducted by our colleagues at INFN in Catania, while I was actively involved in following the work and reviewing the results.

- A comparative study between silicon detectors, which have been thoroughly tested with electron beams from both the ElectronFLASH facility in Pisa and the Elekta LINAC in Turin, and SiC detectors is reported in Section 7.2. This study explores the response of SiC and silicon sensors under equivalent experimental conditions to ultra-high dose-rate (UHDR) beams in Turin. This section also includes a description of additional measurements performed during the same beamtime, where simultaneous measurements with silicon and plastic scintillators were conducted. The plastic scintillator technology, also proposed for FLASH beam monitoring, has been studied by colleagues at INFN Pisa.

- The radiation resistance of SiC detectors was studied within the Ion Microprobe Chamber at the Ruder Bošković Institute (Zagreb, Croatia) both at room temperature and elevated temperatures (500°C). The results are described in Section 7.3.

- The final Section 7.4 examines the use of SiC for X-ray beam position monitoring (XBPM), essential instruments in synchrotron beamlines. An experimental assessment conducted at the NanoMAX facility at MAX IV, the Swedish national synchrotron laboratory, is presented, along with a comparison to simulations performed using TCAD Synopsys Sentaurus.

7.1 SiC for monitoring FLASH beams

Silicon carbide (SiC) could be another excellent candidate as a solid-state sensor for monitoring high dose-rate beams. This is due to several promising characteristics that make it a good compromise between the technological maturity of silicon and the robustness of diamond. The wide bandgap and the energy required for electron-hole pair creation make it more radiation-hard than silicon, while still being more sensitive than diamond (which has a higher pair creation energy), thus providing a higher signal-to-noise ratio [150, 151].

The section of this thesis that focuses on silicon carbide in the context of FLASH radiotherapy was conducted in collaboration with SenSiC STLab and colleagues from the INFN (National Institute of Nuclear Physics) division in Catania. I followed their experimental activities and was able to carry out test campaigns at the same facilities. I present the main results obtained, summarizing the content of two publications [5, 6].

The first noteworthy experimental results were obtained at the Electron-FLASH facility (Pisa, Italy) using some sensor prototypes developed by SenSiC STLab.

The sensors used in this work are PIN junctions (Figure 7.1.1), consisting of a highly doped p^+ layer (0.3 μm, $N_A = 1 \times 10^{19}$ cm^{-3}) above a lightly doped n^- layer (ranging from a minimum of 200 nm to 100 μm, $N_D = 8 \times 10^{13}$ cm^{-3}) on top of a thick n^+ substrate (370 μm, $N_D = 5 \times 10^{18}$ cm^{-3}). Sensors with various active areas (from 1×1 mm^2 to 10×10 mm^2) and active thicknesses (from 0.2 μm to 100 μm) were fabricated. The results for a sensor with a 10 μm active thickness and a 1×1 cm^2 active area are presented in [5].

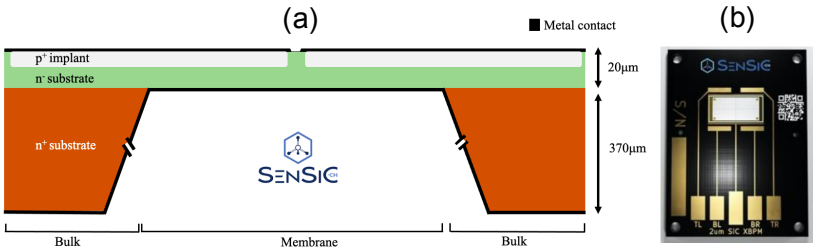

Figure 7.1.1: (a) Schematic overview and (b) picture of a SiC detector developed by the SenSiC company. As an example, a SiC sensor with 20 μm active thickness and the 370 μm substrate is shown along with the possible *free standing membrane* configuration where the substrate is removed.

The company is capable of forming the so-called *free-standing membrane* by removing the 370 μm thick n^+ substrate through selective electrochemical doping etching, as shown in Figure 7.1.1 (a). The creation of ultra-thin membranes, with thicknesses below 20 μm, will reduce beam perturbation, making them suitable for real-time transmission monitoring of UHDR beams. Simulations reported in [5], studying the angular distribution of an electron beam before and after the sensor's non-active substrate, have demonstrated the importance of thinning these sensors, particularly for lower incident energies. An initial characterization

of these *free-standing membrane* sensors, in terms of response as a function of irradiation temperature and radiation damage, was performed using low-energy proton microbeams (1.5 and 3.5 MeV) at the Experimental Physics Division of the Ruder Bošković Institute (Zagreb, Croatia). The results demonstrated promising radiation hardness tolerances, as discussed in Chapter 7.3.

The measurements carried out at the ElectronFLASH facility in Pisa investigated the response of a sensor with a 1×1 cm^2 active area and a 370 μm bulk substrate, in terms of increasing dose-per-pulse. The sensor was reverse biased at 480 V, which is 50 V above its depletion voltage. The pulse duration was fixed at 2 μs, set by the machine. Different doses per pulse at the irradiation points were obtained by using various applicators, which allowed for variation the source-to-surface distance (SSD), and by changing the sensor's position relative to the applicator output. The measurements were also compared with radiochromic films (RCFs), alanine, and a commercially available silicon diode (PTW Dosimetry Diode PR TM60020, 1 mm^2 active area and 20 μm thickness, operated without any bias voltage). The results are shown in Figure 7.1.2, where a linear response is observed up to 2 Gy/pulse, in contrast to the other sensors whose responses saturated earlier. The slight tendency towards saturation in the SiC sensor is due to the maximum peak current limit of the Keithley 6517A used for the measurements.

In this work, the radiation hardness of the sensors was also studied, both by observing the leakage current as a function of the cumulative dose up to 90 kGy (Figure 7.1.2 b), and by monitoring the variability of the charge per pulse for the explored accumulated dose (Figure 7.1.3). Both results suggest no degradation of the sensor, particularly in terms of the signal-to-noise ratio, and demonstrate the reliability and stability of the SiC's performance.

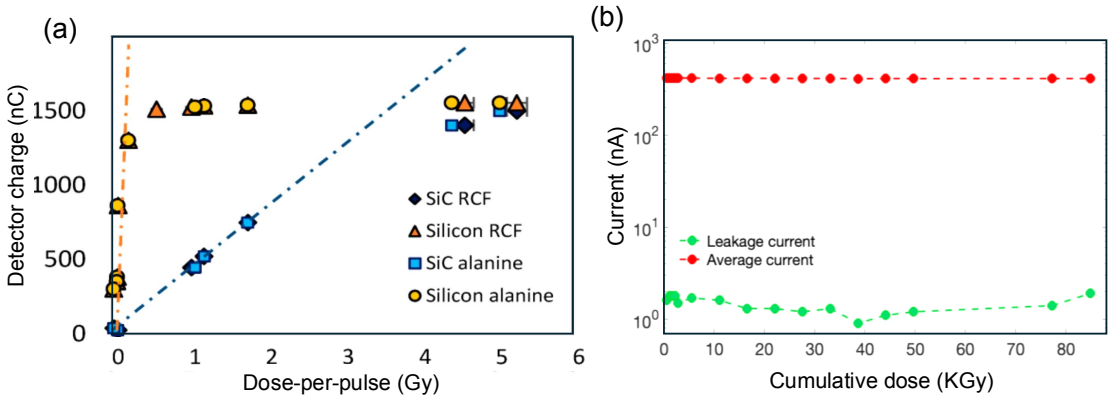

Figure 7.1.2: (a) SiC response measured with the Keithley 6517A electrometer as a function of the dose-per-pulse measured with the RCF and the alanine detectors placed in the same location of the detectors. Cross comparison with a commercially available silicon diode from PTW is also shown. (b) Leakage current of the SiC detectors after each irradiation and average current detected as a function of the cumulative dose delivered at the SiC position.

In the second work on SiC detectors for FLASH therapy applications, the response of new SiC detectors was studied over a broader range of dose-per-pulse and instantaneous dose-rates [6]. Once again, experiments were conducted using

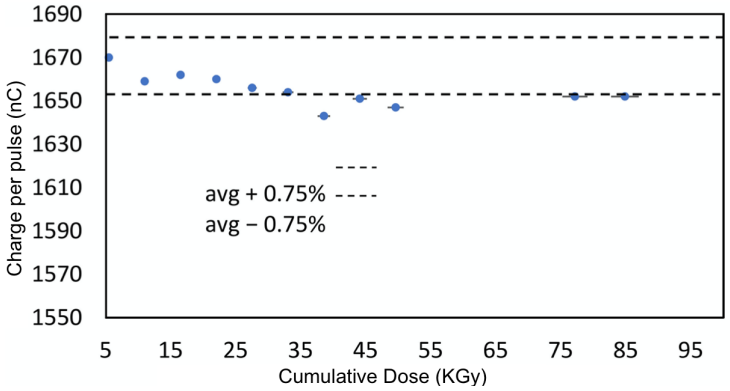

Figure 7.1.3: Charge per pulse measured with the SiC detector after each irradiation as a function of the cumulative dose. The dotted lines delimit the region within the ± 0.75% variation in charge.

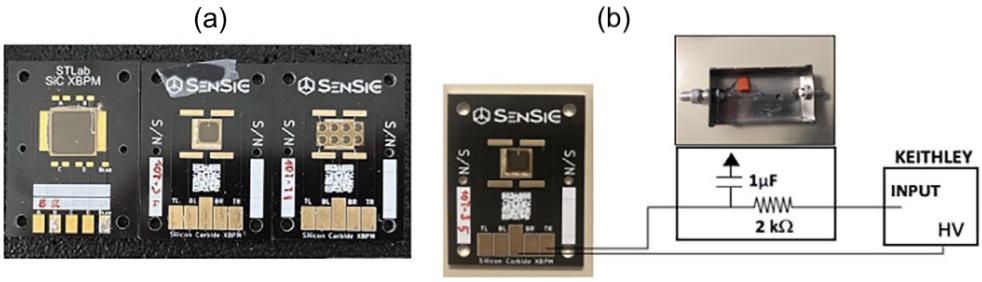

Figure 7.1.4: (a) Photograph of the various available SiC detectors with different active areas and shapes, that is, 100 mm^2, 25 mm^2 and 4.5 mm^2 SiC detectors. (b) The RC circuit realized and used to collect and store the charge produced within the SiC active layer.

pulsed UHDR electron beams of 9 MeV accelerated by the triode gun LINAC Electronflash.

The charge produced per single pulse in SiC detectors of different geometries (with an active area of 4.5, 25, and 100 mm^2, and thicknesses of 10 and 20 μm) was measured using a Keithley 6517A electrometer, connected to a dedicated external RC circuit to avoid the saturation previously observed while correctly measuring the charge generated within the SiC's active layer. The experimental setup is shown in Figure 7.1.4.

Results showed a linear response up to approximately 5 Gy/pulse for all tested detectors (S100-10, S25-10, S25-20) with a final applicator of 30, 40, and 100 mm diameter, as depicted in Figure 7.1.5 (a). Moreover, for the smallest SiC detector (S4.5-10), tested without any applicator, a linear response was observed up to the maximum DPP achievable in this condition of 21 Gy/pulse, and a maximum instantaneous dose-rate of 5.5 MGy/s. The functionality of this sensor was also verified without applying any bias voltage, showing that the linear response was maintained, although with the expected reduced sensitivity, as it can be seen in Figure 7.1.5 (b).

Finally, calibration coefficients were calculated for all SiC detectors with different areas and thicknesses. The dose values measured with the calibrated SiC detectors S100-10 and S25-10 were compared with those obtained using the calibrated PTW FLASH Diamond detector, irradiated under the same conditions. The results showed a good agreement with the FLASH Diamond, within 3% and

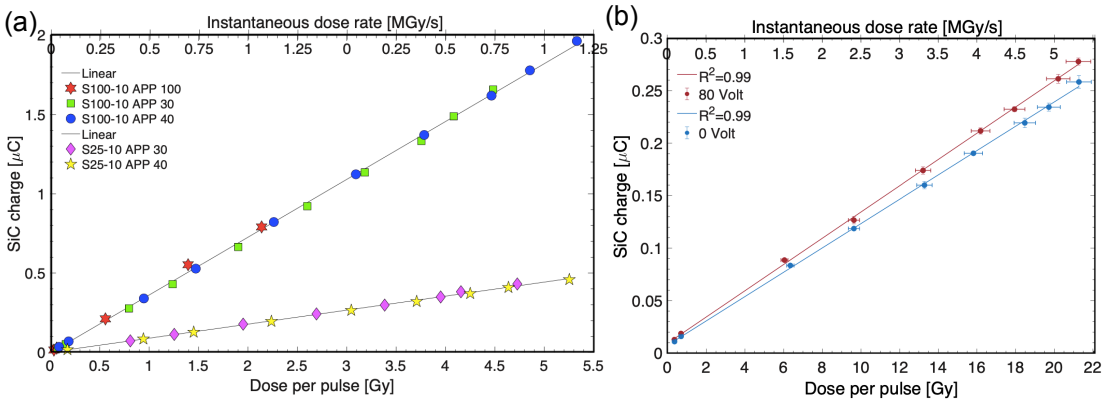

Figure 7.1.5: (a) Collected charge for the S100-10 and S25-10 detectors as a function of the DPP measured with the alanine dosimeters (x axis) and the average instantaneous dose-rate (y axis) obtained with different applicator setup. (b) Measured charge with the S4.5-10 detector at 80 V external applied bias as a function of the DPP (red points) and the corresponding instantaneous dose-rate (top axis). A comparison of the collected charge with the same detector at 0 V external applied bias is also reported (blue points).

1.5% for the SiC detectors S100-10 and S25-10, respectively. This comparison demonstrates the reliability of the calibration procedure used for this characterization and confirms the suitability of these new SiC detectors for dosimetry in flash-RT.

7.2 Simultaneous measurements of SiC and Si detectors (and plastic scintillator)

Having separately characterized silicon and SiC pads under FLASH beams at the ElectronFLASH accelerator (Pisa), simultaneous measurements were performed to compare the performance of a silicon and a SiC sensor in Turin with the Elekta LINAC of the Department of Physics, under the same experimental conditions. In addition, during the same data taking, preliminary measurements were also taken with plastic scintillators under the same experimental conditions as the silicon sensor.

7.2.1 Experimental setup

The selected silicon sensor is a pad with a 2 mm^2 sensitive area and 45 μm thickness, deeply described and characterized in Section 5.3. The SiC sensor, on the other hand, is a pad with a 4.4 mm^2 sensitive area and a thickness of 10 μm, whose response as a function of FLASH beams up to more than 20 Gy/pulse is shown in Figure 7.1.5 (b). A dose calibration factor of (83.33 $\pm$ 2.63) Gy/μC was obtained for this SiC detector on the ElectronFLASH LINAC. Measurements were conducted with an identical internal electric field in both devices, by biasing the silicon at 360 V and the SiC at 80 V (corresponding to an electric field of 80 kV/cm). The experiment was performed using an 10 MeV electron beam in FLASH mode, with a pulse repetition frequency of 6 Hz and a field size of 25 $\times$

25 cm^2 at the isocenter. The two PCBs, where the sensors were mounted, were attached to a rigid structure to place the two pads as close as possible, as shown in Figure 7.2.1. The distance between the two sensors was measured to be 2.1 cm, placing them 1.05 cm from the beam center, and thus in a region of uniform dose (Chapter 4.2, Figure 4.3.5). The signals from silicon and SiC sensors were readout by a Lecroy Digital Oscilloscope (Waverunner 640Zi, up to 40 GSample/s, 4 Bandwidth), connected to two separated channels.

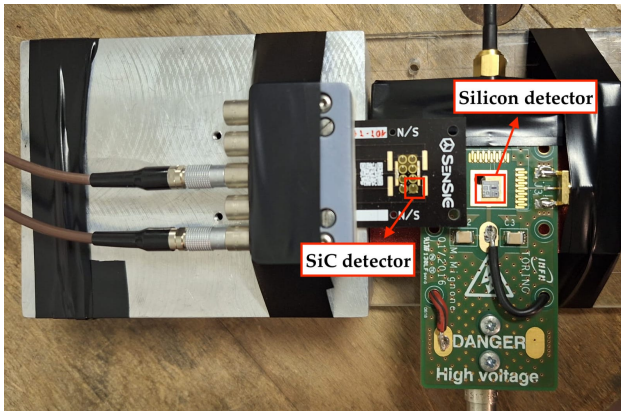

Figure 7.2.1: Picture of the PCBs where the silicon and SiC sensors were mounted. The distance between the two sensors was measured to be 2.1 cm, placing them 1.05 cm from the beam center. The SiC sensor is positioned slightly higher than the silicon sensor by a height equal to the PCB thickness (1 mm).

This setup was then tested under different configurations: aligned with the cross-hair foil, at the isocenter, and in the same position but with a cylindrical PMMA applicator with an internal diameter of 5 cm. Each of these three conditions was tested under both Low Power (LP) and High Power (HP) settings of the LINAC (Section 4.2.1). To determine the corresponding dose-per-pulse values at each position, the calibration described in Chapter 4.2 was used.

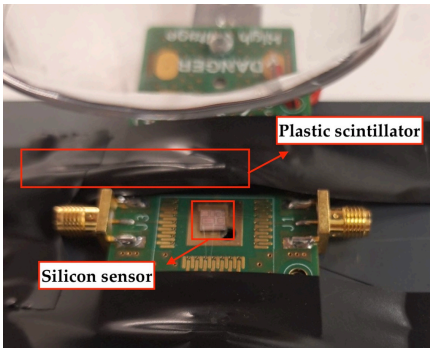

Figure 7.2.2: Picture of the setup for simultaneous measurements with the silicon and plastic scintillator detectors. The scintillating fiber was positioned on the PCB to place its sensitive region as close as possible to the silicon detector.

Subsequently, a similar measurement was conducted to compare the performance of silicon detectors with plastic scintillating fibers [41, 40], studied within the INFN FRIDA collaboration. Plastic scintillators exhibit a fast time response (approximately 1–10 ns), making them highly suitable for real-time dosimetric

measurements. This rapid response allows plastic scintillators not only to provide online dose measurement, but also to resolve individual pulses, enabling their use in real-time verification of beam parameters such as dose-per-pulse, which is of particular radiobiological interest. Additionally, when fashioned into thin fibers, plastic scintillators can be shaped into miniaturized detection volumes with high intrinsic spatial resolution, making them ideal for small-field dosimetry. Some prototypes have already been tested with a 9 MeV FLASH electron beam from the Electronflash, demonstrating satisfactory performance for FLASH applications up to 10 Gy/pulse (IDR $> 10^6$ Gy/s). They are capable of reconstructing the beam's lateral profile and the percentage depth dose curve. The plastic scintillating fibers were optically coupled to transparent optical fibers within an opaque plastic or carbon fiber tube, ensuring mechanical stability. Light-tightness was achieved by wrapping the tube with black tape, extending a few centimeters onto the transparent fiber, as shown in Figure 7.2.2. The transparent optical fibers transported the scintillation light to the imaging system, which consisted of a scientific, back-thinned, back-illuminated CCD camera, coupled with an f/0.95-25 mm C-mount objective lens. For more details on the plastic scintillator measurement system, please refer to [41]. This setup was tested for the first time at the LINAC in our department. The scintillating fiber and the previously described silicon detector were positioned as close as possible to each other. Measurements were conducted under the same setup as the SiC tests but limited to four measurement conditions: at the cross-hair foil and at the isocenter with the applicator, in both LP and HP conditions.

7.2.2 Results

Figure 7.2.3 shows the charge per pulse as a function of dose simultaneously measured by silicon and SiC detectors. The same data is also presented for the charge per pulse normalized to the unit volume, which is $9 \cdot 10^{-2}$ mm^3 for the Si detector and $4.5 \cdot 10^{-2}$ mm^3 for the SiC detector. The charge per pulse shows a linear trend, resulting in a coefficient of determination of a linear fit $R^2 > 0.98$ for both detectors.

As previously mentioned, in the measurements conducted on ElectronFLASH (CPFR, Pisa), a dose calibration factor of (83.33 ± 2.63) Gy/μC was obtained for the SiC detector, which is far from the calibration factor derived from these measurements, (71.58 ± 3.80) Gy/μC. One of the possible reason could be the lower sensitivity of SiC, which can be an advantageous characteristic for high dose-rates, as those reached in Pisa, but may be less efficient for lower dose-rates, as those of the LINAC. This can be observed in Figure 7.2.4 (a). Here the ratio between the charge measured in silicon and SiC is shown as a function of dose. The dashed line represents the ratio of the two volumes ($V_{Si}/V_{SiC} = 2$), and it can be observed that the curve approaches the expected value only for doses greater than 0.6 Gy. Figure 7.2.4 (b) displays only the charge values measured for SiC. In particular, the blue line was obtained using the calibration performed in Pisa (83.33 ± 2.63) Gy/μC, the red curve using the calibration performed in Turin, and the green curve using latter calibration excluding the two lowest measured dose-per-pulse values. In this way, a calibration factor of (77.41 ± 5.00) Gy/μC is

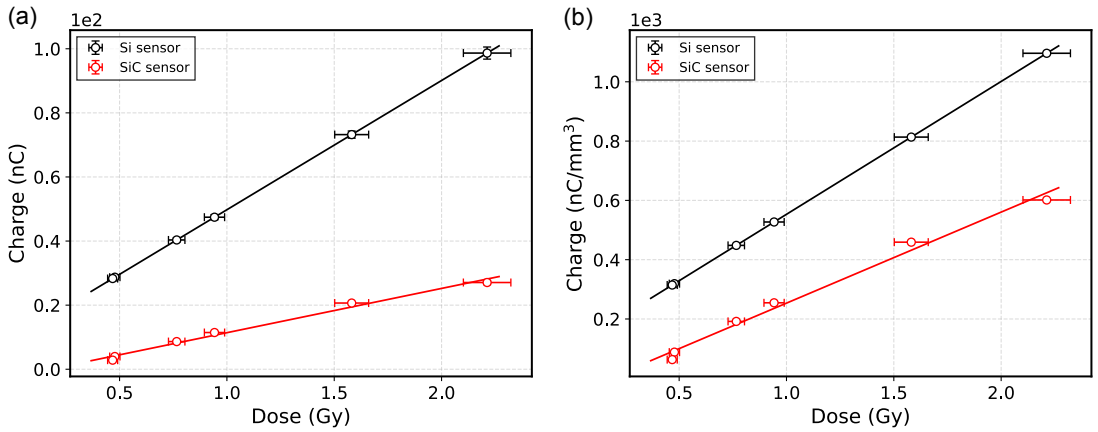

Figure 7.2.3: (a) Charge per pulse of silicon and SiC detector measured simultaneously in 6 different dose conditions. (b) Charge per unit volume as a function of the dose.

obtained, compatible with the one measured in Pisa.

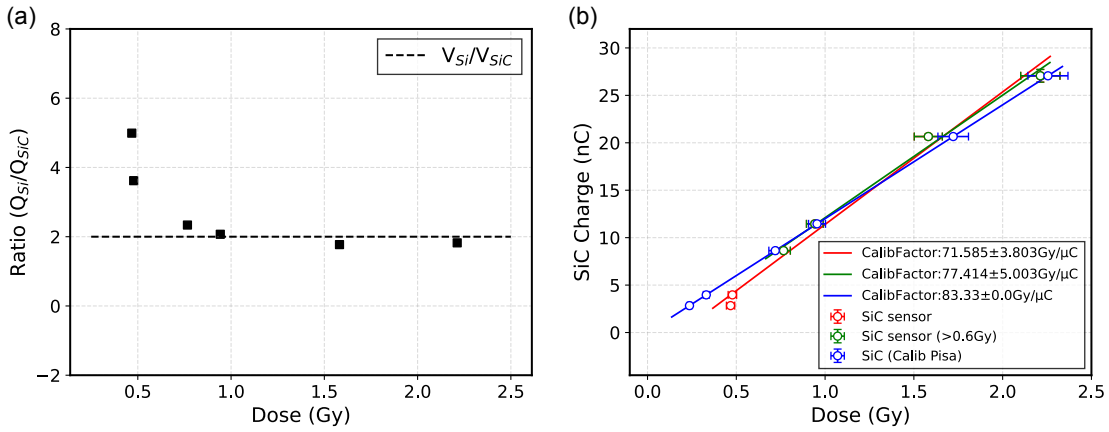

Figure 7.2.4: (a) Ratio between the charge measured in silicon and in SiC for different dose-per-pulse values. The dashed line represents the ratio of the two sensor volumes ($V_{Si}/V_{SiC} = 2$). (b) Charge measured in SiC as a function of dose. Dose values were calculated using the Turin calibration (red data), excluding the first two data points (green data), and the Pisa calibration (blue data).

Another analysis enabled by the data collected during this experiment is the comparison of the signal's temporal profile. Figures 7.2.5, 7.2.6 display the two voltage signals acquired with the oscilloscope (a) and the normalized signals (b). The two figures represent 10 pulses acquired from the two sensors in two experimental conditions (cross-hair foil and isocenter, FLASH HP), selected for illustrative purposes.

It is immediately apparent that the SiC signal, being less sensitive, is more affected by noise, particularly for smaller signals, such as those acquired at the isocenter (Figure 7.2.6). The response speed of the devices was assessed by calculating the rise time (t_r), defined as the time required for the signal to increase from 10% to 90% of the plateau value, and the fall time (t_f), the time required for the signal to decrease from 90% to 10% of the plateau value. Table 7.1 provides

the results obtained for the six measurement conditions, for both the silicon and SiC sensors.

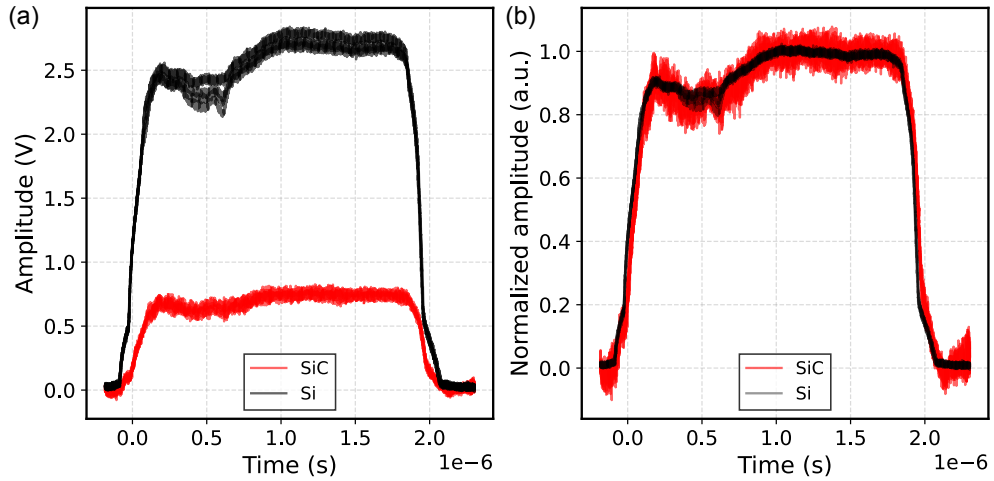

Figure 7.2.5: (a) Output voltage pulses generated by the 10 MeV electron beam in silicon (black) and SiC (red) recorded by the oscilloscope. (Number of pulses: 10; Position: cross-hair foil; Mode: FLASH HP). (b) The normalized signals are reported for both Si and SiC detectors. The oscilloscope input impedance was 50 Ω.

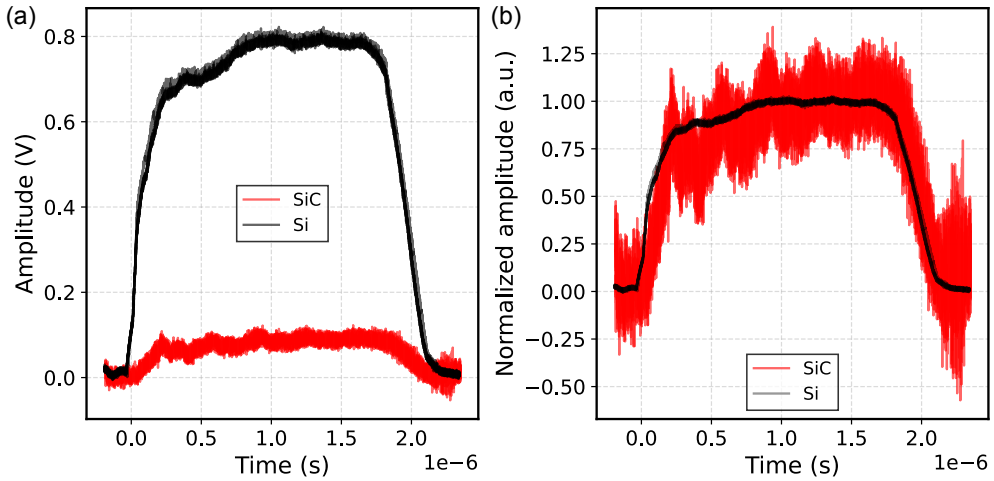

Figure 7.2.6: (a) Output voltage pulses generated by the 10 MeV electron beam in silicon (black) and SiC (red) recorded by the oscilloscope. (Number of pulses: 10; Position: isocenter; Mode: FLASH HP). (b) The normalized signals are reported for both Si and SiC detectors. The oscilloscope input impedance was 50 Ω.

		DPP (Gy)					
		0.47	0.48	0.77	0.94	1.58	2.21
Si	CPP (nC)	28.31 ± 0.33	28.72 ± 0.74	40.34 ± 0.62	47.44 ± 0.81	73.21 ± 1.12	98.66 ± 1.89
	t_r ($\times 10^{-7}$ s)	1.61 ± 0.06	1.92 ± 0.08	1.96 ± 0.07	2.04 ± 0.06	1.77 ± 0.06	2.08 ± 0.07
	t_f ($\times 10^{-7}$ s)	2.54 ± 0.06	2.72 ± 0.06	2.72 ± 0.06	2.28 ± 0.05	2.45 ± 0.05	2.87 ± 0.05
SiC	CPP (nC)	2.84 ± 0.06	3.97 ± 0.16	8.63 ± 0.11	11.46 ± 0.19	20.66 ± 0.22	27.06 ± 0.67
	t_r ($\times 10^{-7}$ s)	1.60 ± 0.07	1.73 ± 0.05	1.87 ± 0.07	2.37 ± 0.08	1.93 ± 0.15	2.30 ± 0.08
	t_f ($\times 10^{-7}$ s)	2.46 ± 0.04	3.19 ± 0.04	2.63 ± 0.05	2.47 ± 0.05	2.29 ± 0.05	2.68 ± 0.06

Table 7.1: Charge per pulse (CPP), rise time (t_r), and fall time (t_f) values for the tested dose-per-pulse, for both silicon and SiC detectors.

Regarding the simultaneous measurements conducted with the silicon and plastic scintillator detectors, the results are shown in Figure 7.2.7. The scintillator signal was evaluated by summing the counts within a region of interest (ROI) centered on the fiber image. Uncertainties on the measured values were determined as the standard deviation of three acquisitions. As the scintillator counts were not calibrated in dose units, only the linearity with respect to dose evaluated from silicon detector measurement was verified. Table 7.2 reports the measurements taken over the 4 experimental conditions. For each dose-per-pulse value, the charge measured by the silicon and the signal in arbitrary units of the plastic scintillator are presented.

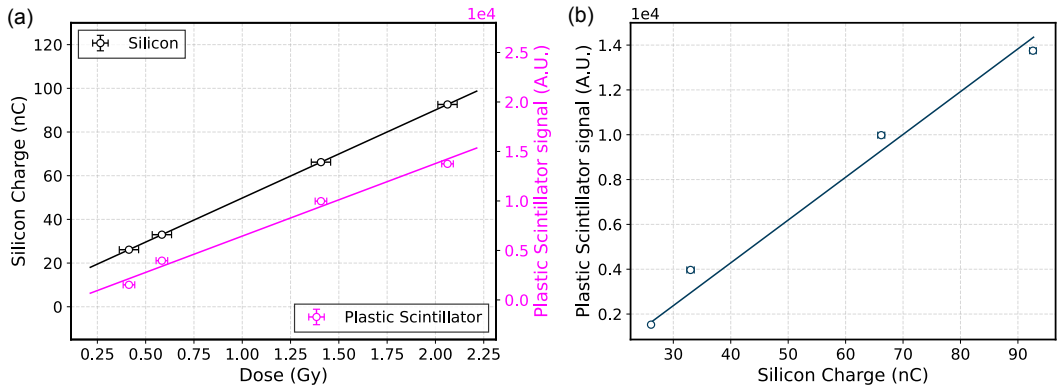

Figure 7.2.7: (a) Charge measured by the silicon sensor (left y-axis) and signal measured by the plastic scintillator (right y-axis) as a function of dose-per-pulse. (b) Correlation of the signal measured by the plastic scintillator and the charge measured in the silicon sensor under the same experimental conditions.

DPP (Gy)	2.06 ± 0.06	1.41 ± 0.04	0.58 ± 0.02	0.41 ± 0.01
Silicon Charge (nC)	92.62 ± 0.58	66.20 ± 0.61	33.00 ± 0.65	26.12 ± 0.18
Plastic Scintillator signal (A.U.)	13749.89 ± 12.60	9980.63 ± 6.69	3967.43 ± 32.58	1526.79 ± 21.11

Table 7.2: Silicon charge and plastic scintillator signal (in arbitrary units) in four dose-per-pulse conditions.

7.2.3 Conclusions

A comparative test was conducted between a silicon sensor with an active area of 2 mm^2 and thickness of 45 μm, and a SiC sensor with an active area of 4.4 mm^2 and thickness of 10 μm. Both sensors were exposed to 10 MeV UHDR electron beams delivered by the Elekta LINAC SL18 accelerator, following the machine modifications described in Chapter 4. The sensors were placed as closely as possible and biased to produce an identical electric field across the active regions, ensuring equivalent experimental conditions. Measurements were taken at the cross-hair foil, at the isocenter, and at the same location with a 5 cm diameter applicator, in both high power (HP) and low power (LP) modes. From the oscilloscope signals, the charge collected by each sensor for each LINAC pulse was calculated. Linear response of charge as a function of dose-per-pulse was confirmed for both sensors ($R^2 > 0.98$) for dose-per-pulse values exceeding 2 Gy/pulse. Excluding the two lowest dose-rate SiC measurements (which presented significant noise), the calibration factor obtained with the ElectronFLASH at Pisa was found to be consistent with the one derived from the measurements conducted in Turin. The temporal profile of the signals was comparable between the two solid-state technologies, with rise times ranging from 160 ns to 230 ns and fall times from 2.28 ns to 319 ns. These time values reflect not only the detectors' response but also the electron bunch structure delivered by the accelerator itself.

A further comparison at four measurement points was performed between the same silicon sensor and a plastic scintillator, positioned as close as possible to the silicon sensor's active area. In this case, only the linear response as a function of dose-per-pulse was investigated. However, future beam tests are planned to repeat these measurements at a greater number of points with a more advanced experimental setup. Background contributions from spurious luminescence due to the Cherenkov effect were not accounted for in this study; in subsequent tests, we plan to estimate and correct for this contribution. Additionally, future measurements will aim to record the temporal profile of the plastic scintillator signal and compare it with simultaneous measurements using the silicon sensor, as was done with the SiC sensor.

7.3 Radiation hardness study of Silicon Carbide sensors under high-temperature proton beam irradiations

Silicon carbide (SiC) thanks to its material properties similar to diamond and its industrial maturity close to silicon represents an ideal candidate for several harsh environments sensing applications where sensors must withstand high particle' irradiations and/or high operational temperatures. In this study, to explore the radiation resistance of SiC sensors to multiple damaging processes, both at room and high temperature, we used the Ion Microprobe Chamber installed at the Ruder Bošković Institute (Zagreb, Croatia), which allowed the possibility to expose small areas within the same device to different ion beams, thus evaluating and comparing effects within a single device. The sensors tested, developed jointly by SenSiC STLab [152], are PIN diodes with ultrathin *free-standing membranes*, realized by means of a recently developed doping-selective electrochemical etching. In this work we report on the changes of the charge transport properties, specifically in terms of the charge collection efficiency (CCE), with respect to multiple localized proton irradiations, performed both at room temperature (RT) and at $500°C$. The results are described in the following publication [7]:

Medina, Elisabetta, et al. "Radiation hardness study of silicon carbide sensors under high-temperature proton beam irradiations." Micromachines 14.1 (2023): 166.

One of the main characteristics required for sensors used in diagnostic applications is the capability of withstanding Harsh Environment (HE) operations. Examples of HE are: (i) X-ray sensors in the extreme intensity beams of synchrotrons and free-electron lasers, with beam powers exceeding 100 kW/cm^2, (ii) electron sensors in sterilization processes and novel radiotherapies or (iii) neutron sensors for safety assessments and process monitoring in nuclear facilities. The high total radiation doses, as well as the instantaneous ones, to which these sensors are exposed require stable and reliable responses over long periods of time, possibly even under high-temperature operation conditions. Nowadays, solid-state technology represents a solution for several sensing applications, thanks to, among others: high signal-to-noise ratio, small size, lateral resolutions and fast response time. However, radiation hardness is a critical characteristic for solid-state sensors. Silicon, due to its low bandgap and low kick-off energy, cannot generally be used in any HE applications. Diamond, on the other hand, due to its very large bandgap, maximum - theoretical - operating temperature and very high kick-off energy, is the most studied semiconductor, in particular with studies focused on the electronic response at high device temperature. However, the very high cost, limited sample size (less than 1 cm^2 for CVD single crystal diamond), high level of impurities and physical limitations on doping control have prompted the scientific community to find alternative solutions. Silicon carbide (SiC), a semiconductor composed of 50% silicon and 50% carbon atoms represents the most obvious candidate, compromising between the low-cost and

industrial maturity of silicon on one hand and the radiation-hardness capabilities close to diamond. In the last 5-10 years SiC has been the protagonist of industrial advances, and the reason for this maturity is its wide use for power electronics applications, particularly in high-end electric vehicles. Despite numerous studies in terms of high-power applications, the characteristics of SiC sensors, especially in high-temperature operations, require specific experiments and investigations, including the one described in the following paragraphs.

Previous research has demonstrated, among others, the detection of alpha particles with SiC-based detectors at high temperatures (up to 500°C), strengthening the potential of these devices for multiple applications in harsh environments [153]. Furthermore, it is now well known that ion implantations, the only method to achieve selective doping of SiC regions in power devices, induce accumulation of point defects which, for high injection doses, can even lead to amorphization. However high-temperature (500°C and above) implantations hinder this effect, thanks to a dynamic annealing process occurring under these conditions. More details regarding ions implantation at high-temperature in silicon carbide can be found in Refs. [85, 154, 155, 156, 157, 158]. Consequently, aware of the good functionality of SiC above 500°C and of the high temperature condition needed during ion implantations, it may be a valid solution, for some applications in extremely harsh environments such as within fusion reactors core vessels, to employ SiC sensors at high temperatures to make them more radiation resistance. An experimental result consistent with this approach is explained in Ref. [151], where a high-power 4H-SiC Schottky diode was irradiated with electrons and showed a drop of the carrier removal rate by about 6 orders of magnitude in the case of 500°C irradiations. The aim of the experiment described in this paper is to study the effect of high-temperature irradiation on a SiC device, comparing the results with those obtained in Ref. [151] in terms of sensor functionality, i.e. local CCE instead of reverse leakage measurement, and though a different beam condition: a focused proton beam instead of a large area electron one. In more details, for this work proton beams with MeV energies were used either to inject charge carriers (probing ion beam) or induce radiation damage (damaging ion beam) in SiC sensors. Damage was induced both at room as well at high temperatures (> 400°C). Proton beams with MeV energies induce both point defects and defect clusters in the crystal lattice, making them an ideal tool for testing the radiation hardness of detectors. Probing was performed at RT. This activity, focusing on proton-induced charge transport properties, is part of a more general effort to establish the functionality of SiC at different ionizing radiation beams and environments, in order to validate their possible use in a wide range of applications. The properties of sensors depending on temperature and device geometries, i.e., " bulk type" or " independent membrane type", see below, and thus to assess the safety ranges for the operational functionality of SiC-based sensors have been studied. The capability of the selected facility to expose small areas (below 100x100 μm^2) with the beam, thus evaluating local effects within a single device reducing uncertainties generated by the device-to-device variabilities, has been exploited.

7.3.1 Materials and Methods

The Ruder Bošković Institute (RBI [159]) accelerator facility consists of two accelerators, 6.0 and 1.0 MV electrostatic tandem accelerators (6.0 MV EN Tandem Van de Graaff and 1.0 MV HVE Tandetron), as well as 9 beam lines, represented schematically in Figure 7.3.1. In this experiment, the SiC sensors were mounted in an ion microprobe vacuum chamber, connected to one of the beamlines, and in which a system of quadrupole lenses (depending on the application it could be doublet, triplet or quintuplet) is able to focus the accelerated ion beam to the micrometer size. The Beam Induced Charge Technique (IBIC) was exploited: fast ions crossing the sensor interact with the electrons of atoms in the material and numerous ionizations along their trajectories are created. The interaction of the ions with the semiconductor device will eventually generate electron-hole (e-h) pairs which can drift due to the built-in electric field (e.g. pn junction), or to an externally applied electric field, generating a measurable current signal at the electrodes. During the irradiation, the ion beam, thanks to the micrometer size, can be scanned over the desired sample regions, so that the collected signal can be correlated to the beam position, enabling 2D mapping of charge transport properties (IBIC maps).

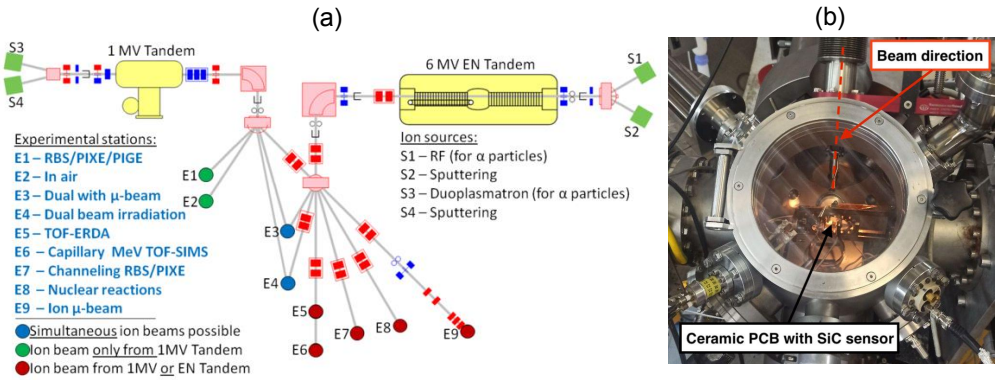

Figure 7.3.1: (a) Beamlines overview at the RBI accelerator facility [159]. THE 6.0 MV EN Tandem Van de Graaff and 1.0 MV HVE Tandetron are represented in yellow. The E9 experimental station corresponds to the Ion Microprobe. (b) The Ion Microprobe Chamber is shown, in which the beam is focused down to micrometer spot size, and in which the sample to be tested is placed (the photo shows the SiC membrane on the support structure).

In the experiment described in this work, a SiC membrane sensor was used, produced by SenSiC company. SiC membranes recently demonstrated promising hard X-ray beam position monitors capabilities [160] as well as promising ultra-high dose-rate electron beam dosimetry monitoring capabilities, in the so-called Flash Radiotherapy application [29, 161]. These devices are semiconductor PIN junctions: they are composed of a thin, 0.3 μm p^+ highly doped (10^{18} cm^{-3}) layer and a 20 μm n^- low doped (10^{14} cm^{-3}) layer on top of a $\sim$ 370 μm thick n^+ (10^{18} cm^{-3}) substrate. The n^+ substrate of the sample used in the experiment has been partially removed by electrochemical etching (expertise of SenSiC STLab), creating a thinned-down circular area in a selected region of the sensor (i.e., a free-standing membrane) [162]. The total sensor area (5×5 mm^2) is divided into 4 pads (2.5×2.5 mm^2 each) and the circular region ($\sim$ 1 mm of radius),

corresponding to the 20 μm membrane, is located in each pad center. On the rest of the sensor the 370 μm bulk is still present under the active layer. The cross-section of the sensor used is shown in Figure 7.3.2. Only one of the 4 pads was connected to the electronics and studied in the Ion Microprobe Chamber.

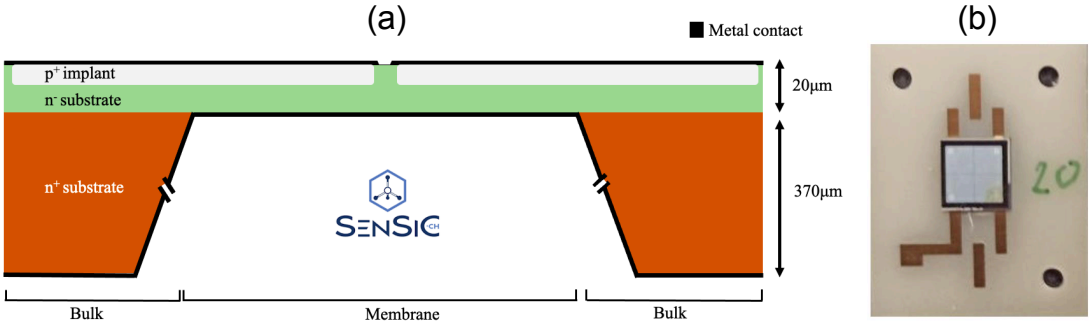

Figure 7.3.2: (a) The structure of the SiC membrane sensor is shown: a thin p^+ layer, a n^- layer, and a thick n^+ substrate. The central area at the 4 pads (circular region of ~2 mm diameter) is thinned using an electrochemical doping-selective etching. (b) Photo of the sensor mounted on a ceramic plate with gold electrodes, subsequently mounted inside the chamber.

Since the device was tested under simultaneous exposure to heat and ion beams, good thermal-resilience of the sensor, as well of the signal processing components, in the vacuum chamber had to be ensured. High purity silver paste was used to mount the SiC sensor on the ceramic PCB, which was in direct contact with a heating element mounted in the vacuum chamber, as represented in Figure 7.3.3. Reverse bias, up to -100 V, was applied through the front electrode, while the back electrode was grounded thus achieving "reverse diode operation", typical for achieving high signal-to-noise ratio in sensing applications. To make the temperature rise possible, the sensor was heated by a resistive heater, contacting the ceramic plate, and the temperature was checked by means of a type K thermocouple. The electronic readout chain processing the sensor's output signal comprises a charge-sensitive preamplifier (ORTEC 142A), a spectroscopy amplifier (ORTEC 570), an analog to digital converter (Canberra8075) module and the in-house developed SPECTOR software [163]. Finally, a source-measurement unit (SMU, Keithley 6485 pico-ammeter) with a current range of 2nA-2mA and 10fA of resolution was used to characterize the current-voltage curve of the device in *dark*, i.e. without beam.

The irradiation and subsequent charge collection study was performed in the Ion Microprobe Chamber already described, using a proton beam focused down to the smallest size of ~ 1 μm radius.

To confirm the micrometer size of the beam, the knife-edge calculation procedure was used. A finely machined metal grid with a defined step size was placed in front of a reference silicon STIM (Scanning Transmission Ion Microscopy) detector. A projection image of the grid on the STIM sensor is shown in Figure 7.3.5. The data from regions near the shadow of the grid edge were reported as the number of events as a function of position (Figure 7.3.6). The sigmoidal profile of the recorded events corresponds to the lateral profile of the beam scan point and was analyzed using a Boltzmann sigmoidal function. The spatial profile of the beam was determined in two dimensions by calculating the number of pixels

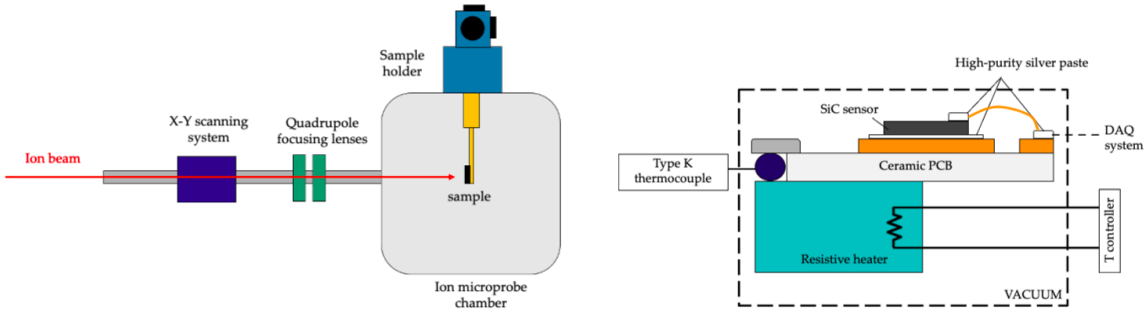

Figure 7.3.3: Schematic of the experimental setup. The SiC sample was mounted (using high-temperature silver paste) on the ceramic plate with printed gold electrodes. The whole device was mounted on a holder for further tests in an irradiation chamber. The detector was heated by a resistive heater below the copper heat sink that was in contact with the back side of the ceramic plate. A type K thermocouple was used for temperature measurement.

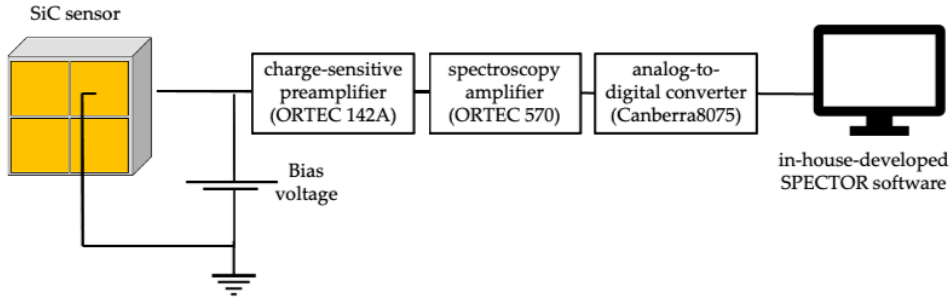

Figure 7.3.4: Schematic of the electronic readout chain processing the sensor's output signal. A charge-sensitive preamplifier (ORTEC 142A), a spectroscopy amplifier (ORTEC 570), an analog to digital converter (Canberra8075) module and the in-house developed SPECTOR software [163] were implemented for the signal study.

(Δx) that fall within the range defined by the values corresponding to 10% and 90% of the upper plateau of the function. Multiplying the value by the conversion factor from pixels to microns for the specific configuration the beam dimension can be derived.

The micrometer beam can be scanned over the detector surface in specific selected areas, with the possibility of choosing both the scanning speed and size of the scan. During the experiment, two different linear accelerators were used, depending on the specific irradiation purpose. A low energy proton beam (1 MeV) was used for the IBIC studies, while a 3.5 MeV proton beam (delivered by the larger of the two accelerators) was used to generate damaged regions. The lower beam energy was used for charge collection efficiency (CCE) measurements. In this case, simulations with SRIM software [164] demonstrated that the energy is deposited completely within the 20 μm active thickness, with a Bragg peak located around half of the active area ($\sim$ at 10 μm depth). On the other hand, the 3.5 MeV proton beam was used to locally induce radiation damage in selected areas of the sensor. In this case, the beam passes completely through the sensor, creating almost homogeneous defects along the trajectory with an average of $\sim 2 \times 10^{-5}$ vacancies produced per ion per micrometer of penetration. It was

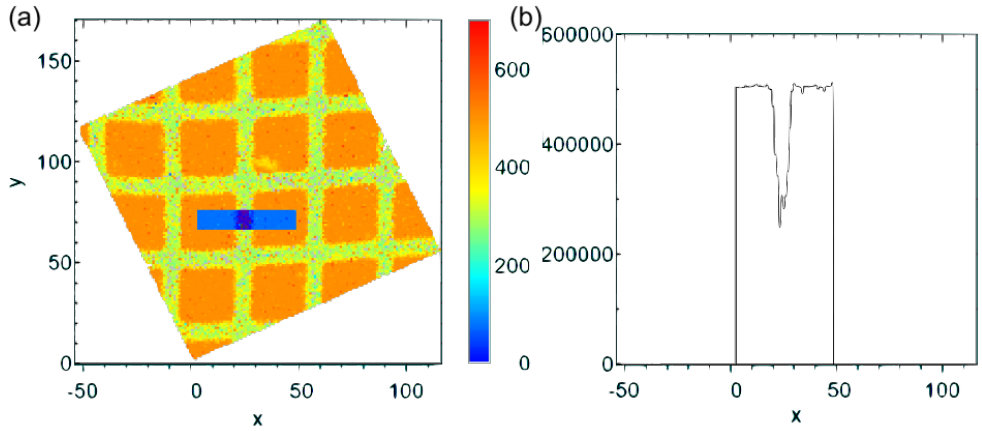

Figure 7.3.5: (a) Projection image of a finely machined metal grid with a defined step size on a reference silicon STIM detector, formed by the interaction between the ions and the sensor. (b) The counts recorded in the selected area (in blue) and projected on x-axis are rapresented. The same procedure is repeated for y-axis.

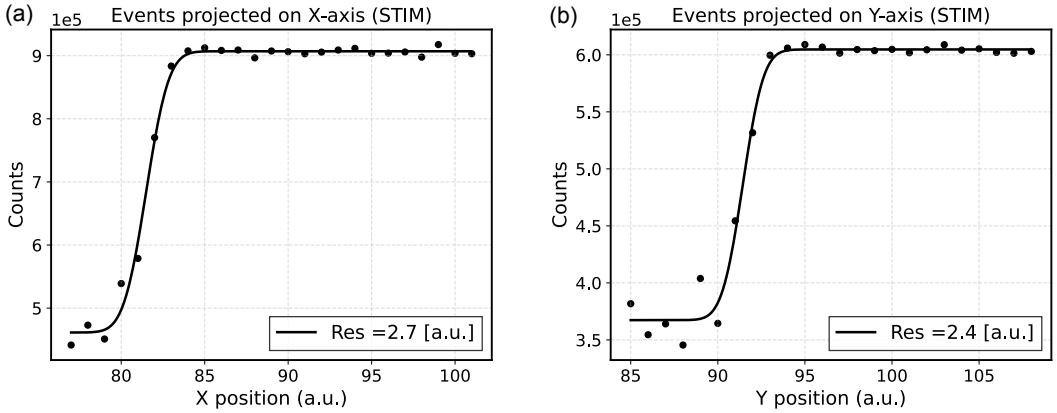

Figure 7.3.6: Count event profile close to the grid projection edge measured by the STIM detector on x-axis (a) and y-axis (b). The black dots representes the number of events measured as a function of position (in a.u.). The solid line rapresent the Boltzman sigmoidal function fitted to the experimental data.

verified by simulations that only ∼10% of the energy is released in 20 μm and that the Bragg peak is located within the substrate. Both simulation results are shown in Figure 7.3.7. To calibrate the charge collected by the silicon carbide during IBIC tests, the STIM detector fixed inside the chamber under the same beam conditions is used, assuming a total collection (100%) of the beam signal. The channel-to-energy calibration is implemented as shown in Formula 7.1, where W_{SiC} and W_{Si} are the average energies for e-h pair creation in SiC and Si (7.28 eV and 3.62, respectively), CHN_{Si} is the channel corresponding to the energy peak measured by the fixed silicon sensor and β is a correction factor containing any differences in the gain set in the electronics:

$$Energy = CHN_{SiC} \cdot \left(\frac{W_{SiC}}{CHN_{Si} \cdot W_{Si}} \cdot \beta\right) \tag{7.1}$$

Depending on the energy of the proton beam a different number of e-h pairs

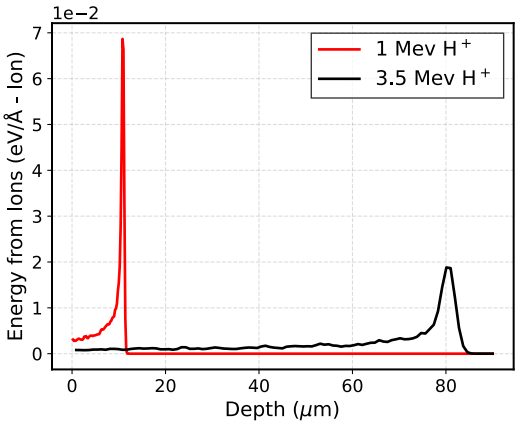

Figure 7.3.7: Energy loss as a function of depth in silicon carbide for a 1MeV (in red) and 3.5 MeV (in black) protons beam produced by the SRIM simulation software.

is created, which move through the sensor generating a measurable signal. In the presence of defects along the path the charge carriers can be trapped in the crystal lattice and consequently reduce the signal. There are mainly two mechanisms of radiation-induced degradation in a semiconductor device, as explained in detail in Ref. [151]: the creation of deep acceptor levels (to which electrons pass from shallow donor levels), and the interaction of radiation defect (vacancy) with a shallow impurity atom to give an electrically neutral (or acceptor) center. Models have showed that the first mechanisms leads to a linear fall of carrier concentration with increasing irradiation dose, while in the second case the decrease is exponential . Experimental data from different researchers [165, 166] have demonstrated that the first mechanism is dominant in SiC devices. Therefore, with the increase of the irradiation dose a linear degradation of SiC performance is expected. However, in the case of high-temperature irradiation, as has already been mentioned, there is the possibility of increased radiation resistance due to less lattice damage under such conditions. The next session describes the results obtained from charge collection efficiency measurements, which are consistent with this scenario.

7.3.2 Results and discussion

For the current-voltage characterization of the device, the previously described pico-ammeter was used. By measurements at room temperature in dark conditions it was verified that up to -60 V of bias voltage the leakage current does not exceed 1 nA, while at -80 V this reaches 8.5 nA, as it is shown in Figure 7.3.8. We decided not to overcome this latter voltage value (corresponding to an electric field of 4 V/μm in the active thickness), because thereafter the leakage current would rise considerably. We made this measurement both before any test in the ion microprobe chamber, and after irradiation (both at room and high temperature). This result indicates that in the chosen range of bias voltages, the device remains in a safe condition and the leakage current is negligible compared

to the signal.

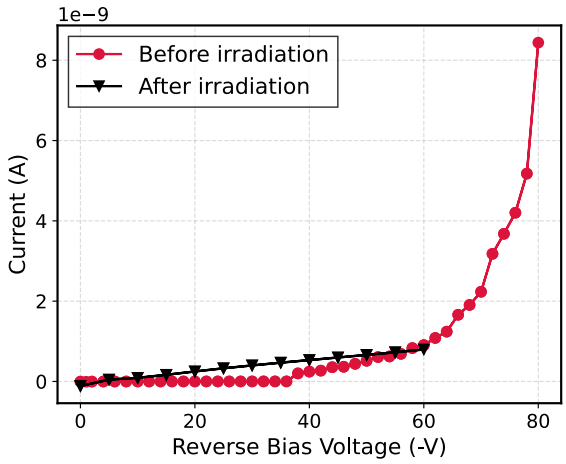

Figure 7.3.8: Dark I-V characterization. In black is represented the curve before any test (irradiation and IBIC), while in red the curve after all irradiations (both at room temperature and at high temperature).

Before starting the sensor damage test and the subsequent charge collection study, we studied the spatial uniformity of the charge collection in the sensor. By scanning the micrometric beam over a desired area, a homogeneous charge collection efficiency was recorded throughout the active area of the sensor. Moreover, the presence of the membrane and the boundary between the membrane and the rest of the sensor with the transmission beam were observed and identified. The reason of this can be related to the contribution of the charges released in the bulk. In the case of the membrane, the signal is only generated by the charges created in the 20 μm active thickness. In the presence of the bulk, however, although the active thickness is still 20 μm, a fraction of carriers generated in the bulk reaches the membrane by diffusion and consequently contributes to the signal. However, the relative difference between the two regions is lower than 10%.

Two regions were subsequently identified on the IBIC map: one on the membrane and one corresponding to the bulk. A study was conducted by varying the voltage from 0 V to 80 V in 5 V steps. Utilizing the channel-energy conversion previously described in Formula 7.1, the energy distributions for the two selected regions were analyzed as a function of voltage. The results are shown in Figure 7.3.9. It can be observed that for voltages starting from 15 V, the distribution is centered at 0.92 MeV, close to the nominal beam energy of 1 MeV. The difference is most likely due to the assumption of 100% efficiency of the reference STIM detector in the conversion formula, which realistically may be lower. In both cases, however, good spectroscopy properties were verified.

Subsequently, the acquired IBIC maps with 3.5 MeV were used to define regions of interest inside or outside the sensor membrane area for probing or inducing radiation damage. For this, small regions of the same sensor were selected. In fact, the facility makes it possible to study the effect of different irradiations on the same sample while keeping the overall properties and removing the uncertainty that there would be by using different sensors for different tests.

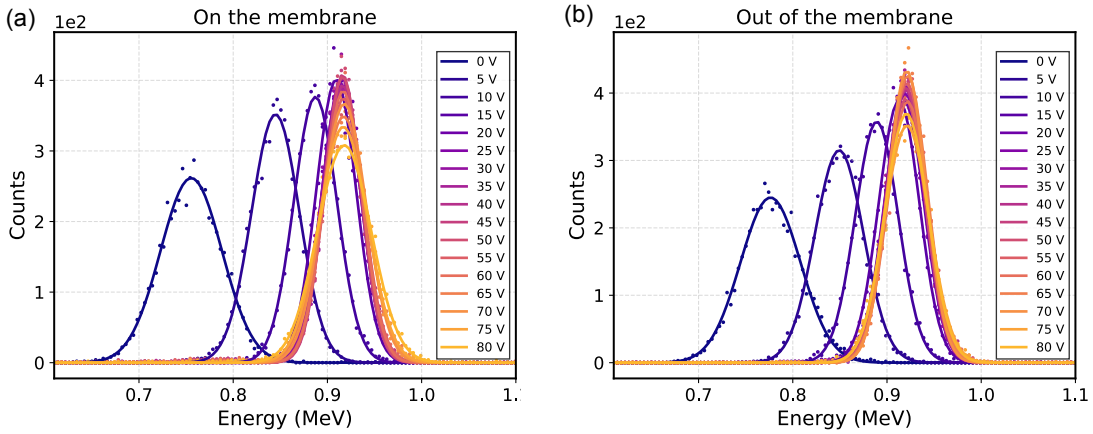

Figure 7.3.9: IBIC spectra obtained in two areas of the SiC sensor, in correspondence of the membrane (a) and the bulk (b) recorded at room temperature in different bias voltage conditions, from 0 V to 80 V.

Several square areas on the sensor surface were selected: four to be irradiated at room temperature and four to be irradiated at high temperature, using different beam fluences. Table 7.3 describes the fluences used to irradiate the sensor, the respective vacancies densities and the respective doses. The dose was obtained by multiplying the stopping power of a 3.5 MeV proton beam in water (107.4 MeV cm^2g^{-1}) by the irradiation fluence with which the sensor was damaged. During the irradiation, the beam was periodically intercepted (chopped) with a gold-plated aluminum sheet. The backscattered spectra collected from the chopper was then used to estimate the total deposited fluence during the irradiation. The chopper calibration setup was described in the [167], and the estimated statistical error of the number of ions is better than 5%. The beam was focused to a micrometer spot size and scanned over the desired rectangular detector region. Therefore, both number of ions and irradiation area size were well defined and used to estimate the irradiation fluence.

Table 7.3: Fluences used to irradiate the sensor at both room and high temperatures, with a 3.5 MeV proton beam (transmission beam). Four fluences were chosen both at room temperature and at high temperature. Respective vacancies densities and the doses are also reported.

	First Fluence	Second Fluence	Third Fluence	Fourth Fluence
Fluence (cm^{-2})	5×10^{12}	8×10^{12}	1×10^{13}	5×10^{13}
Vacancies density (cm^{-3})	9.94×10^{11}	1.59×10^{12}	1.99×10^{12}	9.94×10^{12}
Dose (Gy)	8.6×10^{4}	1.38×10^{5}	1.72×10^{5}	8.6×10^{5}

Initially, we irradiated the 4 zones by subjecting the sensor to high temperature (500°C), and then the operation was repeated at room temperature, selecting different areas from the previous ones. Figure 7.3.10 shows an IBIC map (at 7.5V) acquired after all induced damage. The irradiated regions of the sensor are evidently identifiable, showing lower CCE. As expected, under these conditions it is not possible to distinguish the membrane from the bulk because the energy deposited over the bulk is the same as for the membrane. The regions identified in the figure with A and B correspond to regions on the bulk of the sensor (at

room and high temperature). Zones *C* and *D* are located on the membrane.

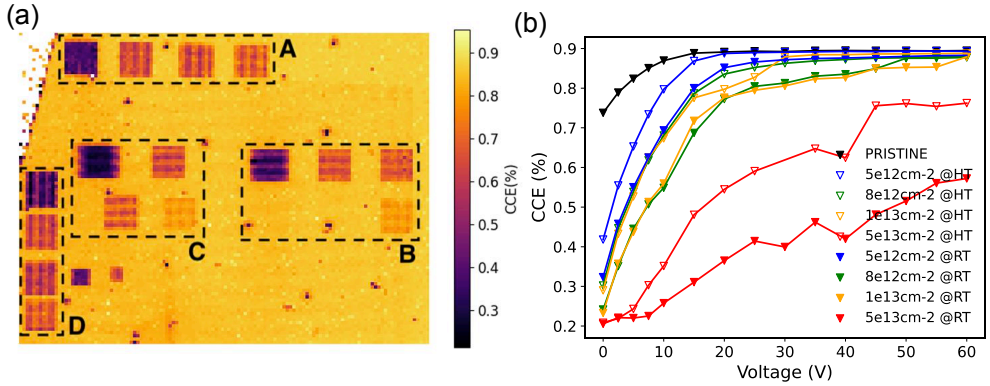

Figure 7.3.10: (a) IBIC map acquired at 7.5 V on the sensor region containing the damaged areas. The framed areas in the *A* region were irradiated at room temperature, and the *B* areas at 500°C, both on the bulk. *C* and *D* areas are located on the membrane irradiated at room temperature and 500 °C respectively. The colorbar on the right shows the CCE values. (b) CCE as a function of the applied bias voltage. Different colors indicate different irradiance fluences, full markers indicate measurements performed in *A* region (room temperature), while empty ones indicate *B* region (500°C).

The charge collection efficiency, obtained with the IBIC technique at room temperature at the lower energy beam (1 MeV) , in the differently irradiated areas has been studied to observe the effect of the different damaging conditions. Furthermore, the signal was studied at different bias, in a range between 0 V and 60 V, by steps of about 5 V each. The overall results are shown in Figure 7.3.10 (b), where also data obtained from a non-irradiated area (labeled as pristine) is shown. A total charge collection (100%) is never achieved, and this is due to the basic assumption we made for the reference silicon STIM detector used for calibration: it may not collect exactly 100% of the charge and this would lead to an increase in the CCE evaluated here. As expected, the higher the irradiation fluence, the worse the charge collection efficiency. The results demonstrate also, for the first time to our knowledge, the effects of the dynamic annealing on the CCE, proving higher collection efficiencies in the areas damaged at high temperature (empty markers) as compared to areas damaged at room temperature (filled markers) for all fluences tested,indicating less radiation damages at 500°C. This result confirms what had previously been assumed: under high-temperature conditions (in which silicon carbide has been shown to work properly), the sensor is able to sustain more irradiation fluences than in the standard, room temperatures, conditions, i.e. dynamic annealing succeeds in partially recovering the crystalline structure of silicon carbide, leading to lower creation of radiation damage along the thickness of the device through which it passes extending the roughness of the SiC sensor. The difference in CCE between those areas varies between about 20% (for low voltages) and 5% for higher voltages applied. Charge collection efficiency always exceeds 80% above 30 V (except for the higher fluence damaging). This indicates a good recovery despite the damages, except for the two most intensely damaged zones (in red). For the first irradiation, the curve reaches 90% of CCE, indicating, also in this case, a higher CCE for irradiations at 500°C.

One of the potential features of this sensor is the presence of the thin membrane (20 μm in this case). The next goals in our work include characterizing the membrane, comparing its performance with the bulk, and investigating the effects of this on the internal electric field and thus on its charge transport properties. In these tests all damages were done at room temperature. A first step in this future work was done at the RBI in conjunction with the tests just described. To this end, seven more zones were selected in another region on the sample, four within the membrane (*F* zones) and three outside (*E* zones) and irradiated at room temperature using the beam parameters described in Table 7.4. The total IBIC map measured after the irradiation is shown in Figure 7.3.11 (a).

Table 7.4: Fluences used to irradiate the sensor inside the membrane and on the bulk, with a 3.5 MeV proton beam (transmission beam). Four fluences were chosen, and the highest one was used just on the membrane. Respective vacancies densities and the doses are also reported.

	First Fluence	**Second Fluence**	**Third Fluence**	**Fourth Fluence**
Fluence (cm^{-2})	6×10^{11}	3×10^{12}	5×10^{12}	1×10^{13}
Vacancies density (cm^{-3})	1.19×10^{11}	5.96×10^{11}	9.94×10^{11}	1.99×10^{12}
Dose (Gy)	1.03×10^{4}	5.16×10^{4}	8.6×10^{4}	1.72×10^{5}

Observing the curves of Figure 7.3.11 (b), where the CCE as a function of the applied bias voltage to the sensor for the different irradiation conditions (also two non-irradiated regions labelled as pristine) is reported, it is clear that the areas selected over the membrane (crosses markers) measure a higher charge (higher CCE) as respect to the areas irradiated over the region with the bulk (triangle markers) at the same irradiation fluence. This result may be partially caused by backscattering events coming from the bulk, which may create more damage on the active thickness of these regions. However, the main reason is more likely to be related to the electric fields established with/without the bulk, which may modify the carrier transport properties. This phenomenon has yet to be fully understood, but it opens the way to a new branch of research in which *SiC membranes* play a leading role in various applications involving strong radiation damaging conditions.

7.3.3 Conclusions

In summary, a *SiC membrane* sensor with a thickness of 20 μm on the membrane (and 370 μm on the bulk) was subjected to several irradiation tests at the Ruder Bošković Institute, specifically within the Ion Microprobe Chamber facility. The ability to deliver a micrometer beam was exploited to study the transport properties of the sensor locally, subjecting the sample multiple irradiation doses at two temperatures (RT and up to 500°C). The uniformity of the sensor surface fabricated by SenSiC was verified for the first time by observation of homogeneous collected charge over the studied areas. After different irradiations, higher charge collection efficiency was observed for areas damaged at high temperatures than those irradiated at room temperature, suggesting that SiC radiation hardness might be further enhanced by operating the sensors in high-temperature operating conditions. Furthermore, preliminary results suggest that sensors on

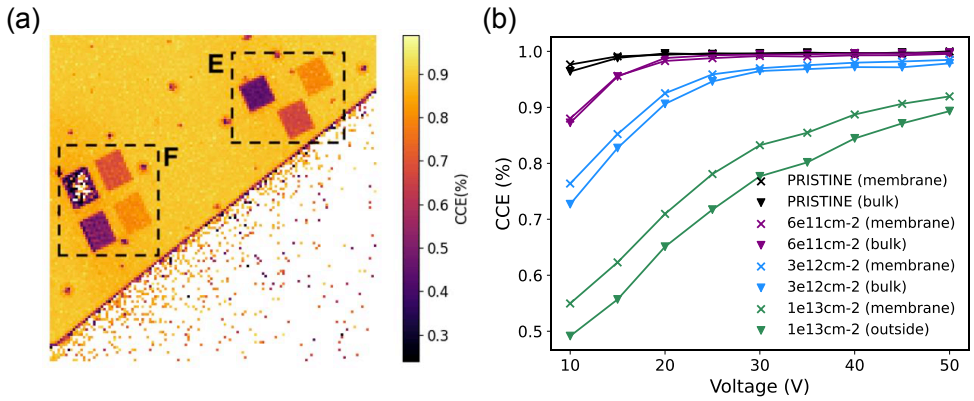

Figure 7.3.11: (a) IBIC map acquired at 10V on the sensor region containing the damaged areas. The framed areas in the *E* region were in the bulk and the *F* areas were on the membrane.The colorbar on the right shows the CCE values. (b) Charge collection efficiencies as a function of the applied bias voltage. Different colors indicate different irradiance fluences, Triangle markers indicate *E* regions, crosses indicate *F* regions.

free-standing membranes could benefit from higher radiation hardness as compared to standard 'bulk' ones. Additional beamtimes in the facility are planned, both to further investigate membrane properties and to test other comparable sensors with ultra-thin membranes (2 μm and 200 nm are already available for testing). Simulations will also be needed to study the physical phenomena that regulate the behavior of charges along the membrane subjected to ultra-high dose deposition beams.

7.4 SiC free-standing membranes as XBPM detectors

In this chapter, a study is described that explores the potential of ultra-thin (< 1 μm) Silicon Carbide (SiC) free-standing membranes, produced by SenSiC STLab, as beam intensity and position monitors for X-ray beamlines. Initial experimental assessments were conducted at the NanoMAX facility at MAX IV, the Swedish national synchrotron laboratory, to evaluate the performance of these ultra-thin devices in monitoring tightly focused (< 1 μm FWHM) 8 keV X-ray beams. To gain a deeper understanding , Sentaurus TCAD simulations were employed alongside experimental investigations. This approach allowed for a detailed analysis of the limitations of the 4-quadrant design and the potential benefits of alternative resistive-type XBPM sensors.

This work is described in a paper (under review) for which I am the lead author:

Ultra-thin Silicon Carbide Free-standing Membranes as Beam Intensity and Position Monitors for X-ray Beamlines, *Journal of Synchrotron Radiation*, 2024

and fits into the context of X-ray position and flux monitoring.

Synchrotron beamlines are highly versatile tools for a wide range of scientific measurements utilizing X-rays, including X-ray absorption and dichroism, which are essential for probing the electronic and magnetic properties of materials. These facilities stand out due to their capability to continuously tune the photon energy with high resolution, their broad energy range, coherency and high brilliance. Among the accessible X-ray energies, of particular significance is the soft X-ray range spanning from 400 to 1600 eV, which includes critical edges such as L2, 3 and M4, 5 of transition metals and rare earths. Many synchrotron facilities operate dedicated beamlines for X-ray absorption experiments within this energy range. To ensure accurate and quantitative analysis of the X-ray absorption data, it is crucial to precisely monitor the photon flux impinging on the sample. This flux can significantly fluctuate with factors like the storage ring current and incoming light polarization. As a result, these beamlines are often equipped with specialized beam intensity monitors (BIMs) as the final optical component before the sample. A successful BIM should exhibit linearity of the signal in relation to the transmitted beam, offer a substantial monitor signal akin to the sample signal, and simultaneously maintain a high beam transmission ratio without distorting the beam shape.

Currently, Beam Intensity Modulation (BIM) technologies for soft and tender X-ray beams predominantly utilize “gold-meshes” and “Diamond conductive thin films” [168, 169, 170]. A critical limitation of these sensors is their lack of positional information, as neither the structure of the gold meshes nor the diamond conductive thin films allow for spatial tracking of the transmitted beam. This tracking is essential for an active feedback loop to compensate for beam position drifts, which helps maintain a more stable intensity on the sample.

Furthermore, mesh-based BIM technologies, such as those employing gold meshes, face notable challenges, particularly the amplification of diffraction effects as beam sizes decrease, leading to distortions that compromise signal linearity. Additionally, these technologies have low quantum efficiency, generating

low signals, resulting in low monitoring accuracies. These constraints collectively impeded the suitability of these sensors as BIM and beam position monitor (BPM) technologies, prompting a thorough exploration of alternative approaches to enhance signal fidelity and obtain spatial information.

Recently, Silicon Carbide (SiC) free-standing membranes have found applications as Beam Position Monitoring (XBPM) for hard X-rays, serving as a substitute for Diamond CVD membranes. These SiC XBPM membranes, available in thicknesses of 2 μm, 10 μm, and 20 μm [160, 171]. Compared to inline Diamond XBPMs [172], Silicon Carbide (SiC) XBPMs, due to their shorter attenuation lengths [173], must be significantly thinner to achieve similar transparency. Specifically, SiC XBPMs need to be about 10 times thinner. The thinnest available Diamond XBPM is currently 20 μm, which causes excessive absorption in the soft and tender X-ray ranges.

This study presents an experimental and theoretical evaluation of ultra-thin, free-standing SiC membranes (< 2 μm), equivalent to < 20 μm Diamond XBPMs, as an innovative solution for beam position and intensity monitoring. The goal is to assess the potential and limitations of these devices compared to gold and diamond (BIM and BPM) sensors. Additionally, the application of Synopsys Sentaurus TCAD, a powerful device simulator [120], is explored in order to investigate and compare alternative layouts to "standard ones" based on arrays of electrically independent 2 $\times$ 2 diodes. Specifically, we simulate and compare standard sensors, considering different possible geometries, with Resistive-XBPM (rXBPM) sensors, which incorporate a resistive layer between the active thickness of the device and its readout electrodes (see Figure 7.4.4) thus connecting the 2 $\times$ 2 diodes through high-resistance transmission lines. In rXBPMs, the charges generated by incident radiation move in proportion to the resistivity they encounter, and the presence of a resistive layer means that the charge is shared between the pads based on the resistivity towards the four electrodes which, in turn, is related to the charge-to-electrodes distance. This structure makes it possible to increase the fill factor and overcome problems of charge collection loss in the gap between the electrodes, improving spatial resolution with large readout pitch. The signal spreads across the resistive layer and becomes visible in the readout pads with an intensity that decreases as a function of the distance between the pads and the center of the X-ray beam. Resistive sensors can thus be compared to current dividers, in which the branch of the divider corresponds to the resistance of the triangular area connecting the point of impact to each of the neighboring pads [174]. The position of the beam on the sensor surface can then be reconstructed as the 2-dimensional center of gravity of the signal intensity at the electrodes. Devices of this type have already been tested both with silicon, such as Position Sensitive Detectors (PSDs) [175, 176, 177, 178] or DC-RSD [176], and with diamond [179, 180].

Silicon carbide sensors based on this technology have not yet been studied, and first tests and simulations are given in this work.

7.4.1 Materials and methods

4-quadrant XBPM sensor at NanoMAX nanoprobe

The "4-quadrant" XBPM sensor consists of four independent diodes, in the specific case considered 4H-SiC Schottky diode, characterized by a 375 μm thick n^-type (doping concentration: $\sim 10^{18}$ cm^{-3}) substrate, and a nominally 250 nm thick n^-type epitaxial layer (doping concentration: $\sim 5 \times 10^{13}$ cm^{-3}). The peculiarity of the sensors presented here is that the n^+ layer is locally removed by an electrochemical doping-selective etching process, creating a thinned-down area in a selected region of the sensor (referred to as free-standing membrane regions). The sensor used in this work has 4 readout pixels on its surface, each spaced 6 μm apart, to monitor the position of the beam as a function of the current measured on each of the pixels and a free-standing central membrane of 2 mm diameter (see Figure 7.4.1).

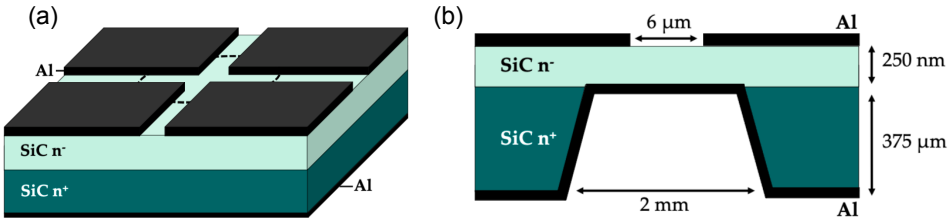

Figure 7.4.1: (a) The 3D structure (not to scale) of an XBPM SiC device is shown, featuring an n^-type layer and a thick n^+ substrate. The central region around the four pads (circular area of approximately 2 mm in diameter) is thinned using electrochemical dopant-selective etching. (b) A 2D cross-section of the device (not to scale), showing the distance between the readout pixels (6 μm), the thickness of the n^-type epitaxial layer (250 nm), and the n^+ substrate (375 μm).

The first experimental characterization of the lateral resolution of these ultra-thin SiC XBPM is performed at the NanoMAX beamline at MAX IV [181, 182]. This beamline features a unique nanoprobe experimental endstation, delivering highly-focused, sub-micrometer spots, ideal for a detailed characterization of the lateral signal response of the thin SiC membranes.

In this test, to work at the ideal beamline configuration, we used 8 keV photons and studied the difference between the currents generated at the four electrodes when crossed by the beam was studied. The experimental setup used is represented in Figure 7.4.2.

Device simulations were performed using Synopsys Sentaurus TCAD, to study the charge collection efficiency (CCE) as a function of the position of the beam on the device. Specifically, the software version V-2023.12 was used, and the built-in 4H-SiC model from the Synopsys Sentaurus TCAD material library was employed.

For such simulations, a simplified, 2-dimensional sensor geometry was implemented using the built-in 4H-SiC model from the Synopsys Sentaurus TCAD material library. A 4H-SiC doped with a low nitrogen density of 5×10^{13} cm^{-3} was included between a uniform cathode on one side and two symmetrical anodes at the edges of the opposite side. The simulated sensor had a width of 10 μm, with thicknesses varying from 100 nm to 6 μm to account for the effect

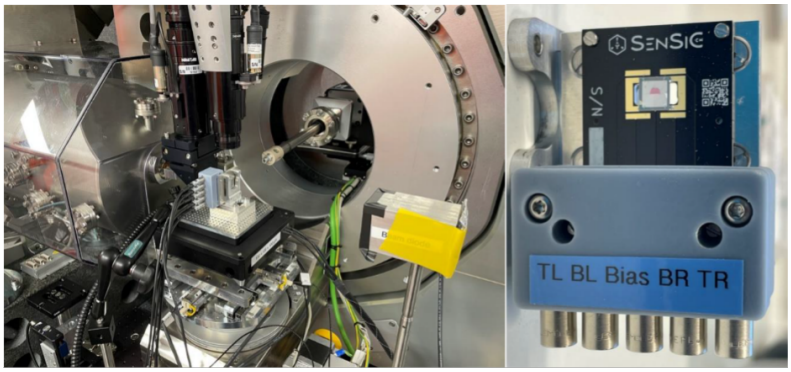

Figure 7.4.2: Pictures of the experimental setup at the MaxIV Institute. The SiC sensor is mounted in the Hard X-ray monochromatic nanoprobe experimental station (NanoMAX).

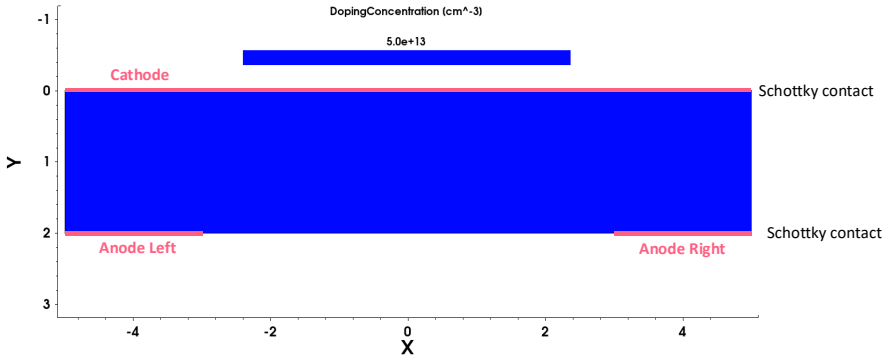

Figure 7.4.3: The 2D Geometry of the simulated standard XBPM sensor. The represented sensor has a width of 10 μm, a thickness of 2 μm, and a distance between anodes of 6 μm. The three electrodes are defined as Schottky contacts specifying the metal work function equal to 4.8 eV.

of membrane thickness, and the distance between anodes ranged from 100 nm to 9 μm to evaluate the impact of inter-pad spacing. The three electrodes are defined as Schottky contacts specifying the metal work function equal to 4.8 eV. An example of a simulated sensor geometry is shown in Figure 7.4.3. In the simulations, the *ComputeFromMonochromaticSource* model was used, which activates the computation of optical generation for a single specified wavelength. A highly collimated 8 keV X-ray beam with a full width at half maximum (FWHM) of 100 nm $\times$ 100 nm, and a photon flux of 1×10^{12} photons/s was simulated. A beam scan is performed by moving the center of the Gaussian beam horizontally across the XBPM, from one anode to the other. The response of the sensor to changes in sensor thickness and bias voltage was investigated. The results of studies carried out using simulations are described in the next section.

Resitive-XBPM sensor at CNR-IMM Laboratory

A preliminary study of the Resistive-XBPM device is also reported in this work.

First, the response of the sensor to changes of the doping concentration of the resistive layer was investigated through TCAD Sentaurus simulations. The 2D simulated geometry of a Resistive-XBPM is illustrated in Figure 7.4.5. It includes a

thin (100 nm) continuous p^+-doped resistive layer positioned beneath the anodes, which are 2 μm in length and configured as Ohmic contacts. A parametric study was conducted by varying the doping concentration of the resistive layer over a range from 10^{14} cm^{-3} to 10^{18} cm^{-3}.

The first prototype by SenSiC is featured on an active layer of 1.5 μm of n^-doped SiC, with a resistive layer of 0.3 μm thickness doped with p^+ positioned between this active layer and the contacts. A schematic of the resistive-XBPM devices is shown in Figure 7.4.4. In the tested prototype, however, the membrane is not yet present. It was tested at the CNR-IMM Laboratory in Catania (Italy). For this, a UV photon source at 325 nm (3.81 eV) was employed which is focalised down to a spot of size of 200 μm, and a power of 12.5 mW, equivalent to a photon flux of 2×10^{16} photons/s (see Figure 7.4.6). By scanning the beam between the two electrodes, spaced 10 mm apart, currents at the respective contacts were recorded using a four-channel pico-amperometer. For this measurement the sensor was inversely polarized at 5 V.

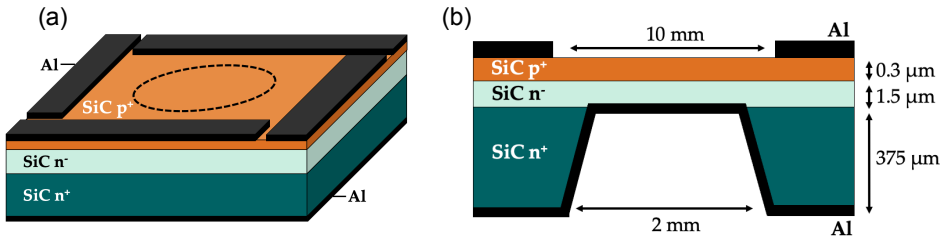

Figure 7.4.4: The structure a Resistive-XBPM SiC device is shown: a p^+ layer is added on top of the n^- layer. The area framed by a dotted line is that reproduced in TCAD simulations.

7.4.2 Results and discussion

4-quadrant XBPM sensor: measurements and simulation results

The first experimental characterizations of the SiC XBPM using highly focused (110 nm $\times$ 110 nm) 8 keV X-rays performed at MAX IV led to the results described below. The high ratio between the size of the gap and the thickness of the device raises concerns about the possibility of inefficiencies in position measurements in the central region of the gap. Figure 7.4.7 (a) shows the measured current, of each of the 4 electrodes on the SiC XBPM with a nominal active thickness of 250 nm and a 6 μm electrode gap. Figure 7.4.7 (b) shows the sum of the measured current from the 4 electrodes. In regions where no electrode is present, little or no current is measured, indicating substantial loss of charge collection efficiency. Within the electrodes the measured current shows small local variations, indicating that the sensor material has an internal grain structure or varying thickness. To further understand the response of the sensor as a function of the applied bias, an experimental investigation was conducted by varying the bias voltage applied to the sensor, thereby modifying the internal electric field. In Figure 7.4.8 the currents of two opposing channels are plotted against the beam position for three different bias voltages: (a) 2.5 V, (b) 10 V, (c) 15 V. A current peak is observed

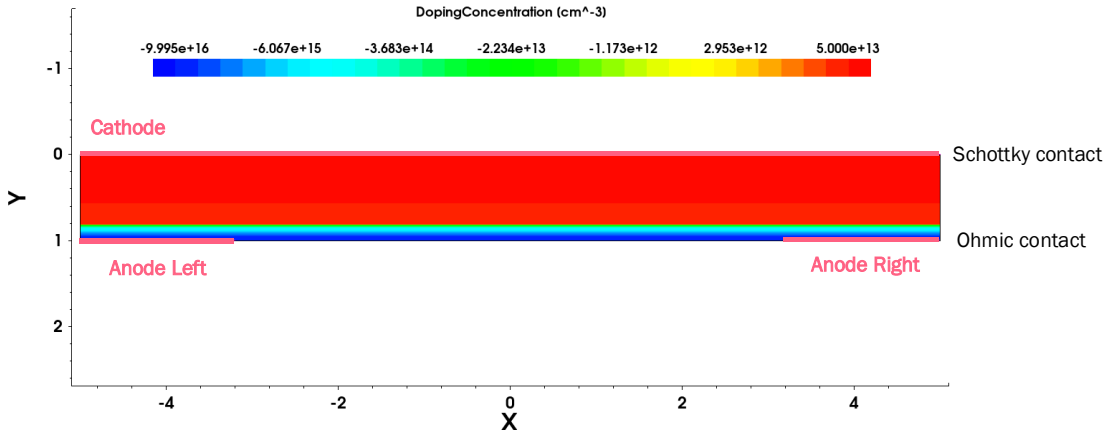

Figure 7.4.5: The 2D simulated geometry of a Resistive-XBPM is presented. The sensor features a thickness of 1 μm and includes a 100 nm thick p^+-doped resistive layer located beneath the anodes, which are configured as Ohmic contacts.

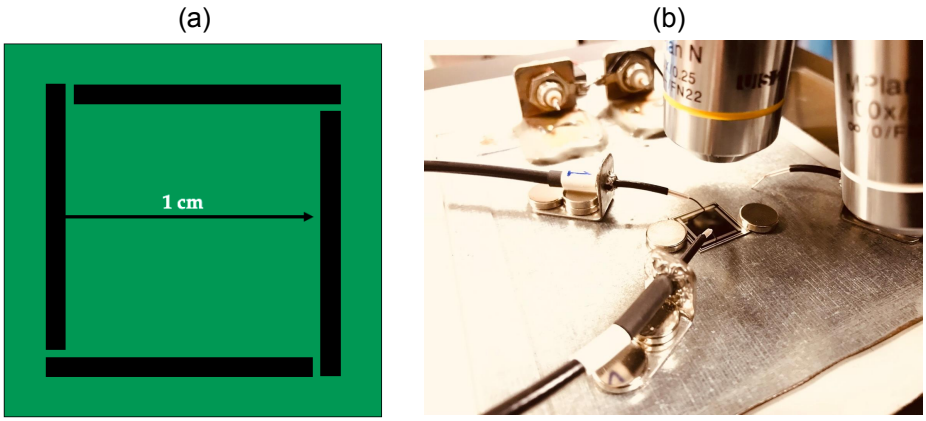

Figure 7.4.6: The experimental setup used for measurements at the CNM-IMM laboratories in Catania, Italy. (a) the schematic of the sensor is shown, where the contacts are spaced 1 cm apart. (b) First prototype of the Resistive-Type XBPM sensor is visible in the probe station.

experimentally at the electrode's edge, and this peak increases with increasing bias voltage. Considering the thickness of the sample under examination (250 nm), the bias voltages at which this peak is observed (10 V and 15 V) correspond to electric field values of 400 kV/cm and 600 kV/cm, respectively. These results suggest that thin membranes, thinner than the inter-pad distance, can have a deleterious effect on the charge collection efficiency of the devices, highlighted by the use of focused X-ray beams.

In order to consolidate these experimental results, a study on XBPM devices was conducted through simulations using TCAD Sentaurus software. Simulations yield the results shown in Figure 7.4.9.

By scanning a highly collimated beam (FWHM of 100 nm $\times$ 100 nm) across two anodes of the sensor, less current is observed in the gap between the anodes, which confirms the observed experimental results (Figure 7.4.7). This effect was studied as a function of the device thickness. The plot in Figure 7.4.9 (b) shows the total current, calculated as the sum of the two currents of the anodes, which

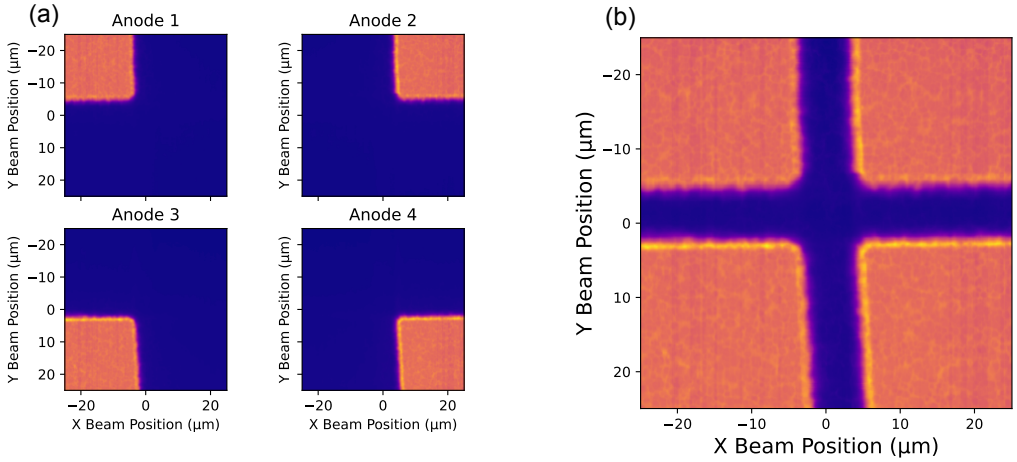

Figure 7.4.7: (a) Current measured on the individual sensor electrodes (Anode 1, Anode 2, Anode 3, Anode 4) when scanning an 8 KeV X-ray beam on its surface. (b) Total current measured on the sensor computed as the sum of the individual electrode currents.

represents the total collected signal generated in the sensor. In this case, an electric field of 20 kV/cm was set in the simulation. It can clearly be seen that when the beam is in the region between -3 μm and +3 μm, the current is reduced by more than 80% for thicknesses of less than 500 nm. As the thickness increases, this effect diminishes, until complete charge collection is achieved for thicknesses of the same order of magnitude as the gap.

The charge collection efficiency (CCE) was evaluated from the simulations as the ratio between the integral of the current in the case of a hypothetical complete collection and the integral of the evaluated current. The results are shown in Figure 7.4.10 (a) where the CCE is represented as a function of the ratio "Gap/Thickness" for 3 simulated electric field values (5 kV/cm, 20 kV/cm and 50 kV/cm). As expected, a higher electric field allows achieving higher collections, but there is a limit to it. Observing the figure, it can be seen that the CCE in the case of an electric field of 5 kV/cm exceeds 60% when the "Gap/Thickness" ratio is approximately less than 4, whereas for an electric field 10 times higher (50 kV/cm) at the same value, charge collection is already almost complete (approximately 100%). These results underscore the complexities involved in monitoring highly collimated beams using sensors characterized by gaps and thicknesses comparable to those previously mentioned.

The challenge becomes more pronounced when dealing with very thin sensors. In such cases, precise beam position tracking is only achievable when the FWHM of the beam is significantly greater than the width of the charge collection loss zone. In such a condition a portion of the signal is inevitably captured by the anodes, even when the beam is precisely centered within the gap, so that position sensitivity is still achieved, though at lower lateral sensitivities. However, while the beam position can be monitored, no reliable intensity monitoring is possible due to the loss of signal in the gap.

Similarly to the scans across two electrodes, the signals at very high electric fields have been studied. Figure 7.4.10 (b) shows the individual anode current normalized to the current measured on the metal anode, under different electric

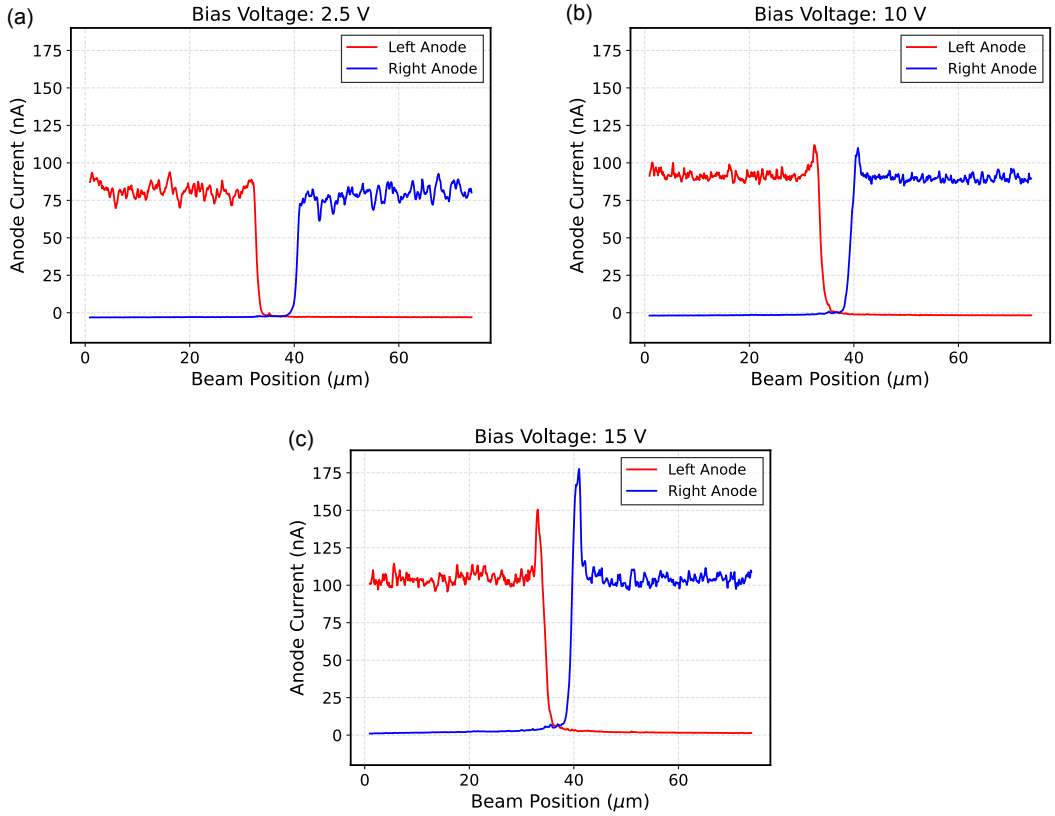

Figure 7.4.8: Current measured on two channels (Left Anode and Right Anode) as a function of beam position for 3 different bias voltages: (a) 2.5 V, (b) 10 V, (c) 15 V.

field conditions. In this case, the sensor thickness is 100 nm. It can immediately be seen that an anomalous current rise occurs at the edge between the anode and the central gap when increasing the electric field, consistently with what is observed experimentally. This effect is due to edges of the metals which results in a local electric field increase and consequent internal charge amplification by avalanche effect. In previous simulations, this effect did not arise because lower electric fields were considered.

Despite the results just described and upon closer examination of the Figure 7.4.9, it can be observed that the thinner the sensor, the quicker the current drops when transitioning from a region where on-anode to a region off-anode (corresponding to positions -3 μm and +3 μm on the horizontal axes of the plots). This effect is due to the lower diffusion, i.e. spreading, of carriers in thinner sensors. This effect can be advantageous for various applications, such as on-off monitoring of the position of even highly collimated beams. The charge spreading width for thin sensors was quantified as the FWHM of the Gaussian obtained by twice differentiating the current as a function of beam position, comparable to an error function. The simulation results are shown in Figure 7.4.11. The FWHM determined using this method approaches the simulated beam FWHM (100 nm) asymptotically when thinner sensors are employed. However, even with a sensor thickness of 50 nm, there is an overestimation of the beam dimension. Based on these results, in order to accurately extract the beam FWHM, it is recommended

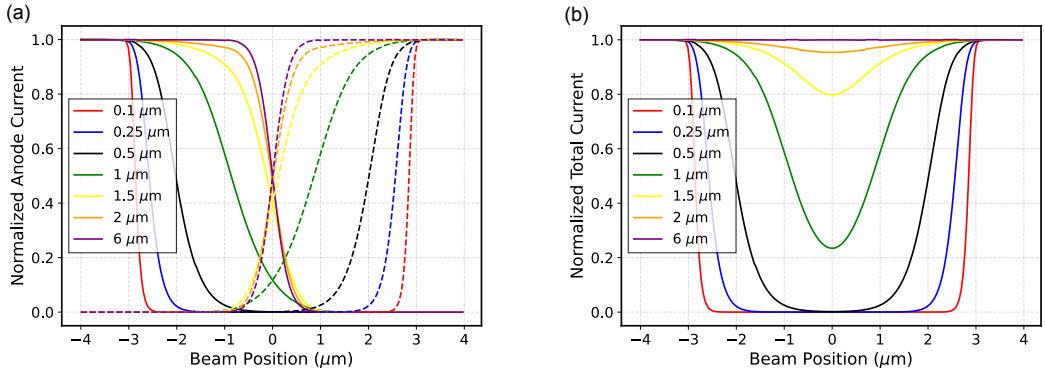

Figure 7.4.9: (a) Normalized current of left (solid line) and right (dashed line) anodes obtained from simulations. (b) Total current (sum of the current of the two anodes). The currents are shown as a function of the position of the X-ray beam, for different thicknesses.

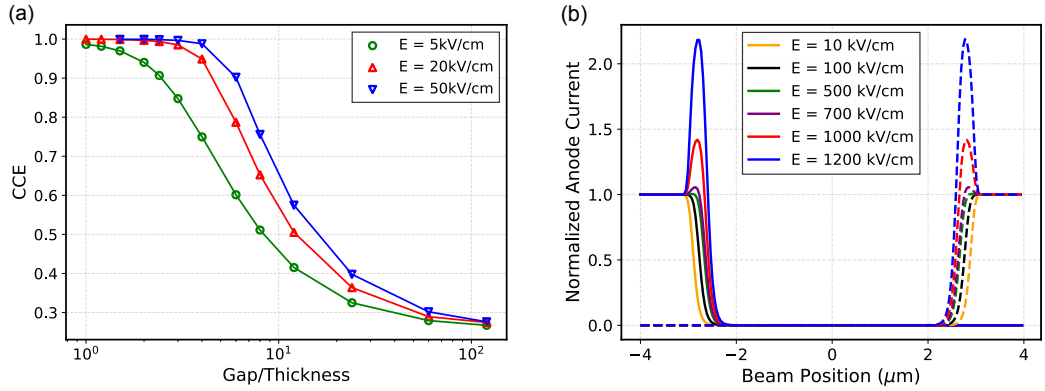

Figure 7.4.10: (a) Charge collection efficiency for 3 simulated electric field values (5 kV/cm, 20 kV/cm, 50 kV/cm) as a function of the ratio Gap/Thickness (b) Simulated current of left (solid line) and right (dashed line) anodes as a function of beam position, for different high electric field values (between 10 kV/cm and 1200 kV/cm)

that the sensor thickness should be at least 10 times smaller than the FWHM.

Resistive-XBPM sensor: measurements and simulation results

Considering the relevance of the effects observed with the simulations on standard 4-quadrant XBPM, a lower CCE of the device between the electrodes and an important distortion of the electric field in the metal-SiC edge at high voltages, an alternative technology was studied through Sentaurus TCAD theoretical simulations: the resistive-XBPMs.

As mentioned in the previous section, in these sensors a highly resistive layer is added to act as a resistive layer between the substrate and the electrodes (see Figure 7.4.4). As previously explained, this configuration enables improved spatial resolution with large pitches between the readout channels. To this end, while maintaining the same overall geometry for the sensors in the TCAD simulations, a thin (100 nm) and continuous p^+-doped resistive layer was included immediately below the anodes. The anodes, 2 μm in length each, were configured as

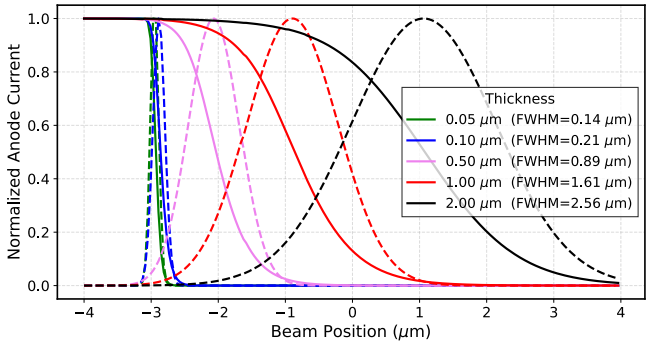

Figure 7.4.11: Simulated anode currents as a function of beam position measured from one anode (solid lines) for different sensor thickness and their respective double differential (dashed lines). The current values are normalized.

Ohmic contacts. For a device with an active thickness of 1 μm, a study was made varying the doping concentration of the resistive layer, in a range between 10^{14} cm^{-3} and 10^{18} cm^{-3}. The simulation results, shown in Figure 7.4.12 (a), show that for sufficiently high doping concentrations ($> 10^{16}$ cm^{-3}), the trend in the current measured in the individual anodes depends linearly on the distance of the beam from the anode and that no CCE loss is observed at the center.

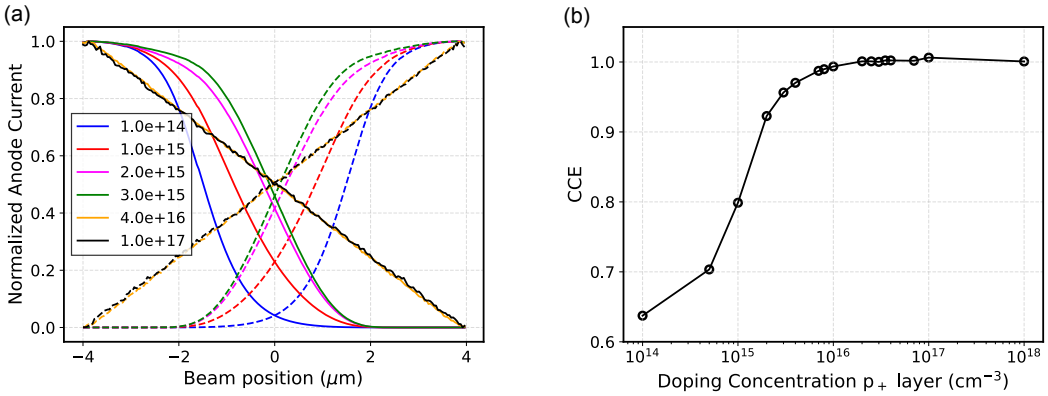

Figure 7.4.12: (a): Electrodes simulated current for resistive-XBPM for different values of p^+ resistive layer doping density (from 10^{14} cm^{-3} to 10^{17} cm^{-3}). (b) Simulated CCE as a function of the p^+ resistive layer doping density for Resisitve-type XBPM devices.

Charge collection efficiency (CCE) was evaluated again as the ratio of the integral of the total current measured on the two electrodes, normalized by the integral of the current assuming that the sensor measures over the entire surface of the device as above the electrode. The results are illustrated in Figure 7.4.12 (b), showing that for all dopant concentrations examined, the CCE exceeds 60 %, reaching values compatible with 100 % for dopant concentrations above 10^{16} cm^{-3}. Finding the correct doping for this to happen before starting to lose charge collection is necessary for different geometries. To validate the simulations results, an experimental measurement was conducted on the first prototype of a Resistive-type XBPM sensor at the CNR-IMM laboratories in Catania, demonstrating its ability to measure a position$^-$dependent signal at the electrodes. The sensor,

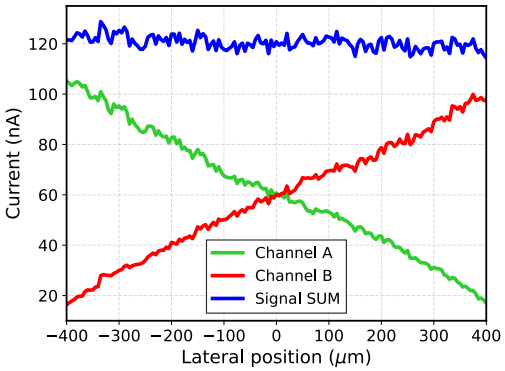

Figure 7.4.13: Measured anode currents from the first Resistive-type XBPM prototype. The total current is also shown (blue data).

featuring an active thickness of 10 μm and a resistive p^+ layer of 0.3 μm, was exposed to a UV photon beam at 325 nm (flux: 2×10^{16} photons/s). Two 1.5 μm-thick aluminum electrodes, positioned 10 mm apart and with an intrapad resistance of 33 kOhm, were connected to a four-channel pico-amperometer (PCR4 [183]). As illustrated in Figure 7.4.13, currents at the left and right anodes range from 20 to 100 nA, depending on the position of the UV beam with respect to each electrode position. This measure reveals a distinct positional dependence of the collected current from the incident beam. The sum of the two currents is constant, of the order of 120 nA. Considering that in this device the membrane is not yet existing, it is expected that in a thinned prototype there will be a constant current only across the membrane (a few mm), and an increase in current outside the membrane area.

7.4.3 Conclusions

Silicon carbide (SiC) sensors are emerging as a promising alternative to current technologies for X-ray position and intensity monitoring. Two technologies developed by SenSiC have been explored in details for these purposes: standard "4-quadrant" XBPM (X-ray Beam Position Monitor) devices, featuring ultra-thin Schottky diodes, and Resistive-XBPM devices, incorporating a resistive layer between the active SiC material and the readout electrodes. Experimental investigations into their performance were conducted under 8 keV X-ray beams at the Swedish MAX IV institute, particularly at the NanoMAX monochromatic nanoprobe, and under UV light at CNR. The experimental results were compared with the respective simulations using Synopsys Sentaurus TCAD software.

Simulations revealed that XBPM devices effectively monitor highly focused 8 keV X-ray beams (110 nm $\times$ 110 nm) only when the gap between electrodes is comparable to the detector thickness. When this condition is not met (i.e., the Gap/Thickness ratio exceeds 1), as in the case of device tested experimentally, a lower total current is collected across the gap, resulting in a charge collection efficiency (CCE) loss. Another observed experimental effect is a current peak at the metal-SiC edge for high voltages, attributed to a localized increase in

the electric field. Position reconstruction for highly collimated beams is thus challenging and possible only for beams with a FWHM greater than the gap between the electrodes or for sufficiently thick sensors.

With the aim of addressing these limitations, first Silicon Carbide Resistive-XBPMs were studied and fabricated. It was observed that by adding a highly doped resistive layer (exceeding 10^{16} for a 1 μm thick active sensor), a single electrode collects a current linearly proportional to the beam distance. This enables an effective position reconstruction without compromising charge collection. A preliminary resistive-XBPM prototype was fabricated and subjected to initial experimental validation at the CNR-IMM laboratories in Catania. The results indicated a correlation between the signal from the two anodes and the beam position, while maintaining a constant total current. The test was conducted using only two of the four pads to facilitate a more effective comparison with simulation results. An enhancement of the experimental setup is planned, which will involve measurements using all four channels and X-rays as the source. Further simulations will be conducted to determine the optimal doping value for each device geometry.

Chapter 8

Conclusions

The work I performed in last three years aimed at contributing to the research in the field of UHDR irradiations from two points of view: the upgrade of a clinical LINAC to deliver UHDR electron beams, and the study of multiple solid state technologies as possible beam monitors.

The Elekta SL 18 MV LINAC has been successfully modified to deliver UHDR electron beams at 10 MeV. These modifications are fully reversible, allowing for rapid switching between conventional and UHDR modes in only a few minutes. The LINAC now achieves a maximum of 2.2 Gy/pulse and an instantaneous dose-rate exceeding 10^5 Gy/s at the crosshair foil position (SSD = 52.9 cm), with a pulse duration of 2 μs. A silicon sensor monitors the pulse stability and reproducibility across different beam deliveries and days. In the future, this LINAC may serve as a platform for testing beam monitoring and dosimetry devices, as well as for radiobiological experiments to further investigate the FLASH effect. Applicators with varied geometries, including perforated models, may facilitate studies on spatially fractionated radiotherapy (SFRT) and its combination with UHDR irradiation.

Three solid-state technologies were extensively studied as potential alternatives to ionization chambers for UHDR beam monitoring. Specifically, silicon pads with active/total thicknesses of 30/655 μm or 45/570 μm and areas of 2 mm^2, 1 mm^2, and 0.25 mm^2 were investigated on electron beams delivered by the ElectronFLASH machine of Pisa. Multiple measurements were conducted up to very high dose-rates of $2.5 \cdot 10^6$ Gy/s, corresponding to approximately 10 Gy in pulses of 4 μs duration. Results exhibited good linearity ($R^2 > 0.99$), and measurements of the charge were consistent between the oscilloscope and the TERA08 front-end electronics.

The results obtained by splitting the sensor output across all 64 channels of the TERA08 chip suggest that adapting the chip to read multiple silicon pads or strips could expand the sensitive area of the beam monitoring device. In this context, work was conducted on a segmented sensor of 146 strips, 128 of which were connected to two 64-channel readout electronics systems, effectively covering an area of 2.6×2.3 cm^2, smaller than the total sensor area of 2.6×2.6 cm^2. Beam shape studies were performed using 6-10 MeV electrons from the Elekta LINAC, both in conventional and fractionated modes using a tungsten collimator mounted on a PMMA applicator, as well as with proton beams at

the CNAO center in Pavia at energies ranging from 62.28 MeV to 226.91 MeV. These measurements demonstrated good agreement with the data acquired using GafChromic EBT XD films and confirmed the ability to spatially resolve electron and proton beams at conventional dose-rates. This technology is promising for beam monitoring applications in SFRT, with future efforts focused on modifying the readout chip to ensure compatibility with FLASH operation modes.

The second technology studied was diamond, in particular a polycrystalline CVD diamond (pCVD) sensor with an active area of 1.3×1.3 mm^2 and thickness of 100 μm was tested on electron beams from a high dose-rate enabled Elekta LINAC. The charge collection efficiency (CCE) and sensitivity observed were within the typical ranges reported for pCVDs. As expected, the charge per pulse was lower than that of the silicon detector, but the pulse characteristics were similar, suggesting that a pCVD diamond detector may be a viable beam monitor. Further studies of the sensor's response at higher dose-rates and pre-irradiation measurements are required to confirm its suitability for real-time beam monitoring under UHDR conditions.

The third technology explored was silicon carbide (SiC). SiC sensors of various geometries, fabricated by SenSiC STLab, were characterized extensively on FLASH electron beams by the INFN Catania colleagues. In Turin, a comparative test between a silicon and an SiC sensor was conducted, exposing both to 10 MeV UHDR electron beams from the Elekta SL18 LINAC. A linear response of the collected charge as a function of dose-per-pulse was confirmed for both sensors at dose-per-pulse values exceeding 2 Gy/pulse, and the calibration factor obtained with the ElectronFLASH in Pisa was consistent with the values derived from the measurements in Turin. The temporal signal profiles of both solid-state technologies were comparable. A further comparison was also conducted between the same silicon sensor and a plastic scintillator at four measurement conditions (two positions tested both in High Power and Low Power modes), with the linearity of the dose-per-pulse response verified. Additional beam tests are planned to replicate these measurements at more dose-per-pulse values with a more advanced experimental setup.

Several SiC sensors by SenSiC STLab were studied through irradiation tests at the Ruder Bošković Institute's Ion Microprobe Chamber. A micrometer ion beam was used to investigate sensor transport properties locally, subjecting samples to various doses at two temperatures (room temperature and up to 500°C). Results suggest that SiC radiation hardness may be further enhanced by operating the sensors at high temperatures. Preliminary results also indicate that sensors on free-standing membranes may have greater radiation hardness than standard bulk ones.

Finally, SiC sensors were evaluated as alternatives for X-ray beam position and intensity monitoring (XBPM) in synchrotron applications. Two technologies developed by SenSiC were investigated in detail: standard "4-quadrant" XBPM devices and Resistive-XBPM devices. Performance evaluations were conducted under 8 keV X-ray beams at the NanoMAX beamline at MAX IV in Sweden and under UV light at CNR. Experimental results were compared with simulations using TCAD Synopsys Sentaurus software. Both measurements and simulations indicated that standard XBPM devices effectively monitor highly focused

8 keV X-ray beams (110 nm $\times$ 110 nm) when the electrode gap is comparable to the detector thickness, to avoid charge collection efficiency (CCE) loss within the gap. Initial prototypes of Silicon Carbide Resistive-XBPMs were fabricated and validated in preliminary experiments at CNR-IMM laboratories in Catania, demonstrating a correlation between the signal from the two anodes and the beam position, while maintaining a constant total current.

The requirements for real-time monitoring of UHDR radiation detection are: high spatial resolution, high temporal resolution, high beam transparency, wide dynamic response range, compact size, large sensitive area, and radiation resistance. The three solid-state technologies investigated successfully met the majority of these criteria.

It is reported in literature that innovative prototypes of thin 2D transmission ionization chambers have demonstrated the capability to withstand the requirements of proton UHDR beams. However, alternative technologies are required for pulsed beams such as those generated by LINACs for radiotherapy , where the high dose-per-pulse are not compatible with the performance achievable by transmission ionization chamber.
Emerging technologies such as integrated current transformers (ICTs) provide highly accurate and reproducible charge measurements in UHDR conditions, but are limited in their ability to provide information on beam flatness and symmetry, as they only measure beam fluence. While this limitation does not seem critical for low-energy beams, it could become important for VHEE beams, especially if pencil beam technology will be adopted.
Solid-state detectors such as silicon, SiC, and diamond seems to be ideal candidates to address the limitations of current technologies. Indeed, the temporal resolution is sufficient to allow sampling of the signal at the level of individual delivered pulses. These detectors collect the signal in a few nanoseconds and, when coupled with readout chips like TERA08 and TERA09, they can respond to the temporal requirements.
Additionally, the possibility of using segmented detectors to provide information on beam symmetry and flatness has been demonstrated. This applies to large beams spot, but provides a spatial resolution also useful for applications in spatially fractionated RT (SFRT) or pencil beams. However, this becomes more complex for diamond detectors, as diamond sensors with areas larger than 1-2 cm^2 are not currently produced.
In terms of dynamic range, both silicon and SiC have shown comparable characteristics, although silicon detectors have been tested up to just over 10 Gy/pulse, while SiC detectors have been tested beyond 20 Gy/pulse. Furthermore, sensor segmentation introduces significant complexity in signal readout. The multichannel TERA chip has demonstrated promising performance; however, future upgrades, such as the inclusion of a current divider per channel, hold the potential to further extend the measurable dose range.
Afterwards, thinning the sensors, as done with free-standing membranes, can still improve their beam transparency. Studies will soon be conducted on silicon devices as well, by thinning available samples or by producing thinner sensors.

SiC detectors appear to respond linearly even when no bias voltage is applied, which is advantageous for clinical applications. However, it is believed that silicon detectors with different geometries (smaller active volumes) can mitigate the signal distortion effects observed at low bias voltages, enabling their use even at lower voltages.
In order to overcome the issues identified in these first trials, a new batch of sensors for this purpose is in the early stages of FBK production. These are based on an innovative technology base on *trench* to better define the active volume of the sensor [184, 185]. Different geometries of silicon pads (featuring smaller active volumes than those previously tested) were assembled into arrays covering various total areas depending on the pad spacing, the single pad active area, and the number of pads per array. Additionally, metal lines were designed to route the signal away from the active detection region and protect the electronics from the intense beams.
Finally, radiation hardness is a crucial factor, as the detectors are fixed in the delivery system and are continuously exposed to radiation. Among the three technologies, diamond is certainly the most radiation-resistant. However, due to challenges in scaling up its production to cover larger beam areas, it is more suitable for dosimetry and microdosimetry than for beam monitoring. Similarly, SiC, with its wider bandgap and higher electron-hole pair creation energy compared to silicon, demonstrates greater radiation resistance. However, no signs of signal degradation, such as an increase in depletion voltage or leakage current, were observed on silicon detectors even after a cumulative dose of approximately 10 kGy. For this reason, it is complex but essential to investigate the cumulative dose limits that a beam monitor must withstand to meet UHDR requirements, to evaluate how these limits influence the choice of one technology over another.
Considering the number of factors and properties yet to be thoroughly investigated, it is not possible to definitively identify a single technology for beam monitoring in UHDR beams. However, it is conceivable that different technologies, including solid-state detectors, could be combined to leverage their specific advantages and address the requirements posed by the extreme environment of FLASH radiotherapy.

Bibliography

[1] Umberto Deut, Aurora Camperi, Cristiano Cavicchi, Roberto Cirio, Emanuele Maria Data, Elisabetta Alessandra Durisi, Veronica Ferrero, Arianna Ferro, Simona Giordanengo, Oscar Martì Villarreal, et al. Characterization of a modified clinical linear accelerator for ultra-high dose rate beam delivery. *Applied Sciences*, 14(17):7582, 2024.

[2] Elisabetta Medina, Arianna Ferro, Mohammad Abujami, Aurora Camperi, Matteo Centis Vignali, Emanuele Data, Damiano Del Sarto, Umberto Deut, Fabio Di Martino, Mohammad Fadavi Mazinani, et al. First experimental validation of silicon-based sensors for monitoring ultra-high dose rate electron beams. *Frontiers in Physics*, 12:1258832, 2024.

[3] Elisabetta Medina, Aurora Camperi, Matteo Centis Vignali, Esther Ciarrocchi, Umberto Deut, Marco Donetti, Fabio Di Martino, Veronica Ferrero, Arianna Ferro, Simona Giordanengo, et al. Monitoring electron and proton beam profiles with segmented silicon sensors. *Nuclear Instruments and Methods in Physics Research Section A: Accelerators, Spectrometers, Detectors and Associated Equipment*, page 169897, 2024.

[4] Elisabetta Medina, Mohammad Abujami, Pietro Aprà, Aurora Camperi, Emanuele Data, Umberto Deut, Mohammad Fadavi Mazinani, Veronica Ferrero, Arianna Ferro, Simona Giordanengo, et al. Characterization of cvd diamond detector with flash electron beam from modified linac accelerator. *Nuclear Instruments and Methods in Physics Research Section A: Accelerators, Spectrometers, Detectors and Associated Equipment*, 1063:169308, 2024.

[5] Francesco Romano, Giuliana Milluzzo, Fabio Di Martino, Maria Cristina D'Oca, Giuseppe Felici, Federica Galante, Alessia Gasparini, Giulia Mariani, Maurizio Marrale, Elisabetta Medina, et al. First characterization of novel silicon carbide detectors with ultra-high dose rate electron beams for flash radiotherapy. *Applied Sciences*, 13(5):2986, 2023.

[6] Giuliana Milluzzo, Marzio De Napoli, Fabio Di Martino, Antonino Amato, Damiano Del Sarto, Maria Cristina D'Oca, Maurizio Marrale, Luigi Masturzo, Elisabetta Medina, Chinonso Okpuwe, et al. Comprehensive dosimetric characterization of novel silicon carbide detectors with uhdr electron beams for flash radiotherapy. *Medical Physics*, 2024.

[7] Elisabetta Medina, Enrico Sangregorio, Andreo Crnjac, Francesco Romano, Giuliana Milluzzo, Anna Vignati, Milko Jakšic, Lucia Calcagno, and Massimo Camarda. Radiation hardness study of silicon carbide sensors under high-temperature proton beam irradiations. *Micromachines*, 14(1):166, 2023.

[8] Adeel Kaiser, John G Eley, Nasarachi E Onyeuku, Stephanie R Rice, Carleen C Wright, Nathan E McGovern, Megan Sank, Mingyao Zhu, Zeljko Vujaskovic, Charles B Simone 2nd, et al. Proton therapy delivery and its clinical application in select solid tumor malignancies. *JoVE (Journal of Visualized Experiments)*, (144):e58372, 2019.

[9] Martin Jermann. Particle therapy statistics in 2014. *International Journal of Particle Therapy*, 2(1):50–54, 2015.

[10] CD Town. Effect of high dose rates on survival of mammalian cells. *Nature*, 215(5103):847–848, 1967.

[11] T Prempree, A Michelsen, and T Merz. The repair time of chromosome breaks induced by pulsed x-rays of ultra-high dose-rate. *International Journal of Radiation Biology and Related Studies in Physics, Chemistry and Medicine*, 15(6):571–574, 1969.

[12] Vincent Favaudon, Laura Caplier, Virginie Monceau, Frédéric Pouzoulet, Mano Sayarath, Charles Fouillade, Marie-France Poupon, Isabel Brito, Philippe Hupé, Jean Bourhis, et al. Ultrahigh dose-rate flash irradiation increases the differential response between normal and tumor tissue in mice. *Science translational medicine*, 6(245):245ra93–245ra93, 2014.

[13] Muhammad Ramish Ashraf, Mahbubur Rahman, Rongxiao Zhang, Benjamin B Williams, David J Gladstone, Brian W Pogue, and Petr Bruza. Dosimetry for flash radiotherapy: a review of tools and the role of radioluminescence and cherenkov emission. *Frontiers in Physics*, 8:328, 2020.

[14] Andreas Schüller, Sophie Heinrich, Charles Fouillade, Anna Subiel, Ludovic De Marzi, Francesco Romano, Peter Peier, Maria Trachsel, Celeste Fleta, Rafael Kranzer, et al. The european joint research project uhdpulse–metrology for advanced radiotherapy using particle beams with ultra-high pulse dose rates. *Physica Medica*, 80:134–150, 2020.

[15] Binwei Lin, Dan Huang, Feng Gao, Yiwei Yang, Dai Wu, Yu Zhang, Gang Feng, Tangzhi Dai, and Xiaobo Du. Mechanisms of flash effect. *Frontiers in Oncology*, 12:995612, 2022.

[16] Shirley Hornsey and DK Bewley. Hypoxia in mouse intestine induced by electron irradiation at high dose-rates. *International Journal of Radiation Biology and Related Studies in Physics, Chemistry and Medicine*, 19(5):479–483, 1971.

[17] Yuqi Ma, Wenkang Zhang, Ziming Zhao, Jianfeng Lv, Junyi Chen, Xueqin Yan, XiaoJi Lin, Junlong Zhang, Bingwu Wang, Song Gao, et al. Current views on mechanisms of the flash effect in cancer radiotherapy. *National Science Review*, 11(10):nwae350, 2024.

[18] Karen Levy, Suchitra Natarajan, Jinghui Wang, Stephanie Chow, Joshua T Eggold, Phoebe Loo, Rakesh Manjappa, Frederick M Lartey, Emil Schüler, Lawrie Skinner, et al. Flash irradiation enhances the therapeutic index of abdominal radiotherapy for the treatment of ovarian cancer. *Biorxiv*, pages 2019–12, 2019.

[19] Marie-Catherine Vozenin, Pauline De Fornel, Kristoffer Petersson, Vincent Favaudon, Maud Jaccard, Jean-François Germond, Benoit Petit, Marco Burki, Gisèle Ferrand, David Patin, et al. The advantage of flash radiotherapy confirmed in mini-pig and cat-cancer patients. *Clinical Cancer Research*, 25(1):35–42, 2019.

[20] M-C Vozenin, Jolyon H Hendry, and CL Limoli. Biological benefits of ultra-high dose rate flash radiotherapy: sleeping beauty awoken. *Clinical oncology*, 31(7):407–415, 2019.

[21] Lech Papiez, Colleen DesRosiers, and Vadim Moskvin. Very high energy electrons (50–250 mev) and radiation therapy. *Technology in cancer research & treatment*, 1(2):105–110, 2002.

[22] Lucia Giuliano, David Alesini, Mostafa Behtouei, Fabio Bosco, Martina Carillo, Giacomo Cuttone, Daniele De Arcangelis, Luigi Faillace, Vincent Favaudon, Luca Ficcadenti, et al. Preliminary studies of a compact vhee linear accelerator system for flash radiotherapy. In *JACoW Publishing*, pages 1229–1232. 2021.

[23] L Giuliano, F Bosco, M Carillo, D De Arcangelis, L Ficcadenti, D Francescone, A De Gregorio, G Franciosini, M Migliorati, A Mostacci, et al. Proposal of a vhee linac for flash radiotherapy. In *Journal of Physics: Conference Series*, volume 2420, page 012087. IOP Publishing, 2023.

[24] Ashley J Cetnar and Dominic J DiCostanzo. The lifetime of a linac monitor unit ion chamber. *Journal of Applied Clinical Medical Physics*, 22(12):108–114, 2021.

[25] S Giordanengo, M Donetti, MA Garella, F Marchetto, G Alampi, A Ansarinejad, Vincenzo Monaco, M Mucchi, IA Pecka, Cristiana Peroni, et al. Design and characterization of the beam monitor detectors of the Italian National Center of Oncological Hadron-therapy (CNAO). *Nuclear Instruments and Methods in Physics Research Section A: Accelerators, Spectrometers, Detectors and Associated Equipment*, 698:202–207, 2013.

[26] Simona Giordanengo, Maria Adelaide Garella, Flavio Marchetto, Faiza Bourhaleb, Mario Ciocca, Alfredo Mirandola, Vincenzo Monaco, Mohammad Amin Hosseini, Cristiana Peroni, Roberto Sacchi, et al. The cnao dose delivery system for modulated scanning ion beam radiotherapy. *Medical physics*, 42(1):263–275, 2015.

[27] S Braccini, G PITTA', M Donetti, Roberto Cirio, Alessandro LA ROSA, MA Garella, Simona Giordanengo, F Marchetto, and Cristiana Peroni. Matrix: an innovative pixel ionization chamber for on-line beam monitoring in hadrontherapy. In *Astroparticle, Particle And Space Physics, Detectors And Medical Physics Applications*, pages 677–681. World Scientific, 2006.

[28] Konrad P Nesteruk. Beam monitor detectors for medical applications. *Reports of Practical Oncology & Radiotherapy*, 19:S32–S36, 2014.

[29] Francesco Romano, Claude Bailat, Patrik Gonçalves Jorge, Michael Lloyd Franz Lerch, and Arash Darafsheh. Ultra-high dose rate dosimetry: Challenges and opportunities for flash radiation therapy. *Medical physics*, 2022.

[30] Maude Gondré, Patrik Gonçalves Jorge, Marie-Catherine Vozenin, Jean Bourhis, François Bochud, Claude Bailat, and Raphaël Moeckli. Optimization of alanine measurements for fast and accurate dosimetry in flash radiation therapy. *Radiation research*, 194(6):573–579, 2020.

[31] Fabio Di Martino, Patrizio Barca, Salvatore Barone, Eleonora Bortoli, Rita Borgheresi, Silvia De Stefano, Massimo Di Francesco, Luigi Faillace, Lucia Giuliano, Luigi Grasso, et al. Flash radiotherapy with electrons: issues related to the production, monitoring, and dosimetric characterization of the beam. *Frontiers in Physics*, 8:570697, 2020.

[32] M McManus, F Romano, ND Lee, W Farabolini, A Gilardi, G Royle, H Palmans, and Anna Subiel. The challenge of ionisation chamber dosimetry in ultra-short pulsed high dose-rate very high energy electron beams. *Scientific reports*, 10(1):9089, 2020.

[33] JW Boag, E Hochhäuser, and OA Balk. The effect of free-electron collection on the recombination correction to ionization measurements of pulsed radiation. *Physics in Medicine & Biology*, 41(5):885, 1996.

[34] F Di Martino, M Giannelli, AC Traino, and M Lazzeri. Ion recombination correction for very high dose-per-pulse high-energy electron beams. *Medical physics*, 32(7Part1):2204–2210, 2005.

[35] Kristoffer Petersson, Maud Jaccard, Jean-François Germond, Thierry Buchillier, François Bochud, Jean Bourhis, Marie-Catherine Vozenin, and Claude Bailat. High dose-per-pulse electron beam dosimetry—a model to correct for the ion recombination in the advanced markus ionization chamber. *Medical physics*, 44(3):1157–1167, 2017.

[36] Faustino Gómez, Diego M Gonzalez-Castaño, Nicolás Gómez Fernández, Juan Pardo-Montero, Andreas Schüller, Alessia Gasparini, Verdi Vanreusel, Dirk Verellen, Giuseppe Felici, Rafael Kranzer, et al. Development of an ultra-thin parallel plate ionization chamber for dosimetry in flash radiotherapy. *Medical Physics*, 49(7):4705–4714, 2022.

[37] Fabio Di Martino, Damiano Del Sarto, Maria Giuseppina Bisogni, Simone Capaccioli, Federica Galante, Alessia Gasperini, Stefania Linsalata, Giulia Mariani, Matteo Pacitti, Fabiola Paiar, et al. A new solution for uhdp and uhdr (flash) measurements: Theory and conceptual design of alls chamber. *Physica Medica*, 102:9–18, 2022.

[38] Wei Zou, Eric S Diffenderfer, Kan Ota, Paul Boisseau, Michele M Kim, Yongliang Cai, Stephen M Avery, David J Carlson, Rodney D Wiersma, Alexander Lin, et al. Characterization of a high-resolution 2d transmission ion chamber for independent validation of proton pencil beam scanning of conventional and flash dose delivery. *Medical Physics*, 48(7):3948–3957, 2021.

[39] Tetsuo Inada, Hiroto Nishio, Saburo Amino, Kimihiko Abe, and Katsumata Saito. High dose-rate dependence of early skin reaction in mouse. *International Journal of Radiation Biology and Related Studies in Physics, Chemistry and Medicine*, 38(2):139–145, 1980.

[40] E Ravera, A Cavalieri, E Ciarrocchi, D Del Sarto, F Di Martino, M Massa, L Masturzo, A Moggi, M Morrocchi, JH Pensavalle, et al. A new calibration method of an array of plastic scintillating fibers for dosimetry in electron flash radiotherapy. *Radiation Measurements*, 177:107254, 2024.

[41] E Ciarrocchi, E Ravera, A Cavalieri, M Celentano, D Del Sarto, F Di Martino, S Linsalata, M Massa, L Masturzo, A Moggi, et al. Plastic scintillator-based dosimeters for ultra-high dose rate (uhdr) electron radiotherapy. *Physica Medica*, 121:103360, 2024.

[42] V. Favaudon, J. M. Lentz, S. Heinrich, A. Patriarca, L. de Marzi, C. Fouillade, and M. Dutreix. Time-resolved dosimetry of pulsed electron beams in very high dose-rate, flash irradiation for radiotherapy preclinical studies. *Nucl. Instrum. Methods Phys. Res. Sect. A Accel. Spectrometers Detect. Assoc. Equip.*, 944:162537, 2019.

[43] R Kranzer, A Schüller, A Bourgouin, T Hackel, D Poppinga, M Lapp, HK Looe, and B Poppe. Response of diamond detectors in ultra-high dose-per-pulse electron beams for dosimetry at flash radiotherapy. *Physics in Medicine & Biology*, 67(7):075002, 2022.

[44] Marco Marinelli, Giuseppe Felici, Federica Galante, Alessia Gasparini, Lucia Giuliano, Sophie Heinrich, Matteo Pacitti, Giuseppe Prestopino, Verdi Vanreusel, Dirk Verellen, et al. Design, realization, and characterization of a novel diamond detector prototype for flash radiotherapy dosimetry. *Medical Physics*, 49(3):1902–1910, 2022.

[45] Gianluca Verona Rinati, Giuseppe Felici, Federica Galante, Alessia Gasparini, Rafael Kranzer, Giulia Mariani, Matteo Pacitti, Giuseppe Prestopino, Andreas Schüller, Verdi Vanreusel, et al. Application of a novel diamond detector for commissioning of flash radiotherapy electron beams. *Medical Physics*, 49(8):5513–5522, 2022.

[46] A. B. Rosenfeld, G. Biasi, M. Petasecca, M. L. F. Lerch, G. Villani, and V. Feygelman. Semiconductor dosimetry in modern external-beam radiation therapy. *Phys Med Biol*, 65(16):16TR01, 2020.

[47] M. Petasecca, F. Moscatelli, and G. U. Pignatel. Analysis and simulation of charge collection efficiency in silicon thin detectors. *Nuclear Instruments and Methods in Physics Research, Section A: Accelerators, Spectrometers, Detectors and Associated Equipment*, 546:291–295, 2005.

[48] M. L. F. Lerch, M. Petasecca, A. Cullen, et al. Dosimetry of intensive synchrotron microbeams. *Radiation Measurements*, 46:1560–1565, 2011.

[49] P. Allport. Applications of silicon strip and pixel-based particle tracking detectors. *Nature Reviews Physics*, 2020.

[50] V. Favaudon, C. Fouillade, and M. C. Vozenin. Ultrahigh dose-rate, "flash" irradiation minimizes the side-effects of radiotherapy. *Cancer Radiother*, 19:526–531, 2015.

[51] P. Montay-Gruel, K. Petersson, M. Jaccard, G. Boivin, J. F. Germond, B. Petit, et al. Irradiation in a flash: Unique sparing of memory in mice after whole brain irradiation with dose rates above 100 gy/s. *Radiother Oncol*, 124:365–369, 2017.

[52] M. Jaccard, M. T. Duran, K. Petersson, J. F. Germond, P. Liger, M. C. Vozenin, et al. High dose-per-pulse electron beam dosimetry: Commissioning of the oriatron ert6 prototype linear accelerator for preclinical use. *Med Phys*, 45:863–874, 2018.

[53] P. Montay-Gruel, A. Bouchet, M. Jaccard, D. Patin, R. Serduc, and W. Aim. X-rays can trigger the flash effect: Ultra-high dose-rate synchrotron light source prevents normal brain injury after whole brain irradiation in mice. *Radiother Oncol*, 129:582–588, 2018.

[54] E. Schüler, S. Trovati, G. King, F. Lartey, M. Rafat, M. Villegas, A. J. Praxel, Jr. Loo, B. W., and P. G. Maxim. Experimental platform for uhdr flash irradiation of small animals using a clinical linear accelerator. *Int. J. Radiat. Oncol. Biol. Phys.*, 97:195–203, 2017.

[55] Michael Lempart, Börje Blad, Gabriel Adrian, Sven Bäck, Tommy Knöös, Crister Ceberg, and Kristoffer Petersson. Modifying a clinical linear accelerator for delivery of ultra-high dose rate irradiation. *Radiotherapy and Oncology*, 139:40–45, 2019.

[56] M. Snyder, J. Vadas, J. Musselwhite, R. Halford, G. Wilson, C. Stevens, and D. Yan. Flash radiotherapy monitor chamber signal conditioning. *Medical Physics*, 48:791–795, 2021.

[57] R. Dal Bello, J. Von Der Grün, S. Fabiano, T. Rudolf, N. Saltybaeva, L.S. Stark, M. Ahmed, M. Bathula, S. Kucuker Dogan, and J. McNeur. Enabling ultra-high dose rate electron beams at a clinical linear accelerator for isocentric treatments. *Radiotherapy and Oncology*, 187:109822, 2023.

[58] A.J. Cetnar, S. Jain, N. Gupta, and A. Chakravarti. Technical note: Commissioning of a linear accelerator producing ultra-high dose rate electrons. *Medical Physics*, 51:1415–1420, 2024.

[59] E. Schüler, S. Trovati, G. King, F. Lartey, M. Rafat, M. Villegas, A.J. Praxel, B.W. Loo, and P.G. Maxim. Experimental platform for ultra-high dose rate flash irradiation of small animals using a clinical linear accelerator. *International Journal of Radiation Oncology*Biology*Physics*, 97:195–203, 2017.

[60] Annalisa Patriarca, Charles Fouillade, Michel Auger, Frédéric Martin, Frédéric Pouzoulet, Catherine Nauraye, Sophie Heinrich, Vincent Favaudon, Samuel Meyroneinc, Rémi Dendale, et al. Experimental set-up for flash proton irradiation of small animals using a clinical system. *International Journal of Radiation Oncology* Biology* Physics*, 102(3):619–626, 2018.

[61] James CL Chow and Harry E Ruda. Flash radiotherapy: Innovative cancer treatment. *Encyclopedia*, 3(3):808–823, 2023.

[62] M. Bazalova-Carter, M. Liu, B. Palma, M. Dunning, D. McCormick, E. Hemsing, J. Nelson, K. Jobe, E. Colby, A. C. Koong, et al. Comparison of film measurements and monte carlo simulations of dose delivered with very high-energy electron beams in a polystyrene phantom. *Med. Phys.*, 42:1606–1613, 2015.

[63] J. C. Crosbie, P. Fournier, S. Bartzsch, M. Donzelli, I. Cornelius, A. W. Stevenson, H. Requardt, and E. Bräuer-Krisch. Energy spectra considerations for synchrotron radiotherapy trials on the id17 bio-medical beamline at the european synchrotron radiation facility. *J. Synchrotron Radiat.*, 22:1035–1041, 2015.

[64] A. Darafsheh, Y. Hao, T. Zwart, M. Wagner, D. Catanzano, J. F. Williamson, N. Knutson, B. Sun, S. Mutic, and T. Zhao. Feasibility of proton flash irradiation using a synchrocyclotron for preclinical studies. *Med. Phys.*, 47:4348–4355, 2020.

[65] S.I.T. Sordina IORT technologies S.P.A (2023). . available online:. https://www.soiort.com/.

[66] Giuseppe Felici, Patrizio Barca, Salvatore Barone, Eleonora Bortoli, Rita Borgheresi, Silvia De Stefano, Massimo Di Francesco, Luigi Grasso, Stefania Linsalata, Daniela Marfisi, et al. Transforming an iort linac into a flash research machine: procedure and dosimetric characterization. *Frontiers in Physics*, 8:374, 2020.

[67] F Di Martino, D Del Sarto, G Bass, S Capaccioli, M Celentano, D Coves, A Douralis, Marrale Marinelli, M Marrale, L Masturzo, et al. Architecture, flexibility and performance of a special electron linac dedicated to flash radiotherapy research: electronflash with a triode gun of the centro pisano flash radiotherapy (cpfr). *Frontiers in Physics*, 11:1268310, 2023.

[68] Gerhard Lutz et al. *Semiconductor radiation detectors*. Number PUBDB-2020-02521. Springer, 2007.

[69] Marco Ferrero, Roberta Arcidiacono, Marco Mandurrino, Valentina Sola, and Nicolò Cartiglia. *An Introduction to Ultra-Fast Silicon Detectors*. CRC Press, 2021.

[70] Imran Akhtar. The fundamentals of particle physics: An introduction. *WORLDWIDE JOURNAL OF PHYSICS*, 1(01):1–10, 2020.

[71] Francesco Riggi. Radiation interaction. In *Educational and Amateur Geiger Counter Experiments: 50+ Activities for Beginners and Beyond*, pages 23–36. Springer, 2024.

[72] Donald E Groom and SR Klein. Passage of particles through matter. *The European Physical Journal C-Particles and Fields*, 15(1-4):163–173, 2000.

[73] Sheng S Li and Sheng S Li. P—n junction diodes. *Semiconductor Physical Electronics*, pages 287–326, 1993.

[74] Stefaan Tavernier and Stefaan Tavernier. Detectors based on ionisation in semiconductor materials. *Experimental Techniques in Nuclear and Particle Physics*, pages 143–165, 2010.

[75] Zhong He. Review of the shockley–ramo theorem and its application in semiconductor gamma-ray detectors. *Nuclear Instruments and Methods in Physics Research Section A: Accelerators, Spectrometers, Detectors and Associated Equipment*, 463(1-2):250–267, 2001.

[76] M Ferrero, R Arcidiacono, M Barozzi, M Boscardin, N Cartiglia, GF Dalla Betta, Z Galloway, M Mandurrino, S Mazza, G Paternoster, et al. Radiation resistant lgad design. *Nuclear Instruments and Methods in Physics Research Section A: Accelerators, Spectrometers, Detectors and Associated Equipment*, 919:16–26, 2019.

[77] Stefano Meroli, Daniele Passeri, and Leonello Servoli. Energy loss measurement for charged particles in very thin silicon layers. *Journal of Instrumentation*, 6(06):P06013, 2011.

[78] Ben L Green, Alan T Collins, and Christopher M Breeding. Diamond spectroscopy, defect centers, color, and treatments. *Reviews in Mineralogy and Geochemistry*, 88(1):637–688, 2022.

[79] Isabella Ciancaglioni, Rita Consorti, Maria Cristina Rossi, and Gennaro Conte. Polycrystalline diamond detectors compared with silicon x-ray dosimeters for clinical use. In *IEEE Symposium Conference Record Nuclear Science 2004.*, volume 7, pages 4445–4447. IEEE, 2004.

[80] Isabella Ciancaglioni. Rivelatori in diamante sintetico poli e monocristallino per radiazioni e particelli ionizzanti. 2008.

[81] Felix Bachmair. *CVD diamond sensors in detectors for high energy physics*. PhD thesis, ETH Zurich, 2016.

[82] Marco Marinelli, E Milani, A Paoletti, A Tucciarone, G Verona Rinati, M Angelone, and M Pillon. Systematic study of pre-irradiation effects in high efficiency cvd diamond nuclear particle detectors. *Nuclear Instruments and Methods in Physics Research Section A: Accelerators, Spectrometers, Detectors and Associated Equipment*, 476(3):701–705, 2002.

[83] Tsunenobu Kimoto and James A Cooper. Physical properties of silicon carbide. 2014.

[84] Marzio De Napoli. Sic detectors: A review on the use of silicon carbide as radiation detection material. *Frontiers in physics*, 10:898833, 2022.

[85] Tsunenobu Kimoto and James A Cooper. *Fundamentals of silicon carbide technology: growth, characterization, devices and applications*. John Wiley & Sons, **2014**.

[86] L Gonella, H Nabholz, and R Wideröe. The turin 100-mev electron synchrotron. *Nuclear Instruments and Methods*, 27(1):141–155, 1964.

[87] V Monti et al. Linac-based thermal neutron source construction and characterization. *IL NUOVO CIMENTO*, 100(121):41, 2018.

[88] AP Chernyaev and SM Varzar. Particle accelerators in modern world. *Physics of Atomic Nuclei*, 77:1203–1215, 2014.

[89] Eline Hageman, Pei-Pei Che, Max Dahele, Ben J Slotman, and Peter Sminia. Radiobiological aspects of flash radiotherapy. *Biomolecules*, 12(10):1376, 2022.

[90] Anna Vignati, Simona Giordanengo, Federico Fausti, Oscar A Martì Villarreal, Felix Mas Milian, Giovanni Mazza, Zahra Shakarami, Roberto Cirio, Vincenzo Monaco, and Roberto Sacchi. Beam monitors for tomorrow: the challenges of electron and photon flash rt. *Frontiers in Physics*, 8:375, 2020.

[91] N. Giannini, G. Gadducci, T. Fuentes, A. Gonnelli, F. Di Martino, P. Puccini, M. Naso, F. Pasqualetti, S. Capaccioli, and F. Paiar. Electron flash radiotherapy in vivo studies. a systematic review. *Frontiers in Oncology*, 14:1373453, 2024.

[92] M. Rahman, A. Trigilio, G. Franciosini, R. Moeckli, R. Zhang, and T.T. Böhlen. Flash radiotherapy treatment planning and models for electron beams. *Radiotherapy and Oncology*, 175:210–221, 2022.

[93] International Atomic Energy Agency. *Absorbed Dose Determination in External Beam Radiotherapy*. Technical Reports Series, Rev. 1. International Atomic Energy Agency, Vienna, Austria, 2024.

[94] A. Subiel, V. Moskvin, G.H. Welsh, S. Cipiccia, D. Reboredo, C. DesRosiers, and D.A. Jaroszynski. Challenges of dosimetry of ultra-short pulsed very high energy electron beams. *Physica Medica*, 42:327–331, 2017.

[95] M. McManus, F. Romano, N.D. Lee, W. Farabolini, A. Gilardi, G. Royle, H. Palmans, and A. Subiel. The challenge of ionisation chamber dosimetry in ultra-short pulsed high dose-rate very high energy electron beams. *Scientific Reports*, 10:9089, 2020.

[96] A. Niroomand-Rad, C.R. Blackwell, B.M. Coursey, K.P. Gall, J.M. Galvin, W.L. McLaughlin, A.S. Meigooni, R. Nath, J.E. Rodgers, and C.G. Soares. Radiochromic film dosimetry: Recommendations of aapm radiation therapy committee task group 55. *Medical Physics*, 25:2093–2115, 1998.

[97] S. Devic, J. Seuntjens, E. Sham, E.B. Podgorsak, C.R. Schmidtlein, A.S. Kirov, and C.G. Soares. Precise radiochromic film dosimetry using a flat-bed document scanner. *Medical Physics*, 32:2245–2253, 2005.

[98] Ashley J Cetnar, Sagarika Jain, Nilendu Gupta, and Arnab Chakravarti. Commissioning of a linear accelerator producing ultra-high dose rate electrons. *Medical Physics*, 51(2):1415–1420, 2024.

[99] F. Costa, S. Sarmento, and O. Sousa. Assessment of clinically relevant dose distributions in pelvic ioert using gafchromic ebt3 films. *Physica Medica*, 31:692–701, 2015.

[100] W. Strydom, W. Parker, and M. Olivares. *Electron beams: Physical and clinical aspects*. McGill University, IAEA, Montreal, QC, Canada; Vienna, Austria, 2006.

[101] E. Konradsson, P. Wahlqvist, A. Thoft, B. Blad, S. Bäck, C. Ceberg, and K. Petersson. Beam control system and output fine-tuning for safe and precise delivery of flash radiotherapy at a clinical linear accelerator. *Frontiers in Oncology*, 14:1342488, 2024.

[102] L. Faillace, D. Alesini, G. Bisogni, F. Bosco, M. Carillo, P. Cirrone, G. Cuttone, D. De Arcangelis, A. De Gregorio, and F. Di Martino. Perspectives in linear accelerator for flash vhee: Study of a compact c-band system. *Physica Medica*, 104:149–159, 2022.

[103] Fondazione Bruno Kessler Center for Sensors and Devices (2023). Available online:. https://sd.fbk.eu/en/ (Accessed on July 12, 2023).

[104] Roberto Sacchi, Vincenzo Monaco, Anna Vignati, Roberto Cirio, Valentina Sola, et al. Energy measurement of clinical proton beams with a telescope of ultra-fast silicon detectors. *Il nuovo cimento C*, 44(143):1–4, 2021.

[105] OA Marti Villarreal, A Vignati, S Giordanengo, M Abujami, G Borghi, M Centis Vignali, E Data, M Ferrero, F Ficorella, C Galeone, et al. Characterization of thin lgad sensors designed for beam monitoring in proton therapy. *Nuclear Instruments and Methods in Physics Research Section A: Accelerators, Spectrometers, Detectors and Associated Equipment*, 1046:167622, 2023.

[106] HF-W Sadrozinski, S Ely, V Fadeyev, Z Galloway, J Ngo, C Parker, B Petersen, A Seiden, A Zatserklyaniy, N Cartiglia, et al. Ultra-fast silicon detectors. *Nuclear Instruments and Methods in Physics Research Section A: Accelerators, Spectrometers, Detectors and Associated Equipment*, 730:226–231, 2013.

[107] Oscar Ariel Marti Villarreal, G Peroglio, A Vignati, S Giordanengo, FM Milian, M Ferrero, L Menzio, M Abujami, C Galeone, OH Ali, et al. Characterization of large lgad sensors for proton counting in particle therapy. *Journal of Instrumentation*, 17(09):C09022, 2022.

[108] A Vignati, S Giordanengo, F Mas Milian, Z Ahmadi Ganjeh, M Donetti, F Fausti, M Ferrero, O Hammad Ali, OA Martì Villarreal, G Mazza, et al. A new detector for the beam energy measurement in proton therapy: a feasibility study. *Physics in Medicine & Biology*, 65(21):215030, 2020.

[109] Alfredo Mirandola, S Molinelli, G Vilches Freixas, A Mairani, E Gallio, D Panizza, S Russo, M Ciocca, M Donetti, G Magro, et al. Dosimetric commissioning and quality assurance of scanned ion beams at the italian national center for oncological hadrontherapy. *Medical physics*, 42(9):5287–5300, 2015.

[110] T Croci, A Morozzi, V Sola, P Asenov, A Fondacci, S Giordanengo, G Borghi, MC Vignali, G Paternoster, M Boscardin, et al. TCAD optimization of LGAD sensors for extremely high fluence applications. *Journal of Instrumentation*, 18(01):C01008, 2023.

[111] Sola V et al. Advances in LGAD technology for high radiation environments (2023). doi:10.1088/1748-0221/6/06/P06013.

[112] Valentina Sola, Roberta Arcidiacono, Patrick Asenov, Giacomo Borghi, Maurizio Boscardin, Nicolò Cartiglia, M Centis Vignali, Tommaso Croci, Marco Ferrero, Alessandro Fondacci, et al. A compensated design of the lgad gain layer. *Nuclear Instruments and Methods in Physics Research Section A: Accelerators, Spectrometers, Detectors and Associated Equipment*, 1040:167232, 2022.

[113] Roberto Cirio, Federico Fausti, L Fanola Guarachi, S Giordanengo, F Marchetto, G Mazza, Vincenzo Monaco, Roberto Sacchi, E Talpacci, M Varasteh Anvar, et al. A simple method to increase the current range of the tera chip in charged particle therapy applications. *Nuclear Instruments and Methods in Physics Research Section A: Accelerators, Spectrometers, Detectors and Associated Equipment*, 798:107–110, 2015.

[114] Alessandro La Rosa, G Mazza, M Donetti, F Marchetto, L Luetto, A Attili, F Bourhaleb, Roberto Cirio, MA Garella, Simona Giordanengo, et al. Design and test of a 64-channel charge measurement ASIC developed in CMOS 0.35 μm technology. *Nuclear Instruments and Methods in Physics Research Section A: Accelerators, Spectrometers, Detectors and Associated Equipment*, 583(2-3):461–468, 2007.

[115] Federico Fausti, G Mazza, F Marchetto, R Sacchi, and Roberto Cirio. Design of a 64 channels current-to-frequency converter asic, front-end electronics for high intensity particle beam detectors. In *2016 12th Conference on Ph. D. Research in Microelectronics and Electronics (PRIME)*, pages 1–4. IEEE, 2016.

[116] F Fausti, G Mazza, S Giordanengo, OH Ali, L Manganaro, V Monaco, R Sacchi, and R Cirio. Single event upset tests and failure rate estimation for a front-end asic adopted in high-flux-particle therapy applications. *Nuclear Instruments and Methods in Physics Research Section A: Accelerators, Spectrometers, Detectors and Associated Equipment*, 918:54–59, 2019.

[117] M. Dunne. Laser-driven particle accelerators. *Science*, 312(5772):374–376, 2006.

[118] G.A.P. Cirrone et al. Proceedings of spie 8779. page 63, 2013.

[119] Allpix Squared. (2023)). available online:. https://allpix-squared.docs.cern.ch/.

[120] Nanosheet FET Device, Anushka Singh, and Archana Pandey. Introduction to the synopsys sentaurus tcad suite and device simulation. *Advanced Field-Effect Transistors: Theory and Applications*, page 232, 2023.

[121] Sentaurus Device User Guide. Version V-2023.12, December 2023.

[122] Jean-Luc Leray and Philippe Paillet. Total dose effects: modeling for present and future–1999 ieee nsrec. In *IEEE Nuclear and Space Radiation Effects Conference*, 1999.

[123] Roxana Radu, Eckhart Fretwurst, Robert Klanner, Gunnar Lindstroem, and Ioana Pintilie. Radiation damage in n-type silicon diodes after electron irradiation with energies between 1.5 mev and 15 mev. *Nuclear Instruments and Methods in Physics Research Section A: Accelerators, Spectrometers, Detectors and Associated Equipment*, 730:84–90, 2013.

[124] Jean A Laissue, Hans Blattmann, and Daniel N Slatkin. Alban köhler (1874-1947): Erfinder der gittertherapie. *Zeitschrift für Medizinische Physik*, 22(2):90–99, 2012.

[125] Tim Schneider, Cristian Fernandez-Palomo, Annaïg Bertho, Jennifer Fazzari, Lorea Iturri, Olga A Martin, Verdiana Trappetti, Valentin Djonov, and Yolanda Prezado. Combining flash and spatially fractionated radiation therapy: the best of both worlds. *Radiotherapy and oncology*, 175:169–177, 2022.

[126] Yolanda Prezado. Divide and conquer: spatially fractionated radiation therapy. *Expert reviews in molecular medicine*, 24:e3, 2022.

[127] W. Yan, M.K. Khan, X. Wu, J. Simone CB 2nd, Fan, E. Gressen, X. Zhang, C.L. Limoli, H. Bahig, S. Tubin, and W.F. Mourad. Spatially fractionated radiation therapy: History, present and the future. *Clinical and Translational Radiation Oncology*, 20:30–38, 2019.

[128] Elke Bräuer-Krisch, Raphaël Serduc, Erik A Siegbahn, Géraldine Le Duc, Yolanda Prezado, Alberto Bravin, Hans Blattmann, and Jean A Laissue. Effects of pulsed, spatially fractionated, microscopic synchrotron x-ray beams on normal and tumoral brain tissue. *Mutation Research/Reviews in Mutation Research*, 704(1-3):160–166, 2010.

[129] Yolanda Prezado, Gregory Jouvion, David Hardy, Annalisa Patriarca, Catherine Nauraye, Judith Bergs, Wilfredo González, Consuelo Guardiola, Marjorie Juchaux, Dalila Labiod, et al. Proton minibeam radiation therapy spares normal rat brain: Long-term clinical, radiological and histopathological analysis. *Scientific reports*, 7(1):14403, 2017.

[130] Yolanda Prezado, Gregory Jouvion, Consuelo Guardiola, Wilfredo Gonzalez, Marjorie Juchaux, Judith Bergs, Catherine Nauraye, Dalila Labiod, Ludovic De Marzi, Frederic Pouzoulet, et al. Tumor control in rg2 glioma-bearing rats: a comparison between proton minibeam therapy and standard proton therapy. *International Journal of Radiation Oncology* Biology* Physics*, 104(2):266–271, 2019.

[131] M. Mohiuddin, M. Fujita, W.F. Regine, A.S. Megooni, G.S. Ibbott, and M.M. Ahmed. High-dose spatially-fractionated radiation (grid): a new paradigm in the management of advanced cancers. *International Journal of Radiation Oncology, Biology, Physics*, 45:721–727, 1999.

[132] H. Steel, S.C. Brüningk, C. Box, U. Oelfke, and S.H. Bartzsch. Quantification of differential response of tumour and normal cells to microbeam radiation in the absence of flash effects. *Cancers*, 13:3238, 2021.

[133] A. Bouchet, E. Brauer-Krisch, Y. Prezado, M. El Atifi, L. Rogalev, and C. Le Clec'h. Better efficacy of synchrotron spatially microfractionated radiation therapy than uniform radiation therapy on glioma. *International Journal of Radiation Oncology, Biology, Physics*, 95:1485–1494, 2016.

[134] Y. Prezado, P. Deman, P. Varlet, G. Jouvion, S. Gil, and C. Le Clec'H. Tolerance to dose escalation in mini-beam radiation therapy applied to normal rat brain: long-term clinical, radiological and histopathological analysis. *Radiation Research*, 184:314–321, 2015.

[135] I. Martínez-Rovira, J. Puxeu-Vaqué, and Y. Prezado. Dose evaluation of grid therapy using a 6 mv flattening filter-free (fff) photon beam: a monte carlo study. *Medical Physics*, 44(10):5378–5383, 2017.

[136] J.E. Reiff, M.S. Huq, M. Mohiuddin, and N. Suntharalingam. Dosimetric properties of megavoltage grid therapy. *International Journal of Radiation Oncology, Biology, Physics*, 33(4):937–942, 1995.

[137] I. Martínez-Rovira, G. Fois, and Y. Prezado. Dosimetric evaluation of new approaches in grid therapy using nonconventional radiation sources. *Medical Physics*, 42(2):685–693, 2015.

[138] W.V. Tenzel. Experience with grid therapy. *Radiology*, 59(3):399–408, 1952.

[139] Y. Prezado and G.R. Fois. Proton-mini-beam radiation therapy: a proof of concept. *Medical Physics*, 40:031712, 2013.

[140] M.D. Wright. Microbeam radiosurgery: an industrial perspective. *Physica Medica*, 31:601–606, 2015.

[141] A. Patriarca, C. Fouillade, M. Auger, F. Martin, F. Pouzoulet, and C. Nauraye. Experimental set-up for flash proton irradiation of small animals using a clinical system. *International Journal of Radiation Oncology, Biology, Physics*, 102:619–626, 2018.

[142] C. Peucelle, C. Nauraye, A. Patriarca, E. Hierso, N. Fournier-Bidoz, and I. Martínez-Rovira. Proton mini-beam radiation therapy: experimental dosimetry evaluation. *Medical Physics*, 42:7108–7113, 2015.

[143] T. Schneider. Technical aspects of proton mini-beam radiation therapy: mini-beam generation and delivery. *Physica Medica*, 100:64–71, 2022.

[144] M. Mohiuddin, C. Lynch, M. Gao, and W. Hartsell. Early clinical results of proton spatially fractionated grid radiation therapy (sfgrt). *British Journal of Radiology*, 2020.

[145] Jake Harold Pensavalle, Francesco Romano, Mariagrazia Celentano, Damiano Del Sarto, Giuseppe Felici, Gaia Franciosini, Luigi Masturzo, Giuliana Milluzzo, Vincenzo Patera, Yolanda Prezado, et al. Realization and dosimetric characterization of a mini-beam/flash electron beam. *Frontiers in Physics*, 11:1269495, 2023.

[146] Federico Picollo, Valentina Carabelli, Emilio Carbone, Daniele Gatto Monticone, Sara Gosso, Paolo Olivero, A Pasquarelli, Ettore Vittone, et al. Fabrication of a diamond-based cellular biosensor with ion beam lithography. In *LNL Annual Reports 2011*, volume 2011, pages 153–154. INFN Laboratori Nazionali di Legnaro, 2012.

[147] A Fidanzio, L Azario, P Viola, P Ascarelli, E Cappelli, G Conte, and A Piermattei. Photon and electron beam dosimetry with a cvd diamond detector. *Nuclear Instruments and Methods in Physics Research Section A: Accelerators, Spectrometers, Detectors and Associated Equipment*, 524(1-3):115–123, 2004.

[148] AJ Whitehead, R Airey, CM Buttar, J Conway, G Hill, S Ramkumar, GA Scarsbrook, RS Sussmann, and S Walker. Cvd diamond for medical dosimetry applications. *Nuclear Instruments and Methods in Physics Research Section A: Accelerators, Spectrometers, Detectors and Associated Equipment*, 460(1):20–26, 2001.

[149] Mara Bruzzi, Fred Hartjes, Stefano Lagomarsino, David Menichelli, Stefano Mersi, Stefania Miglio, Monica Scaringella, and Silvio Sciortino. Defect analysis of a diamond particle detector by means of photoconductivity and thermal spectroscopy characterization. *physica status solidi (a)*, 199(1):138–144, 2003.

[150] Zahir Muhammad, Yan Wang, Yue Zhang, Pierre Vallobra, Shouzhong Peng, Songyan Yu, Ziyu Lv, Houyi Cheng, and Weisheng Zhao. Radiation-tolerant electronic devices using wide bandgap semiconductors. *Advanced Materials Technologies*, 8(2):2200539, 2023.

[151] Alexander A Lebedev, Vitali V Kozlovski, Klavdia S Davydovskaya, and Mikhail E Levinshtein. Radiation hardness of silicon carbide upon high-temperature electron and proton irradiation. *Materials*, 14(17):4976, 2021.

[152] Stlab srl, (catania, italy), **2020**. available online: https://www.stlab.eu.; sensic gmbh, (villigen, switzerland), **2021**. available online: https://www.sensic.ch.

[153] C Weiss, J Wilson, G Tiebel, P Steinegger, E Griesmayer, H Frais-Kölbl, R Dressler, M Camarda, and M del Mar Carulla Areste. High-temperature performance of solid-state sensors up to 500° c. *Nuclear Instruments and Methods in Physics Research Section A: Accelerators, Spectrometers, Detectors and Associated Equipment*, 1040:167182, 2022.

[154] JM Bluet, J Pernot, J Camassel, S Contreras, JL Robert, JF Michaud, and T Billon. Activation of aluminum implanted at high doses in 4h–sic. *Journal of Applied Physics*, 88(4):1971–1977, 2000.

[155] Hideaki Tanaka, Satoshi Tanimoto, Mitsugu Yamanaka, and Masakatsu Hoshi. Electrical characteristics of al+ ion-implanted 4h-sic. In *Materials Science Forum*, volume 389, pages 803–806. Trans Tech Publications Ltd., Zurich-Uetikon, Switzerland, **2002**.

[156] W Wesch, A Heft, E Wendler, T Bachmann, and E Glaser. High temperature ion implantation of silicon carbide. *Nuclear Instruments and Methods in Physics Research Section B: Beam Interactions with Materials and Atoms*, 96(1-2):335–338, 1995.

[157] Naoya Takahashi, Suguru Itoi, Yoshiki Nakashima, WeiJiang Zhao, Hiroshi Onoda, and Shigeki Sakai. High temperature ion implanter for sic and si devices. In *2015 15th International Workshop on Junction Technology (IWJT)*, pages 6–7. IEEE, **2015**.

[158] Hyunpil Boo, Jong-Han Lee, Min Gu Kang, KyungDong Lee, Seongtak Kim, Hae Chul Hwang, Wook Jung Hwang, Hee Oh Kang, Sungeun Park, Sung Ju Tark, et al. Effect of high-temperature annealing on ion-implanted silicon solar cells. *International Journal of Photoenergy*, 2012, 2012.

[159] RBI. Ruer Bošković Institute. available online:. https://www.irb.hr/eng/Divisions/Division-of-Experimental-Physics/Laboratory-for-ion-beam-interactions/Articles/Accelerators.

[160] Selamnesh Nida, Alexander Tsibizov, Thomas Ziemann, Judith Woerle, Andy Moesch, Clemens Schulze-Briese, Claude Pradervand, Salvatore Tudisco, Hans Sigg, Oliver Bunk, et al. Silicon carbide x-ray beam position monitors for synchrotron applications. *Journal of Synchrotron Radiation*, 26(1):28–35, 2019.

[161] Francesco Romano, M Del Mar Carulla Areste, and Massimo Camarda. Feasibility study of using innovative technology based on silicon carbide detectors for flash irradiations. In *Conference presentation abstract of the Flash Radiotherapy & Particle Therapy Conference (FRPT2021), Physica Medica (inpress)*, **2022**.

[162] Mahsa Mokhtarzadeh, Maria Carulla, Roksolana Kozak, and Christian David. Optimization of etching processes for the fabrication of smooth silicon carbide membranes for applications in quantum technology. *Micro and Nano Engineering*, 16:100155, 2022.

[163] D Cosic, M Bogovac, and M Jakšić. Data acquisition and control system for an evolving nuclear microprobe. *Nuclear Instruments and Methods in Physics Research Section B: Beam Interactions with Materials and Atoms*, 451:122–126, 2019.

[164] James F. Ziegler. Srim - the stopping and range of ions in matter. available online:. https://www.srim.org.

[165] AA Lebedev, KS Davydovskaya, AM Strelchuk, and VV Kozlovski. Radiation resistance of 4h-sic schottky diodes under irradiation with 0.9-mev electrons. *Journal of Surface Investigation: X-ray, Synchrotron and Neutron Techniques*, 11(5):924–926, 2017.

[166] AA Lebedev, KS Davydovskaya, AN Yakimenko, AM Strel'chuk, and VV Kozlovskii. A study of the effect of electron and proton irradiation on 4h-sic device structures. *Technical Physics Letters*, 43(11):1027–1029, 2017.

[167] Andreo Crnjac, Natko Skukan, Georgios Provatas, Mauricio Rodriguez-Ramos, Michal Pomorski, and Milko Jakšić. Electronic properties of a synthetic single-crystal diamond exposed to high temperature and high radiation. *Materials*, 13(11):2473, 2020.

[168] K Kummer, A Fondacaro, F Yakhou-Harris, V Sessi, Paulius Pobedinskas, SD Janssens, Ken Haenen, Oliver Aneurin Williams, J Hees, and NB Brookes. Thin conductive diamond films as beam intensity monitors for soft x-ray beamlines. *Review of Scientific Instruments*, 84(3), 2013.

[169] Kewin Desjardins, Michal Pomorski, and John Morse. Ultra-thin optical grade sccvd diamond as x-ray beam position monitor. *Journal of Synchrotron Radiation*, 21(6):1217–1223, 2014.

[170] E Griesmayer, P Kavrigin, C Weiss, and S Kalbfleisch. Applications of single-crystal cvd diamond xbpm detectors with nanometre x-ray beams. In *13th International Conference on Synchrotron Radiation Instrumentation, SRI 2018*, page 060052. American Institute of Physics, 2019.

[171] SenSiC. Radiation Hard Silicon Carbide Sensors for real-time process monitoring and control. . available online:. https://www.sensic.ch/.

[172] Cividec Instrumentation. B9 diamond xbpm® detector, 2023. Accessed: 2023-10-31.

[173] Burton L. Henke, Eric M. Gullikson, and John C. Davis. X-ray interactions: photoabsorption, scattering, transmission, and reflection at e= 50-30,000 ev, z= 1-92. *Atomic Data and Nuclear Data Tables*, 54(2):181–342, 1993.

[174] M Tornago, R Arcidiacono, N Cartiglia, M Costa, M Ferrero, M Mandurrino, F Siviero, V Sola, A Staiano, A Apresyan, et al. Resistive ac-coupled silicon detectors: principles of operation and first results from a combined analysis of beam test and laser data. *Nuclear Instruments and Methods in Physics Research Section A: Accelerators, Spectrometers, Detectors and Associated Equipment*, 1003:165319, 2021.

[175] M Mandurrino, R Arcidiacono, A Bisht, G Borghi, M Boscardin, N Cartiglia, M Centis Vignali, G-F Dalla Betta, M Ferrero, F Ficorella, et al. The second production of rsd (ac-lgad) at fbk. *Journal of Instrumentation*, 17(08):C08001, 2022.

[176] LUCA Menzio, R Arcidiacono, G Borghi, M Boscardin, N Cartiglia, M Centis Vignali, M Costa, GF Dalla Betta, M Ferrero, F Ficorella, et al. Dc-coupled resistive silicon detectors for 4d tracking. *Nuclear Instruments and Methods in Physics Research Section A: Accelerators, Spectrometers, Detectors and Associated Equipment*, 1041:167374, 2022.

[177] Y Uesugi, R Mori, H Yamashiro, Taikan Suehara, T Yoshioka, and K Kawagoe. Study of position sensitive silicon detector (psd) for siw-ecal at ilc. *Journal of Instrumentation*, 15(05):C05033, 2020.

[178] N Cartiglia, F Moscatelli, R Arcidiacono, P Asenov, M Costa, T Croci, M Ferrero, A Fondacci, L Lanteri, L Menzio, et al. Resistive read-out in thin silicon sensors with internal gain. In *Proceedings of the 31st International Workshop on Vertex Detectors (VERTEX2022)*, page 011029, 2024.

[179] Tuba Çonka Yıldız, Wolfgang Freund, Jia Liu, Matthias Schreck, Dmitry Khakhulin, Hazem Yousef, Christopher Milne, and Jan Grünert. Diamond sensors for hard x-ray energy and position resolving measurements at the european xfel. *Synchrotron Radiation*, 31(5), 2024.

[180] TS Santra, TK Bhattacharyya, P Patel, FG Tseng, and TK Barik. Diamond, diamond-like carbon (dlc) and diamond-like nanocomposite (dln) thin films for mems applications. *Microelectromechanical systems and devices*, pages 460–466, 2012.

[181] Dina Carbone, Sebastian Kalbfleisch, Ulf Johansson, Alexander Björling, Maik Kahnt, Simone Sala, Tomas Stankevic, Angel Rodriguez-Fernandez, Björn Bring, Zdenek Matej, et al. Design and performance of a dedicated coherent x-ray scanning diffraction instrument at beamline nanomax of max iv. *Synchrotron Radiation*, 29(3):876–887, 2022.

[182] Ulf Johansson, Dina Carbone, Sebastian Kalbfleisch, Alexander Björling, Maik Kahnt, Simone Sala, Tomas Stankevic, Marianne Liebi, Angel Rodriguez Fernandez, Björn Bring, et al. Nanomax: the hard x-ray nanoprobe beamline at the max iv laboratory. *Journal of Synchrotron Radiation*, 28(6):1935–1947, 2021.

[183] PCR4. picoammeter by SenSiC. available online:. https://www.sensic.ch/electronic-readout.

[184] G Paternoster, G Borghi, Roberta Arcidiacono, M Boscardin, N Cartiglia, M Centis Vignali, GF Dalla Betta, M Ferrero, F Ficorella, M Mandurrino, et al. Novel strategies for fine-segmented low gain avalanche diodes. *Nuclear Instruments and Methods in Physics Research Section A: Accelerators, Spectrometers, Detectors and Associated Equipment*, 987:164840, 2021.

[185] A Bisht, G Borghi, M Boscardin, M Centis Vignali, F Ficorella, O Hammad Ali, and G Paternoster. Development of lgad sensors at fbk. *Nuclear Instruments and Methods in Physics Research Section A: Accelerators, Spectrometers, Detectors and Associated Equipment*, 1039:167018, 2022.